DEVELOPMENT OF NOVEL ENVIRONMENT-FRIENDLY MATERIALS USING EXPERIMENTAL AND COMPUTATIONAL METHODS

A Dissertation
Submitted to the Graduate Faculty
of the
North Dakota State University
of Agriculture and Applied Science

By

Ramsharan Pandey

In Partial Fulfillment of the Requirements
for the Degree of
DOCTOR OF PHILOSOPHY

Major Department:
Coatings and Polymeric Materials

April 2024

Fargo, North Dakota

North Dakota State University
Graduate School

Title

Development of Novel Environment-Friendly Materials Using Experimental and Computational Methods

By

Ramsharan Pandey

The Supervisory Committee certifies that this ***disquisition*** complies with North Dakota State University's regulations and meets the accepted standards for the degree of

DOCTOR OF PHILOSOPHY

SUPERVISORY COMMITTEE:

Dr. Dean C. Webster
Chair

Dr. Adam C. Gladen (co-advisor)

Dr. Ghasideh Pourhashem

Dr. Bakhtiyor Rasulev

Dr. Scott W. Pryor

Approved:

April 12, 2024 — Date

Dr. Dean C. Webster — Department Chair

ABSTRACT

The environmental issues stemming from the production and use of fossil-based and environmentally hazardous materials are of great concern. Therefore, environment-friendly materials need to be pursued which can either be achieved by improving the production and performance of conventional materials or by replacing conventional fossil-based materials with renewable environment-friendly materials.

The first part of this dissertation covered the synthesis and characterization of novel coatings for ice and biofouling release applications. Conventional systems for ice removal are time, energy, and chemical-intensive posing issues related to greenhouse gas emissions, soil and water contamination, and other environmental pollution. Similarly, conventional systems for preventing marine biofouling involve the use of biocide-containing coating which is detrimental to marine ecosystem. The goal here was to develop potentially environment-friendly ice and biofouling release coatings. To achieve this goal, a polyurea-siloxane base coating was synthesized and modified with silicone oils. The first set of coating formulations used different non-reactive silicone oils as additives while the second set of coating formulations grafted different carbinol functional polydimethylsiloxane into the base coating. These coatings were characterized for their surface properties and tested for ice adhesion, interfacial toughness, and a range of laboratory bioassays. They showed low ice adhesion strength and low interfacial toughness making them a promising candidate for ice-shedding applications.

The second part of this dissertation covered the use of sustainability assessment tools such as techno-economic analysis (TEA) and life cycle assessment (LCA) for different early-stage technologies. TEA and LCA were performed for scaled-up production of lignin-based foam from laboratory scale data to determine its selling price and environmental impacts. Factors

contributing to higher cost and environmental impacts along with the potential advantage of lignin-based foam compared to conventional rigid polyurethane foams were discussed. Similarly, LCA was performed for salt hydrate cellulose nanocrystal composites for thermochemical energy storage applications and molten salt biomass torrefaction system to identify environmental impact hotspots from the processes and input raw materials. The results from the analyses suggested potential areas for improvement to reduce the environmental impacts of these new technologies.

Overall, this dissertation contributes to the advancement of eco-friendly and sustainable materials development.

ACKNOWLEDGMENTS

As I conclude my dissertation, I want to express deep gratitude to everyone who has been part of this transformative journey. The past five years of my PhD have been intellectually fulfilling and rewarding, providing opportunities to work on interdisciplinary projects. I've honed my skills in material synthesis, characterization, sustainability assessment, and computational methods. This academic exploration has broadened my knowledge and allowed me to contribute meaningfully to diverse research areas. I am sincerely thankful for the unwavering support and mentorship that have shaped my growth throughout this rewarding experience.

I would like to thank my major advisor Dr. Dean C. Webster for the opportunity to work under his mentorship and guidance. Thank you for your support in difficult times. The past couple of years in your research group have been very enriching. You taught me how to think independently and grow as a researcher. The skills and knowledge that I gained under you will be useful for my lifelong career. I would greatly miss the group meetings which have been very helpful for me to learn and understand concepts, gain research ideas, and learn about experimental techniques.

I would like to thank my co-advisor Dr. Adam C. Gladen. It was a pleasure working with you. Thank you for your dedication to teaching me the values of hard work, motivation, dedication, and critical thinking. This has been and will be instrumental in shaping my future career. Thank you for providing all the resources and help that were needed for the successful completion of research work and also for personal growth. I would also like to thank my former advisor Dr. Ghasideh Pourhashem. Thank you so much for instilling my interest in sustainability science and teaching all the valuable skills. Your guidance has been very helpful throughout my degree.

Thanks to my committee members Dr. Bakhtiyor Rasulev and Dr. Scott W. Pryor for your guidance during my proposal writing, defense, and research work. Dr. Pryor, you have been very inspirational to me during my early years at NDSU. I am very grateful to you for helping me develop research skills, critical and independent thinking, and integrity.

To my parents, I would like to thank you for your unwavering support, belief in me, and endless encouragement. I am forever grateful for the countless sacrifices you have made to bring me to where I am today. Your unwavering support has been a constant source of strength and the driving force behind every accomplishment. To my wife, Anupa Bhatta, thank you for your love, unwavering support, encouragement, and dedication. Thank you for standing by my side through every challenge and success. Your selfless help and support have been instrumental in my success. I am grateful for the love and light you bring into my life each day. To my brother, sister, and all the family members, thank you for your love, support, and encouragement. Your presence has been the source of strength and happiness.

To Dr. Na Wu, thank you for helping me with process modeling work and economic analysis. Your guidance has been instrumental for me in developing valuable skills. I could not have asked for a better mentor. To Dr. David Boucher and Dr. Daniel Bellido Aguilar, thank you for your guidance and for helping me explore experimental works on ice-shedding coatings. David, thank you for answering all my questions and helping me in the self-segregating coating project. I would also like to express my gratitude to the group members: Dr. Alexander Hart, Wanli Cheng, Maryam Safaripour, and Joseph Dahlgren. I would like to thank group members Shokoofeh Ghasemi and Iryna Bon for being supportive during my graduate studies. You guys were very encouraging during difficult times, and I will always cherish our friendship. Thank you Shokoofeh for the helpful discussions and suggestions in the research work. To group

members, Lee Kohlin and Behrooz Heidari, thank you for your help in the molten salt-biomass torrefaction project.

I would also like to thank Jim Bahr, Shane Stafslien, Lyndsi Vanderwal, Greg Strommen, Fred Haring, and Dr. Chunju Gu for their support in laboratory work and use of instruments. I would also like to thank our collaborators at the University of Michigan: Dr. Anish Tuteja and Tyler Olson. Thank you, Tyler, for performing interfacial toughness tests for my coating samples. To Dr. Dilpreet Bajwa and Daniel Blake from Montana State University, thank you for your help in providing experimental details for the salt-CNC thermochemical energy storage project.

To CPM administration: Janice, Ben, Sarah, Rachel, and Michael for helping me with all the administrative work. Thank you to all the CPM faculties for being nice and helpful throughout my graduate study here.

I am very grateful to the sponsors: the National Science Foundation Grant IIA-1355466, the Office of Naval Research (award number N00014-22-1-2129), the US Department of Energy (award number DE-EE0009678) for funding my work. I would also like to thank the PPG Foundation for their generous scholarships, NSF for a conference travel grant, and the American Coatings Association for grants to attend conferences.

Finally, I would like to thank North Dakota State University for providing me with the opportunity to pursue my PhD here.

DEDICATION

I would like to dedicate this dissertation to my parents, Ram Prasad Pandey, and Sita Pandey, for their unwavering support and sacrifices that enabled me to reach this milestone.

TABLE OF CONTENTS

LIST OF TABLES

LIST OF FIGURES

LIST OF APPENDIX TABLES

LIST OF APPENDIX FIGURES

CHAPTER 1. GENERAL INTRODUCTION

1.1. Need for environment-friendly materials

The ongoing environmental problems, primarily due to the production and use of conventional fossil-based and environmentally hazardous materials, are of great concern. The production and use of these materials pose problems such as resource depletion, pollution due to environmental emissions, and adverse impacts on terrestrial and aquatic ecosystems. Conventional materials which are predominantly derived from fossil fuels contribute to finite resource depletion as they are consumed at a higher rate than their renewal rate. The production and use of these materials also cause the release of harmful pollutants and greenhouse gases into the atmosphere. This contributes to climate change as well as poses risks to human and animal health. Moreover, the toxic components released to the terrestrial and aquatic environment due to the production of these materials affect the vegetation and the ecosystem in these environments.

Therefore, environment-friendly materials are being pursued to overcome the above-mentioned challenges. There are two facets when talking about environment-friendly materials: improving the production and performance of conventional materials, and using renewable environment-friendly materials. The first method involves improving the process of material production by reducing waste, energy consumption, and overall material use. The process can also be improved by replacing the process/technology involving toxic materials with more environmentally friendly materials and technology and promoting the effective lifetime of the material. The new materials/technology can either be fossil-based or renewable materials. The second method involves replacing fossil-based materials and technologies with renewable materials and technologies. One example of replacing fossil-based materials is through biobased materials. However, in doing all these, the new materials need to be characterized for their

performance, application-wise and through the sustainability perspective compared to the conventional system.

1.2. Sustainability metrics: Incorporating economic and environmental factors

Sustainability is a broad term and involves three main pillars: economic, environmental, and social. The social aspect is a complex metric to analyze, however, both the economic and environmental metrics are relatively well-defined and can easily be incorporated into the early-stage technologies. Early-stage technologies are usually defined in terms of technology readiness levels (TRLs) as given in Table 1.1. Sustainability assessment can be used in any stage of TRLs, however, earlier use is more recommended as this can help to improve the process and avoid material with high environmental impacts as well as high costs. Techno-economic analysis (TEA) and life cycle assessment (LCA) are two metrics that are commonly used for assessing the economic and environmental sustainability of new materials and technologies, respectively. TEA is a method of analyzing the economic competitiveness of a product or process. Usually, TEA involves process modeling to generate mass and energy balance along with equipment sizing which are used to determine capital costs, operating costs, and revenues. This helps to identify the higher-cost processes and materials that need to be either improved or replaced with lower-cost processes or materials. The different costs associated with TEA are:

i. Capital costs: These include the costs for land, construction, purchase and installment of equipment, and working capital.

ii. Operating costs: These include costs for procuring raw materials, utilities, maintenance costs, personnel costs, and labor costs.

iii. Revenues: Revenues come from selling the products produced by the facility.

The technical feasibility of alternative technology/materials does not necessarily mean they are economically and environmentally competitive or better than conventional technology/materials. The economic and environmental feasibility of chemical production can be assessed at different levels based on the research stage. The maturity of technology and research for any chemical process is usually measured in terms of technology readiness level (TRL) [1]. TRLs are rated up to 9 different levels, as shown in Table 1. Level 1 corresponds to the lowest level of readiness while level 9 corresponds to the full-fledged production system working with desired results.

Table 1.1. Description of Technology Readiness Levels (TRLs) (adapted from [1,2])

TRL level	Stage in production	Description
TRL 1	Idea generation	The first stage is research. Review of relevant technologies.
TRL 2	Concept Formulation	Application areas and basic working processes are highlighted.
TRL 3	Concept demonstration	Initial laboratory works conducted; basic mechanism demonstrated by experimental results.
TRL 4	Concept validation	Validating if all unit processes can be integrated, preliminary simulation works done and process designing starts.
TRL 5	Laboratory scale	Unit processes are integrated, and lab-scale prototypes are tested and validated. Detailed process design begins.
TRL 6	Pilot scale	The laboratory scale process extended to the pilot scale process. Scaling issues are identified and solved. The working environment of the pilot scale should represent the actual production environment. Pilot-scale production starts.
TRL 7	Full-scale demo plant	Pilot scale processing conditions are optimized, and a full-scale demo plant is started in the field. The final stage of detailed engineering design begins.
TRL 8	Full-scale plant commissioned	The design and full-scale construction are complete. Full-scale processing parameters are fully optimized and detailed operating procedures are identified. Startup phase of the plant.
TRL 9	Normal production phase	The plant starts production at full capacity with design conditions and expected outputs.

LCA, on the other hand, is a method to assess the environmental impacts of a product or process by looking into the flow of materials and energies at different stages of the product or process life cycle. The general framework of LCA is given in Figure 1.1. The different steps in conducting LCA are:

i. Goal and scope definition: In this step, the goal of pursuing the LCA is clearly defined with the scope and system boundary for analysis. The functional unit for quantifying the impacts is also defined in this stage.

ii. Inventory analysis: The input-output flows of all the material, energy, and emissions within the system boundary are defined in this stage. The data for all the inventories is collected for the impact analysis.

iii. Impact assessment: Impact analysis of each of the inputs and the cumulative impact of the whole process are analyzed following the standard analysis methods. There can be mid-point or end-point indicators that can be used for the impact analysis. It needs to be identified early on in the scope definition. Once the impact analysis is completed, the interpretation of the results is carried out. Since LCA is an iterative process, the analysis can be updated as more data or information is obtained for the specific process.

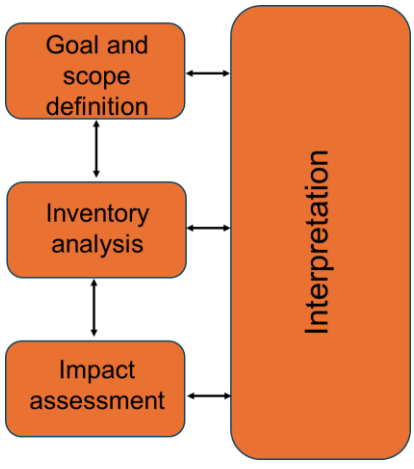

Figure 1.1. Life cycle analysis framework based on ISO 14040 [3]

This dissertation deals with both approaches to producing environment-friendly materials. The first part of the dissertation covers the synthesis and characterization of ice and biofouling release coatings which are expected to be better than conventionally used methods for ice removal and bio-foulants. The second part of the dissertation covers the use of TEA and LCA in the production of biobased polymer, specifically lignin foam; thermochemical energy storage material based on salt hydrates and cellulose nanocrystals; and molten salt biomass torrefaction system.

1.3. Section I

1.3.1. Ice accretion – Challenges and economic-environmental impact implications

Ice is a common foulant in cold climates. Ice can build up on surfaces such as marine vessels navigating through arctic climates, airplanes flying in high altitude and cold climatic regions, and wind turbines and electrical transmission lines in cold regions. The unwanted accretion of ice on these surfaces can prevent proper functioning of these systems creating safety issues as well as premature failure. Ice accumulation in marine vessels can increase drag and load, reducing power efficiency and increasing fuel consumption, thus increasing environmental emissions. Similarly, ice accumulation in airplanes can affect the aerodynamic performance, by increasing drag and reducing lift. This can lead to performance degradation and safety issues. Ice accumulation in wind turbines and electrical transmission lines can reduce power production and transmission efficiency, respectively, along with safety issues. Apart from these, ice can also cause material degradation, either during settlement or during the removal. This can introduce active corrosion sites in metallic substrates. All these factors can lead to increased costs of maintaining these structures.

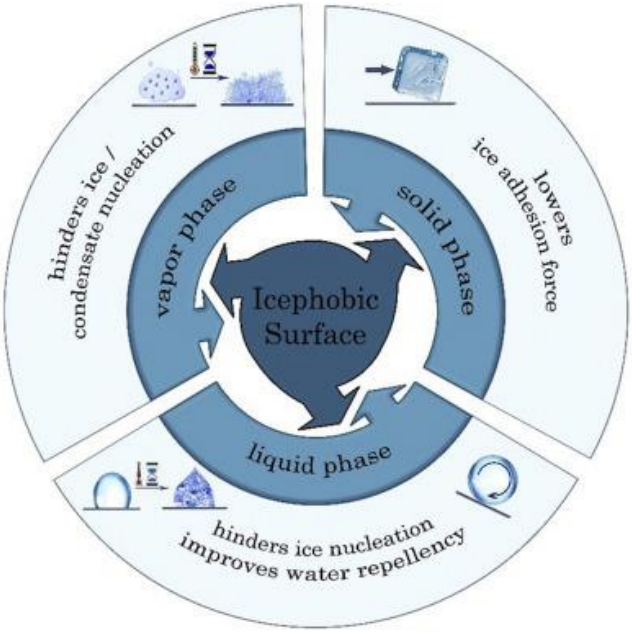

Figure 1.2. Properties of an ideal icephobic surface (reproduced from [4])

The traditional method of ice removal involves the use of heat to melt ice, mechanical scraping, or deicing liquids. These methods are very time-consuming, labor and energy-intensive, and not environment friendly. For example, the chemicals used in deicing can wash away and contaminate soil and water affecting the soil health and aquatic ecosystem [5]. Passive methods of ice removal through the application of coatings can be a way to overcome some of these environmental impacts and cost issues. An ideal coating that can be applied on these surfaces should be able to either prevent the formation of ice on the surface or lower the ice adhesion strength if ice is formed on the surface (Figure 1.2) [4]. Water can exist in three different phases: solid, liquid, and vapor. The solid phase refers to ice, the liquid phase to liquid water, and the vapor phase to water vapors. Icephobic coatings should be able to lower the adhesion strength of solid phase water i.e. ice, able to repel water or delay to ice formation for liquid phase water, and able to prevent vapor condensate nucleation to form ice. Apart from

these, the coating surface should also show good mechanical properties such as tensile strength, chemical resistance, impact resistance, and good durability.

1.3.2. Wettability on different surfaces

The wetting of a surface by water usually occurs in different states depending on the surface roughness as shown in Figure 1.3 [6]. For an atomically smooth or homogeneous surface, water can wet the surface as seen in Figure 3(a). The work of adhesion of water in contact with the solid coating surface can be determined by the Young-Dupre equation (equation 1.1).

$$W_a = \gamma_{lv} (1 + cos\theta_e) \quad (1.1)$$

where W_a is the work of adhesion, γ_{lv} is the liquid-vapor surface tension, and θ_e is the equilibrium contact angle. Therefore, in the liquid state, water repellency from a surface is highly dependent on the contact angle of the liquid with the surface. A higher contact angle results in lower adhesion strength. Rough or heterogeneous surfaces usually result in two modes of wetting with the surface: Wenzel mode and Cassie-Baxter mode [7,8]. In Wenzel mode, the water droplet completely wets the surface, thus having increased contact area and higher adhesion. In Cassie-Baxter mode, air is trapped between the liquid and the rough surface, reducing the contact between the surface and the droplet, thus having lower adhesion. The resulting contact angles for these kinds of surfaces are defined by Wenzel and Cassie Baxter's models. The apparent contact angles for Wenzel mode are lower than Young's contact angle while the apparent contact angles for the Cassie-Baxter mode are higher than Young's contact angle.

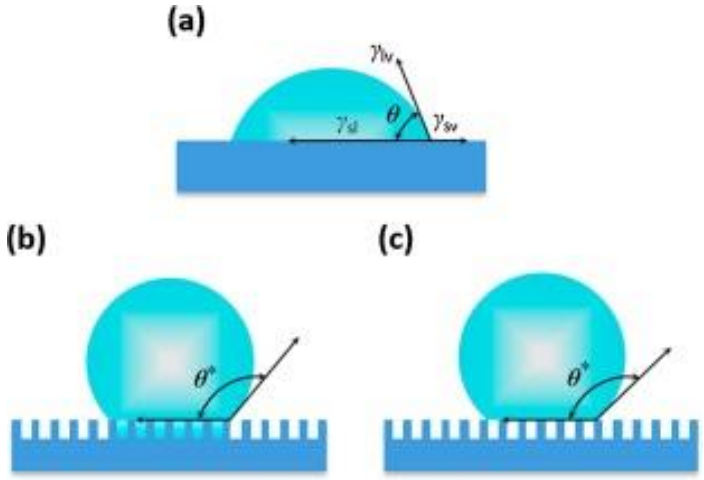

Figure 1.3. Wetting mechanisms of a liquid on a surface. (a) On a flat surface. (b) Wenzel mode on a rough surface. (c) Cassie-Baxter mode on a rough surface (reproduced from [6])

The adhesion of ice, which is a frozen state of water, with the substrate is more complex than that with a liquid state and does not resemble the same property as seen with the liquid due to the formation of a crystalline structure. Generally, hydrophilic surfaces have higher ice adhesion while hydrophobic surfaces have lower ice adhesion. In rough surfaces, if the water in the Wenzel state freezes, ice adhesion strength is high due to higher contact area with the surface and mechanical interlocking. If the water freezes in the Cassie-Baxter state, ice adhesion strength is low due to the lower contact area of ice with the surface.

1.3.3. Methods of preventing ice accumulation

Different methods have been explored as a passive method of reducing ice adhesion to the substrate. The generally used methods include elastomers, superhydrophobic surfaces, hydrophilic surfaces, amphiphilic surfaces, slippery surfaces, and self-segregating coatings.

1.3.3.1. Elastomers

Elastomers are soft materials with very low modulus. Due to their low modulus, ice can be easily detached from their surfaces with deformation of their surface, usually referred to as deformation incompatibility (DI) [9]. However, their main drawback is that due to their low

modulus, these materials are not durable and are easily damaged. The durability of these materials can be tuned to some extent by modifying the cross-link density and incorporating self-healing capability, however, these may not be sufficient for the long-term stability of these surfaces [10,11].

1.3.3.2. Superhydrophobic surfaces (SHSs)

SHSs are widely studied for anti-icing applications. SHSs show very high-water contact angle, usually above 150° such that water droplets can easily roll off from the surface. The non-wetting property of lotus leaf, which has a Cassie-Baxter type surface property, is one of the examples of naturally occurring SHS [12]. This inspired researchers to fabricate artificial SHSs in the lab. Different micro and nano-textured surfaces have been developed and studied [13–15]. Maghsoudi et al. prepared microtextured silicone rubber with a water contact angle greater than 160° and showed that ice adhesion strength reduced with smaller micro-nanostructures [16]. Davis et al. prepared a superhydrophobic nanocomposite composed of a polyurethane backbone and silica-fluoroacrylic hydrophobic surface and showed lower ice adhesion [17]. SHSs can either delay the freezing of water droplets or lower ice adhesion strength through ice formation in the Cassie-Baxter state [18]. However, there are debates on whether SHS is good for ice-shedding applications. SHSs do not perform well in high-humidity conditions [19–21]. The textured microstructures can promote water vapor condensation giving rise to frost formation quickly such that ice can build up around these frosts [22]. Due to mechanical interlocking and larger surface contact, ice adhesion strength becomes high.

1.3.3.3. Hydrophilic surfaces and amphiphilic surfaces

Hydrophilic surfaces have also been studied for anti-icing applications based on the observation of skates that slide easily on ice surfaces [23]. Hydrophilic surfaces can delay the

freezing of water which can easily spread over the surface creating a hydration layer [24,25]. Ice that forms over it has low adhesion strength. Ozbay et al. studied a range of hydrophobic, and hydrophilic lubricating liquids for icephobic properties and found that hydrophilic surfaces are more suitable for anti-icing applications [26]. However, hydrophilic surfaces can result in higher adhesion strength for large-scale applications [27].

Amphiphilic surfaces include both hydrophilic and hydrophobic moieties in its structure. Yu et al. developed an amphiphilic organo-gel that showed delayed water freezing and low ice adhesion strength [28]. Similar results were seen in other studies using amphiphilic surfaces [29,30]. Similar to hydrophilic surfaces, amphiphilic surfaces can also delay ice formation and create a hydration layer by absorbing water through the hydrophilic part and reducing ice adhesion [31]. The balance between hydrophilic and hydrophobic parts is very important in determining the ice adhesion properties of these surfaces.

1.3.3.4. Slippery surfaces

One of the sub-categories of SHSs includes replacing the air entrapment in the Cassie-Baxter state with slippery liquids such that ice that forms over its surface can easily slide off with very low ice adhesion strength. These types of surfaces are usually called SLIPS (slippery liquid-infused porous surfaces). These surfaces resemble the characteristics of pitcher plants [32]. The working mechanism of SLIPS is shown in Figure 1.4. SLIPS have micro/nanoporous surfaces that are filled with lubricating liquids, usually fluorinated or silicone oils that result in very low ice adhesion strength [18]. However, the major drawbacks of these types of systems are the complexity of their fabrication and their durability. The slippery liquids get washed away over time through multiple icing-deicing cycles, thereby reducing the oil on the surface. This can result in loss of icephobic property.

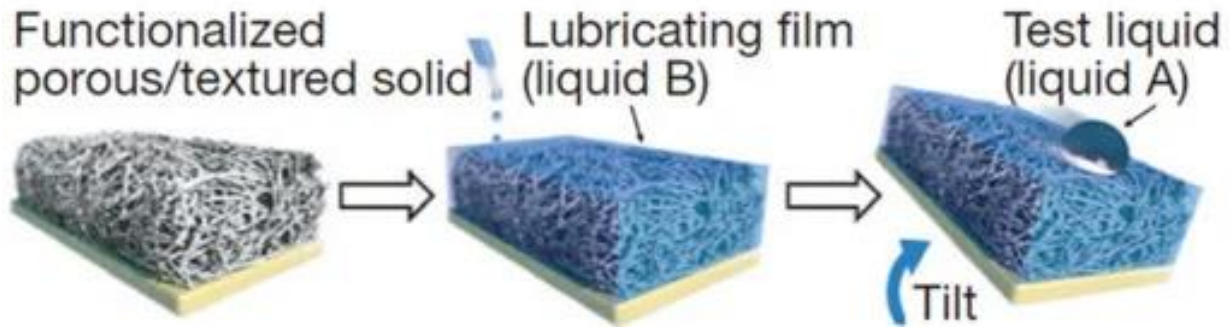

Figure 1.4. The working mechanism of SLIPS where low surface energy, non-reactive lubricating liquid covers the pores and surface of the porous surface and provides low adhesion strength to ice and water (reproduced from [33])

Different facile methods of incorporating lubricating liquids into the polymer matrix have also been studied [34–36]. However, these systems also have durability problems. To overcome the drawback of slippery liquid-infused surfaces, hydrophobic moieties can be grafted into the backbone matrix. These hydrophobic moieties usually have low surface energy and can segregate towards the surface acting as a polymer brush. They can provide surface flexibility and deformation for easy removal of ice. Since they are covalently grafted with the matrix, they will remain attached to the matrix. This improves the shorter durability problem seen with free oils. Zheng et al. crosslinked hydroxyl-terminated PDMS oils with an epoxy system and showed reduced ice adhesion strength compared to bare epoxy coating [37]. Zhou et al. prepared a self-segregating coating with a polyurethane backbone and silicone-fluorine on the surface and showed hydrophobic properties [38].

1.3.4. Scales of ice accumulation

Ice accumulation can occur on several scales. Depending on the application areas, from small-sized substrates like sensors to large-scale substrates like airplane wings, wind turbines, ship hulls, or solar panels, ice length can vary greatly. For a given surface, the ice adhesion strength is constant. However, depending on the length scale of the ice, the force required to

remove ice does not scale linearly [39]. After a certain length scale of ice, the force required to remove ice becomes constant irrespective of the length of ice. The length of ice at this point is called critical length and the force is called critical force. Based on this observation, ice removal from a surface irrespective of the length scale of ice, can be broadly divided into two categories: strength-controlled regime and toughness-controlled regime [39]. In the strength-controlled regime, the force required to remove ice is dependent on ice adhesion strength while in the toughness-controlled region, the force required to remove ice is dependent on the interfacial toughness strength of the surface/material. The interfacial toughness of a material is the ability of a material to resist the propagation of crack. Easier crack propagation through the substrate-ice interface helps to detach the ice from the substrate easily. Based on this theory, low interfacial toughness materials are more prone to easier removal of ice, irrespective of the length scale of ice after critical length surpasses. Therefore, low interfacial toughness (LIT) materials are essential for large-scale de-icing [40,41] such that ice accumulated on these surfaces can be removed under a small external force, gravity, vibration, or wind. The interfacial toughness of a material is related to ice adhesion strength [39] by equation 1.2.

$$\Gamma = \frac{(F_{ice}^{cr})^2}{2E_{ice}h} \tag{1.2}$$

Where Γ is the interfacial toughness, F_{ice}^{cr} is the critical force, E_{ice} is the elastic modulus of ice (≈ 8.5 GPa), and h is the thickness of the ice layer.

1.3.5. Marine biofouling – Challenges and economic-environmental impact implications

Marine biofouling is the unwanted settlement of marine organisms on surfaces submerged in the marine environment. Marine biofouling is a challenging problem concerning the maritime transportation and protection of submerged marine structures as seen in Figure 1.5. Marine biofouling on ship hulls can significantly increase the weight and drag, reduce speed and

maneuverability, and thus increase fuel consumption. Fuel consumption alone can increase by 30-40% for fouled ships compared to unfouled ships [42]. The estimated cost of marine biofouling alone for the US Navy is greater than $1 billion per year [42]. The settlement of marine organisms on ship hulls can damage the protective coatings and this area can act as a site for corrosion initiation. Biofouling in ships also results in higher dry-docking time for cleanups which increases the maintenance costs and loss of revenue due to ship downtime. Higher fuel consumption for fouled marine vessels results in higher greenhouse gas emissions that can significantly increase environmental pollution. Marine biofouling can also transfer the invasive marine organisms from one location to the other which can disrupt the local ecosystem of that particular location. Therefore, biofouling has both economic and environmental implications, necessitating the development of effective biofouling mitigation strategies.

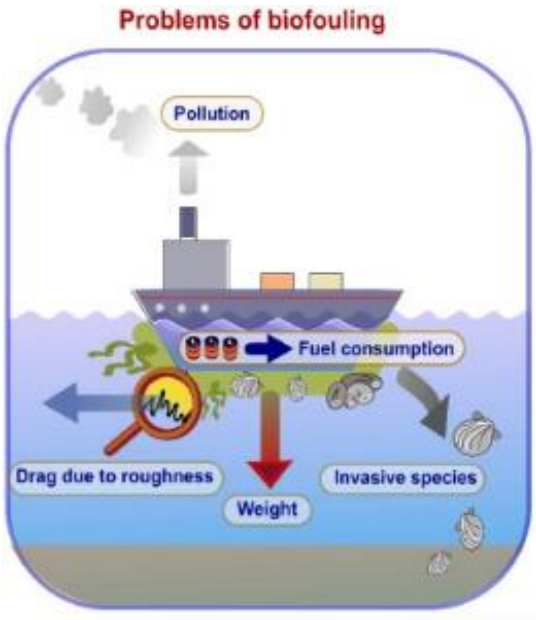

Figure 1.5. Problems of biofouling and drawbacks of coatings (reproduced from [43])

1.3.6. Mechanism of biofouling

There are estimated to be more than 4000 marine organisms that can adhere and settle on a surface ranging from microfoulants such as marine bacteria, diatom, algae, and macrofoulants

such as barnacles, hydroids, corals, tubeworms, bryozoans, and mussels [44]. This vast number of organisms results in different modes of adhesion and biofouling which are influenced by several factors such as water temperature, salinity, availability of nutrients, and presence of other organisms. Biofouling begins as soon as the surfaces are submerged in marine environments. Typically, biofouling starts with the adsorption of different biomolecules such as proteins, polysaccharides, and glycoproteins from the nearby water onto the submerged surface forming a conditioned film [45]. This film generally serves as a substrate for other foulants to adhere to. Microfoulants such as bacteria and diatoms attach to the conditioned film and then colonize creating a biofilm layer [45]. This layer acts as a substrate for other large foulants such as sponges, barnacles, mussels, and corals. These macrofoulants once attached grow and mature and they can release more larvae into the surrounding water. These larvae can further spread biofouling. Although these series of events seem linear, biofouling of these species can occur in any order. A general schematic of the process of biofouling is shown in Figure 1.6.

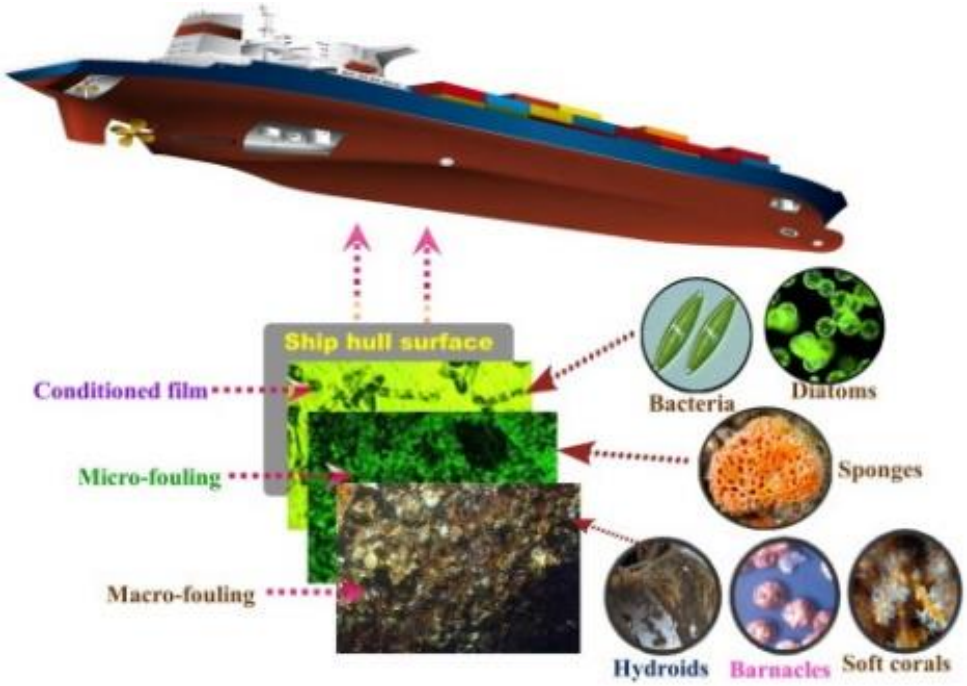

Figure 1.6. Different steps of marine fouling (reproduced from [46])

Microorganisms such as bacteria and algae attach to the surface either physically through their appendages or chemically in the form of van der Waals forces, electrostatic interactions, and surface charges [45]. Different microbes in the conditioning film produce extracellular polymeric substance (EPS) which is a sticky matrix of proteins and polysaccharides. This substance helps provide a stable environment for the attachment of other foulants. Macrofoulants such as barnacles and mussels secrete adhesive proteins into the substrate and then attach. Larvae, often follow the chemical signals from the biofilms and mature organisms to find a suitable attachment area. They also utilize their appendages to explore and find suitable adhering areas on the surface. Since biofouling is a very complex phenomenon, combating biofouling requires a holistic and multifaceted approach involving the development of advanced materials.

1.3.7. Methods of preventing biofouling

The earliest method of preventing biofouling centered around the use of pitch, tar, wax, and heavy metals such as copper-based paints. Around the 1960s, paints with tributyl tin (TBT) based compounds appeared to show effective inhibition to bifoulants adherence. However, TBT was found to be toxic to non-targeted marine species, aquatic ecosystems, and human health [47–49]. This led to the worldwide ban on the production of TBT-based paints in 2003 and a ban on any marine vessels coated with TBT-based paints in 2008 [50]. This ban led to the use of copper as the main biocide in antifouling paints [51]. However, copper is also somewhat toxic to aquatic ecosystems [52]. This led to an increased interest in alternative strategies for mitigating biofouling.

Generally, coatings used to mitigate biofouling can be divided into two categories: antifouling (AF) and fouling release (FR). A schematic of different strategies used to control biofouling and the drawbacks of coatings in fouling control is shown in Figure 1.7. Antifouling

coatings prevent the attachment of biofoulants by inhibiting their attachment or growth. These coatings use biocides as additives in the coatings creating a toxic surface to prevent the adhesion of biofoulants. Some forms of AF coatings use the mechanism of self-polishing along with mild use of toxic biocides to overcome the use of harsh toxic biocides and provide effective fouling control over time [45]. In such coatings, the coating surface wears away gradually such that fresh layers of biocides are exposed again providing effective fouling control. On the other hand, FR coatings do not use biocides and prevent or reduce the adhesion of biofoulants solely by their mechanical and surface properties.

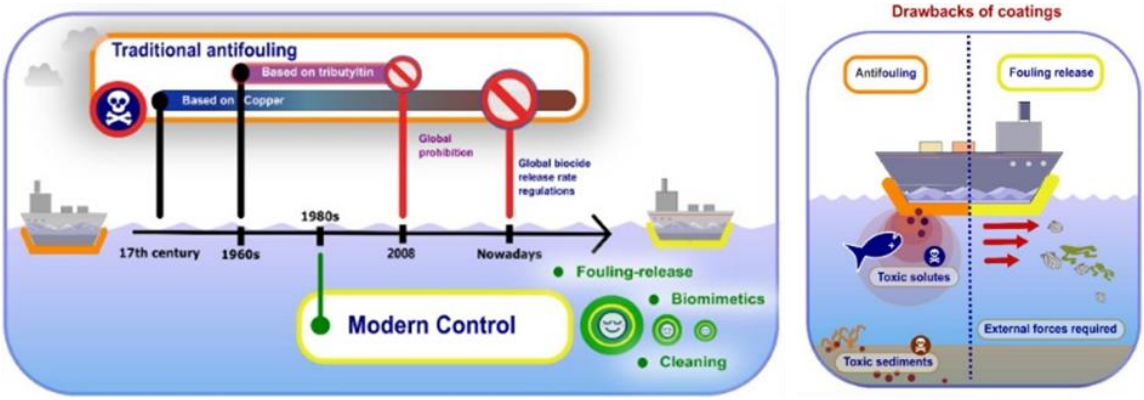

Figure 1.7. Historical development of biofouling controls and drawbacks of coating (reproduced from [43])

FR coatings are an environment-friendly alternative to AF coatings. These coatings are generally ultra-smooth with low surface free energy such that the fouling organisms cannot adhere strongly. A small external force is required to remove foulants. When the marine vessels are in motion, the hydrodynamic pressure created by water on the ship hulls can remove the foulants. It also reduces the overall fuel consumption due to reduced water drag and the service life of these forms of coatings is usually 10-15 years (higher than AF coatings) [45]. Most of the fouling release coatings are based on either fluoro-polymers or silicone polymers. Fluoro-polymers have very low surface tension values, around 10-20mN/m and they have chemical,

heat, and UV stability [45]. However, they are very costly, have poor adhesion, and are also detrimental to marine organisms and human health. Silicone-based polymers are used as their alternatives with good fouling release performance. However, silicone polymers alone are very soft materials, have poor mechanical properties, and have low adhesion strength with the substrates. Silicone materials can be used along with durable polymer matrices such as polyurethane, polyurea, or epoxy to improve the adhesion and durability issues. Siloxane-polyurethane matrix has been extensively studied as a fouling release coating at NDSU [53–58]. The polyurethane part provides good mechanical properties and adhesion while the siloxane part self-segregate towards the surface and provides low surface-free energy fouling release properties.

The siloxane-polyurethane coating showed some promising results with biological assays and field tests. Several modifications were tested to further improve the performance of these coatings. Most of these modifications included using an amphiphilic copolymer either used as a non-reactive additive to the matrix or grafted into the matrix. Amphiphilic moieties can include, for example, polyethylene glycol as the hydrophilic part and PDMS as the hydrophobic part. Several other amphiphilic additives have been developed and tested for biofouling assays [59–61]. The results from these studies showed that biofouling is a complex phenomenon and different surface properties can influence the overall performance of these coatings. The presence of specific surface structures, surface activity, modulus, functionality, type of polyol, and solvent, as well as a good balance between the ratio of different components, are equally important.

1.4. Section II

1.4.1. Renewable and biobased materials

With the growing concerns about the use of non-renewable fossil fuels as a source of energy and materials production, there are interests in substituting these with renewable and biobased alternatives. For energy applications, we are heavily dependent on the use of fossil fuels. Fossil fuels are the primary energy source in the transportation sector, industrial applications, and household space heating purposes. Fossil fuels are the primary contributor to different environmental issues such as global warming, ozone depletion, water, air, and land pollution, and emission of particulate matter. Renewable alternatives such as solar energy, wind energy, biofuels, and biobased chemicals are being considered to replace fossil-based energy and material production but their economic and environmental viability are still ambiguous. Even though these alternatives are renewable, their production and processing might use excess resources and fossil-based chemicals. This can result in these renewable alternatives being deemed less sustainable. Therefore, a holistic system analysis for both environmental impact and economic viability must be conducted. LCA looks into the product/process life cycle, identifies their environmental impacts, and hotspots that need to be improved, and provides future research direction. Similarly, TEA considers technical feasibility along with the economic implication of the product/process and determines if it is economically feasible and competitive compared to conventional product/process.

1.4.2. Lignin based polymers

Lignin is the most abundant aromatic biopolymer found on earth. Lignin is a polyphenolic material made up of three basic units called monolignols which include: p-hydroxyphenyl (H) or p-coumaryl, Guaiacyl (G), and Syringyl (S) units [62]. These monolignols

form a heterogenous three-dimensional polymer network by radical-radical coupling reactions. Lignin has different functional groups associated with its structure including aliphatic and aromatic hydroxyls, methoxyl and carbonyl groups, benzyl alcohol, and non-cyclic benzyl ether [63]. The composition of natural lignin varies with plant species and is highly dependent on the growth conditions as well. Likewise, the structure of technical lignin obtained from various chemical extraction processes also varies. For example, organosolv and biorefinery lignin are highly pure with lower molecular weight and narrower polydispersity index while kraft and lignosulfite lignin and highly impure and have wider polydispersity index [64]. Technical lignin is less reactive due to the formation of highly stable C-C linkages through condensation reactions during chemical lignin extractions [65]. However, technical lignin can be chemically modified to overcome its structural variabilities. Lignin has potential in various composites, thermoplastics, and thermosets applications. Lignin reactivity can be improved by functionalizing it with more reactive functional groups such as phenols, acrylates, epoxies, amines, and vinyls before using in different applications. The promising applications of lignin include phenol-formaldehyde resin, epoxy resins, polyurethane foams, carbon fibers, and other macromolecular applications [66].

Phenol-formaldehyde resins are widely used as adhesives in paper industries, binders in wood composites and particle boards, and various coatings applications. The presence of aromatic hydroxyl groups in lignin makes it a good candidate to replace phenol in phenol-formaldehyde resins. However, most of the ortho and para sites of lignin are blocked by other functional groups which makes it less reactive with formaldehyde [66]. Thermal degradation through pyrolysis, hydrocracking, and oxidative depolymerization have been tried to improve the reactivity of lignin. Studies have shown that almost 50% of phenol can be replaced by biorefinery lignin without compromising the properties of adhesives [67], while 30% of kraft

lignin has been used to replace phenol for wood composite applications [68]. Lignin phenol has similar curing behavior compared to commercial resin, however, the curing temperature is higher due to the high glass transition temperature of lignin. Other modifications have been tried to improve this by incorporating other compounds such as starch and urea [69]. However, the use of lignin in substituting phenol is highly dependent on market conditions because phenol from fossil fuels is cheaper. Therefore, studies need to focus on using low-cost lignin and achieving commercial standards.

Lignin can also be incorporated into conventional epoxy resins either directly or through modification. Lignin can be directly reacted with epichlorohydrin to get epoxy resin; however, the properties of such resin are highly dependent on the lignin quality and its molecular weight [70–72]. Lignin can be treated with phenol, carbonyl, or unsaturated nitrogen compounds to improve its reactivity and then again react with peroxides or epichlorohydrin. These aminated or phenolated lignin can crosslink with epoxy to get epoxy resins [73]. The aliphatic and aromatic hydroxyl group in lignin can act as a polyol and react directly with isocyanate to yield polyurethanes [74]. Lignin has been used to produce both soft and hard foams [75,76]. Lignin-based polyurethane foams have shown low density, high strength-to-weight ratio, low thermal conductivity, and good hydrolytic stability [76]. Other applications of lignin include photo stabilizers due to the presence of aromatic rings which can absorb UV light and capture radicals. Lignin has also been studied to produce carbon fibers [77–79]. However, lower carbon conversion, low modulus, and structural defects in lignin pose some challenges in this area. Other already-established markets of lignin include vanillin production, concrete binders, and dispersants [80]. The current market potential of lignin applications is shown in Table 1.2.

Table 1.2. Market potential of prospective macromolecular lignin applications

Lignin application	Market potential	Growth rate	Year	Reference
Aromatics	191.8 billion US$	6.7%	2017	[81]
Phenolic resins and adhesives	12.63 billion US$	5.4%	2019	[82]
Polyurethanes and foams	65.5 billion US$	7.0%	2018	[83]
Epoxy resins	7.6 billion US$	5.85%	2019	[84]
Carbon fibers	2.49 billion US$	10.9%	2016	[85]

The bulk of lignin produced today is from paper and pulp industries which is burned as a low-value fuel. Valorizing lignin into high-value products can improve the economics of biorefineries and potentially reduce their overall environmental footprints. While the use of untransformed lignin in polymer applications may have higher environmental benefits, the use of chemicals to modify and improve lignin properties can result in higher environmental impacts as well as costs. A summary of techno-economic and life cycle analysis studies on different applications of lignin is given in Table 1.3.

Table 1.3. TEA and LCA studies of lignin-based products

Process	Lignin source	Comments	Reference
Unmodified lignin application			
LCA and TEA of different lignin applications	Biorefinery lignin	Three application areas: lignin as soil organic carbon replacement, direct burning of lignin on-site, and co-firing lignin in a coal power plant GHG emission was lowest for lignin use in land amendment followed by co-firing in coal power plants and then onsite burning Uncertainty in the cost for land amendment and external power requirements can reduce the economic advantage of lignin use in land amendment	[86]
LCA of lignin in reducing life cycle GHG emission of biorefinery	Biorefinery lignin	Two scenarios were studied: on-site burning of lignin and co-firing lignin in a coal power plant Co-firing lignin with coal has a lower life cycle impact, however, the uncertain future of coal power plants makes lignin use uncertain	[87]
LCA of biorefinery when lignin is used as a co-product or fuel	Pulp industry and biorefinery	Using lignin as a co-product for other applications has minimal influence on the environmental performance of pulp and bioethanol industries, there is negligible burden-shifting The allocation method has different results, but still, the overall environmental performance is not impacted much	[88]

Table 1.3. TEA and LCA studies of lignin-based products (continued)

Depolymerized lignin products			
TEA of depolymerized lignin	Kraft lignin (KL)	Kraft lignin depolymerized as a substitute for polyol and phenol Depolymerized KL for polyol substitute: 1440 $/ton, oxy depolymerized KL: 1623 $/ton, depolymerized KL for phenol substitute: 1421 $/ton Phenol substitute is not feasible due to the lower price of phenol Depolymerized and oxypropylated depolymerized kraft lignin are a feasible substitute for fossil-based polyols Kraft lignin biorefinery economics is highly sensitive to the market price of products	[89]
LCA of catechol production	Depolymerized lignin from candlenut	There is a minor reduction in GHG emissions while upgrading lignin to catechol. Due to the use of dichloromethane in the purification of extracted lignin, the environmental impacts were higher in categories other than GHG emissions and fossil fuel depletion. Suggested to perform LCA of different production pathways to find the sustainable conversion process.	[90]
TEA of catechol production	Olive tree pruning	The valorization ratio was around 3. The final price of catechol was 1100 $/ton	[91]
TEA and LCA of lignin upgrading into automotive and marine fuels	Biorefinery lignin	Pyrolytic conversion of lignin through hydrodeoxygenation Low conversion yield and emission depend on the allocation method When emission is allocated to both ethanol and lignin, lignin does not meet the renewable fuel standard (RFS) standard Hydrogen and energy required during hydroprocessing are the major contributors to GHG emission Centralized lignin processing is not profitable because of higher transportation costs due to the low energy density of raw lignin	[92]

Table 1.3. TEA and LCA studies of lignin-based products (continued)

TEA of jet-fuel production	Biorefinery lignin	Price of jet fuel: 6.35 -1.76 $/gal Co-production of jet fuel increased the viability of the integrated biorefinery while reducing ethanol price Conversion efficiency is still low (around 30%), but there is a possibility for higher yield (up to 94%) The economy of scale plays a vital role in determining the final price	[93]
TEA of lignin upgrading to biofuel and chemicals	Kraft lignin	Lignin upgraded to bio-oil and BTEX (benzene, toluene, ethylbenzene, xylene) BTEX production under current technology does not offset biofuel price Liquid extraction and hydrotreatment steps are costly Phenolic and solvent recovery technology needs to be improved to increase efficiency Better thermodynamic modeling is needed to understand the process	[94]
Economic analysis of bio-phenol production	Kraft lignin	Smaller capacity biorefinery (<10000 tons per year) is not economically attractive due to higher fixed costs Biorefinery feasibility is highly dependent on the bio phenol selling price, solvent, and kraft lignin price	[95]
TEA of lignin upgrading to higher-value chemicals	Biorefinery lignin	Lignin upgraded to catechol, phenol, cresols, acetic acid, formic acid, furfural, and acetaldehyde through hydrothermal liquefaction Demonstrated lignin valorization can reduce the economic burden for a second-generation biorefinery and reduce the ethanol cost Challenges remain due to uncertainty in feedstock prices and prices of lignin-valorized chemicals	[96]

Table 1.3. TEA and LCA studies of lignin-based products (continued)

LCA of adipic acid production from lignin	Biorefinery lignin	Biobased adipic acid performs better than conventional adipic acid in many impact categories due to the use of renewable feedstock and no NO_x emissions	[97]
		NaOH and heating requirements had a major share in most of the impact categories	
		Lignin valorization into adipic acid is more environmentally beneficial than solely burning lignin as a fuel	
		Further research should focus on optimizing heat and chemical requirements during depolymerization, improving catalyst selectivity with the substrate, exploring newer catalysts with less toxicity, and also exploring newer bacteria strains that can perform in harsher pH conditions	
TEA of vanillin production	Kraft lignin	Optimized reaction temperature, feed concentration of lignin, and oxygen partial pressure for the process based on economics	[98]
		The optimum conditions are 110 ℃, 5 bar, and 20 g/l with 9.25 % conversion	
		Low conversion rate, but still the rate of return is high (22.63%) with 6.19 years as the payback period	
		A better solvent for liquid extraction in vanillin separation is necessary for higher benefits	
LCA of vanillin production	Alkali lignin	Depolymerized lignin through liquefaction to get vanillin	[99]
		LCA and green design metrics used for assessing vanillin production	
		Factors such as lignin loading, different catalysts, reactor residence time, temperature, and water CO_2 ratio were analyzed	
		Environmental benefits are seen with shorter residence time, lower temperature, and using non-toxic catalysts which may not agree with higher yield, higher lignin loading has a positive effect	
		Suggested further research on the interaction between different input parameters, and optimizing energy use and catalyst choice	

Table 1.3. TEA and LCA studies of lignin-based products (continued)

Macromolecular lignin application and carbon products			
Hot spot analysis of lignin valorization pathways in phenol-formaldehyde resin	Kraft lignin	The energy required for lignin valorization technologies is high The impact of energy use can be reduced by integrating surplus steam and energy from paper and pulp industry	[100]
TEA and LCA of lignin valorization to eugenol and phenolic products	Biorefinery lignin	Considered ionic liquid pretreatment Lignin valorization can reduce ethanol costs due to the higher economic value of the latter GHG emission is higher for phenolic compounds due to the use of chemicals like isopropanol for hydrogenolysis and higher energy required for product separation	[101]
TEA of activated carbon production	Biorefinery lignin	Lignin from hydrolysis and fermentation sludge is used to make activated carbon using both physical and chemical activation Economic results show the cost of lignin-based activated carbon is lower than the current market price	[102]
TEA of integrating lignin biorefinery with a pulp mill	Kraft lignin	Assessed two production pathways: phenolic resin and carbon fiber Both phenolic resin production by lignin precipitation and carbon fiber production by solvent pulping are profitable Phenolic resin production looks economically attractive for the near term while carbon fiber production looks promising for long term Capital costs are still higher, so government incentive is recommended	[103]

In general, there is still high uncertainty in terms of economics and environmental impacts for different applications of lignin. Much of the lignin-based products that have been studied are experimental and there is not much information on their economic competitiveness and environmental impacts compared to conventional counterparts. Therefore, more TEA and LCA studies are needed to determine which products are more sustainable, both economically and environmentally.

1.4.3. Thermochemical energy storage materials

Residential heating is one of the major consumers of energy in the United States (US). In 2020, more than 95% of housing in the US uses space heating equipment, among which more than 60% are single-family houses [104]. The major fuel sources for the residential areas include natural gas (48%), electricity (42%), fuel oil or kerosene (4%), propane (4%), and wood biomass (2%). Water heating has a similar mix of fuel sources. A 2015 data on energy consumption in the US shows that more than 43% of household energy consumption goes to space heating while water heating consumes more than 19% [105]. Actual energy consumed in 2015 was 3900 trillion Btu energy for space heating in households while more than 1700 trillion Btu for water heating which results in more than 35 and 14 million Btu on average energy consumption per household for space heating and water heating, respectively [105]. Annual greenhouse gas emissions from household energy use in the US is 0.96 Gt CO2 eq/year in 2019 [106]. To reduce the environmental carbon footprint of burning fossil fuels for domestic heating, several alternatives have gained increased research interest. Among them thermal energy storage (TES) systems based on solar heating are one of the most promising ones. TES includes sensible, latent, and thermochemical energy storage systems [107]. As shown in Figure 1.8, sensible heat storage works as a function of specific heat capacity i.e., the increase and decrease of the temperature of

heat storage material while latent heat storage works as a function of latent heat of fusion or vaporization i.e., change of phase of heat storage material without the change in their temperature. The main drawbacks of these two systems are that they require a large volume of space, have higher energy loss, and are not suitable for long-term heat storage. To overcome these, thermochemical energy storage (TCES) systems have been widely researched. This system is based on the absorption and desorption of heat energy by water molecules attached to compounds (Figure 8).

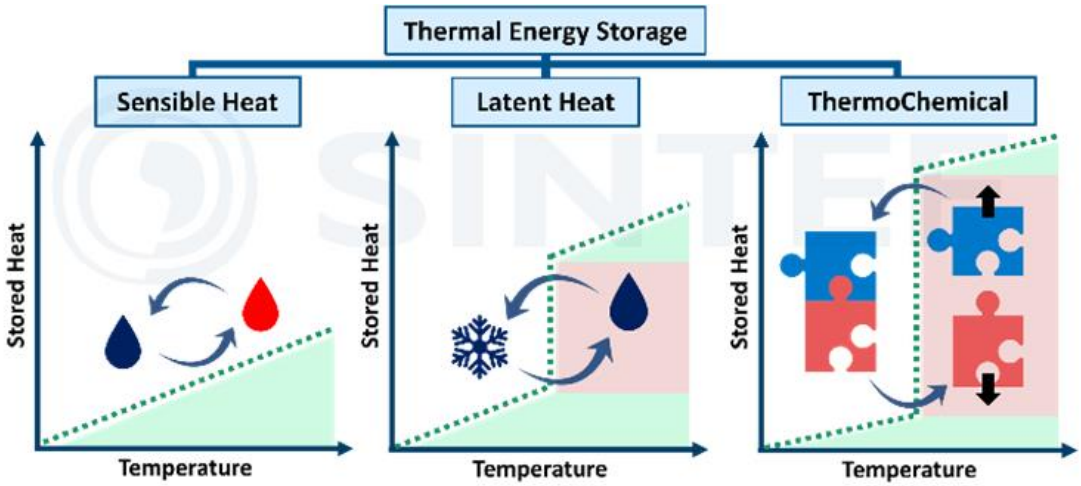

Figure 1.8. Working principle of different thermal energy storage systems (reproduced from [108])

Different hygroscopic salts have been tested for thermochemical energy storage [109,110]. The choice of salts can depend on several performance criteria such as energy density, thermal conductivity, stability, reaction kinetics, corrosiveness, and cost. Some of the salts that showed promising results based on these criteria include magnesium sulfate, calcium chloride, strontium bromide, strontium chloride, zinc sulfate, and sodium sulfide [111–115].

The inherent disadvantage of just using salt particles is their lack of cycle stability. Pure salt particles are not stable, and they tend to agglomerate, melt, or hydrothermally degrade over multiple hydration-dehydration cycles. Agglomeration reduces the available surface area of the

salt particles to absorb water, thus reducing the overall energy storage ability. Therefore, several alternatives to improve the cycle stability of salt particles have been proposed. The common method to improve salt cycle stability is by incorporating a porous host material that contains salt particles. The host matrix immobilizes salt particles and prevents them from agglomeration. Different porous materials have been studied including silica gel, zeolites, and natural rocks. Other materials have also been used to improve the properties of the salt particles including expanded natural graphite, activated carbon, and nanoparticles such as carbon nanotubes, silica, titanium dioxide, copper oxide, and alumina [116]. Courbon et al. synthesized a silica gel-strontium bromide composite and showed that the cycle stability and energy storage density of the composite significantly improved compared to salt alone [117]. However, silica gel has lower thermal conductivity, therefore, measures to improve thermal conductivity need to be considered [118]. Graphite, activated carbon, and carbon nanotubes have been used to improve the thermal conductivity of different salt particles and have shown improved performance [119–121].

Recently, cellulose nanocrystal (CNC) has been used to improve the stability of salt particles [122,123]. CNC particles and calcium chloride salt were dispersed and sonicated. The mixture resulted in a tangled network with a higher amount of CNC in the composite showing a film-like structure. Transmission electron microscope images showed that salt particles are interlocked between the CNC particles/network, thus stabilizing and preventing them from agglomeration. Cellulose is the most abundant biopolymer found on earth. The major sources of cellulose are agricultural residues and pulp fibers. Cellulose has many different applications in different industries ranging from the paper industry to textile, polymers, coatings, and pharmaceutical industries. Nanocellulose is cellulose with dimensions on the nanoscale (10-9 m). They have very good mechanical and tensile strength. Based on the structure of the

nanocellulose, they can be nanocellulose fiber (nanowhiskers) or cellulose nanocrystals. Cellulose is a highly crystalline polymer, but it also has amorphous regions. So, cellulose is not completely crystalline. Cellulose nanocrystals (CNC) can be produced by different methods including mechanical processing, chemical processing, mechano-chemical processing, and biological processing. Different nanocellulose extraction processes result in different crystallinity. One of the most popular and traditional methods of CNC production is acid hydrolysis. Concentrated acid can hydrolyze and break apart cellulose into nano-fibrillated particles. Sulfuric acid is the most common acid used. It hydrolyzes the amorphous part and gives highly crystalline nanocellulose crystals. When sulfuric acid is used, the sulfate ions attach to the cellulose fibril and create a negative charge which repels each other [124]. This action helps in separating the fibrils. However, the presence of the sulfate group reduces thermal stability. To remove the negative charge from the fibril, it needs to be neutralized by either washing or reacting with a sodium hydroxide base. Moreover, the cellulose feed material should be relatively pure and free from hemicellulose and lignin to get a high yield. Looking into the production step of CNC, it seems to be very chemical and energy-intensive.

One of the primary reasons to look for alternatives to traditional natural gas heating systems is to find a sustainable method of heating. Therefore, to determine if the sought-after technology is sustainable compared to conventional methods, a life cycle analysis (LCA) of the new systems should be performed and compared. Life cycle assessment (LCA) is a tool to determine the environmental impacts of different materials and processes. The determination of the environmental impact of any product or process requires a holistic approach that encompasses all the processes and inputs that come through the supply chain and the outputs that come out thereof. The inputs can be in the form of materials or energies and the output can be

either in the form of emissions (to water, air, or land) or products. Therefore, life cycle assessment incorporates the impact of a product based on the processes for its production along with other ancillary products and processes that are required to produce that product [125]. Thermochemical energy storage systems do not use any fossil fuels for energy storage processes, however, the materials and energy used in its life cycle can have a significant contribution which may be higher than traditional systems. Therefore, LCA is an important tool for analyzing the environmental impact of products and processes that can help guide the decision-making process.

There have been few life cycle studies of the production of cellulose nanocrystals [126–129]. Most of those studies are based on laboratory-scale data. There are only a few facilities that have produced cellulose nanocrystals on a pilot scale [130]. So, one of the challenges in getting a more accurate environmental impact of cellulose nanocrystals is the lack of commercial-scale data. However, lab-scale and pilot-scale data can also provide insights into the potential environmental impact of these materials. The major drawbacks highlighted by previous studies about cellulose nanocrystals include a high volume of chemical and water use, a high amount of energy use, and the lack of commercial-scale data (optimized process). Process simulation of scaled-up production of CNC on an industrial scale based on pilot scale data would be very useful for sustainability assessment which includes both economic and life cycle environmental metrics.

There are only a few studies available that performed the life cycle assessment of TES systems, among which most are for phase change materials [131–135]. TES system is coupled with solar heating which can either be concentrated solar heating with a power cycle or flat plate collectors [131,136,137]. In most cases, TES systems are used as auxiliary heating systems in

conjunction with conventional systems [138]. TES systems have shown lower environmental impacts compared to conventional heating systems [132,133,138]. One of the main reasons behind the lower environmental impact of TESS systems is the use of renewable solar energy and minimal use of conventional energies during its operational phase. However, the raw materials used in energy storage are one of the major contributors to higher environmental impacts during the manufacturing phase [133,137,139]. Therefore, it is imperative to perform a life cycle environmental analysis of different raw materials to screen the materials that have lower environmental impacts during the early stage of research. To the best of our knowledge, there are not any studies that considered LCA on different salt hydrates and CNC-salt hydrate composites for thermal energy storage.

1.4.4. Biomass torrefaction

Biomass is widely used as a source of fuels and chemicals. However, due to the inherent bulky, recalcitrant nature of biomass, its applications in many areas are limited due to technical, environmental, and economic reasons. Torrefaction is a thermochemical process where biomass undergoes a mild form of heat treatment, usually in the range of 200-300℃ for half an hour to up to two hours [140]. It's a thermochemical process because of the application of heat and chemical changes that follow with it. Torrefaction helps to remove the moisture and volatile organic compounds in biomass and increase the overall carbon content. This helps to improve the energy density of biomass, its combustion characteristics, long-term storage ability, simplified handlings, uniformity in properties, and better grindability for densification purposes [140,141]. Biomass is made up of three major components: lignin, cellulose, and hemicellulose. During torrefaction, cellulose and hemicellulose decompose releasing volatiles. The composition of volatiles generally includes carbon monoxide, carbon dioxide, methane, hydrogen, acetic acid,

furans, and other minor components. The variation in the composition of volatiles mostly depends on feedstock type and the degree of torrefaction severity. Both woody and non-woody biomass are used for torrefaction. Woody biomass is mostly lignin and has lower hemicellulose content while non-woody biomass has lower lignin content and higher hemicellulose content. Thus, woody biomass has higher energy density and is harder to torrefy at lower temperatures. They require higher temperatures and longer residence time to achieve a similar level of torrefaction of non-woody biomass. Hemicellulose is easier to decompose and volatilize at lower temperatures.

Biomass torrefaction has been done traditionally by heating dry biomass in an inert environment. However, several new methods have been explored recently to improve the process. Wet torrefaction or hydrothermal torrefaction is a process where torrefaction is conducted with the addition of water or steam. The presence of water or steam can improve the reaction rates, lower residence time, and mitigate the thermal degradation of biomass. However, hydrothermal torrefaction can have several disadvantages including corrosion of reactors due to the presence of moisture, high operating pressure, high water and energy requirements, and scaling-up issues. Recently molten salt-based torrefaction has been studied as a new method of torrefaction. In molten salt torrefaction, salt particles melt below the torrefaction temperature and work as a heat transfer medium such that there is more uniform heat transfer to the biomass, and torrefaction can be conducted at significantly lower temperatures and shorter residence time. Molten salts have been dominantly used in biomass pyrolysis and gasification studies. The results from those studies showed that pyrolysis and gasification can be conducted at lower temperatures than standard processing temperatures [142]. Different salt blends have been studied for these applications including alkali and transition metal cations. The anions included

nitrates, chlorides, and carbonates [143]. Hathaway et al. used a ternary blend of lithium, sodium, and potassium carbonate salts in the gasification of biomass blends [144]. The results showed that the use of molten salts improved syngas production by 25% and reduced tar production by 75%. The reaction rate also increased up to 600%. In another study, the gasification of biochar in a binary blend of sodium and potassium carbonates yielded a superior char yield with uniform structure, lower aromaticity, and higher external pores [145].

Similar to gasification, molten salts have been used in pyrolysis studies. Yang et al. conducted molten salt pyrolysis of biowaste with a blend of sodium-potassium nitrate and sodium nitrite at 300°C [146]. The result showed a higher decomposition of biowaste. The author also suggested that cations from the salt helped in catalyzing the reaction while anions participated in the reactions. Similar results were suggested by another study that used lithium-sodium-potassium carbonates [147–149]. The quality of bio-oil and biochar was superior compared to the conventional pyrolysis process. Potassium-zinc chloride salt blends were useful to get a higher yield of hydrogen and superior mesoporous structure of biochar. Carbonate salts have shown improved devolatilization of lignin at reduced temperatures [150–152]. Among different salt blends, the one containing lithium has shown better results [153,154]. The reasoning behind better performance with lithium salts may be due to the higher electronegativity compared to other salts and smaller atomic radii improving its mobility [155]. Lithium salts also helped in inhibiting the corrosion of reactors by other salts [156].

Very few studies are available in the literature where molten salt torrefaction of biomass feedstocks were conducted. The use of molten zinc chloride salt in wet torrefaction showed that the temperature of torrefaction is significantly reduced [157]. The torrefied biomass was further used in the pyrolysis process and resulted in higher quality bio-oil and bio-char. Purnomo also

showed that molten salt torrefaction can improve the quality of bio-coal (torrefied biomass) using sodium-potassium acetate salts [158]. A recent work by Backer and Gladen used a ternary blend of lithium-sodium-potassium nitrate in the torrefaction of pine [159]. The result showed that salt torrefaction can result in a severely torrefied product at a comparable temperature to a traditional process while a similar product can be obtained at significantly lower temperatures. The study identified the higher catalytic effect of lithium followed by potassium and then sodium in the torrefaction process. One of the major requirements for the salt or salt blends to be used in torrefaction is their melting temperature. They need to have a lower melting temperature than the torrefaction temperature to have effective catalysis.

To determine if a new process is economically and environmentally viable, TEA and LCA need to be done. However, since the molten salt process is a fairly new technique, there are no prior LCA-TEA works on this. Few studies in the literature used process modeling and techno-economic analysis to assess the economics of torrefied biomass production. Bach et al. and Yousef used process modeling to optimize the biomass torrefaction process [160,161]. Batidzirai et al. presented a comprehensive review of biomass torrefaction technology from a techno-economic perspective [162]. Shah et al. determined the unit torrefaction cost for cellulosic biomass to be $17.5/ton while this cost can further be reduced to $12/ton with process improvements [163]. Similarly, Akbari et al. conducted TEA analysis of wet and dry torrefaction of five different biomass feedstocks including wheat straw, pine, grape pomace, animal manure, and algae [164]. Dry torrefaction showed more economic cost of production compared to wet torrefaction systems except for animal manure. The study determined the lowest cost for the dry torrefaction process to be 2.29$/GJ and for the wet process to be 4.14 $/GJ. LCA studies on wet and dry torrefaction of different biomass showed the global warming potential (GWP) to be

between 50-400 g CO2 eq per MJ energy of torrefied biomass [165]. In another study, pine torrefaction showed lower GWP, around 17.5 g CO2 eq per MJ of torrefied pellet while torrefaction of rice husk and corn stover showed 12.5-36.9 g CO2 eq per MJ and 11.35 g CO2 eq per MJ energy of torrefied biomass, respectively [166–168]. The difference in different values of GWP is because of differences in system boundary, torrefaction conditions, and feedstock types. It is very complex to do the comparison of LCA between different studies due to these variabilities and also the product would be different. However, LCA can give us a general idea of how the process looks in terms of environmental impact and help us identify the major areas that need to be improved to lower the impact.

1.5. Research scope and purpose

The purpose of this research is to use both experimental and computational techniques to explore the use of environmentally friendly materials in different applications. This dissertation is divided into two sections. The first part deals with the experimental methods to synthesize and characterize environmentally friendly coatings for ice and biofouling release applications while the second part deals with the use of computational tools such as TEA and LCA in assessing the novel material production technologies for their environmental sustainability.

The second chapter of this dissertation delves into the use of different silicone oil additives in moisture-curable urea siloxane matrix and its application in ice shedding and fouling release applications. Several silicone oils including both dimethyl silicone oils and phenyl methyl dimethyl silicone oils with varying molecular weights and percentage composition in the formulation were explored. Different characterization techniques such as microscopy, contact angles, surface energies, ice adhesion, interfacial toughness, and biofouling assays were employed to assess the coating formulations. The hypothesis was that the silicone oil used in the

formulation leaches out to the surface of the coating and helps in lowering the ice adhesion strength and improving fouling release properties. One of the drawbacks of using these free oils in the formulation is their durability. Over time, the oil in the matrix gets depleted as it continually gets washed away. To address this, we explored the use of reactive oils in the urea siloxane matrix in the third chapter. Different carbinol functional PDMS oils were tested. The hypothesis here is that the low surface free energy silicone oil chains self-segregate towards the surface with a more durable and mechanically robust urea siloxane backbone segregating towards the substrate. The low surface energy silicone oil chains can lower the ice adhesion strength and also prevent the loss of oils since they are already tethered to the coating matrix, thus improving durability. Different characterization techniques such as atomic force microscopy, contact angles, surface energies, interfacial toughness, and tensile tests were employed.

In the fourth chapter, the use of process modeling, economic analysis, and life cycle assessment tools were employed to assess the sustainability of lignin-based foam. The lab scale process was scaled up to a 10-ton-per-day processing capacity and the economic analysis was done to determine the selling price of foam along with identifying key economic parameters that influence the selling price. Life cycle assessment was also done to determine the hotspots in environmental impacts of producing lignin-based foam. Uncertainty is economic analysis and life cycle assessment are important aspects for higher confidence in results. This chapter utilizes uncertainty analysis and sensitivity analysis in the economic analysis of foam production. The fifth chapter of this manuscript utilizes the LCA tool to screen materials and identify process hotspots for the production of salt hydrate-CNC composites for thermochemical energy storage applications. Since, the use of these composite materials in energy storage applications is a new

and early-stage technology, identifying the major hotspots in environmental impacts in the production of these materials can help in selecting suitable materials and improve the production process. Screening based on the cost of materials was also analyzed. In the sixth chapter, LCA was again used to assess the environmental impact of the molten-salt biomass torrefaction process. The objective here was to identify the major hotspots contributing to the environmental impacts and find methods to improve the molten salt torrefaction system. The results for molten-salt torrefaction were also compared with the traditional torrefaction process.

1.6. References

1. Buchner GA, Zimmermann AW, Hohgräve AE, Schomäcker R. Techno-economic Assessment Framework for the Chemical Industry - Based on Technology Readiness Levels. Ind Eng Chem Res 2018;57:8502–17. https://doi.org/10.1021/acs.iecr.8b01248.
2. DOE US. Technology readiness assessment guide. DOE G 2011;413:3–4.
3. Finkbeiner M, Inaba A, Tan RBH, Christiansen K, Klüppel HJ. The new international standards for life cycle assessment: ISO 14040 and ISO 14044. International Journal of Life Cycle Assessment 2006;11:80–5. https://doi.org/10.1065/LCA2006.02.002.
4. Azimi Yancheshme A, Momen G, Jafari Aminabadi R. Mechanisms of ice formation and propagation on superhydrophobic surfaces: A review. Adv Colloid Interface Sci 2020;279:102155. https://doi.org/10.1016/J.CIS.2020.102155.
5. Fay L, Shi X. Environmental impacts of chemicals for snow and ice control: State of the knowledge. Water Air Soil Pollut 2012;223:2751–70. https://doi.org/10.1007/S11270-011-1064-6.

6. Shen Y, Wu X, Tao J, Zhu C, Lai Y, Chen Z. Icephobic materials: Fundamentals, performance evaluation, and applications. Prog Mater Sci 2019;103:509–57. https://doi.org/10.1016/J.PMATSCI.2019.03.004.
7. Wenzel RN. Resistance of solid surfaces to wetting by water. Ind Eng Chem 1936;28:988–94. https://doi.org/10.1021/IE50320A024.
8. Cassie A, Baxter S. Wettability of porous surfaces. Transactions of the Faraday Society 1944;40:546–51.
9. Zhuo Y, Xiao S, Amirfazli A, He J, Zhang Z. Polysiloxane as icephobic materials – The past, present and the future. Chemical Engineering Journal 2021;405:127088. https://doi.org/10.1016/J.CEJ.2020.127088.
10. He Z, Xiao S, Gao H, He J, Zhang Z. Multiscale crack initiator promoted super-low ice adhesion surfaces. Soft Matter 2017;13:6562–8. https://doi.org/10.1039/C7SM01511A.
11. Zhuo Y, Håkonsen V, He Z, Xiao S, He J, Zhang Z. Enhancing the Mechanical Durability of Icephobic Surfaces by Introducing Autonomous Self-Healing Function. ACS Appl Mater Interfaces 2018;10:11972–8. https://doi.org/10.1021/ACSAMI.8B01866.
12. Barthlott W, Neinhuis C. Purity of the sacred lotus, or escape from contamination in biological surfaces. Planta 1997;202:1–8. https://doi.org/10.1007/S004250050096.
13. Xing R, Latthe SS, Bhosale AK, Li R, Madhan Kumar A, Liu S. A novel and facile approach to prepare self-cleaning yellow superhydrophobic polycarbonates. J Mol Liq 2017;247:366–73. https://doi.org/10.1016/J.MOLLIQ.2017.10.028.

14. Liu S, Liu X, Latthe SS, Gao L, An S, Yoon SS, et al. Self-cleaning transparent superhydrophobic coatings through simple sol–gel processing of fluoroalkylsilane. Appl Surf Sci 2015;351:897–903. https://doi.org/10.1016/J.APSUSC.2015.06.016.

15. Liu S, Liu S, Wang Q, Zuo Z, Liang X. Design and synthesis of robust superhydrophobic coating based on epoxy resin and polydimethylsiloxane interpenetrated polymer network. Prog Org Coat 2023;175:107336. https://doi.org/10.1016/J.PORGCOAT.2022.107336.

16. Maghsoudi K, Vazirinasab E, Momen G, Jafari R. Icephobicity and durability assessment of superhydrophobic surfaces: The role of surface roughness and the ice adhesion measurement technique. J Mater Process Technol 2021;288:116883. https://doi.org/10.1016/J.JMATPROTEC.2020.116883.

17. Davis A, Yeong YH, Steele A, Bayer IS, Loth E. Superhydrophobic nanocomposite surface topography and ice adhesion. ACS Appl Mater Interfaces 2014;6:9272–9. https://doi.org/10.1021/AM501640H.

18. Latthe SS, Sutar RS, Bhosale AK, Nagappan S, Ha CS, Sadasivuni KK, et al. Recent developments in air-trapped superhydrophobic and liquid-infused slippery surfaces for anti-icing application. Prog Org Coat 2019;137:105373. https://doi.org/10.1016/J.PORGCOAT.2019.105373.

19. Wu X, Silberschmidt V V., Hu ZT, Chen Z. When superhydrophobic coatings are icephobic: Role of surface topology. Surf Coat Technol 2019;358:207–14. https://doi.org/10.1016/J.SURFCOAT.2018.11.039.

20. Nosonovsky M, Hejazi V. Why superhydrophobic surfaces are not always icephobic. ACS Nano 2012;6:8488–91. https://doi.org/10.1021/NN302138R.

21. Boinovich LB, Emelyanenko AM. Anti-icing Potential of Superhydrophobic Coatings. Mendeleev Communications 2013;23:3–10. https://doi.org/10.1016/J.MENCOM.2013.01.002.

22. Shi K, Duan X. A review of ice protection techniques for structures in the arctic and offshore harsh environments. Journal of Offshore Mechanics and Arctic Engineering 2021;143. https://doi.org/10.1115/1.4050893/1107900.

23. Chen J, Luo Z, Fan Q, Lv J, Wang J. Anti-Ice Coating Inspired by Ice Skating. Small 2014;10:4693–9. https://doi.org/10.1002/SMLL.201401557.

24. Jung S, Dorrestijn M, Raps D, Das A, Megaridis CM, Poulikakos D. Are superhydrophobic surfaces best for icephobicity? Langmuir 2011;27:3059–66. https://doi.org/10.1021/LA104762G.

25. Chen J, Dou R, Cui D, Zhang Q, Zhang Y, Xu F, et al. Robust prototypical anti-icing coatings with a self-lubricating liquid water layer between ice and substrate. ACS Appl Mater Interfaces 2013;5:4026–30. https://doi.org/10.1021/AM401004T.

26. Ozbay S, Yuceel C, Erbil HY. Improved Icephobic Properties on Surfaces with a Hydrophilic Lubricating Liquid. ACS Appl Mater Interfaces 2015;7:22067–77. https://doi.org/10.1021/ACSAMI.5B07265.

27. Dhyani A, Wang J, Halvey AK, Macdonald B, Mehta G, Tuteja A. Design and applications of surfaces that control the accretion of matter. Science (1979) 2021;373. https://doi.org/10.1126/SCIENCE.ABA5010.

28. Yu Y, Jin B, Jamil MI, Cheng D, Zhang Q, Zhan X, et al. Highly Stable Amphiphilic Organogel with Exceptional Anti-icing Performance. ACS Appl Mater Interfaces 2019;11:12838–45. https://doi.org/10.1021/ACSAMI.8B20352.

29. Upadhyay V, Galhenage T, Battocchi D, Webster D. Amphiphilic icephobic coatings. Prog Org Coat 2017;112:191–9. https://doi.org/10.1016/J.PORGCOAT.2017.07.019.

30. Rahimi AR, Murphy M, Upadhyay V, Faiyaz K, Battocchi D, Webster DC. Amphiphilically modified self-stratified siloxane-glycidyl carbamate coatings for anti-icing applications. J Coat Technol Res 2021;18:83–97. https://doi.org/10.1007/S11998-020-00402-8.

31. Zhou X, Sun Y, Liu J, Zhou X, Sun Y, Liu J. Designing Anti-Icing Surfaces by Controlling Ice Formation. Adv Mater Interfaces 2021;8:2100327. https://doi.org/10.1002/ADMI.202100327.

32. Bohn HF, Federle W. Insect aquaplaning: Nepenthes pitcher plants capture prey with the peristome, a fully wettable water-lubricated anisotropic surface. Proceedings of the National Academy of Sciences 2004;101:14138–43. https://doi.org/10.1073/PNAS.0405885101.

33. Wong TS, Kang SH, Tang SKY, Smythe EJ, Hatton BD, Grinthal A, et al. Bioinspired self-repairing slippery surfaces with pressure-stable omniphobicity. Nature 2011 477:7365 2011;477:443–7. https://doi.org/10.1038/nature10447.

34. Zhu L, Xue J, Wang Y, Chen Q, Ding J, Wang Q. Ice-phobic coatings based on silicon-oil-infused polydimethylsiloxane. ACS Appl Mater Interfaces 2013;5:4053–62. https://doi.org/10.1021/AM400704Z.

35. Cui W, Pakkanen TA. Icephobic performance of one-step silicone-oil-infused slippery coatings: Effects of surface energy, oil and nanoparticle contents. J Colloid Interface Sci 2020;558:251–8. https://doi.org/10.1016/J.JCIS.2019.09.119.

36. Yeong YH, Milionis A, Loth E, Sokhey J. Self-lubricating icephobic elastomer coating (SLIC) for ultralow ice adhesion with enhanced durability. Cold Reg Sci Technol 2018;148:29–37. https://doi.org/10.1016/J.COLDREGIONS.2018.01.005.

37. Zheng Q, Lv J, Zhang J, Feng J. Fabrication and application of icephobic silicone coatings on epoxy substrate. Prog Org Coat 2021;161:106483. https://doi.org/10.1016/J.PORGCOAT.2021.106483.

38. Zhou Y, Liu C, Gao J, Chen Y, Yu F, Chen M, et al. A novel hydrophobic coating film of water-borne fluoro-silicon polyacrylate polyurethane with properties governed by surface self-segregation. Prog Org Coat 2019;134:134–44. https://doi.org/10.1016/J.PORGCOAT.2019.04.078.

39. Golovin K, Dhyani A, Thouless MD, Tuteja A. Low-interfacial toughness materials for effective large-scale deicing. Science (1979) 2019;364:371–5. https://doi.org/10.1126/SCIENCE.AAV1266.

40. Mohseni M, Dijvejin ZA, Golovin K. Designing scalable elastomeric anti-fouling coatings: Shear strain dissipation via interfacial cavitation. J Colloid Interface Sci 2021;589:556–67. https://doi.org/10.1016/J.JCIS.2021.01.019.

41. Azimi Dijvejin Z, Jain MC, Kozak R, Zarifi MH, Golovin K. Smart low interfacial toughness coatings for on-demand de-icing without melting. Nature Communications 2022 13:1 2022;13:1–12. https://doi.org/10.1038/s41467-022-32852-6.

42. Carve M, Scardino A, Shimeta J. Effects of surface texture and interrelated properties on marine biofouling: a systematic review. Biofouling 2019;35:597–617. https://doi.org/10.1080/08927014.2019.1636036.

43. Qiu H, Feng K, Gapeeva A, Meurisch K, Kaps S, Li X, et al. Functional polymer materials for modern marine biofouling control. Prog Polym Sci 2022;127:101516. https://doi.org/10.1016/J.PROGPOLYMSCI.2022.101516.

44. Callow JA, Callow ME. Trends in the development of environmentally friendly fouling-resistant marine coatings. Nature Communications 2011 2:1 2011;2:1–10. https://doi.org/10.1038/ncomms1251.

45. Lejars M, Margaillan A, Bressy C. Fouling release coatings: A nontoxic alternative to biocidal antifouling coatings. Chem Rev 2012;112:4347–90. https://doi.org/10.1021/CR200350V.

46. Selim MS, Shenashen MA, El-Safty SA, Higazy SA, Selim MM, Isago H, et al. Recent progress in marine foul-release polymeric nanocomposite coatings. Prog Mater Sci 2017;87:1–32. https://doi.org/10.1016/J.PMATSCI.2017.02.001.

47. Antizar-Ladislao B. Environmental levels, toxicity and human exposure to tributyltin (TBT)-contaminated marine environment. A review. Environ Int 2008;34:292–308. https://doi.org/10.1016/J.ENVINT.2007.09.005.

48. Beyer J, Song Y, Tollefsen KE, Berge JA, Tveiten L, Helland A, et al. The ecotoxicology of marine tributyltin (TBT) hotspots: A review. Mar Environ Res 2022;179:105689. https://doi.org/10.1016/J.MARENVRES.2022.105689.

49. Fent K. Worldwide Occurrence of Organotins from Antifouling Paints and Effects in the Aquatic Environment. Antifouling Paint Biocides 2006:71–100. https://doi.org/10.1007/698_5_050.

50. Dafforn KA, Lewis JA, Johnston EL. Antifouling strategies: History and regulation, ecological impacts and mitigation. Mar Pollut Bull 2011;62:453–65. https://doi.org/10.1016/J.MARPOLBUL.2011.01.012.

51. Omae I. General aspects of tin-free antifouling paints. Chem Rev 2003;103:3431–48. https://doi.org/10.1021/CR030669Z.

52. Amara I, Miled W, Slama R Ben, Ladhari N. Antifouling processes and toxicity effects of antifouling paints on marine environment. A review. Environ Toxicol Pharmacol 2018;57:115–30. https://doi.org/10.1016/J.ETAP.2017.12.001.

53. Majumdar P, Ekin A, Webster DC. Thermoset siloxane-urethane fouling release coatings. ACS Symposium Series 2007;957:61–75. https://doi.org/10.1021/BK-2007-0957.CH005.

54. Majumdar P, Webster DC. Influence of solvent composition and degree of reaction on the formation of surface microtopography in a thermoset siloxane–urethane system. Polymer (Guildf) 2006;47:4172–81. https://doi.org/10.1016/J.POLYMER.2006.02.085.

55. Majumdar P, Webster DC. Surface microtopography in siloxane–polyurethane thermosets: The influence of siloxane and extent of reaction. Polymer (Guildf) 2007;48:7499–509. https://doi.org/10.1016/J.POLYMER.2007.10.044.

56. Bodkhe RB, Stafslien SJ, Daniels J, Cilz N, Muelhberg AJ, Thompson SEM, et al. Zwitterionic siloxane-polyurethane fouling-release coatings. Prog Org Coat 2015;78:369–80. https://doi.org/10.1016/J.PORGCOAT.2014.07.011.

57. Bodkhe RB, Thompson SEM, Yehle C, Cilz N, Daniels J, Stafslien SJ, et al. The effect of formulation variables on fouling-release performance of stratified siloxane-polyurethane coatings. J Coat Technol Res 2012;9:235–49. https://doi.org/10.1007/S11998-011-9362-X.

58. Pade M, Webster DC. Self-stratified siloxane-polyurethane fouling-release marine coating strategies: A review. Marine Coatings and Membranes 2019:1–36.

59. Rahimi AR, Murphy M, Faiyaz K, Stafslien SJ, Vanderwal L, Pade M, et al. Amphiphilic marine coating systems of self-stratified PDMS-PEG surfaces with an epoxy-polyurethane matrix. J Coat Technol Res 2022;19:795–812. https://doi.org/10.1007/S11998-021-00561-2.

60. Benda J, Stafslien S, Vanderwal L, Finlay JA, Clare AS, Webster DC. Surface modifying amphiphilic additives and their effect on the fouling-release performance of siloxane-polyurethane coatings. Biofouling 2021;37:309–26. https://doi.org/10.1080/08927014.2021.1901891.

61. Benda J, Narikiyo H, Stafslien SJ, Vanderwal LJ, Finlay JA, Aldred N, et al. Studying the Effect of Pre-Polymer Composition and Incorporation of Surface-Modifying Amphiphilic Additives on the Fouling-Release Performance of Amphiphilic Siloxane-Polyurethane Coatings. ACS Appl Mater Interfaces 2022;14:37229–47. https://doi.org/10.1021/ACSAMI.2C10983.

62. Ponnusamy VK, Nguyen DD, Dharmaraja J, Shobana S, Banu JR, Saratale RG, et al. A review on lignin structure, pretreatments, fermentation reactions and biorefinery potential. Bioresour Technol 2019;271:462–72. https://doi.org/10.1016/j.biortech.2018.09.070.

63. Katahira R, Elder TJ, Beckham GT. Chapter 1: A Brief Introduction to Lignin Structure. RSC Energy and Environment Series 2018;2018-Janua:1–20. https://doi.org/10.1039/9781788010351-00001.

64. Strassberger Z, Tanase S, Rothenberg G. The pros and cons of lignin valorisation in an integrated biorefinery. RSC Adv 2014;4:25310–8. https://doi.org/10.1039/c4ra04747h.

65. Bertella S, Luterbacher JS. Lignin Functionalization for the Production of Novel Materials. Trends Chem 2020;2:440–53. https://doi.org/10.1016/j.trechm.2020.03.001.

66. Glasser WG. About Making Lignin Great Again—Some Lessons From the Past. Front Chem 2019;7:1–17. https://doi.org/10.3389/fchem.2019.00565.

67. Zhang W, Ma Y, Wang C, Li S, Zhang M, Chu F. Preparation and properties of lignin-phenol-formaldehyde resins based on different biorefinery residues of agricultural biomass. Ind Crops Prod 2013;43:326–33. https://doi.org/10.1016/j.indcrop.2012.07.037.

68. Kouisni L, Fang Y, Paleologou M, Ahvazi B, Hawari J, Zhang Y, et al. Kraft lignin recovery and its use in the preparation of lignin-based phenol formaldehyde resins for plywood. Cell Chem Technol 2011; 45.7:515.

69. Turunen M, Alvila L, Pakkanen TT, Rainio J. Modification of phenol-formaldehyde resol resins by lignin, starch, and urea. J Appl Polym Sci 2003;88:582–8. https://doi.org/10.1002/app.11776.

70. van de Pas DJ, Torr KM. Biobased epoxy resins from deconstructed native softwood lignin. Biomacromolecules 2017;18:2640–8.

71. Asada C, Basnet S, Otsuka M, Sasaki C, Nakamura Y. Epoxy resin synthesis using low molecular weight lignin separated from various lignocellulosic materials. Int J Biol Macromol 2015;74:413–9. https://doi.org/10.1016/J.IJBIOMAC.2014.12.039.

72. Hirose S, Hatakeyama T, Hatakeyama H. Novel Epoxy Resins Derived from Biomass Components. Procedia Chem 2012;4:26–33. https://doi.org/10.1016/J.PROCHE.2012.06.004.

73. Stewart D. Lignin as a base material for materials applications: Chemistry, application and economics. Ind Crops Prod 2008;27:202–7. https://doi.org/10.1016/j.indcrop.2007.07.008.

74. Griffini G, Passoni V, Suriano R, Levi M, Turri S. Polyurethane Coatings Based on Chemically Unmodified Fractionated Lignin. ACS Sustain Chem Eng 2015;3:1145–54. https://doi.org/10.1021/acssuschemeng.5b00073.

75. Bernardini J, Cinelli P, Anguillesi I, Coltelli MB, Lazzeri A. Flexible polyurethane foams green production employing lignin or oxypropylated lignin. Eur Polym J 2015;64:147–56. https://doi.org/10.1016/j.eurpolymj.2014.11.039.

76. Li Y, Ragauskas AJ. Kraft Lignin-Based Rigid Polyurethane Foam. Journal of Wood Chemistry and Technology 2012;32:210–24. https://doi.org/10.1080/02773813.2011.652795.

77. Meister JJ. Modification of lignin. vol. 42. 2002. https://doi.org/10.1081/MC-120004764.

78. Wang H, Pu Y, Ragauskas A, Yang B. From lignin to valuable products–strategies, challenges, and prospects. Bioresour Technol 2019;271:449–61. https://doi.org/10.1016/j.biortech.2018.09.072.

79. Karunarathna MS, Smith RC. Valorization of lignin as a sustainable component of structural materials and composites: Advances from 2011 to 2019. Sustainability (Switzerland) 2020;12. https://doi.org/10.3390/su12020734.

80. Bajwa DS, Pourhashem G, Ullah AH, Bajwa SG. A concise review of current lignin production, applications, products and their environment impact. Ind Crops Prod 2019;139:111526. https://doi.org/10.1016/j.indcrop.2019.111526.

81. Global Aromatics Manufacturing Market Size and Research Report n.d. https://www.bccresearch.com/market-research/chemicals/aromatics-manufacturing-global-markets.html (accessed June 18, 2020).

82. Phenolic Resins Market Size | Industry Trends Report, 2020-2026 n.d. https://www.polarismarketresearch.com/industry-analysis/phenolic-resin-market (accessed June 8, 2020).

83. Polyurethane Market Size, Share | Global PU Industry Report 2019-2025 n.d. https://www.grandviewresearch.com/industry-analysis/polyurethane-pu-market (accessed June 8, 2020).

84. Epoxy Resin Market Size, Share, Overview - Industry Report, 2020-2026 n.d. https://www.polarismarketresearch.com/industry-analysis/epoxy-resins-market (accessed June 8, 2020).

85. Carbon Fiber Market Size Worth $6.36 Billion By 2025 | CAGR: 10.9% n.d. https://www.grandviewresearch.com/press-release/global-carbon-fiber-market (accessed June 8, 2020).

86. Pourhashem G, Adler PR, McAloon AJ, Spatari S. Cost and greenhouse gas emission tradeoffs of alternative uses of lignin for second generation ethanol. Environmental Research Letters 2013;8. https://doi.org/10.1088/1748-9326/8/2/025021.

87. Scown CD, Gokhale AA, Willems PA, Horvath A, McKone TE. Role of lignin in reducing life-cycle carbon emissions, water use, and cost for United States cellulosic biofuels. Environ Sci Technol 2014;48:8446–55. https://doi.org/10.1021/es5012753.

88. Secchi M, Castellani V, Orlandi M, Collina E. Use of Lignin side-streams from biorefineries as fuel or co-product? Life cycle analysis of bio-ethanol and pulp production processes. Bioresources 2019;14:4832–65.

89. Dessbesell L, Yuan Z, Hamilton S, Leitch M, Pulkki R, Xu CC. Bio-based polymers production in a kraft lignin biorefinery: techno-economic assessment. Biofuels, Bioproducts and Biorefining 2018;12:239–50. https://doi.org/10.1002/bbb.1834.

90. Montazeri M, Eckelman MJ. Life Cycle Assessment of Catechols from Lignin Depolymerization. ACS Sustain Chem Eng 2016;4:708–18. https://doi.org/10.1021/acssuschemeng.5b00550.

91. Mabrouk A, Erdocia X, Alriols MG, Labidi J. Economic analysis of a biorefinery process for catechol production from lignin. J Clean Prod 2018;198:133–42. https://doi.org/10.1016/j.jclepro.2018.06.294.

92. Obydenkova S V., Kouris PD, Hensen EJM, Heeres HJ, Boot MD. Environmental economics of lignin derived transport fuels. Bioresour Technol 2017;243:589–99. https://doi.org/10.1016/j.biortech.2017.06.157.

93. Shen R, Tao L, Yang B. Techno-economic analysis of jet-fuel production from biorefinery waste lignin. Biofuels, Bioproducts and Biorefining 2019;13:486–501. https://doi.org/10.1002/bbb.1952.

94. Funkenbusch LLT, Mullins ME, Vamling L, Belkhieri T, Srettiwat N, Winjobi O, et al. Technoeconomic assessment of hydrothermal liquefaction oil from lignin with catalytic upgrading for renewable fuel and chemical production. Wiley Interdiscip Rev Energy Environ 2019;8:1–12. https://doi.org/10.1002/wene.319.

95. Dessbesell L, Yuan Z, Leitch M, Paleologou M, Pulkki R, Xu CC. Capacity Design of a Kraft Lignin Biorefinery for Production of Biophenol via a Proprietary Low-Temperature/Low-Pressure Lignin Depolymerization Process. ACS Sustain Chem Eng 2018;6:9293–303. https://doi.org/10.1021/acssuschemeng.8b01582.

96. Bbosa D, Mba-Wright M, Brown RC. More than ethanol: a techno-economic analysis of a corn stover-ethanol biorefinery integrated with a hydrothermal liquefaction process to convert lignin into biochemicals. Biofuels, Bioproducts and Biorefining 2018;12:497–509. https://doi.org/10.1002/bbb.1866.

97. Corona A, Biddy MJ, Vardon DR, Birkved M, Hauschild MZ, Beckham GT. Life cycle assessment of adipic acid production from lignin. Green Chemistry 2018;20:3857–66. https://doi.org/10.1039/c8gc00868j.

98. Khwanjaisakun N, Amornraksa S, Simasatitkul L, Charoensuppanimit P, Assabumrungrat S. Techno-economic analysis of vanillin production from Kraft lignin: Feasibility study of lignin valorization. Bioresour Technol 2020;299:122559. https://doi.org/10.1016/j.biortech.2019.122559.

99. Isola C, Sieverding HL, Numan-Al-Mobin AM, Rajappagowda R, Boakye EA, Raynie DE, et al. Vanillin derived from lignin liquefaction: a sustainability evaluation. International Journal of Life Cycle Assessment 2018;23:1761–72. https://doi.org/10.1007/s11367-017-1401-0.

100. Lettner M, Solt P, Rößiger B, Pufky-Heinrich D, Jääskeläinen AS, Schwarzbauer P, et al. From wood to resin-identifying sustainability levers through hotspotting lignin valorisation pathways. Sustainability (Switzerland) 2018;10. https://doi.org/10.3390/su10082745.

101. Martinez-Hernandez E, Cui X, Scown CD, Amezcua-Allieri MA, Aburto J, Simmons BA. Techno-economic and greenhouse gas analyses of lignin valorization to eugenol and phenolic products in integrated ethanol biorefineries. Biofuels, Bioproducts and Biorefining 2019;13:978–93. https://doi.org/10.1002/bbb.1989.

102. Fish D, Fox C, Garcia-perez M. Conversion of lignin to high value, large market products. 2016:1–29.

103. Téguia CD, Albers R, Stuart PR. Analysis of economically viable lignin-based biorefinery strategies implemented within a kraft pulp mill. Tappi J 2017;16:157–69. https://doi.org/10.32964/tj16.3.157.

104. EIA. U.S. Energy Information Administration - EIA - Independent Statistics and Analysis 2023. https://www.eia.gov/consumption/residential/data/2020/c&e/pdf/ce3.1.pdf (accessed July 10, 2023).

105. EIA. U.S. Energy Information Administration - EIA - Independent Statistics and Analysis 2022. https://www.eia.gov/consumption/residential/data/2020/#fueluses (accessed January 1, 2023).

106. Berrill P, Gillingham KT, Hertwich EG. Drivers of change in US residential energy consumption and greenhouse gas emissions, 1990–2015. Environmental Research Letters 2021;16:034045. https://doi.org/10.1088/1748-9326/ABE325.

107. Alva G, Liu L, Huang X, Fang G. Thermal energy storage materials and systems for solar energy applications. Renewable and Sustainable Energy Reviews 2017;68:693–706. https://doi.org/10.1016/J.RSER.2016.10.021.

108. Thermochemical Energy Storage: The next generation thermal batteries? - #SINTEFblog. https://blog.sintef.com/sintefenergy/thermochemical-energy-storage-the-next-generation-thermal-batteries/ (accessed February 27, 2024).

109. Clark RJ, Mehrabadi A, Farid M. State of the art on salt hydrate thermochemical energy storage systems for use in building applications. J Energy Storage 2020;27:101145. https://doi.org/10.1016/J.EST.2019.101145.

110. Zbair M, Bennici S. Survey Summary on Salts Hydrates and Composites Used in Thermochemical Sorption Heat Storage: A Review. Energies 2021, Vol 14, Page 3105 2021;14:3105. https://doi.org/10.3390/EN14113105.

111. Rammelberg HU, Osterland T, Priehs B, Opel O, Ruck WKL. Thermochemical heat storage materials – Performance of mixed salt hydrates. Solar Energy 2016;136:571–89. https://doi.org/10.1016/J.SOLENER.2016.07.016.

112. Richter M, Habermann EM, Siebecke E, Linder M. A systematic screening of salt hydrates as materials for a thermochemical heat transformer. Thermochim Acta 2018;659:136–50. https://doi.org/10.1016/J.TCA.2017.06.011.

113. Clark R-J, Gholamibozanjani G, Woods J, Kaur S, Odukomaiya A, Al-Hallaj S, et al. Experimental screening of salt hydrates for thermochemical energy storage for building heating application. J Energy Storage 2022;51:104415.

114. Van Essen VM, Cot Gores J, Bleijendaal LPJ, Zondag HA, Schuitema R, Bakker M, et al. Characterization of salt hydrates for compact seasonal thermochemical storage. vol. 48906. 2009.

115. Trausel F, De Jong AJ, Cuypers R. A Review on the Properties of Salt Hydrates for Thermochemical Storage. Energy Procedia 2014;48:447–52. https://doi.org/10.1016/J.EGYPRO.2014.02.053.

116. Zhao Q, Lin J, Huang H, Wu Q, Shen Y, Xiao Y. Optimization of thermochemical energy storage systems based on hydrated salts: A review. Energy Build 2021;244:111035. https://doi.org/10.1016/J.ENBUILD.2021.111035.

117. Courbon E, D'Ans P, Permyakova A, Skrylnyk O, Steunou N, Degrez M, et al. A new composite sorbent based on SrBr2 and silica gel for solar energy storage application with high energy storage density and stability. Appl Energy 2017;190:1184–94. https://doi.org/10.1016/J.APENERGY.2017.01.041.

118. Yu N, Wang RZ, Lu ZS, Wang LW. Development and characterization of silica gel–LiCl composite sorbents for thermal energy storage. Chem Eng Sci 2014;111:73–84. https://doi.org/10.1016/J.CES.2014.02.012.

119. Kiplagat JK, Wang RZ, Oliveira RG, Li TX. Lithium chloride – Expanded graphite composite sorbent for solar powered ice maker. Solar Energy 2010;84:1587–94. https://doi.org/10.1016/J.SOLENER.2010.06.014.

120. Nakaso K, Teshima H, Yoshimura A, Nogami S, Hamada Y, Fukai J. Extension of heat transfer area using carbon fiber cloths in latent heat thermal energy storage tanks. Chemical Engineering and Processing: Process Intensification 2008;47:879–85. https://doi.org/10.1016/J.CEP.2007.02.001.

121. Jo B, Banerjee D. Enhanced specific heat capacity of molten salt-based carbon nanotubes nanomaterials. J Heat Transfer 2015;137. https://doi.org/10.1115/1.4030226/375304.

122. Gladen A, Bajwa D. A Novel Composite Material of Hygroscopic Salt Stabilized by Nanocellulose for Thermochemical Energy Storage. Proceedings of the ASME 2021 15th International Conference on Energy Sustainability, ES 2021 2021. https://doi.org/10.1115/ES2021-63814.

123. Gladen AC, Bajwa D. An Improved Thermochemical Energy Storage Material Using Nanocellulose to Stabilize Calcium Chloride Salt. J Sol Energy Eng 2022;144. https://doi.org/10.1115/1.4053904/1136904.

124. Kumar A, Negi YS, Choudhary V, Bhardwaj NK. Characterization of Cellulose Nanocrystals Produced by Acid-Hydrolysis from Sugarcane Bagasse as Agro-Waste. Journal of Materials Physics and Chemistry 2014;2:1–8. https://doi.org/10.12691/JMPC-2-1-1.

125. Jolliet O, Saadé-Sbeih M, Shaked S, Jolliet A, Crettaz P. Environmental Life Cycle Assessment. Environmental Life Cycle Assessment 2015:1–298. https://doi.org/10.1201/B19138.

126. De Figueirêdo MCB, De Freitas Rosa M, Lie Ugaya CM, De Souza Filho MDSM, Da Silva Braid ACC, De Melo LFL. Life cycle assessment of cellulose nanowhiskers. J Clean Prod 2012;35:130–9. https://doi.org/10.1016/J.JCLEPRO.2012.05.033.

127. Leão RM, Miléo PC, Maia JMLL, Luz SM. Environmental and technical feasibility of cellulose nanocrystal manufacturing from sugarcane bagasse. Carbohydr Polym 2017;175:518–29. https://doi.org/10.1016/J.CARBPOL.2017.07.087.

128. Arvidsson R, Nguyen D, Svanström M. Life cycle assessment of cellulose nanofibrils production by mechanical treatment and two different pretreatment processes. Environ Sci Technol 2015;49:6881–90. https://doi.org/10.1021/ACS.EST.5B00888.

129. Piccinno F, Hischier R, Seeger S, Som C. Life cycle assessment of a new technology to extract, functionalize and orient cellulose nanofibers from food waste. ACS Sustain Chem Eng 2015;3:1047–55. https://doi.org/10.1021/ACSSUSCHEMENG.5B00209.

130. Gu H, Reiner R, Bergman R, Rudie A. LCA study for pilot scale production of Cellulose Nano Crystals (CNC) from wood pulp 2015.

131. Pelay U, Azzaro-Pantel C, Fan Y, Luo L. Life cycle assessment of thermochemical energy storage integration concepts for a concentrating solar power plant. Environ Prog Sustain Energy 2020;39:e13388. https://doi.org/10.1002/EP.13388.

132. Masruroh NA, Li B, Klemeš J. Life cycle analysis of a solar thermal system with thermochemical storage process. Renew Energy 2006;31:537–48. https://doi.org/10.1016/J.RENENE.2005.03.008.

133. Bernal DC, Muñoz E, Manente G, Sciacovelli A, Ameli H, Gallego-Schmid A. Environmental assessment of latent heat thermal energy storage technology system with phase change material for domestic heating applications. Sustainability (Switzerland) 2021;13:11265. https://doi.org/10.3390/SU132011265/S1.

134. Horn R, Burr M, Fröhlich D, Gschwander S, Held M, Lindner JP, et al. Life Cycle Assessment of Innovative Materials for Thermal Energy Storage in Buildings. Procedia CIRP 2018;69:206–11. https://doi.org/10.1016/J.PROCIR.2017.11.095.

135. Nienborg B, Gschwander S, Munz G, Fröhlich D, Helling T, Horn R, et al. Life Cycle Assessment of thermal energy storage materials and components. Energy Procedia 2018;155:111–20. https://doi.org/10.1016/J.EGYPRO.2018.11.063.

136. Colelli G, Chacartegui R, Ortiz C, Carro A, Arena AP, Verda V. Life cycle and environmental assessment of calcium looping (CaL) in solar thermochemical energy

storage. Energy Convers Manag 2022;257:115428. https://doi.org/10.1016/J.ENCONMAN.2022.115428.

137. Lamnatou C, Motte F, Notton G, Chemisana D, Cristofari C. Building-integrated solar thermal system with/without phase change material: Life cycle assessment based on ReCiPe, USEtox and Ecological footprint. J Clean Prod 2018;193:672–83. https://doi.org/10.1016/J.JCLEPRO.2018.05.032.

138. De Laborderie A, Puech C, Adra N, Blanc I, Beloin-Saint-Pierre D, Padey P, et al. Environmental Impacts of Solar Thermal Systems with Life Cycle Assessment. Renewable Energy Congress 2011-Sweden Climate Change Issues (CC) 2011. https://doi.org/10.3384/ecp110573678ï.

139. Kylili A, Fokaides PA, Ioannides A, Kalogirou S. Environmental assessment of solar thermal systems for the industrial sector. J Clean Prod 2018;176:99–109. https://doi.org/10.1016/J.JCLEPRO.2017.12.150.

140. Tumuluru JS, Ghiasi B, Soelberg NR, Sokhansanj S. Biomass Torrefaction Process, Product Properties, Reactor Types, and Moving Bed Reactor Design Concepts. Front Energy Res 2021;9:728140. https://doi.org/10.3389/FENRG.2021.728140.

141. Barskov S, Zappi M, Buchireddy P, Dufreche S, Guillory J, Gang D, et al. Torrefaction of biomass: A review of production methods for biocoal from cultured and waste lignocellulosic feedstocks. Renew Energy 2019;142:624–42. https://doi.org/10.1016/J.RENENE.2019.04.068.

142. Liu Y, Zhang J, Hu H, Dai Q, Zou C, Cao C, et al. Influence mechanisms of torrefaction on syngas production from bio-waste molten salt thermal treatment. Fuel 2024;363:130965. https://doi.org/10.1016/J.FUEL.2024.130965.

143. Nunes VMB, Queirós CS, Lourenço MJV, Santos FJV, Nieto de Castro CA. Molten salts as engineering fluids – A review: Part I. Molten alkali nitrates. Appl Energy 2016;183:603–11. https://doi.org/10.1016/J.APENERGY.2016.09.003.

144. Hathaway BJ, Honda M, Kittelson DB, Davidson JH. Steam gasification of plant biomass using molten carbonate salts. Energy 2013;49:211–7. https://doi.org/10.1016/J.ENERGY.2012.11.006.

145. Xie Y, Yang H, Zeng K, Zhu Y, Hu J, Mao Q, et al. Study on CO2 gasification of biochar in molten salts: Reactivity and structure evolution. Fuel 2019;254:115614. https://doi.org/10.1016/J.FUEL.2019.06.022.

146. Yang Y, Hu H, Yang F, Tang H, Liu H, Yi B, et al. Thermochemical conversion of lignocellulosic bio-waste via fast pyrolysis in molten salts. Fuel 2020;278:118228. https://doi.org/10.1016/J.FUEL.2020.118228.

147. Xie Y, Zeng K, Flamant G, Yang H, Liu N, He X, et al. Solar pyrolysis of cotton stalk in molten salt for bio-fuel production. Energy 2019;179:1124–32. https://doi.org/10.1016/J.ENERGY.2019.05.055.

148. Zeng K, Yang X, Xie Y, Yang H, Li J, Zhong D, et al. Molten salt pyrolysis of biomass: The evaluation of molten salt. Fuel 2021;302:121103. https://doi.org/10.1016/J.FUEL.2021.121103.

149. Zhu X, Sun M, Zhu X, Guo W, Luo Z, Cai W, et al. Molten salt shielded pyrolysis of biomass waste: Development of hierarchical biochar, salt recovery, CO2 adsorption. Fuel 2023;334:126565. https://doi.org/10.1016/J.FUEL.2022.126565.

150. Jalalabadi T, Moghtaderi B, Allen J. The interplay between ternary molten carbonate and biomaterials during pressurized slow pyrolysis. React Chem Eng 2022;7:674–90. https://doi.org/10.1039/D1RE00544H.

151. Jalalabadi T, Glenn M, Tremain P, Moghtaderi B, Donne S, Allen J. Modification of Biochar Formation during Slow Pyrolysis in the Presence of Alkali Metal Carbonate Additives. Energy and Fuels 2019;33:11235–45. https://doi.org/10.1021/ACS.ENERGYFUELS.9B02865.

152. Jalalabadi T, Drewery M, Tremain P, Wilkinson J, Moghtaderi B, Allen J. The impact of carbonate salts on char formation and gas evolution during the slow pyrolysis of biomass, cellulose, and lignin. Sustain Energy Fuels 2020;4:5987–6003. https://doi.org/10.1039/D0SE01031F.

153. Nygård HS, Olsen E, Nygård HS, Olsen E. Molten salt pyrolysis of milled beech wood using an electrostatic precipitator for oil collection. AIMS Energy 2015 3:284 2015;3:284–96. https://doi.org/10.3934/ENERGY.2015.3.284.

154. Nygård HS, Olsen E. Effect of Salt Composition and Temperature on the Thermal Behavior of Beech Wood in Molten Salt Pyrolysis. Energy Procedia 2014;58:221–8. https://doi.org/10.1016/J.EGYPRO.2014.10.432.

155. Gao M, Ji D, Yu F, Ai N, Jiang H, Ji J. Influence of molten salts on pyrolysis characteristics of rice straw. Proceedings of 2012 International Conference on Biobase Material Science and Engineering, BMSE 2012 2012:151–5. https://doi.org/10.1109/BMSE.2012.6466201.

156. Coyle RT, Thomas TM, Schissel P. Corrosion of selected alloys in eutectic lithium-sodium-potassium carbonate at 900C 1986. https://doi.org/10.2172/6211643.

157. Su Y, Liu L, Dong Q, Xie Y, Wang P, Zhang S, et al. Investigation of molten salt in wet torrefaction and its effects on fast pyrolysis behaviors. Energy Sources, Part A: Recovery, Utilization, and Environmental Effects 2020;42:577–85. https://doi.org/10.1080/15567036.2019.1587104.

158. Purnomo V, F Luo. Torrefaction of biomass in molten salts to obtain useful bioproducts as renewable chemical resources. The 10th joint conference on chemistry, 2015.

159. Backer M, Gladen A. Impact of salt composition and temperature on low-temperature torrefaction of pine in molten nitrate salts. Energy 2023;263:126044. https://doi.org/10.1016/J.ENERGY.2022.126044.

160. Bach QV, Skreiberg Ø, Lee CJ. Process modeling and optimization for torrefaction of forest residues. Energy 2017;138:348–54. https://doi.org/10.1016/J.ENERGY.2017.07.040.

161. Haseli Y. Process Modeling of a Biomass Torrefaction Plant. Energy and Fuels 2018;32:5611–22. https://doi.org/10.1021/ACS.ENERGYFUELS.7B03956.

162. Batidzirai B, Mignot APR, Schakel WB, Junginger HM, Faaij APC. Biomass torrefaction technology: Techno-economic status and future prospects. Energy 2013;62:196–214. https://doi.org/10.1016/J.ENERGY.2013.09.035.

163. Shah A, Darr MJ, Medic D, Anex RP, Khanal S, Maski D. Techno-economic analysis of a production-scale torrefaction system for cellulosic biomass upgrading. Biofuels, Bioproducts and Biorefining 2012;6:45–57. https://doi.org/10.1002/BBB.336.

164. Akbari M, Oyedun AO, Kumar A. Techno-economic assessment of wet and dry torrefaction of biomass feedstock. Energy 2020;207:118287. https://doi.org/10.1016/J.ENERGY.2020.118287.

165. Akbari M, Oyedun AO, Gemechu E, Kumar A. Comparative life cycle energy and greenhouse gas footprints of dry and wet torrefaction processes of various biomass feedstocks. J Environ Chem Eng 2021;9:105415. https://doi.org/10.1016/J.JECE.2021.105415.

166. Adams PWR, Shirley JEJ, McManus MC. Comparative cradle-to-gate life cycle assessment of wood pellet production with torrefaction. Appl Energy 2015;138:367–80. https://doi.org/10.1016/J.APENERGY.2014.11.002.

167. Thengane SK, Burek J, Kung KS, Ghoniem AF, Sanchez DL. Life cycle assessment of rice husk torrefaction and prospects for decentralized facilities at rice mills. J Clean Prod 2020;275:123177. https://doi.org/10.1016/J.JCLEPRO.2020.123177.

168. Kaliyan N, Morey RV, Tiffany DG, Lee WF. Life Cycle Assessment of Corn Stover Torrefaction Plant Integrated with a Corn Ethanol Plant and a Coal Fired Power Plant. American Society of Agricultural and Biological Engineers Annual International Meeting 2013, ASABE 2013 2013;1:1-. https://doi.org/10.13031/AIM.20131580611.

CHAPTER 2. EFFECT OF SILICONE OIL ADDITIVES ON MOISTURE-CURABLE UREA-SILOXANE COATING FOR ICE AND BIOFOULING RELEASE APPLICATIONS

2.1. Abstract

The effect of incorporating non-reactive silicone oil additives into a moisture-curable urea-siloxane coating on ice adhesion and fouling release properties was studied. A single-component moisture-curable urea-siloxane coating was synthesized and modified by incorporating a series of silicone oil additives. The urea linkage provides good adhesion and mechanical strength while the siloxane chains provide durability and flexibility to the coating. Ice adhesion, contact angle, surface morphology, interfacial toughness, and biofouling assays with Navicula incerta, Chlorella Vulgaris, Cellulophaga lytica, and Amphibalanus amphitrite were studied. The results showed that the addition of oils reduces the adhesion strength and interfacial toughness of ice. There was also a correlation between ice adhesion strength and barnacle adhesion strength. Higher molecular weight oils showed better performance than lower molecular weight oils. The presence of oils on the surface of the coating was verified by atomic force microscopy and digital microscope images. The results show the promising potential of these coatings in ice-shedding and fouling release applications.

2.2. Introduction

Ice accretion on the surfaces of transmission lines, wind turbines, airplanes, and ships can have a multitude of detrimental effects ranging from safety issues to catastrophic failures. Ice and snow accretion on the transmission lines can cause power failure while ice accretion on wind turbines can lower energy generation. Similarly, ice accretion on the surface of airplanes and ships significantly increases the drag and reduces fuel efficiency in addition to safety issues.

Delaying the formation and easy removal of ice from these surfaces is very important for safety, reliability, and proper functioning. Active methods of ice removal include mechanical scrubbing, heating, and spraying of deicing chemicals. These methods are very time-consuming, costly, and not long-lasting. The run-off of deicing chemicals on water and soil can have detrimental effects on aquatic ecosystems and soil fertility, respectively [1,2]. Therefore, passive preventive measures have been explored in recent years. Passive preventive measures include the application of coatings on the surface. The coatings on the surface should either delay the formation of ice or it should have very low ice adhesion such that ice can be easily removed, either by its weight or slight external force. The coating's surface should also be durable, and its ice adhesion property should not diminish significantly over time. However, ice adhesion is a complex phenomenon and several factors affect the adhesion of ice on a coating surface including surface properties, modulus, coating thickness, porosity, roughness, and crosslink density [3]. Different icephobic surfaces have been explored including coatings with textured hydrophobic surfaces, low surface energy coatings, heterogeneous/amphiphilic coatings, and liquid-infused layers [4–6].

Superhydrophobic surfaces (SHS) include micro and nano-textured roughness with low surface-free energies which prevent water retention on the surface by sliding or bouncing of water droplets [7]. These surfaces do not always act as icephobic surfaces, for example, in high humidity environments, water vapor can rapidly freeze on the micro/nanotextured surfaces to form ice crystals, and start accumulating ice layers. These kinds of surfaces promote heterogeneous nucleation of ice crystals. These ice layers are harder to remove due to mechanical interlocking on the rough surface and ice adhesion can be several magnitudes higher than the smooth hydrophobic surfaces. Another drawback of SHS is their poor durability as the

micro/nano textures can be easily destroyed by small mechanical forces like icing/deicing processes. Slippery liquid-infused porous surfaces (SLIPS) are another strategy for anti-icing applications where the slippery hydrophobic liquid is entrapped inside a porous matrix and on the surface, which acts as a lubricating layer that prevents ice accumulation [8]. However, this method lacks long-term durability due to the depletion of the lubricant over time due to washing away [9]. Elastic coating materials have also been explored for anti-icing applications due to their low ice adhesion property [10–12]. In such materials, cross-linking density and plasticization are lowered to reduce ice adhesion strength. However, this also reduces their mechanical properties like toughness and thus their durability. The fundamental challenge with icephobic coatings is maintaining low ice adhesion and robust mechanical properties over time [13]. Therefore, it is essential to control both the bulk and surface properties of these coatings to ensure mechanical durability as well as ice-shedding properties.

Silicone oils have been explored as an additive to the coating matrix to improve the icephobicity due to their low surface tension and icephobic properties [14–18]. The principle behind this is that the oils form a low shear and weak interaction with the base coating such that ice can be easily removed by washing off the lubricant during deicing [19]. The oils help in reducing the work of adhesion. Also, these oils promote homogeneous nucleation of ice crystals with higher nucleation energy barriers such that they delay ice formation. These silicone oils can be incorporated into the matrix either by covalently bonding with the underlying matrix or as a non-reactive additive in the formulation. These kinds of coatings have already shown promising results in anti-fouling/fouling release (AF/FR) coatings for marine applications [20–23]. There is a wide range of marine biofoulants with complex surface adhesion properties [24]. Hard foulants like barnacles and mussels behave differently compared to soft foulants like algae, bacteria, and

biofilm [25]. However, there is a similarity between these two foulants. Both ice and biofoulants tend to dislike low surface energy surfaces [26–30]. Low surface energy materials are good for ice shedding for smaller-scale applications and may not scale for larger interfaces [31].

Ice adhesion occurs in multiscale from very small length scale to several meters. Therefore, two different characterization methods are employed to evaluate the ice-shedding property of the coatings [32]. In shorter length scales, per unit area, ice adhesion strength plays a major role in determining ice-shedding properties while this measure does not necessarily work for longer length scales. There is an asymptotic relationship between force required to remove ice and the length scale of ice, which means force required to remove ice remains constant after a certain length of ice [32]. For a longer scale, interfacial toughness plays an important role such that a constant shear force is needed after a certain length scale of ice. Therefore, even a low ice adhesion strength coating can have higher interfacial toughness. For larger-scale ice shedding, low interfacial toughness materials are required, rather than just low ice adhesion strength materials [33,34]. There is also a need for materials with dual-purpose ice and biofouling release applications that can transform today's maritime industry [35].

The objective of this study is to investigate the effect of incorporation of silicone oil additives in urea-siloxane coating for ice and biofouling release properties. Different silicone oil additives were used in the coating's formulation at different amounts to study ice adhesion, contact angle, surface energy, and surface morphology. We hypothesize that the oils leach out from the polymer network over time and provide a lubricating property to the surface, thus enabling easy removal of ice and biofoulants. The formulations with low ice adhesion strength were further tested for interfacial toughness and with a range of biofouling assays.

2.3. Materials and methods

2.3.1. Materials

Methoxyfunctional, methyl-phenyl polysiloxane resin (Silres SY 231) was provided by Wacker Chemie AG. DOWSIL 3074 Intermediate, another methoxyfunctional, methyl-phenyl silicone resin was provided by Dow Inc. Polyfunctional aliphatic polyisocyanate (HDI trimer), Desmodur N 3600 was provided by Covestro AG. N-butylaminopropyltimethoxysilane (SIB1932.2) was purchased from Gelest Inc. All the silicone oils (Table 1) were also purchased from Gelest Inc. Toluene and butyl propionate were purchased from VWR International, LLC. Ethyl-3-ethoxypropionate (EEP), methyl ethyl ketone (MEK), and dibutyltin diacetate (DBTDAc) were purchased from Sigma-Aldrich. Toluene was dehydrated with 4 Å molecular sieves purchased from Sigma Aldrich. All other reagents were used as received. Steel panels with a smooth finish (3×6 in2, 0.5-mm-thick, QD-36 type) and aluminum panels (4×8 in2, 0.6 mm thick, type A, alloy 3003 H14) were purchased from Q-Lab. Aluminum panels were used for biofouling assays. They were sandblasted and primed with Intergard 264 (International Paint) using air-assisted spray. Falcon 24-well, sterile polystyrene cell culture plates were purchased from VWR International (PA, USA) and were modified with 1-in. diameter circular disks cut from coated primed aluminum panels.

2.3.2. Synthesis of a polyurea resin

A polyurea resin was synthesized following US patent 8,133,964 [36,37] (Figure 2.1). Briefly, 81.6 g of Desmodur N 3600 was dissolved in 60 g of butyl propionate in a 500 ml 3-neck round bottom flask with mechanical stirrer, nitrogen inlet, and thermometer. The solution was heated to 50 ℃. Then, 104.9 g of SIB 1932.2 was added dropwise to the solution with continued mixing. The reaction was exothermic, so the temperature of the solution was

maintained between 50-60 ℃. After the addition was complete, the solution was heated for 30 minutes at 50 ℃.

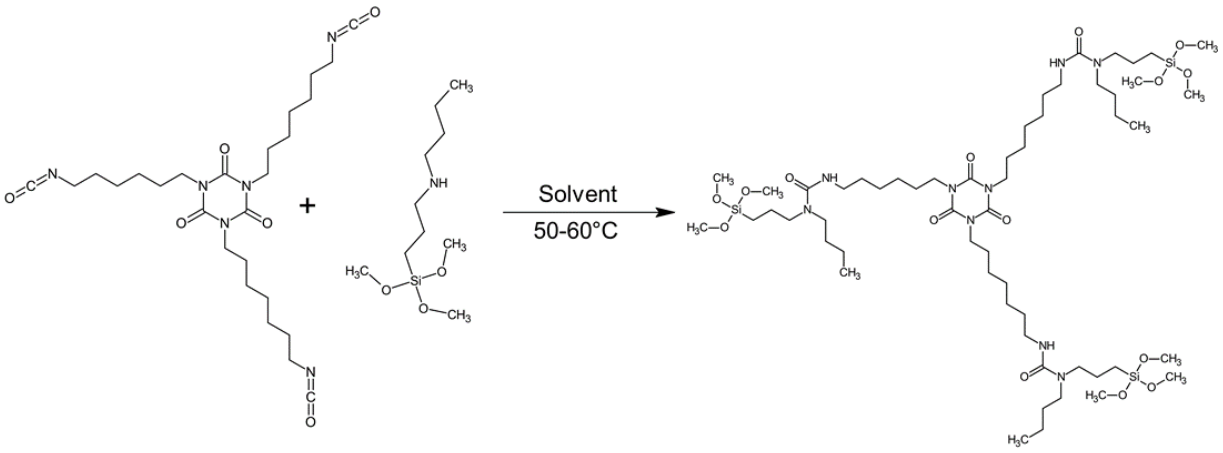

Figure 2.1. Synthesis of methoxysilane functional polyurea resin.

2.3.3. Fourier transform infrared (FTIR) spectroscopy

FTIR spectroscopy was done to determine if all the isocyanates reacted during urea resin synthesis. FTIR measurement was done using a Thermo Scientific Nicolet 8700 FTIR.

2.3.4. Percent solids determination

The percent solids of the polyurea resin were determined following ASTM 2369. Briefly, an empty aluminum pan was weighed. Resin (1-2 g) is put in the pan and weighed again. The pan was put in an oven at 110° C for 1 hour and then weighed again. Percent solids are then determined by the equation 2.1.

$$Percent\ solids = \frac{Final\ weight\ of\ pan\ and\ resin - Weight\ of\ empty\ pan}{Intial\ weight\ of\ resin} \qquad (2.1)$$

All measurements were done in triplicate.

2.3.5. Coatings formulation and curing

Coatings were formulated following US Patent 8,133,964 [36,37]. Briefly, the polyurea resin with around 76% total solids (12.6 g) was mixed with Silres SY 231 siloxane resin (2.4 g). EEP (1.5 g) and toluene (0.64 g) were added to the mixture. DBTDAc catalyst was also added at

0.4% of the total solids of the coatings along with different amounts of silicone oils (Table 2.1). The vial with the mixture was then mixed with a magnetic stirrer at 350 rpm for one hour. After the mixing was complete, the mixture was allowed to settle for half an hour. Coatings were applied using an RDS 60 wire rod on primed Al-panels for biofouling assays and on steel Q-panels for all other tests. The coatings were allowed to cure under ambient conditions for seven days in a dust-free enclosed cabinet before testing. The coatings were tack-free after overnight curing.

In another set of experiments, coatings were prepared with DOWSIL 3074 intermediate instead of Silres SY 231. The weight and preparation method were similar to Silres SY 231 resin.

Silicone oils used in this study are named using the convention: AB-X-XX. 'A' represents repeating unit 1 and 'B' represents repeating unit 2. 'X' represents the weight percent of repeating unit 1 and 'XX' represents the degree of polymerization. The repeating units can be either diphenyl (DP), dimethyl (DM), or phenylmethyl (PM). For example, PMDM-101-045 means that it is a copolymer of phenyl-methyl siloxane (PM) and dimethyl siloxane (DM) with 10 weight percent of phenyl-methyl siloxane and an overall average degree of polymerization of 45 units.

Table 2.1. Silicone oils used in this study

Formulation	Oil	%		Formulation	Oil	%
F-0	Base coating	0		F-9	PMDM-010-045	5
F-1	DM-100-027	1		F-10	PMDM-010-125	1
F-2	DM-100-081	5		F-11	PMDM-010-125	5
F-3	DM-100-185	1		F-12	PMDM-010-125	6.5
F-4	DM-100-185	5		F-13	PMDM-010-563	5
F-5	DM-100-185	6.5		F-14	PMDM-050-020	5
F-6	DM-100-378	5		F-15	PMDM-060-035	5
F-7	PM-100-020	5		F-16	PMDP-050-004	5
F-8	PMDM-010-020	5				

2.3.6. Ice-adhesion measurement

There are not yet universally accepted ice adhesion test procedures and different studies use different ways of measurements [38–40]. In brief, our measurement setup consisted of a cooling unit, a test stand with a cooling flat plate, a pushing force gauge that can move back and forth in one direction, and a cylindrical silicone mold for ice growth. The cooling unit was set at -20℃. Q-panel with the cured coating was fixed on top of the cooling plate and mold was placed on top of the coating. Distilled water was put in the mold and let it freeze completely. The time of freezing varied between different coatings between 50-80 minutes. Once the ice was formed, the mold was taken off. The clearance between the coated plate and the tip of the force gauge was set to a minimum (~1 mm). Ice was pushed horizontally at a speed of 10 mm per minute and the force required to dislodge the ice from the surface was noted. Each coating was tested in triplicate and an average value was noted. The lower the force required, the higher the icephobicity of the coating. The ice adhesion setup is provided in Figure A5 in Appendix A.

2.3.7. Interfacial toughness measurement

Coatings with formulations from Table 2.2 were prepared in a 3×8 in2, 0.5-mm-thick panel purchased from Q-Lab for interfacial toughness measurement. The setup for the interfacial toughness measurement is provided in Figure S6 in Supporting Information. Briefly, the coated panel is attached to a Peltier cooling plate using 3M 300LSE double-sided tape. The temperature of the Peltier plate was maintained at -10℃. Some samples had issues with frost development, so the temperature was slightly increased to -9℃ to prevent frost formation. 3D-printed rectangular cuvettes of various lengths between 1 cm and 16 cm with 1 cm width, each were placed onto the sample. Typically, 3 to 5 cuvettes can be fit for each test cycle. Deionized water was used to fill the bottom layer of the cuvettes using a pipette. Once the bottom layer freezes, the rest of the

cuvettes were filled with water again. This is done to prevent water leaks from the cuvette. Once the water was filled, we waited for approximately 20 minutes to allow for the ice to be completely frozen. Once the ice is frozen, the ice is pushed off using a motorized force gauge at a speed of 73.50 μm/s and the peak ice removal force was recorded. After the ice removal, the Peltier plates were powered off and the samples were allowed to come back to room temperature. Excess moisture was removed in between icing cycles using a handheld air blower. Several icing cycles were carried out until there were at least 5 data points for each length of the cuvette.

Table 2.2. Formulations tested for biofouling assays and interfacial toughness

Formulation #	Oil	%	Oil commercial name
F-0	No oil	-	-
F-4	DM-100-185	5.0%	DMST23
F-5	DM-100-185	6.5%	DMST23
F-9	PMDM-010-045	5.0%	PMM1021
F-10	PMDM-010-125	1.0%	PMM1025
F-11	PMDM-010-125	5.0%	PMM1025
F-12	PMDM-010-125	6.5%	PMM1025

2.3.8. Biological laboratory assays

Four different laboratory biological assays were performed to evaluate the AF/FR performance of coatings with commercial and internal standards according to previously described methods [41–44]. The internal standards used for comparison are given in Table 2.3. The assays included bacterical (Cellulophaga lytica) biofilm growth and adhesion, diatom (Navicula incerta) growth and release, green microalgae (Chlorella vulgaris) cell attachment and biofilm growth, and adult barnacle (Amphibalanus amphitrite) 2-week attachment and adhesion. Details of the experimental procedures are provided in the Appendix A.

Table 2.3. Standard coatings used as a control in this study for comparison with our formulations

ID	Name	Composition
T2	Dow Corning® T2	Silicone elastomer-based commercial FR coating
PU	Polyurethane	NDSU prepared polyurethane standard coating
700	Intersleek® 700	Silicone elastomer-based commercial FR coating
900	Intersleek® 900	Amphiphilic-based commercial FR coating
1100 SR	Intersleek® 1100 SR	Amphiphilic-based commercial FR coating with slime release technology

The formulations tested for biological fouling assays are given in Table 2. These are the same formulations tested for interfacial toughness measurement.

2.3.9. Surface characterization

Surface characterization of the coating was performed by Atomic Force Microscopy (AFM). The sample panel was placed on the sample holder of the Oxford Asylum Jupiter XR microscope. A silicon cantilever (AC240) probe was calibrated and used for scanning the sample. Height and phase images were gathered from the scans. Similarly, surface characterization was also carried out with X-ray photoelectron spectroscopy (XPS). A Thermo Scientific K-Alpha XPS equipped with Al Kα (1486.68 eV) X-ray source and Ar+ ion source (up to 4000 eV) was used for elemental composition of the coating surfaces and depth profiling. A total of 29 etch cycles were performed.

2.3.10. Contact angle and surface energy measurements

All the coatings were characterized for water contact angle (WCA), methylene iodide contact angle (MICA), and surface free energy using Kruss® DSA 100 (Drop Shape Analyzer). Surface-free energy was calculated using the Owens-Wendt method. All the measurements were quantified with Kruss® Advance software.

2.3.11. Mechanical characterization

The film thickness of the coatings was measured with a Byko-Test 8500 coating thickness gauge. The gauge is based on the principle of electromagnetic induction. The gauge was zeroed against the standard and calibrated, and then the thickness of the coating was measured at different places on the coating.

Pencil hardness was done following ASTM D 3363. The pencil with the hardest lead was dragged into the coating surface at a 45° angle and the process was repeated with lower hardness pencils. Gouge resistance was noted with the hardest pencil that will not cut or tear film and mar resistance was noted with the hardest pencil that will not make a scratch.

König pendulum hardness test was done following ASTM D 4366 in which the panel was loaded in the machine and time was counted for the pendulum to go from 6° to 3° angle. The process was repeated for different places on the coating.

Impact tests of the coatings were performed following ASTM D 2794 using a falling dart or Gardner impact tester. The front and reverse impact strength of the coatings were noted based on the coating side on the Q-panel. The maximum drop height of the 4lb weight load in the tester was 43 inches. A coated Q-panel was placed (both the front coated side and back side) in the tester and the maximum weight was dropped. The process was repeated with decreasing height until no deform was seen on the coating surface upon impact. The impact value was then noted as the product of the drop height and weight of the load.

A crosshatch adhesion test was done following ASTM D 3359. The coating was crosshatched using a crosshatch cutter kit and taped with cross-hatch adhesion tape. The tape was then removed and the removal of the coating was observed. Based on the extent of removal

of the coating, the result was matched with the standard where 0B is the poorest and 5B is the best.

The extent of solvent resistance of the coatings was tested with MEK double rubs following ASTM D 5402. A hammerhead was wrapped with cheesecloth and soaked MEK. The hammer was then rubbed back and forth, recording the double rubs until the coating failure was observed. The coating fails when the substrate is exposed. The cheesecloth was soaked after every 50 rubs.

A conical mandrel test was done following ASTM D 522 to test the flexibility of the coating. The coated panel was loaded in the conical mandrel and bent. The panel was then inspected for any cracks in the coating.

2.4. Results and Discussion

Ice accretion on surfaces of airplanes, ships, and wind turbines has operational safety and reliability issues with potential catastrophic failures. Anti-icing or in general, ice-shedding coatings are a desired choice to overcome the challenges posed by ice accretion on these surfaces. The coatings that are to be applied on these surfaces should be easy to apply and provide good mechanical properties including excellent adhesion, impact resistance, durability, and flexibility along with low ice adhesion properties. A single component moisture curable polyurea-siloxane coating has shown good mechanical properties along with safety and ease of application [36]. The backbone of the coating is formed by aliphatic polyurea linkages, and the polymer crosslinks via the polycondensation of the alkoxy groups present in the siloxane and the silane groups of the polyurea resin. The surface properties of the coatings such as ice adhesion and surface-free energy are expected to be reduced by silicone oil additives on the base coating formulation.

2.4.1. Poly-urea resin and urea-siloxane coating

The synthesis of N-substituted urea resin was confirmed by FTIR (Appendix A Figure A7). The complete disappearance of the isocyanate (NCO) peak at around 2250 cm-1 confirms the reaction of the NCO group. The solids content of resin was 76%. The curing mechanism of urea siloxane follows hydrolysis-condensation process (Figure 2.2). The methoxy groups in the urea resin and the siloxane resin (Silres SY 231) hydrolyze in the presence of moisture forming silanols. Silanols can polycondense resulting in a crosslinked structure.

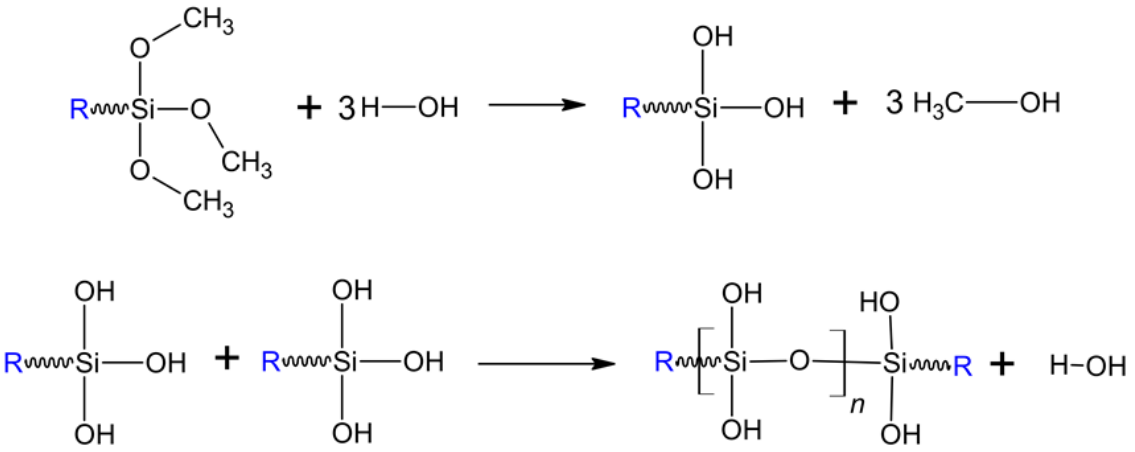

Figure 2.2. Reaction scheme of polyurea-polysiloxane coating

2.4.2. Coatings characterization

Initially, a base coating (no oil additives) without any catalyst was prepared. After two weeks of ambient curing, MEK double rubs were tested for chemical resistance of the coating which was less than 50. To accelerate the curing and improve chemical resistance, 0.4% DBTDAc was added to the formulation. After one week of curing the coating showed 200+ MEK double rubs and after two weeks of curing, it showed 400+ MEK double rubs. MEK double rubs were lower with lower humidity in the ambient conditions. For all further coatings, 0.4% DBTDAc was used as catalyst.

2.4.2.1. Mechanical measurements

The results of mechanical tests for the initial set of coatings with the silicone oil additives (Table 2.1) is given in Table A1 in the Appendix A. The results show that the coatings have excellent adhesion, very high flexibility, impact resistance, chemical resistance, and good hardness. The addition of silicone oils did not impact the mechanical properties of the coatings to any significant extent. Cross hatch adhesion tests showed that the coatings have very good adhesion to the steel substrate. The silane and urea groups provide a strong hydrogen bonding with the substrate. All coatings with the oil additives passed the conical mandrel bend tests without any cracks. This shows that the coating is very flexible, and the addition of oils does not impact its flexibility. The aliphatic polymeric backbone and polysiloxane provide the coating with the necessary flexibility and high impact resistance which makes the coating very durable. Coatings with PMDM-010-125 silicone oil (F-10 to F-12) were slightly brittle as seen by lower reverse impact resistance (without coating). Coatings with PMDM-010-563 had lower impact resistance. The base coating showed moderate pencil hardness of 1H. The addition of silicone oils made the coatings slightly softer with most formulations having a pencil hardness of 1B. Pencil hardness is a qualitative test and shows the hardness of the bulk coating. We also see a similar trend in pendulum hardness. Pendulum hardness gives the measure of surface hardness. The addition of oils reduces the hardness which means oil is present on the surface of the coating. The majority of the formulations had 200+ MEK double rubs which showed that the coatings had excellent chemical resistance.

2.4.3. Ice adhesion

The results of the initial ice adhesion tests showed a reduction in the ice adhesion strength of the coatings for most of the oil additives (Figure 2.3). Ice adhesion is the measure of

shear force/stress required to dislodge the ice from the coating surface. Our hypothesis here is that the addition of silicone oil additive in the coating formulation creates an interfacial slippage layer from the oil leaching out of the coating matrix to the surface. Since oils have very low shear modulus, they provide ease in the removal of ice. The base coating without any oil additives already shows icephobic characteristics with less than 100 kPa ice adhesion strength. One possible reason for this may be the presence of siloxane on the surface of the coating. Siloxanes are known to be hydrophobic which also helps in their icephobic properties. Among the oil additives, DM-100-185 and PMDM-010-125 showed the lowest ice adhesion strength compared to the other oils. Therefore, we also tested these oils further at 1% and 6.5% in the coating's formulation. DM-100-185 oil at 5% (F-4) and 6.5% (F-5) showed very low ice adhesion strength. One reason for its low ice adhesion strength might be that PDMS oils are known to be very hydrophobic and help lower the ice adhesion strength [45,46]. PDMS also has lower surface tension than the siloxane used in the base system and will tend to predominate on the surface. Compared to other PDMS oils, DM-100-185 showed the lowest ice adhesion strength. Phenyl methyl silicone oil PMDM-010-125 at 1% (F-10), 5% (F-11), and 6.5% (F-12) also showed low ice adhesion strength. One similarity of this oil with the PDMS oil with the lowest ice adhesion strength is its molecular weight. DM-100-185 has 13,650 MW while PMDM-010-125 has 10,000 MW. Compatibility/miscibility of the oils can be another influencing factor in ice adhesion as well. Our coating matrix contains phenyl-methyl siloxane as its backbone (from the Silres Sy231 resin). Therefore, PMDM oils may be more compatible with the base matrix compared to DM oils. The impact resistance test for PMDM-010-563 showed a low value, which may mean that the oil is more compatible with the matrix, so it is more evenly distributed making the coating comparatively brittle. Compatibility of oils is also a factor of

molecular weight. Higher molecular weight oils can have lower compatibility compared to lower molecular weight oils due to their longer chains.

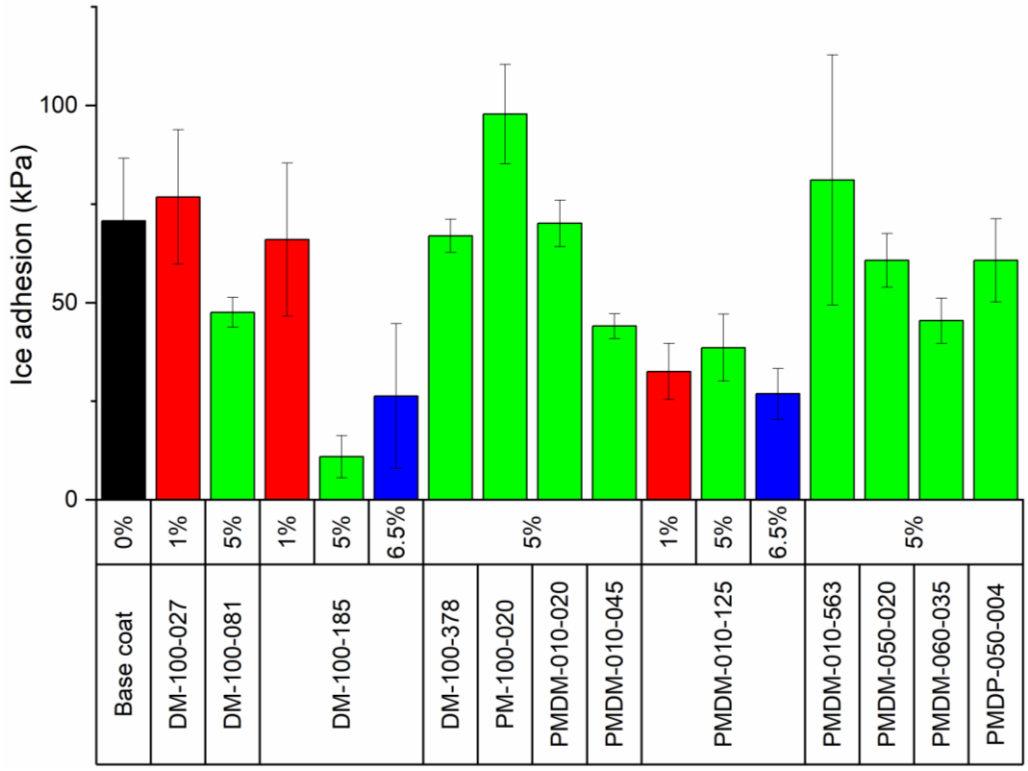

Figure 2.3. Ice adhesion of coatings with different oil additives.

2.4.4. Contact angle and surface free energy

Measurement of contact angles gives information on hydrophobicity and surface free energy of the surface which is very important in understanding the surface characteristics of the coatings. Water is used as a polar liquid and methylene iodide is a non-polar liquid for the measurement of contact angles. The result of the contact angle measurement is given in Figure 2.4. The base coating without any oil additives showed a hydrophobic nature with a greater than 95° water contact angle. The addition of PDMS oil showed an increase in both WCA and MICA. We saw a decrease in both WCA and MICA with the phenyl methyl silicone oils. However, there is an increase in both WCA and MICA with phenyl methyl dimethyl silicone oils having 10% phenyl methyl content. When the phenyl methyl content of the silicone oil increased, we saw a

decrease in both WCA and MICA. The fact that phenyl groups are more polar than methyl groups, phenyl groups tend to be less hydrophobic than methyl groups. This is reflected in our contact angle results.

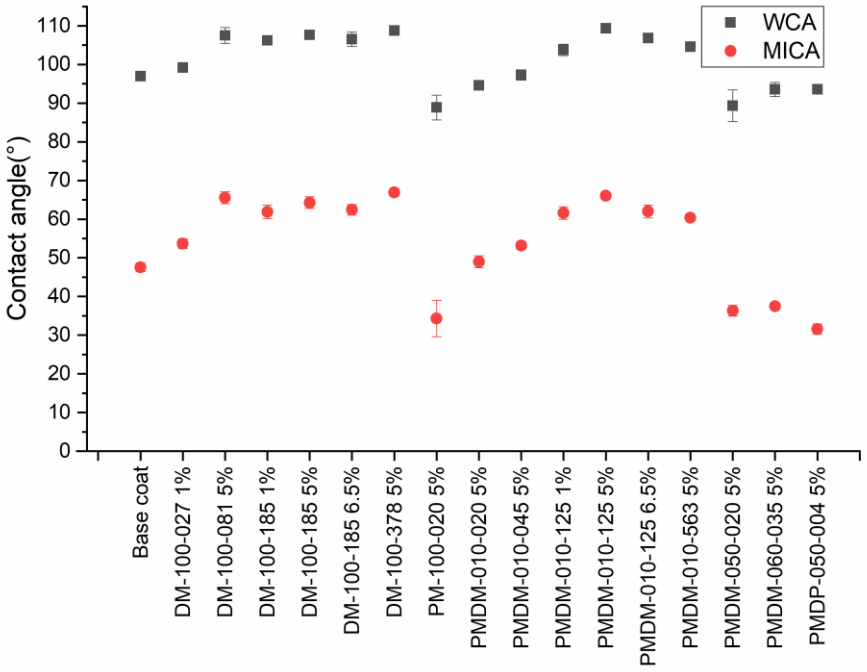

Figure 2.4. Contact angles of coatings with different oil additives

To determine the effect of oil additives on surface properties, we also determined the surface-free energy of the coatings (Figure 2.5). Silicone oil additives showed a reduction in the surface free energy of the coatings. Since the surface tension of silicone oils is lower than the surface free energy of our coating, it shows that oils are present on the surface of the coating because the surface free energy of the coating decreases with the addition of oils.

We saw a positive correlation between the contact angles and ice adhesion strength. This means that hydrophobic coatings also showed icephobic properties. The surface free energy also showed a positive correlation with ice adhesion strength and contact angles. Hydrophobic and icephobic surfaces showed lower surface free energies.

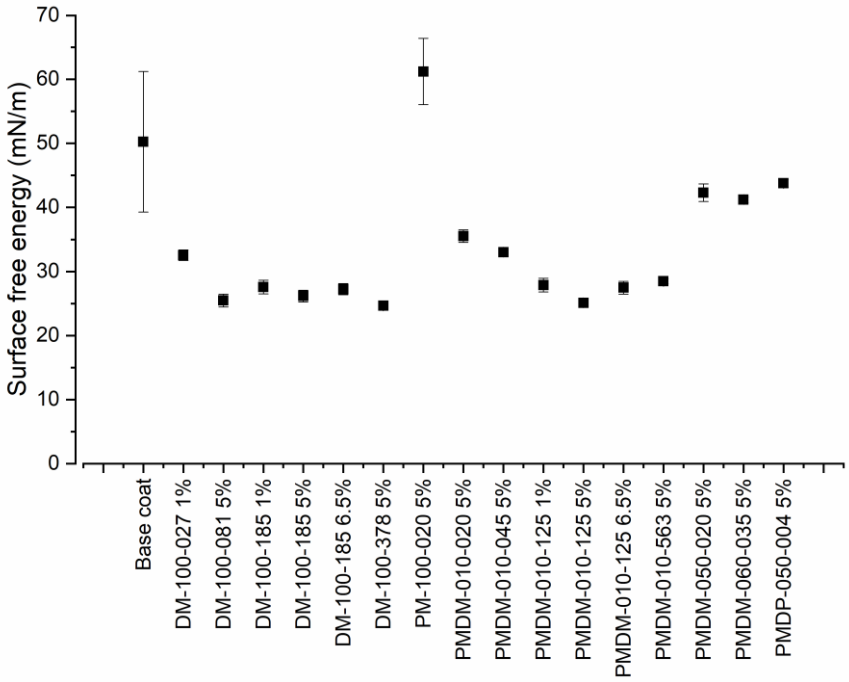

Figure 2.5. Surface free energy of coatings with different oil additives

2.4.5. Atomic force microscopy

AFM images of several representative formulations were taken to characterize the surface of the coatings (Figure 2.6). The images showed that coatings with oil additives have two distinct domains consisting of oil on the surface of the base matrix. This shows that oil leaches out of the coating. The presence of oil domains on the surface of the coating can help reduce ice adhesion strength [47]. As shown in Figures 2.6 A and B, the base coating has no domains. For F-4, the size of the domains of silicone oil are not uniform. The frequency of smaller-size domains was higher than the larger-size domains. The oils are distributed throughout the coating and we did not see any agglomeration. For F-12, the size of the domain of silicone oil is larger compared to F-4 and there is more variability in the distribution of different size domains. The digital microscope images of some of the formulations are shown in Figure A8 in Appendix A. Lower percentage oils in the formulation have lower size oil droplets compared to higher percentage oils in the formulation.

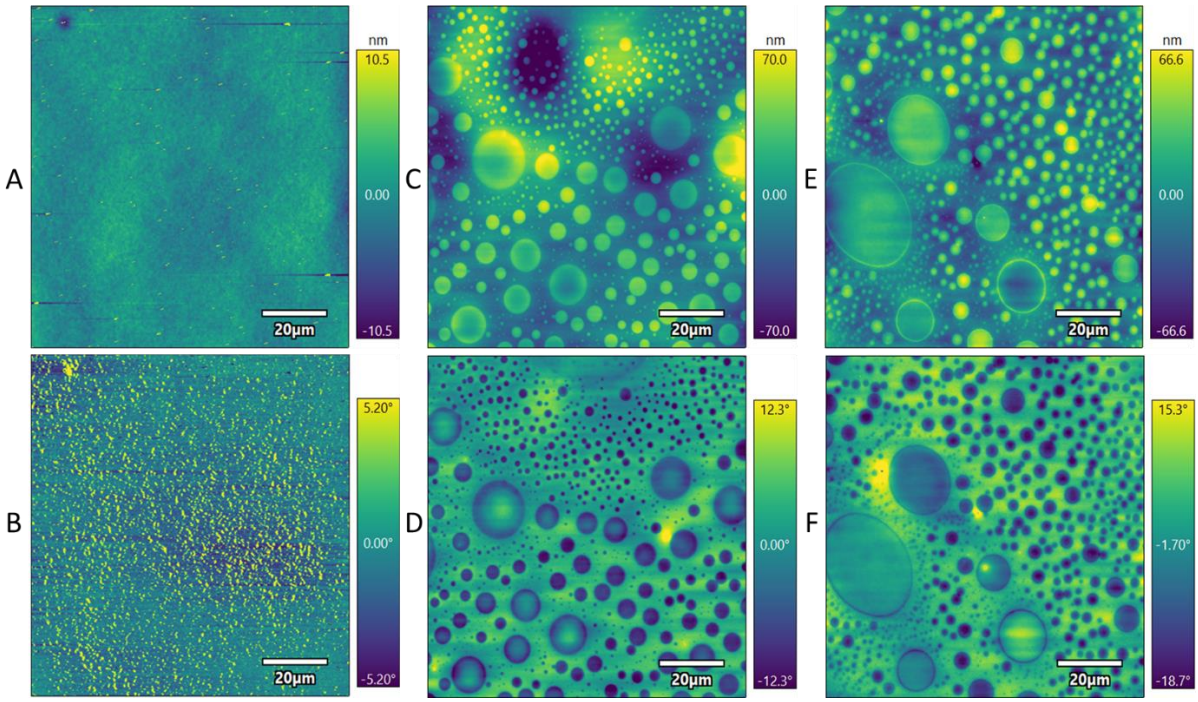

Figure 2.6. AFM images with phase and height images for coatings with different oil additives (a and b: F-0 with no oil; c and d: F-4 with 5% DM-100-185; e and f: F-12 with 6.5% PMDM-010-125); top image represents the height and bottom image represents phase image

2.4.6. XPS characterization

XPS scanning results with depth profiling are shown in Figure 2.7. A total of 29 etches (scan #) were done with each etch depth of 30 nm. The result shows that different oils have different influences on the distribution of the matrix constituents. Formulations with dimethyl silicone oil that show the urea linkage is more prevalent in higher depths away from the surface and silicon is more towards the surface. With phenyl methyl dimethyl silicone oil copolymers, the composition is uniform at higher depths, similar to the base coating. This may be due to the compatibility of the oil with the matrix as the matrix also contains phenyl methyl silicone moieties.

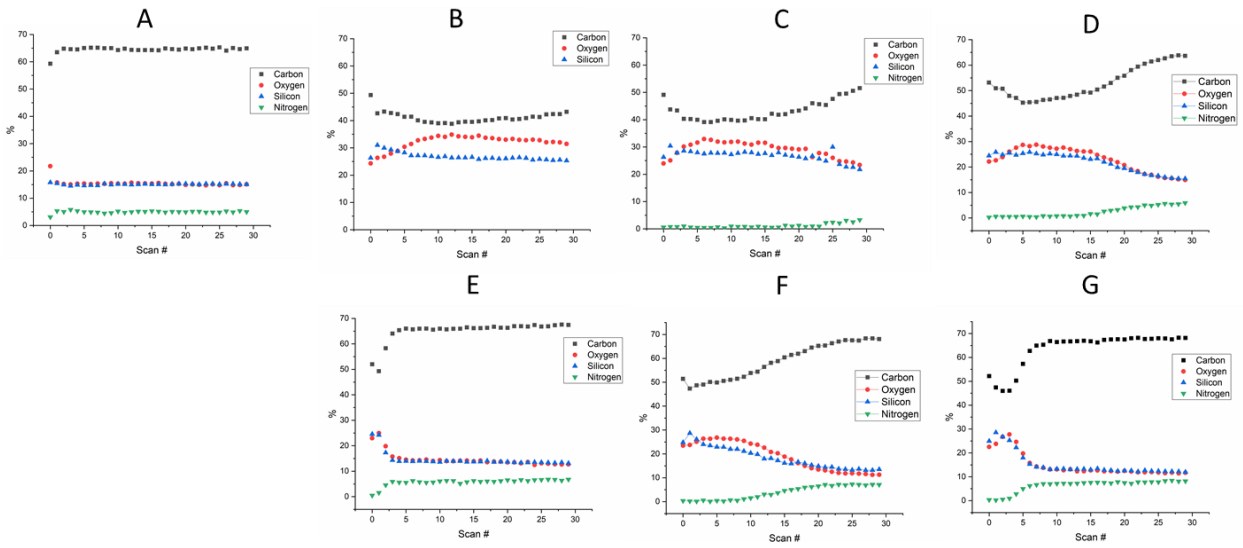

Figure 2.7. XPS depth scanning profile for different formulations (A. Base coating, B. 5% DM-100-185, C. 6.5% DM-100-185, D. 5% PMDM-010-045, E. 1% PMDM-010-125, F. 5% PMDM-010-125, G. 6.5% PMDM-010-125)

2.4.7. Coatings formulated with DOWSIL (DC3074) resin

We also prepared F-4, F-10, and F-12 coatings with DOWSIL 3074 resin instead of Silres SY 231. The results of ice adhesion, contact angles, and surface free energy are given in Figure 2.8. The results were comparable with formulations containing Silres SY 231 resin.

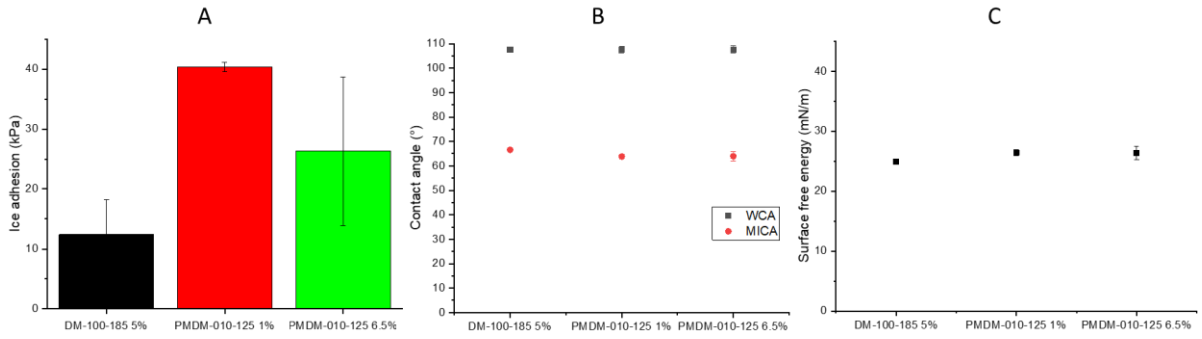

Figure 2.8. Ice adhesion (figure A), contact angle (figure B), and surface free energy (figure C) tests for coating with DOWSIL 3074 resin

2.4.8. Interfacial toughness measurement

Lower interfacial toughness materials are important for large-scale ice-shedding surfaces. Lower interfacial toughness helps to reduce the overall force required to remove ice by

promoting the easier propagation of a crack in the ice-substrate interface [32]. Surface microstructures and domains can help promote crack propagation and lower the interfacial toughness of materials [48]. A total of 7 different formulations (Table 2.2) were selected to perform interfacial toughness measurements. The results of interfacial toughness measurements are shown in Figure 2.9 and the summary of the measurements is given in Table 2.4. F-0, which is the base coating without any oil additives resulted in cohesive debonding of the ice from the coating surface, so interfacial toughness results are not reported. For all other formulations, the results show that they have very low interfacial toughness. As a general consensus, interfacial toughness values of less than 1 J/m2 are considered low interfacial toughness materials. All of the 6 formulations with silicone oils resulted in an interfacial toughness value of less than 1 J/m2. Among all the formulations, F-4 with 5% DM-100-185 oil showed the lowest interfacial toughness. This is the same formulation that showed the lowest ice adhesion strength in the initial screening tests.

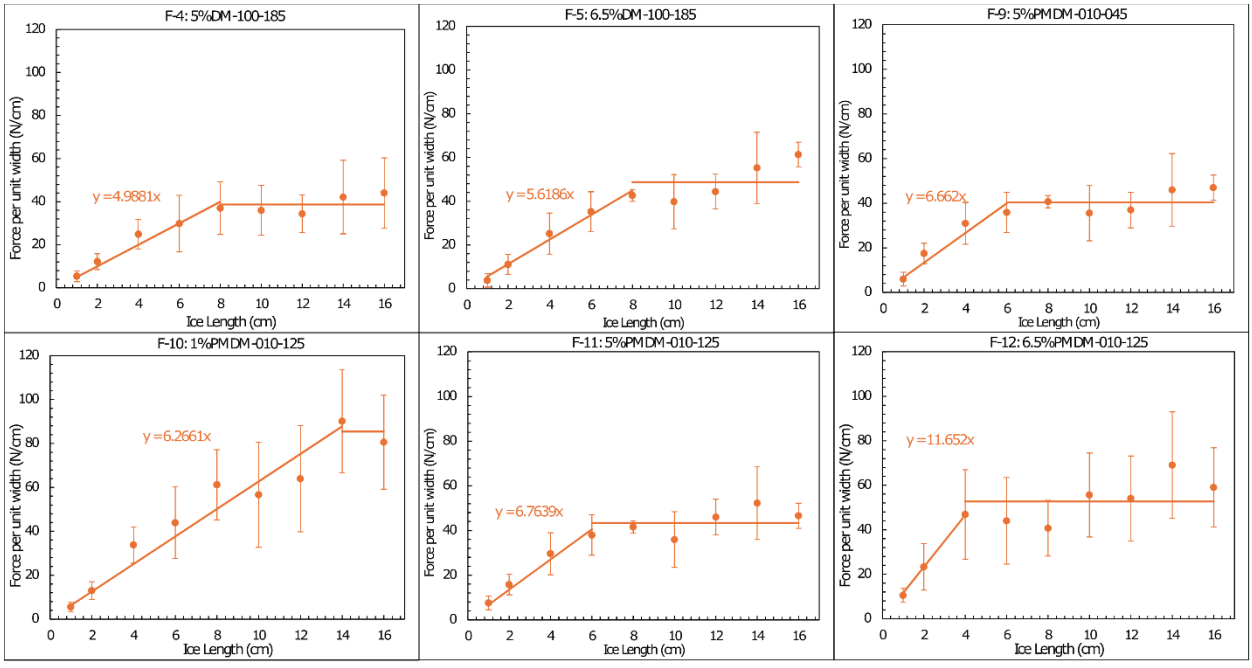

Figure 2.9. Force per unit width results for different ice lengths for different formulations

The ice adhesion strength results from the interfacial toughness measurement experiment varied from our initial screening results because of different test setups. Ice adhesion to polymer substrates can depend on various factors. The primary reason for the very low ice adhesion strength in our screening tests was that we did ice adhesion measurements in fresh panels and only for one cycle. However, interfacial toughness tests are done for multiple icing cycles for the same panels. The oily layer on the top of the coating panels can be washed away with each icing deicing cycle. Another difference in test setup is related to the temperature of freezing. For initial screening, the temperature of the Peltier plate was maintained at -20℃ while for interfacial toughness tests was maintained at -10℃. However, we saw a similar trend in the results between initial screening tests and interfacial toughness tests. The critical length showed a different trend in the results. F-12 with 6.5% PMDM-010-125 oil showed the lowest critical length of 4 cm.

Table 2.4. Summary of results of interfacial toughness measurement

Formulation	Composition	Dry film thickness (μm)	τ_{ice} (kPa)	Γ (J/m^2)	L_{cr} (cm)	F_{cr} (N/cm)
F-0	Base coating (BC)	57.0±6.7	Cohesive failure			
F-4	BC + 5% DM-100-185	56.5±1.0	49.9±25.3	0.15±0.032	8±6.4	38.7±4.2
F-5	BC + 6.5% DM-100-185	63.0±7.6	56.2±21.6	0.23±0.088	8±5.8	48.7±9.2
F-9	BC + 5% PMDM-010-045	65.3±11.9	66.6±23.1	0.16±0.040	6±3.3	40.3±5.1
F-10	BC + 1% PMDM-010-125	54.8±2.2	62.7±14.4	0.71±0.11	14±4.5	85.4±6.8
F-11	BC + 5% PMDM-010-125	67.1±7.6	67.6±29.8	0.18±0.051	6±4.6	43.4±6.1
F-12	BC + 6.5% PMDM-010-125	57.5±2.5	116.5±47.7	0.27±0.10	4±3.2	52.8±9.8

τ_{ice}: Ice adhesion strength, Γ: Interfacial toughness, L_{cr}: Critical length, F_{cr}: Critical force

2.4.9. Biofouling assays

Prior to carrying out the biological assays, the coatings were subjected to 30 days of immersion in water. This procedure is used to ensure that the coatings are stable under immersion and to leach out any potentially toxic materials. The coatings are then subjected to leachate toxicity tests using the marine organisms used for the assays. The results of leachate toxicity for *N. incerta*, *C. vulgaris*, and *C. lytica* are provided in the Appendix A. None of the coating formulations were toxic to the marine microorganisms.

Navicula incerta is a common diatom microalga which is responsible for slime formation and is known to prefer to adhere to hydrophobic silicone elastomers [18]. The results of water-jet treatment for microalgae, *N. incerta* are shown in Figure 2.10. Since our coating has a siloxane backbone matrix and the oils are silicone based, therefore, all of our formulations had very high initial cell attachment compared to the standards. However, our control coating (F-0 with no oil) had higher removal of the microalgae compared to other formulations with oil additives. Among oil additives, we see higher removal of the microalgae with F-9 at 20 psi water-jet pressure.

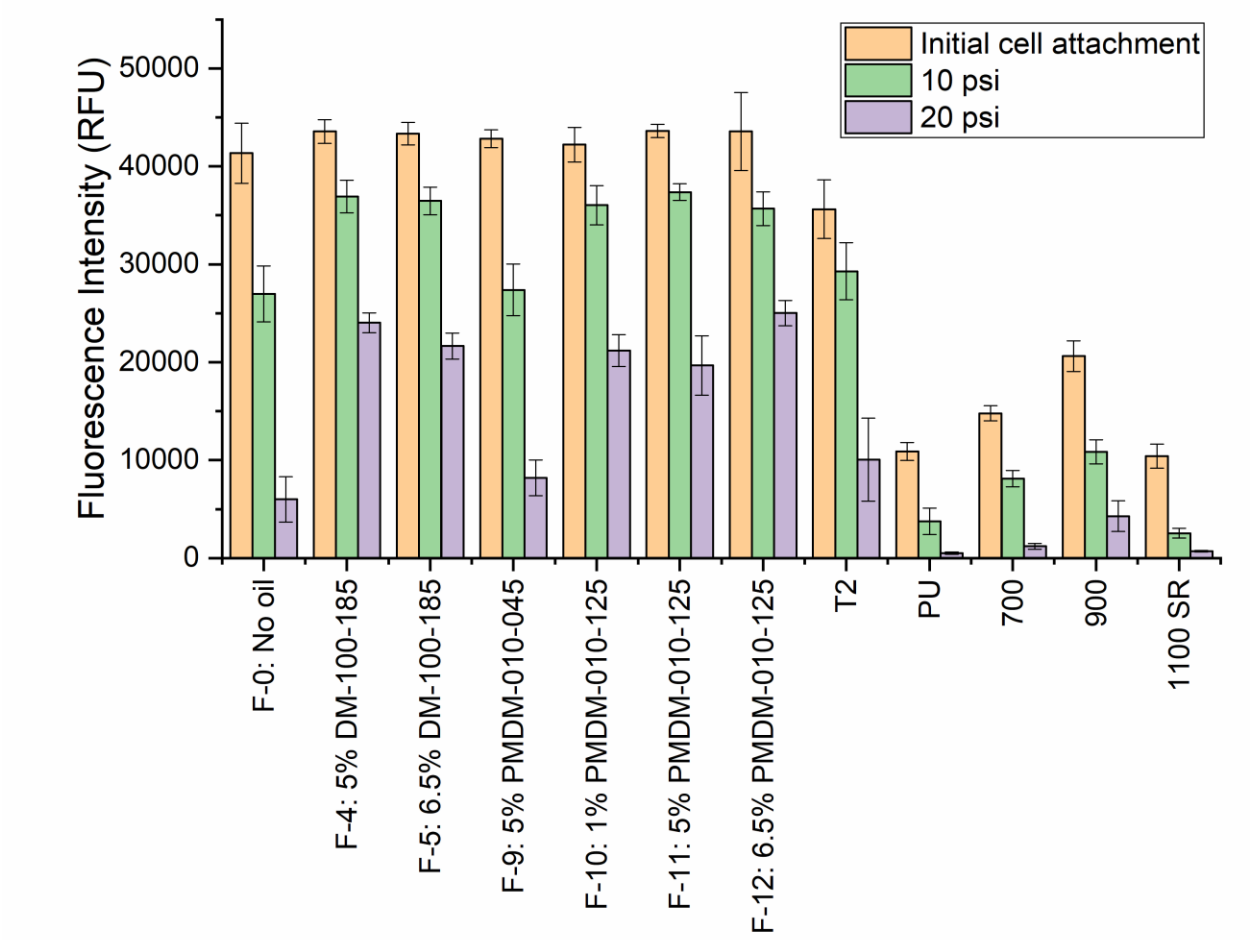

Figure 2.10. Initial cell attachment of microalgae *N. incerta* and biomass remaining after water-jet removal. The orange bars represent cell attachment while green and purple bars represent biomass remaining after 10 and 20 psi water-jet treatments, respectively

C. vulgaris is a commonly found microalgae in marine environments which can adhere to ship hulls and can influence the corrosion process [49]. These microalgae can adhere to both hydrophobic and hydrophilic substrates making it challenging to control them [50]. Compared to the base formulation with no oil, formulations with oil showed lower cell attachment of green microalgae *C. vulgaris* as shown in Figure 2.11. F-12 with 6.5% PMDM-010-125 oil showed the lowest attachment of the microalgae on its surface. However, the performance of the experimental coatings were not comparable to commercial standards such as 1100 SR which has very low cell attachment.

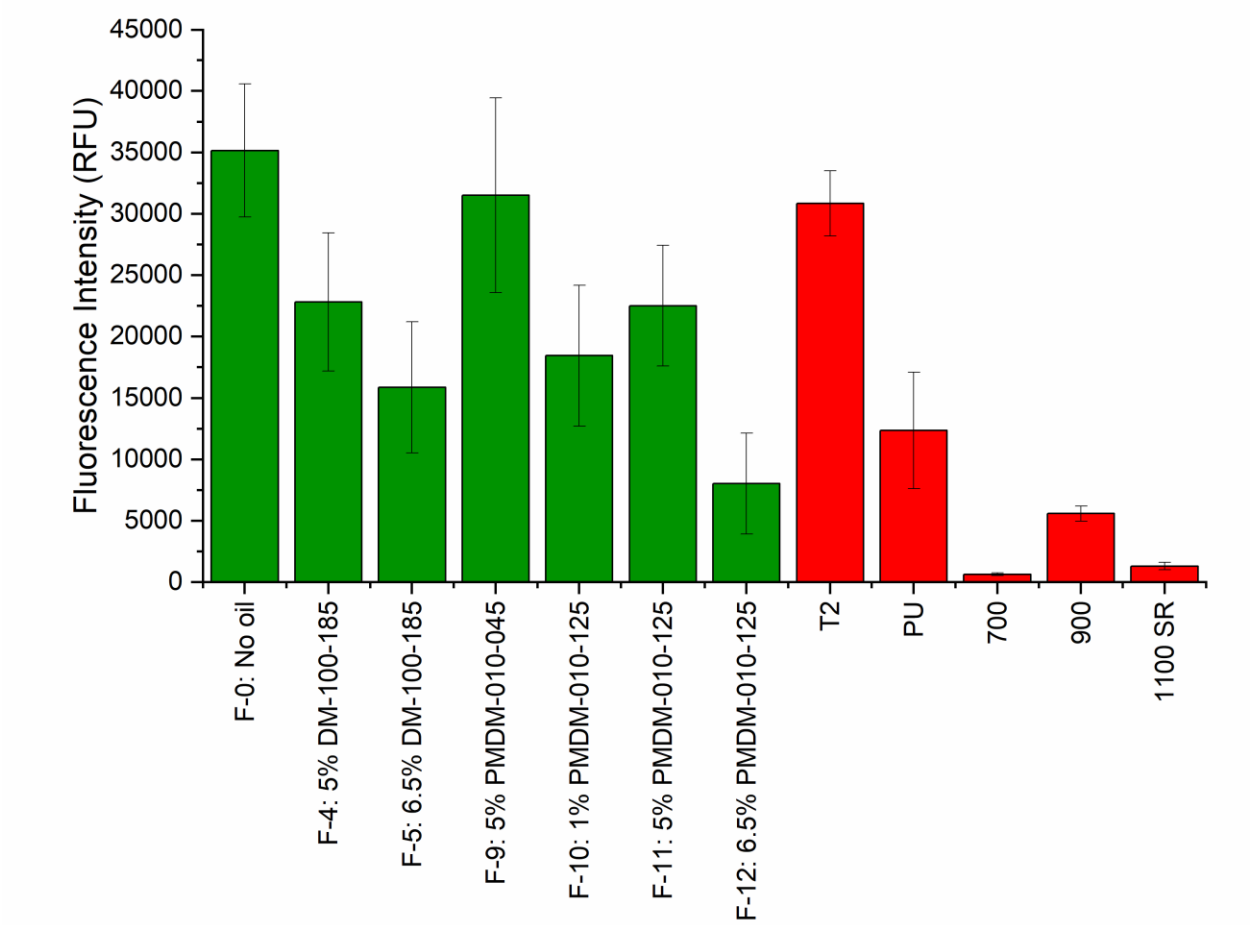

Figure 2.11. 2 hours cell attachment of green microalgae *C. vulgaris*. Red bars represent standards while the green bars represent our formulations

C. lytica is another major marine microorganism that can adhere to a wide range of surfaces including both hydrophilic and hydrophobic surfaces [25]. Formulations F-5, F-9, and F-11 showed very high biofilm removal at 20 psi water-jet treatment (Figure 2.12). These showed comparable performance with Intersleek 700 and better performance than T2 Silastic and polyurethane standards.

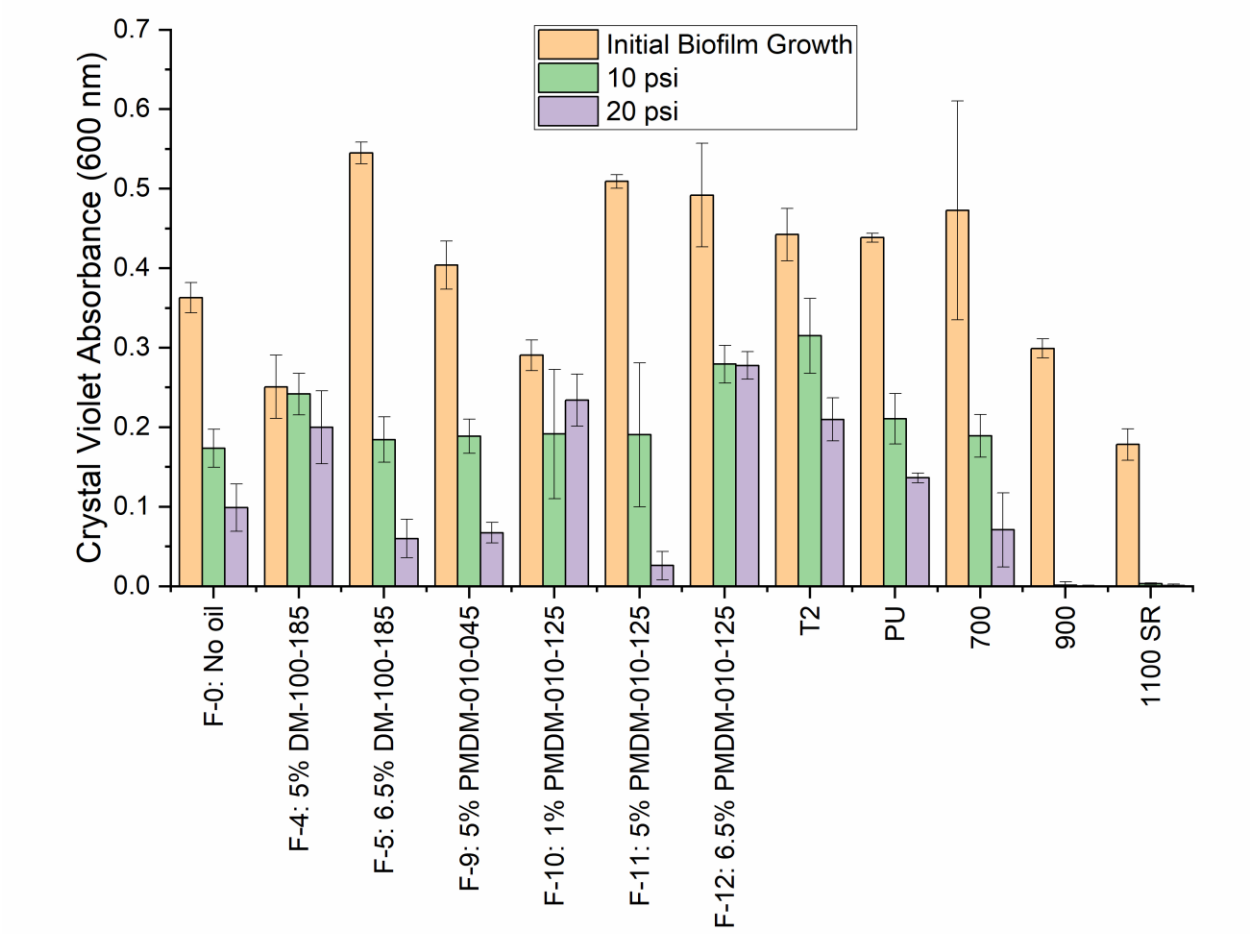

Figure 2.12. Initial biofilm growth after 24 hr of marine bacteria *C. lytica* and biomass remaining after water-jet treatment. The orange bars represent initial biofilm growth while green and purple bars represent biomass remaining after 10 and 20 psi water-jet treatments, respectively

Adult barnacles are major macrofoulants that can adhere to ship hulls and impact the performance of marine vessels. *A. amphitrite* is a barnacle that adheres easily to hydrophilic surfaces and also has high adhesion strength on hydrophobic surfaces as well [51]. Formulations F-4, F-5, F-10, and F-12 showed lower barnacle adhesion compared to the control (Figure 2.13).

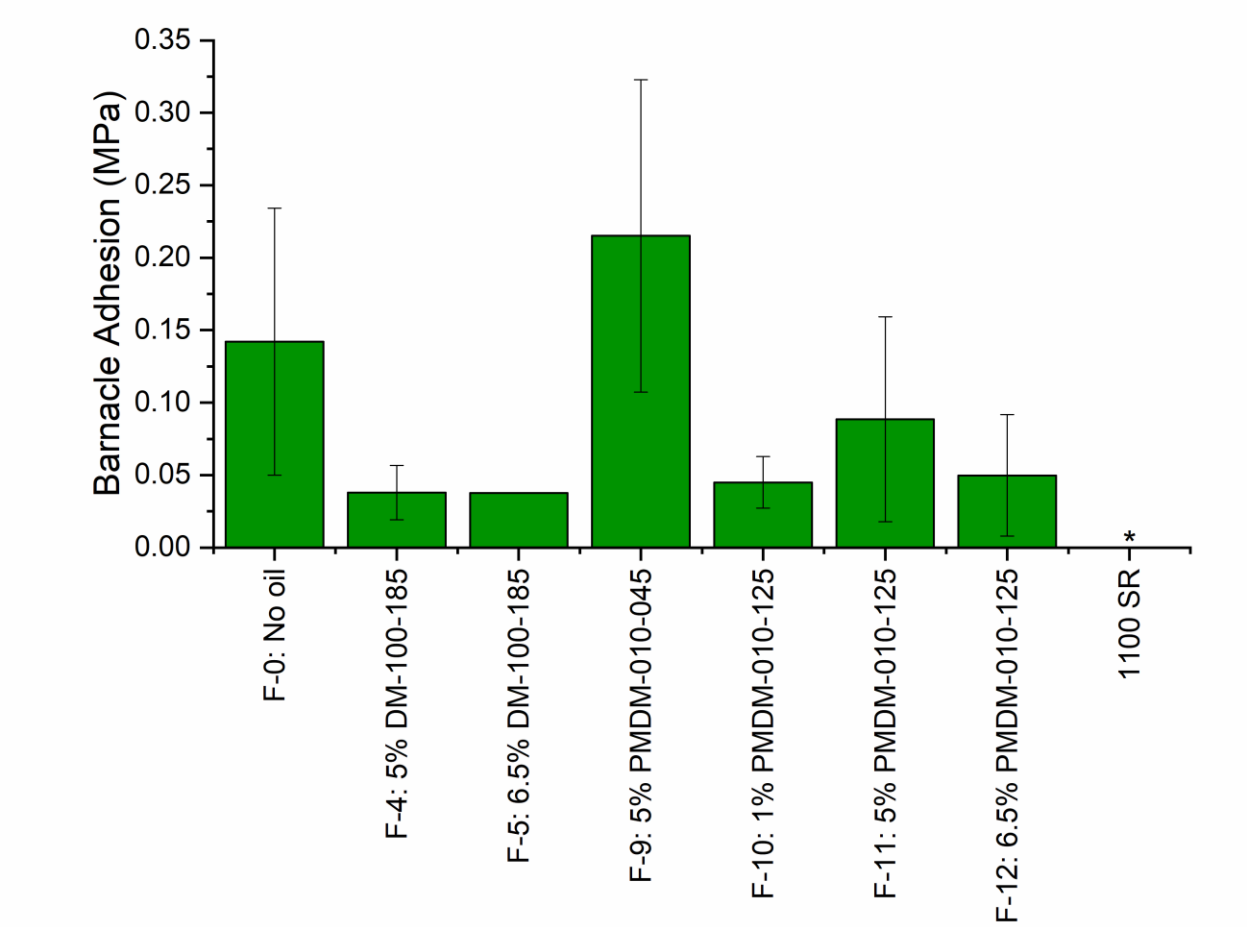

Figure 2.13. *A. amphitrite* barnacle adhesion strength for different formulations. * - no barnacles attached.

2.5. Discussion

The base coating matrix has phenyl methyl silicone moieties on its backbone. So, we expected phenyl methyl silicone oils to be more compatible while dimethyl and diphenyl silicone oils to be less compatible with the matrix. Diphenyl silicone oils were not compatible with the matrix as expected, but we also saw compatibility of dimethyl silicone oils with the matrix. F-4 with dimethyl silicone oil gave the lowest ice adhesion among all the formulations while F-12 with phenyl methyl silicone oil gave the second lowest ice adhesion result after DM-100-185 oil. We find that the molecular weight of the silicone oils also played an important role in the performance of the coatings. Lower molecular weight oils tend to give higher ice adhesion.

Increasing the molecular weight reduced the ice adhesion strength. However, once the oil reaches a certain molecular weight, ice adhesion tends to increase again. So, there is an interplay between the molecular weight of the oils and the matrix that governs the surface properties of these coatings.

Icing can occur on multiple scales. Therefore, having a low ice adhesion strength surface and a low interfacial surface is desirable for practical applications [9]. Systems F-4, F-9, and F-11 showed low ice adhesion strength as well as low interfacial toughness. Therefore, these coatings show some promising applications for ice-shedding applications. Comparing the result of ice adhesion (initial screening result) and the barnacle adhesion, we see a positive correlation between them as seen in Figure 2.14. F-9 showed higher barnacle adhesion strength compared to other formulations. One differentiating factor of the oil used in this formulation with other best-performing oils is the molecular weight. PMDM-010-045 is around 3000-4000 MW compared to DM-100-185 which has around 13,650 MW and PMDM-010-125 which has around 10,000 MW.

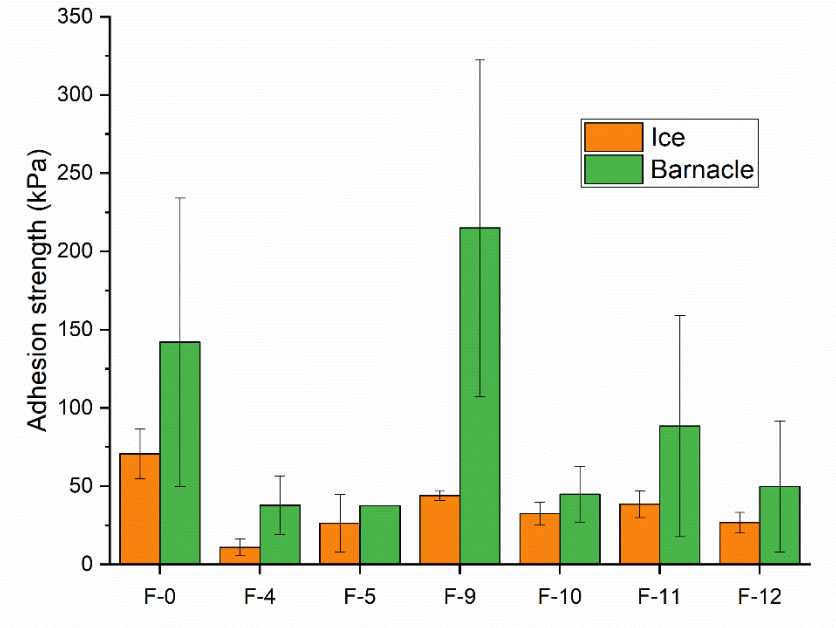

Figure 2.14. Comparison between ice and barnacle adhesion strength

Overall, the coatings in this study showed a very good mechanical performance as well as low interfacial toughness properties. However, since these coatings are prepared with non-reactive silicone oils, the free oils on the surface can deplete over time and the performance of the coating can degrade. Therefore, future studies can explore the use of incorporating reactive oils and their performance.

2.6. Conclusions

In this study, we developed a polyurea-siloxane moisture-curable resin for icing-releasing applications and also tested the same set of coatings for fouling-release applications. The base coating showed excellent mechanical properties and durability with good toughness and adhesion to the substrate. The addition of dimethyl and phenyl methyl silicone oils to the base coating lowered the ice adhesion strength of the coating, without any negative influence on the mechanical properties of the coatings. The molecular weight of the silicone oils influenced the surface properties of the coating. Dimethyl silicone oil with higher molecular weight showed very low ice adhesion strength while similar molecular weight phenyl methyl silicone oil also showed low ice adhesion strength. Contact angle and surface free energy characterization showed a negative and positive correlation with ice adhesion strength, respectively. AFM and digital microscope images showed the presence of silicone oils on the surface of the coating. These coatings demonstrated a very low interfacial toughness value of less than 0.2 J/m2. There was a positive correlation between ice adhesion strength and barnacle adhesion strength.

2.7. References

1. C.C. Ryerson, Assessment of Superstructure Ice Protection as Applied to Offshore Oil Operations Safety, US Army Research (2009). https://digitalcommons.unl.edu/usarmyresearch/49 (accessed March 27, 2024).
2. K. Shi, X. Duan, A review of ice protection techniques for structures in the arctic and offshore harsh environments, Journal of Offshore Mechanics and Arctic Engineering 143 (2021). https://doi.org/10.1115/1.4050893/1107900.
3. A. Chi Wang, C. Wu, D. Pisignano, Z. Lin Wang, L. Persano, A.M. Wagner, D.S. Spencer, N.A. Peppas, J. Appl Polym Sci, R. Muthuraj, M. Misra, A. Kumar Mohanty, J. Appl, P. Sarkar, A.K. Bhowmick, S. Stratton, O.S. Manoukian, R. Patel, A. Wentworth, S. Rudraiah, S.G. Kumbar, J. Appl Polym, C. Wang, M.C. Gupta, Y. Han Yeong, K.J. Wynne, J. Li, J. Zhu, J. Wang, S. Yuan, J. Lin, J. Shen, B. Van der Bruggen, J. Li, A.I. Isayev, Q. Wang, M.D. Soucek, N. Kanbargi, Factors affecting the adhesion of ice to polymer substrates, J Appl Polym Sci 135 (2018) 45734. https://doi.org/10.1002/APP.45734.
4. R. Menini, M. Farzaneh, Advanced Icephobic Coatings, Http://Dx.Doi.Org/10.1163/016942410X533372 25 (2012) 971–992. https://doi.org/10.1163/016942410X533372.
5. A. Dhyani, J. Wang, A.K. Halvey, B. Macdonald, G. Mehta, A. Tuteja, Design and applications of surfaces that control the accretion of matter, Science (1979) 373 (2021). https://doi.org/10.1126/SCIENCE.ABA5010.

6. S. Nazifi, Z. Huang, A. Hakimian, H. Ghasemi, Fracture-controlled surfaces as extremely durable ice-shedding materials, Mater Horiz 9 (2022) 2524–2532. https://doi.org/10.1039/D2MH00619G.
7. D. Bottone, V. Donadei, H. Niemelä, H. Koivuluoto, S. Seeger, Coral-like silicone nanofilament coatings with extremely low ice adhesion, Scientific Reports 2021 11:1 11 (2021) 1–12. https://doi.org/10.1038/s41598-021-98215-1.
8. A.N. Harper, G. Liu, Thickness of the Ice-Shedding Lubricant Layer in Equilibrium with an Underlying Cross-Linked Polymer Film, ACS Appl Polym Mater 2 (2020) 1369–1377. https://doi.org/10.1021/ACSAPM.9B01240.
9. K. Golovin, A. Tuteja, A predictive framework for the design and fabrication of icephobic polymers, Sci Adv 3 (2017). https://doi.org/10.1126/SCIADV.1701617.
10. K. Golovin, S.P.R. Kobaku, D.H. Lee, E.T. DiLoreto, J.M. Mabry, A. Tuteja, Designing durable icephobic surfaces, Sci Adv 2 (2016). https://doi.org/10.1126/SCIADV.1501496.
11. Y. Zhuo, S. Xiao, A. Amirfazli, J. He, Z. Zhang, Polysiloxane as icephobic materials – The past, present and the future, Chemical Engineering Journal 405 (2021) 127088. https://doi.org/10.1016/J.CEJ.2020.127088.
12. P.F. Ibáñez-Ibáñez, F.J. Montes Ruiz-Cabello, M.A. Cabrerizo-Vílchez, M.A. Rodríguez-Valverde, Ice adhesion of PDMS surfaces with balanced elastic and water-repellent properties, J Colloid Interface Sci 608 (2022) 792–799. https://doi.org/10.1016/J.JCIS.2021.10.005.
13. J. Chen, Z. Luo, R. An, P. Marklund, M. Björling, Y. Shi, J. Chen, P. Marklund, M. Björling, Y. Shi, Z. Luo, Novel Intrinsic Self-Healing Poly-Silicone-Urea with Super-

Low Ice Adhesion Strength, Small 18 (2022) 2200532. https://doi.org/10.1002/SMLL.202200532.

14. J. Yuan, Y. Huang, H. Li, L. Jiang, Y. Dan, Preparation and anti-icing performance of cross-linked polysiloxane coatings containing silicone oil, React Funct Polym 170 (2022) 105124. https://doi.org/10.1016/J.REACTFUNCTPOLYM.2021.105124.

15. H. Zheng, G. Liu, B.B. Nienhaus, J. V. Buddingh, Ice-Shedding Polymer Coatings with High Hardness but Low Ice Adhesion, ACS Appl Mater Interfaces 14 (2022) 6071–6082. https://doi.org/10.1021/ACSAMI.1C23483.

16. Y. Yu, L. Chen, D. Weng, Y. Hou, Z. Pang, Z. Zhan, J. Wang, Effect of Doping SiO2Nanoparticles and Phenylmethyl Silicone Oil on the Large-Scale Deicing Property of PDMS Coatings, ACS Appl Mater Interfaces 14 (2022) 48250–48261. https://doi.org/10.1021/ACSAMI.2C13650.

17. X.W. Zhao, J. Peng, S.H. Gao, K.Y. Zhu, Y.H. Zhao, X.H. Li, X.Y. Yuan, Self-healing anti-icing coatings prepared from PDMS polyurea, Sci China Technol Sci 64 (2021) 1535–1543. https://doi.org/10.1007/S11431-021-1831-7.

18. R. Holland, T.M. Dugdale, R. Wetherbee, A.B. Brennan, J.A. Finlay, J.A. Callow, M.E. Callow, Adhesion and motility of fouling diatoms on a silicone elastomer, Biofouling 20 (2004) 323–329. https://doi.org/10.1080/08927010400029031.

19. A.K. Halvey, B. Macdonald, A. Dhyani, A. Tuteja, Design of surfaces for controlling hard and soft fouling, Philos Trans A Math Phys Eng Sci 377 (2019). https://doi.org/10.1098/RSTA.2018.0266.

20. T.P. Galhenage, D. Hoffman, S.D. Silbert, S.J. Stafslien, J. Daniels, T. Miljkovic, J.A. Finlay, S.C. Franco, A.S. Clare, B.T. Nedved, M.G. Hadfield, D.E. Wendt, G. Waltz, L.

Brewer, S.L.M. Teo, C.S. Lim, D.C. Webster, Fouling-Release Performance of Silicone Oil-Modified Siloxane-Polyurethane Coatings, ACS Appl Mater Interfaces 8 (2016) 29025–29036. https://doi.org/10.1021/ACSAMI.6B09484.

21. A.R. Rahimi, M. Murphy, K. Faiyaz, S.J. Stafslien, L. Vanderwal, M. Pade, J.A. Finlay, A.S. Clare, D.C. Webster, Amphiphilic marine coating systems of self-stratified PDMS-PEG surfaces with an epoxy-polyurethane matrix, J Coat Technol Res 19 (2022) 795–812. https://doi.org/10.1007/S11998-021-00561-2.

22. J. Benda, H. Narikiyo, S.J. Stafslien, L.J. Vanderwal, J.A. Finlay, N. Aldred, A.S. Clare, D.C. Webster, Studying the Effect of Pre-Polymer Composition and Incorporation of Surface-Modifying Amphiphilic Additives on the Fouling-Release Performance of Amphiphilic Siloxane-Polyurethane Coatings, ACS Appl Mater Interfaces 14 (2022) 37229–37247. https://doi.org/10.1021/ACSAMI.2C10983.

23. V. Upadhyay, T. Galhenage, D. Battocchi, D. Webster, Amphiphilic icephobic coatings, Prog Org Coat 112 (2017) 191–199. https://doi.org/10.1016/J.PORGCOAT.2017.07.019.

24. T.P. Galhenage, D. Hoffman, S.D. Silbert, S.J. Stafslien, J. Daniels, T. Miljkovic, J.A. Finlay, S.C. Franco, A.S. Clare, B.T. Nedved, M.G. Hadfield, D.E. Wendt, G. Waltz, L. Brewer, S.L.M. Teo, C.S. Lim, D.C. Webster, Fouling-Release Performance of Silicone Oil-Modified Siloxane-Polyurethane Coatings, ACS Appl Mater Interfaces 8 (2016) 29025–29036. https://doi.org/10.1021/ACSAMI.6B09484.

25. M. Lejars, A. Margaillan, C. Bressy, Fouling release coatings: A nontoxic alternative to biocidal antifouling coatings, Chem Rev 112 (2012) 4347–4390. https://doi.org/10.1021/CR200350V.

26. H. Qiu, K. Feng, A. Gapeeva, K. Meurisch, S. Kaps, X. Li, L. Yu, Y.K. Mishra, R. Adelung, M. Baum, Functional polymer materials for modern marine biofouling control, Prog Polym Sci 127 (2022) 101516. https://doi.org/10.1016/J.PROGPOLYMSCI.2022.101516.

27. P. Hu, Q. Xie, C. Ma, G. Zhang, Silicone-Based Fouling-Release Coatings for Marine Antifouling, Langmuir 36 (2020) 2170–2183. https://doi.org/10.1021/ACS.LANGMUIR.9B03926.

28. H. Wang, R. Chen, D. Song, G. Sun, J. Yu, Q. Liu, J. Liu, J. Zhu, P. Liu, J. Wang, Silicone-modified polyurea-interpenetrating polymer network fouling release coatings with excellent wear resistance property tailored to regulations, J Colloid Interface Sci 653 (2024) 971–980. https://doi.org/10.1016/J.JCIS.2023.09.129.

29. D.L. Beemer, W. Wang, A.K. Kota, Durable gels with ultra-low adhesion to ice, J Mater Chem A Mater 4 (2016) 18253–18258. https://doi.org/10.1039/C6TA07262C.

30. Y.H. Yeong, A. Milionis, E. Loth, J. Sokhey, Self-lubricating icephobic elastomer coating (SLIC) for ultralow ice adhesion with enhanced durability, Cold Reg Sci Technol 148 (2018) 29–37. https://doi.org/10.1016/J.COLDREGIONS.2018.01.005.

31. M. Mohseni, Z.A. Dijvejin, K. Golovin, Designing scalable elastomeric anti-fouling coatings: Shear strain dissipation via interfacial cavitation, J Colloid Interface Sci 589 (2021) 556–567. https://doi.org/10.1016/J.JCIS.2021.01.019.

32. K. Golovin, A. Dhyani, M.D. Thouless, A. Tuteja, Low-interfacial toughness materials for effective large-scale deicing, Science (1979) 364 (2019) 371–375. https://doi.org/10.1126/SCIENCE.AAV1266.

33. Z. Azimi Dijvejin, M.C. Jain, R. Kozak, M.H. Zarifi, K. Golovin, Smart low interfacial toughness coatings for on-demand de-icing without melting, Nature Communications 2022 13:1 13 (2022) 1–12. https://doi.org/10.1038/s41467-022-32852-6.

34. S. Nazifi, Z. Huang, A. Hakimian, H. Ghasemi, Fracture-controlled surfaces as extremely durable ice-shedding materials, Mater Horiz 9 (2022) 2524–2532. https://doi.org/10.1039/D2MH00619G.

35. Q. Rao, Y. Lu, L. Song, Y. Hou, X. Zhan, Q. Zhang, Highly Efficient Self-Repairing Slippery Liquid-Infused Surface with Promising Anti-Icing and Anti-Fouling Performance, ACS Appl Mater Interfaces 13 (2021) 40032–40041. https://doi.org/10.1021/ACSAMI.1C09491.

36. E.B. Iezzi, Novel Isocyanate-Free Moisture-Curable Polymers for Single-Component Polysiloxane Topcoats, COATINGSTECH 14 (2017) 22–28.

37. E.B. Iezzi, Single-component coating having alkoxysilane-terminated N-substituted urea resins, U.S. Patent No. 8,133,964 (2012).

38. S. Rønneberg, J. He, Z. Zhang, The need for standards in low ice adhesion surface research: a critical review, J Adhes Sci Technol 34 (2020) 319–347. https://doi.org/10.1080/01694243.2019.1679523.

39. S. Rønneberg, Y. Zhuo, C. Laforte, J. He, Z. Zhang, Interlaboratory Study of Ice Adhesion Using Different Techniques, Coatings 2019, Vol. 9, Page 678 9 (2019) 678. https://doi.org/10.3390/COATINGS9100678.

40. A. Work, Y. Lian, A critical review of the measurement of ice adhesion to solid substrates, Progress in Aerospace Sciences 98 (2018) 1–26. https://doi.org/10.1016/J.PAEROSCI.2018.03.001.

41. S. Stafslien, J. Daniels, J. Bahr, B. Chisholm, A. Ekin, D. Webster, B. Orihuela, D. Rittschof, An improved laboratory reattachment method for the rapid assessment of adult barnacle adhesion strength to fouling-release marine coatings, J Coat Technol Res 9 (2012) 651–665. https://doi.org/10.1007/S11998-012-9409-7.

42. S.J. Stafslien, J. Daniels, B. Mayo, D. Christianson, B. Chisholm, A. Ekin, D. Webster, G. Swain, Combinatorial materials research applied to the development of new surface coatings IV. A high-throughput bacterial biofilm retention and retraction assay for screening fouling-release performance of coatings, Biofouling 23 (2007) 45–54. https://doi.org/10.1080/08927010601137856.

43. F. Cassé, S.J. Stafslien, J.A. Bahr, J. Daniels, J.A. Finlay, J.A. Callow, M.E. Callow, Combinatorial materials research applied to the development of new surface coatings V. Application of a spinning water-jet for the semi-high throughput assessment of the attachment strength of marine fouling algae, Biofouling 23 (2007) 121–130. https://doi.org/10.1080/08927010701189583.

44. P. Majumdar, E. Lee, N. Patel, K. Ward, S.J. Stafslien, J. Daniels, B.J. Chisholm, P. Boudjouk, M.E. Callow, J.A. Callow, S.E.M. Thompson, Combinatorial materials research applied to the development of new surface coatings IX: An investigation of novel antifouling/fouling-release coatings containing quaternary ammonium salt groups, Biofouling 24 (2008) 185–200. https://doi.org/10.1080/08927010801894660.

45. L. Zhu, J. Xue, Y. Wang, Q. Chen, J. Ding, Q. Wang, Ice-phobic coatings based on silicon-oil-infused polydimethylsiloxane, ACS Appl Mater Interfaces 5 (2013) 4053–4062. https://doi.org/10.1021/AM400704Z.

46. Q. Zheng, J. Lv, J. Zhang, J. Feng, Fabrication and application of icephobic silicone coatings on epoxy substrate, Prog Org Coat 161 (2021) 106483. https://doi.org/10.1016/J.PORGCOAT.2021.106483.

47. T. Bharathidasan, S.V. Kumar, M.S. Bobji, R.P.S. Chakradhar, B.J. Basu, Effect of wettability and surface roughness on ice-adhesion strength of hydrophilic, hydrophobic and superhydrophobic surfaces, Appl Surf Sci 314 (2014) 241–250. https://doi.org/10.1016/J.APSUSC.2014.06.101.

48. Z. He, S. Xiao, H. Gao, J. He, Z. Zhang, Multiscale crack initiator promoted super-low ice adhesion surfaces, Soft Matter 13 (2017) 6562–6568. https://doi.org/10.1039/C7SM01511A.

49. H. Liu, M. Sharma, J. Wang, Y.F. Cheng, H. Liu, Microbiologically influenced corrosion of 316L stainless steel in the presence of Chlorella vulgaris, Int Biodeterior Biodegradation 129 (2018) 209–216. https://doi.org/10.1016/J.IBIOD.2018.03.001.

50. P. Wang, D. Zhang, Z. Lu, Slippery liquid-infused porous surface bio-inspired by pitcher plant for marine anti-biofouling application, Colloids Surf B Biointerfaces 136 (2015) 240–247. https://doi.org/10.1016/J.COLSURFB.2015.09.019.

51. P.K. Sarkar, S.S. Pawar, S.K. Rath, B. Kandasubramanian, Anti-barnacle biofouling coatings for the protection of marine vessels: synthesis and progress, Environmental Science and Pollution Research 2022 29:18 29 (2022) 26078–26112. https://doi.org/10.1007/S11356-021-18404-3.

CHAPTER 3. SELF-SEGREGATING MOISTURE-CURABLE UREA-SILOXANE COATING FOR ICE-SHEDDING APPLICATIONS

3.1. Abstract

The effect of incorporating carbinol functional siloxane on moisture-curable urea-siloxane coating for ice-shedding applications was studied. Carbinol functional siloxane were grafted into the coating by reacting it with isocyanate. Incorporating carbinol functional siloxane into the matrix can improve the ice-shedding property of the coating along with durability since the grafted siloxane do not wash away with each icing-deicing cycle. Different carbinol functional siloxane at 5% and 10% ratio to isocyanate were grafted and tested for contact angle, surface free energy, surface morphology, surface composition, mechanical strength, ice adhesion, and interfacial toughness. The incorporation of carbinol functional siloxane in the matrix changed the surface properties of the coating compared to base coating which lowered the ice adhesion and interfacial toughness of the coating. All the formulations incorporating carbinol functional siloxane resulted in less than 1 J/m2 interfacial toughness making these coatings suitable for large-scale deicing applications. Surface characterization of the coatings showed self-segregating behavior of the PDMS chains from carbinol functional siloxane with distinct domains which improved the ice-shedding property of the coating. These types of coating can also be useful in fouling release applications.

3.2. Introduction

The development of a dual functional coating with application in both ice and fouling release applications can be pivotal in maritime industries. Marine vessels traveling in both warm and arctic climates can experience marine biofouling as well as ice fouling. The accumulation of biofoulants on ship hulls and surfaces can reduce power efficiency, thus triggering higher

environmental emissions, reducing maneuverability, and promoting material degradation through corrosion. Traditionally, marine vessels that navigate through both warm and arctic climates are coated with abrasion-resistant low-friction ice coating along with some other antifouling/fouling release coatings [1–3]. Having a coating that performs well in both environments can help reduce the cost and environmental impacts. Though marine biofouling and ice fouling are different processes, studies have suggested that the mechanism of biofouling and ice release at the coating and foulants interface share some similarities such as low surface energy, hydrophobicity, and surface textures [4, 5].

Previous studies have explored the use of soft elastomeric materials, hydrophobic-hydrophilic-amphiphilic materials, and slippery liquid-infused porous surfaces (SLIPS) coatings in both fouling release and ice shedding applications [6, 7]. Silicone-based elastomers are the most widely used systems in marine fouling-release coatings [8]. These materials have very low surface energy and are known to be hydrophobic, thus they have also been used as icephobic materials [9]. Irajizad et al. introduced the concept of stress-localized fracture and fabricated a coating material that consists of two-phase materials [10]. They used a silicone elastomer with high modulus as phase I and a silicone organogel with low modulus as phase II. However, these materials are very soft due to the flexibility of Si-O-Si bonds granting them a very low modulus, thus they are susceptible to damage. Super-hydrophobic surfaces (SHS) are widely studied for anti-icing applications. However, SHSs may not necessarily have low ice adhesion [11, 12]. Instead, these superhydrophobic surfaces are prone to frost formation, promoting heterogeneous nucleation sites for ice to form due to the presence of nanopatterns on the surface. In addition to this, these coatings are not durable as the surfaces are prone to mechanical damage. Similarly, hydrophilic surfaces, either through the impregnation of hydrophilic liquids such as ethylene

glycol and formamide [13] or through surface modification to incorporate hydrophilic moieties [11] have been explored for ice-shedding applications. These coatings work on the principle that the hydrophilic surface delays the freezing or ice nucleation of water by spreading the water molecules and creating a hydration layer which reduces the ice adhesion strength. However, these kinds of surfaces are not practical for large-scale ice removal [14]. Zwitterions are another class of materials with stronger hydrophilicity and have been widely used to synthesize amphiphilic materials and introduced in polydimethylsiloxane (PDMS) matrices as additives for fouling release applications [15–18]. The introduction of these additives has shown better fouling-release performance for a wide variety of marine biofoulants compared to other classes of materials. These surfaces prevent biofouling under the principle that the hydrophobic and hydrophilic surfaces create surface heterogeneity preventing foulants from adhering to one type of surface. Amphiphilic materials have also been studied for anti-icing applications and have shown anti-icing properties [19–22]. However, there remain challenges with scaling up amphiphilic materials due to their complex and costly synthesis process.

SLIPS are another class of widely studied materials for fouling release and ice-shedding applications [23, 24]. SLIPS material acts as a reservoir for a slippery liquid (typically fluorinated or silicone oils), which leaches to the surface forming a slick layer [25]. The interfacial modulus is essentially zero due to the presence of mobile oils and thus these surfaces can provide very low adhesion for ice and some marine biofoulants. However, this class of coatings has several drawbacks including limited durability, leaching of toxic fluids to the environment, and complex synthesis [25, 26]. Over time, the oil in the coating depletes due to the loss of oil, and the material does not provide the same performance. To improve the performance of oil-containing coatings, different grafting techniques have been explored [4, 27–30]. One

advantage of grafting the oil to the coating is the improvement in durability as the oil does not wash off from the coating surface over time as they are covalently grafted, and they provide a similar slippage layer on the surface of the coatings. Different self-segregating coatings where these reactive PDMS oils segregate to the surface of the coatings have been studied [31–33]. Most of the coating backbone/matrix includes more durable, mechanically robust surfaces such as polyurethanes, epoxies, and polyureas [34–36] that have higher surface free energy and the grafted material has lower surface free energy. Thus, when the coating is applied the mechanically robust component self-segregates towards the substrate-coating interface while the low surface energy component segregates towards the coating-air interface.

Ice accumulation can occur over several length scales and the force required to remove ice at different length scales does not scale linearly [37]. Instead, there is a certain length scale of ice, called the critical length, after which the force required to remove ice will be constant. The force at this point is called the critical force. Around this length scale, a crack inside the ice initiates and starts to transfer through the ice and substrate interface. The transfer of cracks facilitates the separation of ice from the substrate. Different materials exhibit varying resistances to the propagation of such cracks, influencing their effectiveness in de-icing applications [37]. Low interfacial toughness (LIT) materials are suitable for large-scale de-icing and fouling release applications [38, 39]. Here, interfacial toughness is the ability of the material to resist the crack propagation along the interface. Several LIT materials have been explored in the past and they have suggested that ice accumulated on these surfaces can be removed under a small external force, gravity, vibration, or wind. Studies in the past have also suggested that the presence of domains on the surface impacts the ice and fouling release properties of the material [40, 41]. The size of these domains, which are dominantly PDMS, can influence the surface properties.

Few studies have considered the incorporation of two materials with different modulus for icephobic applications. Nafizi et al. developed a durable coating with three different phases of materials – polyurethane matrix with PDMS gel and silica [42]. The authors claimed that the mechanical and chemical heterogeneity aids crack propagation and easier removal of ice. In another study by Wang et al., they incorporated PVC microparticles in PDMS elastomers for large scale deicing applications [43]. The incorporation of hard PVC particles in soft PDMS matrix helped in lowering both ice adhesion strength and interfacial toughness. Even though these previous studies showed low ice adhesion strength and interfacial toughness property, they either lacked durability or their synthesis was a very complex process. Therefore, our main motive behind this work is to develop durable LIT materials that can be made using a facile synthesis process.

In this study, we explored a self-segregating durable coating with a polyurea-siloxane matrix and hydroxyl terminated PDMS oils. The PDMS on the coating surface creates a distinctive domain structure. The objective of this study is to assess the ice release properties of these coatings and determine the impact of the composition on the performance. We will use different carbinol functional siloxane on the urea-siloxane base matrix and test the surface properties, ice adhesion, and interfacial toughness performance. This study will be useful in understanding the influence of surface domains on ice adhesion and interfacial toughness. These types of coatings can also be effective for fouling-release applications.

3.3. Materials and methods

3.3.1. Materials

Aliphatic polyisocyanate (HDI trimer – Desmodur N3600) was provided by Covestro AG. N-butylaminopropyltrimethoxysilane (SIB 1932.2) and carbinol functional

poly(dimethylsiloxane) shown in Table 3.1 were purchased from Gelest Inc. Butyl propionate and toluene were purchased from VWR International LLC. Toluene was dehydrated with 4 Å molecular sieves purchased from Sigma Aldrich. Methoxyfunctional, methyl-phenyl polysiloxane (Silres SY231) was provided by Wacker Chemie AG. Ethyl-3-ethoxypropionate (EEP), methyl amyl ketone (MAK), and dibutyltin diacetate (DBTDAc) were purchased from Sigma-Aldrich. All reagents were used as received unless specified. Aluminum panels (4×8 in2, 0.6 mm thick, type A, alloy 3003 H14) were purchased from Q-Lab. These panels were sandblasted and primed with Intergard 264 (International Paint) using air-assisted spray before applying the coating. QD-36 steel panels were also purchased from Q-Lab.

Table 3.1. Carbinol functional siloxanes used in this study

Carbinol functional siloxane	Functionality	Molecular weight (g/mol)
MCR-C12	1	1,000
MCR-C18	1	5,000
MCR-C22	1	10,000
DMS-C15	2	1,000
DMS-C23	2	10,000

3.3.2. Coatings formulation and preparation

The formulations used in this study are given in Table 3.2. Carbinol functional siloxanes were reacted with an HDI trimer first to get a prepolymer. The prepolymer consists of HDI trimer (isocyanate) reacted with carbinol functional siloxane (5 or 10% equivalents) and the remainder of the isocyanates were reacted with methoxy functional amino-silane (SIB 1932.2). For example, for a formulation with 10% MCR C12 siloxane, 3.67 g of HDI trimer was mixed with 2 g of MCR C12 siloxane. 1% DBTDAc catalyst was prepared in MAK. 0.1% catalyst (based on % equivalent of NCO:OH) was added to the mixture. The mixture was mixed with a magnetic stirrer at 350 rpm for three hours at 80°C. After the reaction of carbinol functional

siloxane with isocyanate was complete, 4.24 g of SIB 1932.2 (amino-silane) was added to the mixture along with 2.69 g of butyl propionate solvent. The mixture was again mixed with a magnetic stirrer at 350 rpm for one hour at 50℃. After the reaction was complete, 2.8 g of Silres SY 231 (siloxane resin) was added to the mixture. 2.5% of the DBTDAc catalyst was prepared in a mixture of toluene and EEP (30:70 proportion). 0.4% of this catalyst mixture is then added to the coating formulation and then mixed with a magnetic stirrer at 350 rpm for one hour.

Table 3.2. Formulations used in this study

Formulation	Carbinol functional siloxane	OH:NCO
F-0	-	-
F-1	MCR C-12	0.05
F-2	MCR-C12	0.10
F-3	Mono-functional carbinol siloxane	
	MCR C-12	0.0425
	MCR-C18	0.005
	MCR C-22	0.0025
F-4	Mono-functional carbinol siloxane	
	MCR C-12	0.085
	MCR-C18	0.01
	MCR C-22	0.005
F-5	Mono + di-functional carbinol siloxane	
	MCR C-12	0.0225
	MCR C-18	0.0025
	MCR C-22	0.0025
	DMS C-15	0.02
	DMS-C23	0.0025
F-6	Mono + di-functional carbinol siloxane	
	MCR C-12	0.045
	MCR C-18	0.005
	MCR C-22	0.005
	DMS C-15	0.04
	DMS-C23	0.005

After the mixing was complete, the mixture was allowed to settle down for half an hour. Coatings were then applied on steel panels and the previously primed Al-panels using a RDS 90 wire rod. The coatings were allowed to cure in the ambient conditions for two weeks in a dust-free enclosed cabinet. The coatings were tack-free after overnight curing. The control coating was prepared following a previous study [44].

The reaction schemes are shown in Figures 3.1, 3.2, and 3.3. The structure of the prepolymer shown is just a representative structure and one of the many possible structures that could happen.

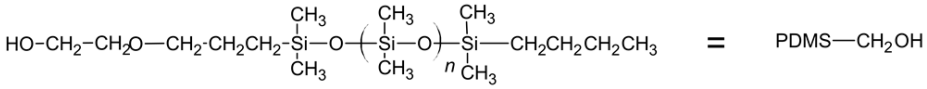

Structure of mono-functional carbinol

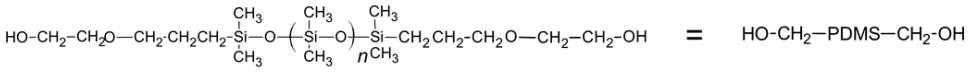

Structure of di-functional carbinol

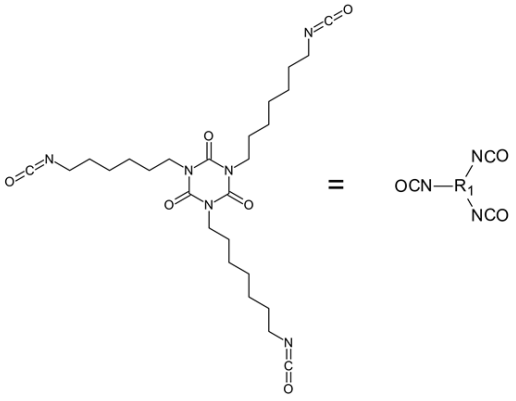

Structure of Desmodur N 3600 Isocyanate

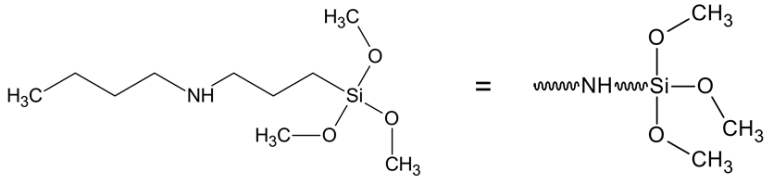

Structure of SIB 1932.2 amino-silane

Figure 3.1. Structures of raw materials used in this study

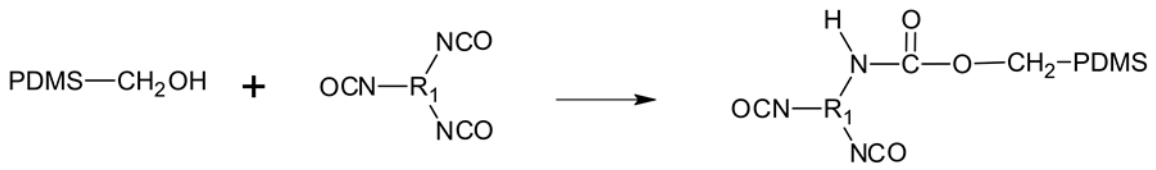

Reaction of isocyanate with carbinol

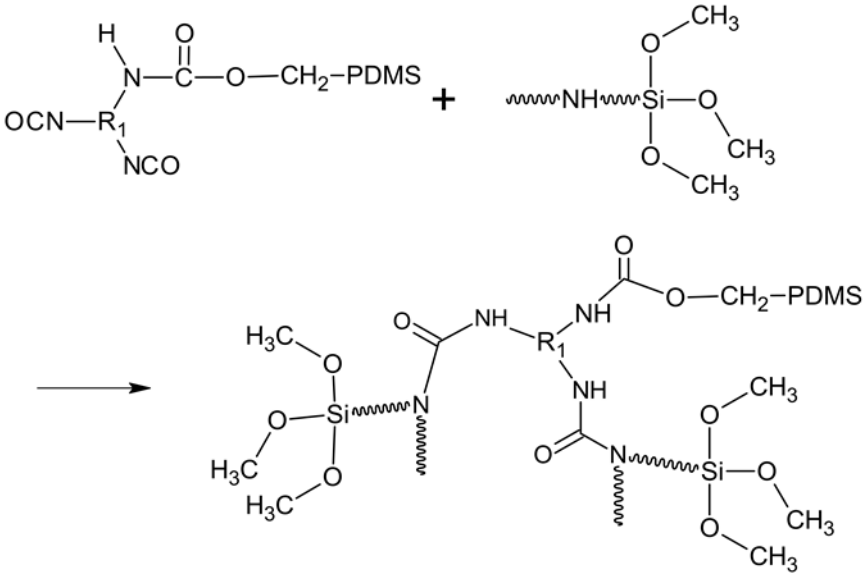

Reaction of remaining isocyanate with amino-silane

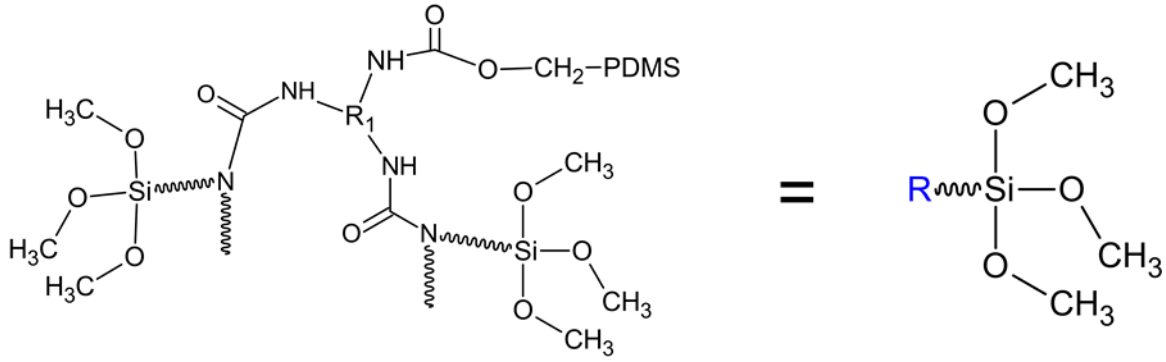

Structure of pre-polymer

Figure 3.2. Reaction mechanism of carbinol and amino-silane with isocyanate and structure of siloxane-containing alkoxy silane polyurea pre-polymer

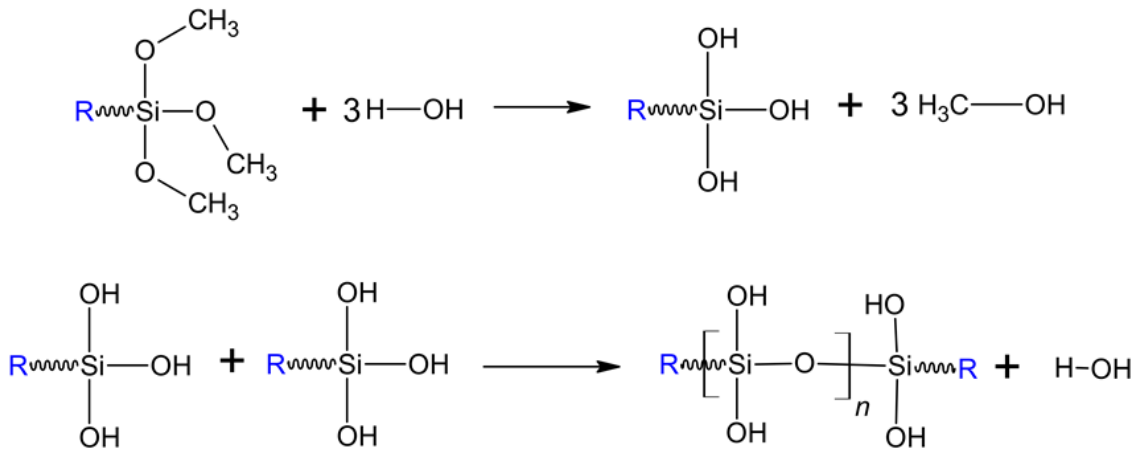

Figure 3.3. Hydrolysis-condensation curing mechanism of siloxane-containing alkoxy silane polyurea prepolymer and siloxane resin

3.3.3. Coatings characterization

3.3.3.1. Nuclear magnetic resonance (NMR)

A Bruker Avance III HD 400 MHz NMR instrument was used to collect and record all 1H-NMR spectra for confirming the reaction of carbinol functional siloxane and amino-silane. All samples were dissolved in deuterated chloroform ($CDCl_3$) with 1% (v/v) TMS. Bruker TopSpin software was used to analyze NMR spectra.

3.3.3.2. Vapor sorption test

Water vapor adsorption and desorption tests were conducted using a VSTAR vapor sorption analyzer (Quantachrome Instruments, Inc./Anton Paar, GmbH). Initially, the coating sample was carefully removed from the steel Q panels and degassed to remove any initial moisture in the coating. Around 0.08 g of peeled coating film was then placed into the analyzer tube and sealed. The manifold temperature was maintained at 110 ℃ and the analysis temperature used was 25 ℃. Helmholtz equation of state was used for vapor analysis.

3.3.3.3. Contact angles and surface free energy

Both water contact angle (WCA) and methylene iodide contact angle (MICA) were measured for all the formulations. A Kruss® DSA 100 (Drop Shape Analyzer) was used for all

the measurements. The coating from each formulation was removed from the substrate and contact angles were measured on both the top and bottom sides of the coating. Coating samples were placed on the sample platform of the instrument and 3 μl of water and methylene iodide were dosed using a dual-pressure dosing unit. The contact angle measurements were taken for each sample with at least three measurements. The surface free energy of the coating was calculated from the two contact angles using the Owens-Wendt method. All the calculations were done by the inbuilt software.

3.3.3.4. Atomic force microscopy (AFM)

An Oxford Asylum Jupiter XR AFM microscope was used to map the surface of the coatings. A silicon cantilever (AC240) probe with resonant frequency 50-990 kHz and a spring constant of 0.6-3.5 N/m was used in tapping mode for scanning the sample. Phase images were obtained from the scans and were analyzed in the in-built Asylum software.

3.3.3.5. XPS measurements

X-ray photoelectron spectroscopy (XPS) was used to conduct depth profiling and determine the elemental composition of the coating. A Thermo Scientific K-Alpha XPS equipped with Al Kα (1486.68 eV) X-ray source and Ar+ ion source (up to 4000 eV) was used for the measurement. Base coating and 10% mono-functional carbinols from both partially and fully reacted conditions were used as samples for characterization. The characterization was done for both the top and bottom sides of the coating.

3.3.3.6. Young's modulus measurement

An Instron 34TM-5 was used for tensile tests to determine Young's modulus. The coatings applied on the steel panels were cut and peeled off using a blade. The free-standing

coating film was cut into a size of 5 mm width and mounted on the tensile tester. The test was done at a speed of 5 mm/min.

3.3.4. Ice adhesion and interfacial toughness

Ice adhesion and interfacial toughness measurements were conducted in a custom-built ice adhesion machine. The setup for ice adhesion measurement is shown in Figure B1 in Appendix B. The coating applied on the primed Al-panel was mounted on the Peltier plate with screws and O-rings. Rectangular molds made of acrylonitrile-butadiene-styrene of various lengths ranging between 1 cm to 12 cm were placed on top of the panel. Distilled water was used to fill the bottom layer of the molds using a pipette. Once the bottom layer froze, the rest of the molds were filled with water again. Water filling needs to be done in two steps to prevent leakage of water from the mold. After the water was filled, we waited for approximately 30 minutes to allow for the water to be completely frozen. The ices along with the mold are then pushed off using a motorized force gauge at a speed of 0.36 in/min. The peak force of ice removal was recorded. After the ice removal from the coating panels, the panels were taken out of the Peltier plate and allowed to come to room temperature. If any water droplets were present in the panels, they were dried gently using KimWipes. Then the same process was repeated. Each ice length was measured for at least 12 data points for each formulation. Ice adhesion strength and interfacial toughness were calculated based on a previous study [37]. Ice adhesion strength calculation only considered the force values up to the critical point. Linear line was fit with different length scales up to the critical length and ice adhesion strength was calculated using the slope of the line. For the base coating, there were cohesive debonding of ice at longer ice length scales, so only 1 and 2 cm lengths were used.

3.4. Results and discussion

Non-reactive silicone oil additives often used to reduce adhesion in coating formulations have one inherent disadvantage of short durability. The free oils can wash away from the coating surface over time and may not provide the same original functionality. To improve the durability and still provide good performance with lower ice adhesion/interfacial toughness, we grafted carbinol functional PDMS into the matrix and tested them.

3.4.1. Synthesis of siloxane-containing alkoxy silane polyurea

The synthesis of the siloxane-containing alkoxy silane polyurea resin was carried out in two steps. First the carbinol-functional siloxane was reacted with the polyisocyanate. The extent of conversion of carbinols with the isocyanate was characterized by NMR. The results of the NMR analysis are provided in Appendix B (Figures B2-B7). As a representative sample, we did the NMR test for the formulation with a mixture of mono-functional carbinol siloxane (F-4). When the carbinols were reacted with the isocyanate at room temperature for 24 hours, the extent of conversion from NMR analysis showed that only about 30% of carbinols reacted with isocyanate. When the carbinols were reacted with the isocyanate at 80℃ for 3 hours, NMR analysis confirmed 100% reaction of carbinols with isocyanate. Thus, these latter conditions were used for subsequent experiments. In the second step the reaction of amino-silane with isocyanate was carried out and completion was confirmed by NMR analysis.

3.4.2. Coatings characterization

3.4.2.1. Contact angles and surface free energy

Water and methylene iodide contact angle measurement along with surface energy calculation from them can provide valuable information about the coating surface characteristics in terms of its hydrophobicity/hydrophilicity. Contact angles and surface free energy of the drop

contact with the coating surface were measured for all the formulations on top and bottom side of the coating film and are shown in Figures 3.4. The formulations with siloxane-containing alkoxy silane polyurea showed the increase in water contact angle on the top side of the coating for most of the formulations. However, there was higher increment in water contact angle on the bottom side of the coating suggested that the carbinol functional siloxane might have also segregated towards the coating substrate interface. Initially, the base coating without any carbinol functional siloxane had higher surface free energy. However, the formulations with siloxane-containing alkoxy silane polyurea showed a decreasing trend in surface-free energy. Carbinol functional siloxane are known to have low surface tension due to the presence of PDMS chains. Since the base coating already has lower surface free energy on the top side of the coating, there was no big change in the top surface free energy of the coating with carbinol functional siloxane incorporated formulations. However, the decrease in surface free energy for the bottom surface was more visible compared to the base coating.

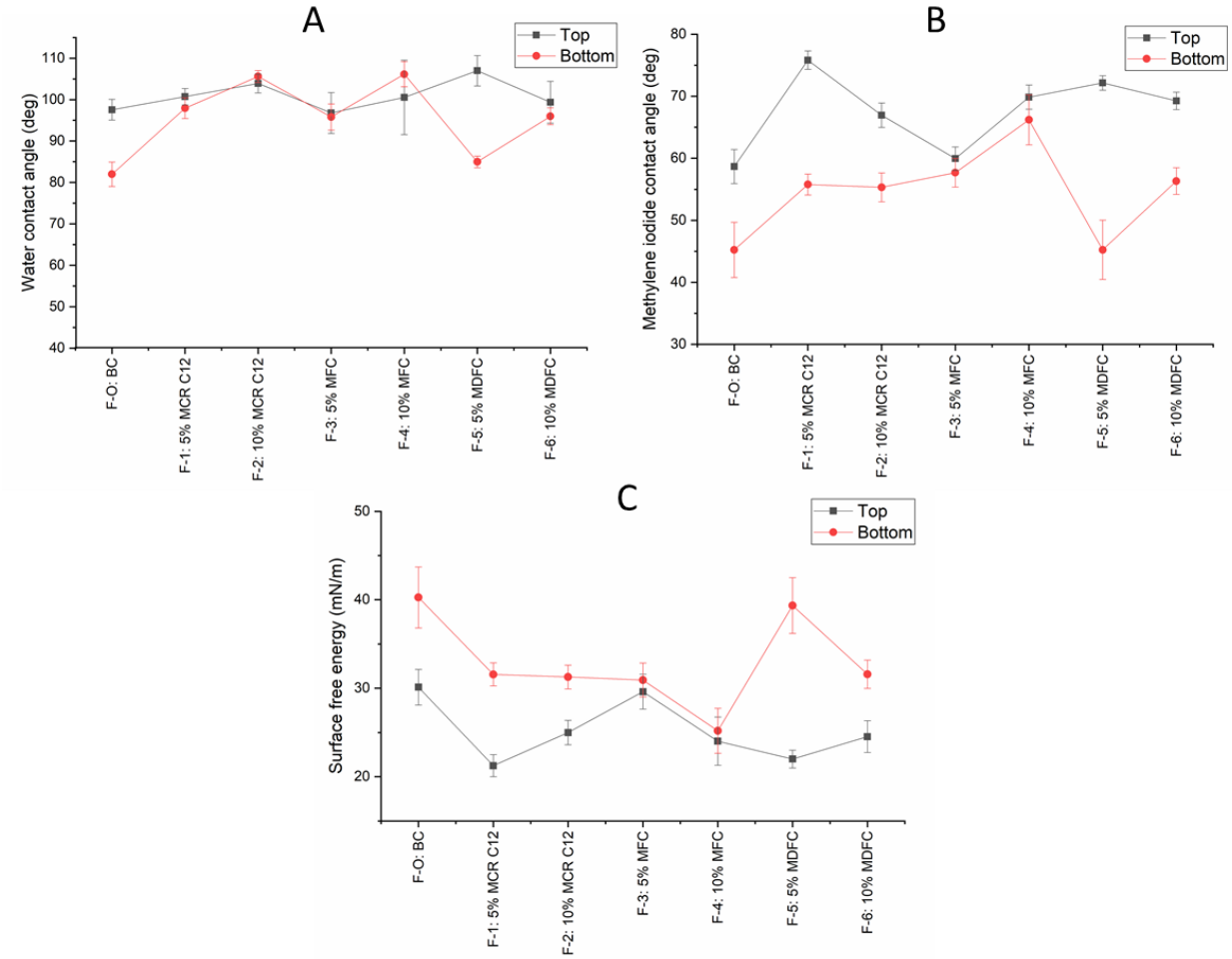

Figure 3.4. A. Water contact angle; B. methylene iodide contact angle; and C. surface free energy

3.4.2.2. Vapor sorption tests

The water vapor absorption-desorption test results are shown in Figure 3.5. The results show that base coating has higher water absorption compared to coatings with carbinol functional siloxane. The reason for lower water absorption for coatings with carbinol functional siloxane might be due to the presence of hydrophobic PDMS chains from the siloxane.

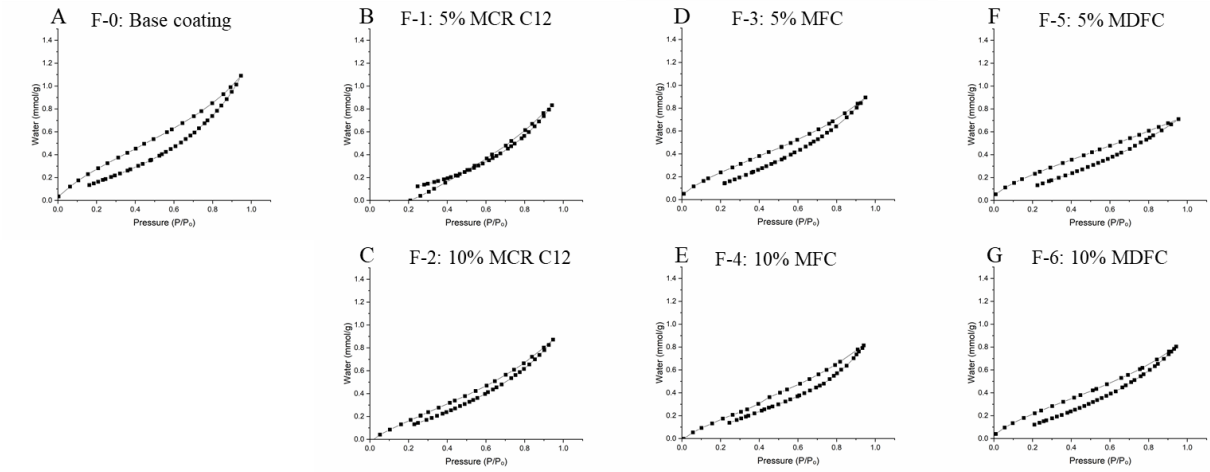

Figure 3.5. Water vapor absorption and desorption profile for base coating and other formulations

3.4.2.3. Atomic force microscopy (AFM)

AFM images of the top side of the coating film were taken for all the formulations to analyze the surface morphology. AFM phase image of base coating (Figure 3.6) showed that there is no presence of domains.

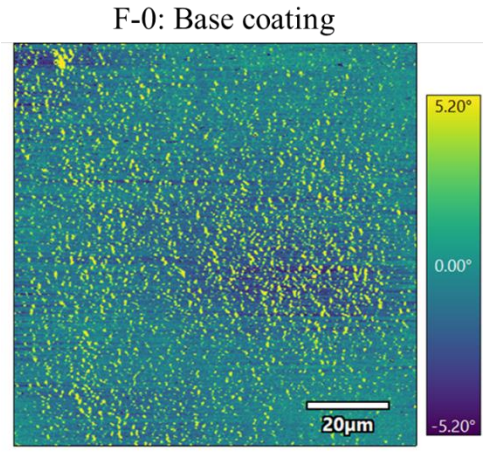

Figure 3.6. AFM phase image of the base coating

Formulations with siloxane-containing alkoxy silane polyurea resin resulted in the formation of domains as seen in Figure 3.7. For MFC, the 5% formulation had smaller and more domains in the surface compared to the 10% formulation. For MDFC, the domain size and

distribution were similar between 5% and 10%, however, the 10% formulation had a greater number of domains. The presence of domains in all the formulations showed the self-segregating nature of the PDMS chains from carbinol functional siloxane grafted in the coatings.

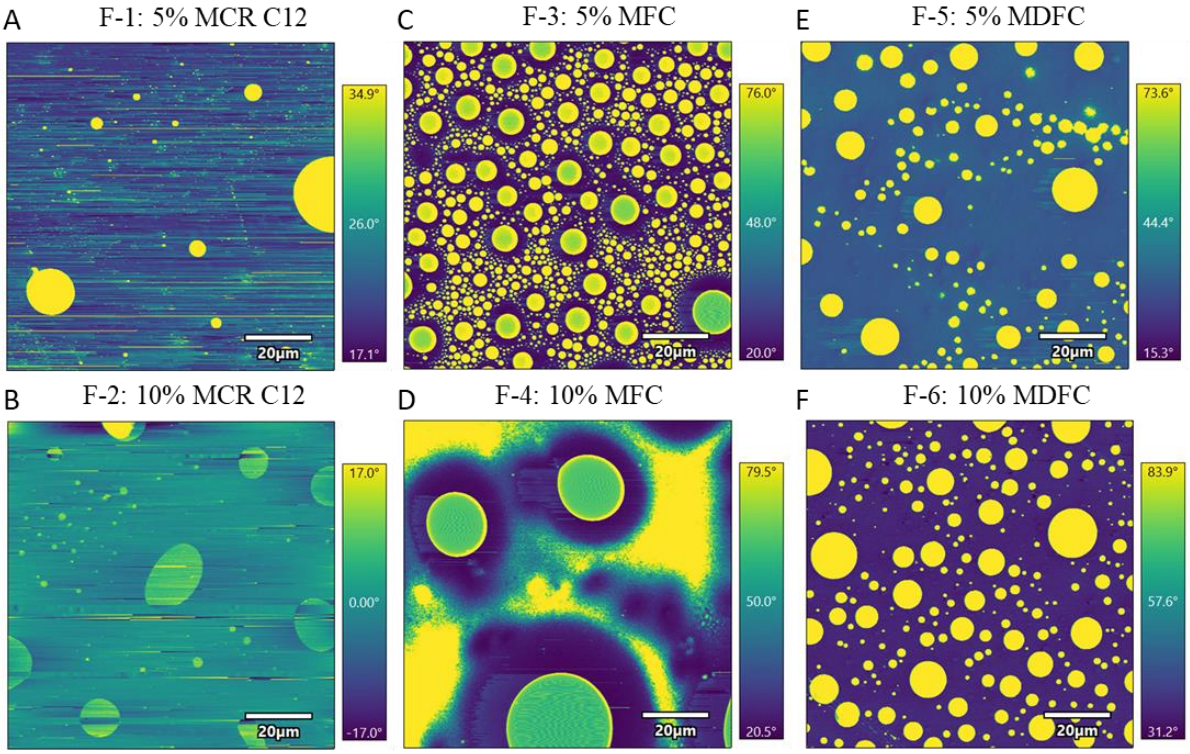

Figure 3.7. AFM phase images of the coatings

3.4.2.4. XPS measurements

XPS depth profiling was done to determine the elemental composition and distribution of different components of the coatings as seen in Figure 3.8. The comparison between the top and bottom sides of the base coating shows that a higher amount of silicon is present on the top side. This may be due to the self-stratification of the siloxane part of the coating towards the coating-air interface while the urea part towards the coating-substrate interface. Siloxane has lower surface free energy due to the presence of silicone. The higher nitrogen amount in the bottom side of the coating also proves the presence of a large amount of urea part in the coating-substrate interface.

The incorporation of carbinol functional siloxane changed the distribution of the urea part and made it more uniform throughout the coating. This is evident from the fact that the adhesion was lower for the formulations with carbinol functional siloxane. It was easier to peel off the film with carbinol functional siloxane from the steel panel compared to the base coating. It was also observed that some parts of the coating applied on steel panels without primer delaminated when mounted on the cold Peltier plate. This may be due to the lower urea part and also due to the presence of the PDMS chains from the carbinol functional siloxane on the coating substrate interface. There was an increase in the silicon atomic content in the bottom side of the coating and it was similar compared to the top side of the coating. This shows the uniform distribution of the carbinol functional siloxane throughout the coating. These results also agree with the contact angle results where a decrease in surface free energy of the bottom side of the coating was observed. Therefore, the distribution of the PDMS domains from carbinol functional siloxane might be uniform throughout the coating. This will be an added advantage to the coating since it can provide similar performance even when the top side of the coating is damaged, thus better durability.

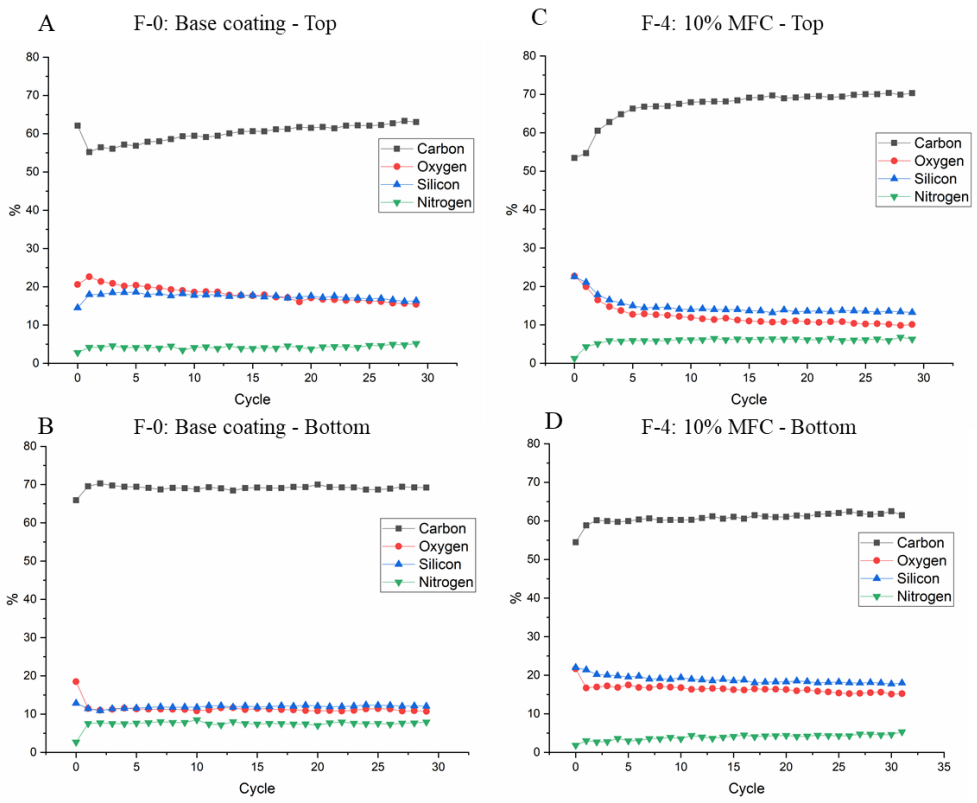

Figure 3.8. XPS depth profiling on the top and bottom side of the coating film

3.4.2.5. Young's modulus

Young's modulus was measured to see the effect of incorporating carbinol functional siloxane in the matrix on the mechanical properties of the coatings (Figure 3.9). The base coating had a higher modulus compared to other formulations. The incorporation of carbinol functional siloxane reduced the modulus of the coatings. Carbinol functional siloxane consists of PDMS chains which are known to have low modulus, thus their incorporation in the base matrix decreased the mechanical strength. The carbinol functional siloxane can act as plasticizers to the base matrix. In general, a higher amount of carbinol functional siloxane incorporation into the matrix reduced the mechanical strength in the same order as seen by the lower modulus of the formulations with 10% carbinol functional siloxane compared to 5% carbinol functional siloxane. However, compared to silicone elastomer, for example, Sylgard 184 which has

modulus below 5 MPa [45, 46], these values were almost two orders of magnitude higher. It shows that these coatings are more robust and durable compared to elastomers.

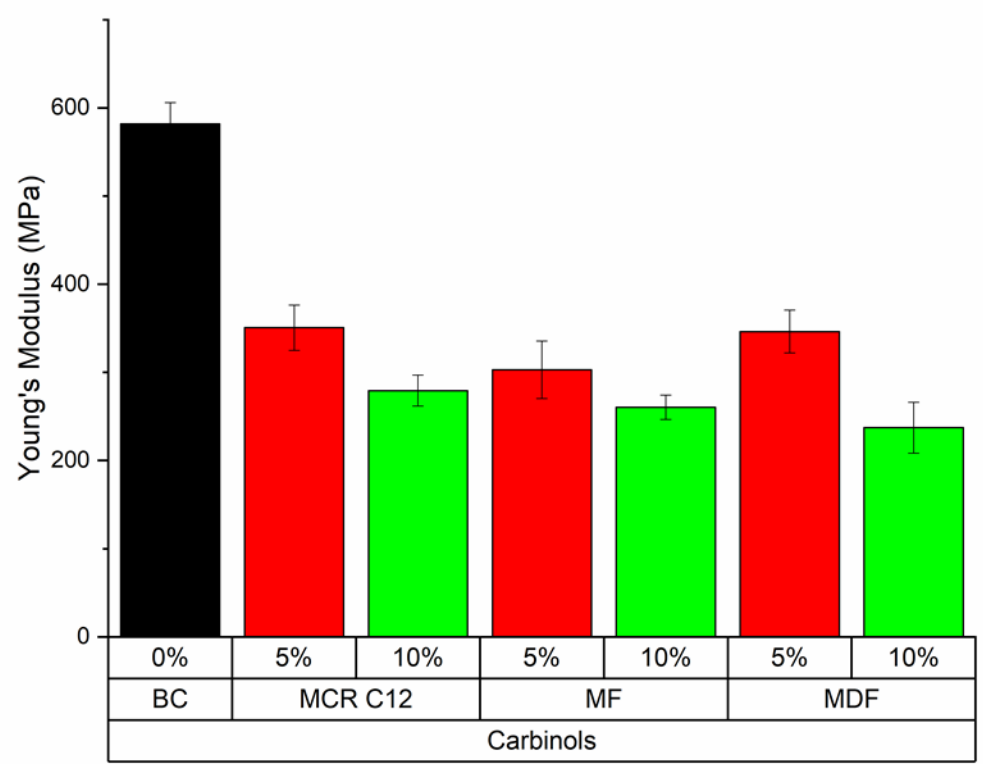

Figure 3.9. Young's modulus of base coatings and different formulations

3.4.3. Ice adhesion and interfacial toughness

The force required to remove ice at different scales was measured for all formulations and is shown in Figures 3.10. These data are important to understand the performance of coating for both small- and large-scale ice removal. For small-scale ice removal, adhesion strength is predominant, meaning that lower ice adhesion strength is favorable for material selection. However, for large-scale ice removal, interface toughness is predominant, meaning that lower interfacial toughness is favorable. Ideally, having both low ice adhesion strength and low interfacial toughness is desirable for coating material. This is because ice accumulation can occur in different scales and it will be beneficial to have both of these properties for efficient ice removal. The base coating showed high ice adhesion strength. Interfacial toughness could not be

determined due to the cohesive debonding of ice at a larger scale. This shows that the base coating resists the propagation of crack, thus it is not desirable for large-scale ice removal. However, the incorporation of carbinol functional siloxane showed improved ice-shedding properties, both in the ice adhesion strength-controlled region and interfacial toughness-controlled region.

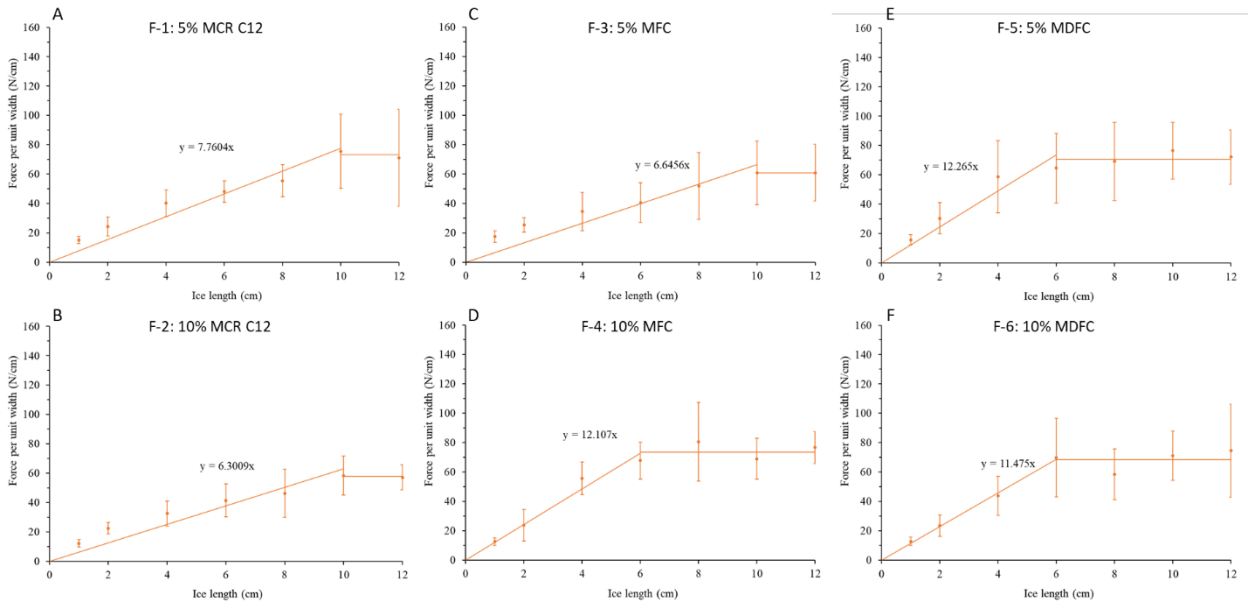

Figure 3.10. Force per unit width for different ice lengths for different formulations

In general, all the carbinol functional siloxane incorporated formulations showed lower interfacial toughness as given in Table 3.3. Interfacial toughness less than 1 J/m2 is suitable for large-scale deicing and all of these formulations showed less than 1 J/m2. Formulations with 10% MCR C12 (F-2) and 5% MFC (F-3) showed the lowest interfacial toughness and ice adhesion strength. Correlating these results with the AFM phase images, we see that the 5% MFC coating (F-3) has a lot of smaller size domains on the surface compared to other formulations which might have helped in lowering the interfacial toughness. For 10% MCR C12 (F-2), it is hard to say from the AFM images on the presence of these smaller size domains on

the surface. One reason may be that the whole surface of this coating might be covered by a slick layer of PDMS brushes from the carbinol functional siloxane reacted with the matrix.

Table 3.3. Summary of results of interfacial toughness measurement

Formulation	Film thickness (μm)	τ_{ice} (kPa)	Γ (J/m^2)	L_{cr} (cm)	F_{cr} (N/cm)
F-0: Base coating	64.4±14.8	212.40±76.28	Cohesive failure		
F-1: 5% MCR C12	114.6±17.8	77.60±15.91	0.53±0.045	10.0±2.44	73.39±3.11
F-2: 10% MCR C12	102.5±23.4	63.01±19.87	0.33±0.010	10.0±3.37	57.81±0.86
F-3: 5% MFC	84.9±12.6	66.46±32.75	0.36±0.002	10.0±5.98	60.75±0.15
F-4: 10% MFC	87.1±13.0	121.07±17.74	0.53±0.088	6.0±1.43	73.54±6.14
F-5: 5% MDFC	88.0±24.9	122.65±34.72	0.49±0.069	6.0±2.22	70.61±5.01
F-6: 10% MDFC	97.7±14.2	114.75±30.53	0.46±0.095	6.0±2.37	68.50±7.04

τice: Ice adhesion strength, Γ: Interfacial toughness, Lcr: Critical length, Fcr: Critical force

3.5. Conclusions

Moisture-curable urea-siloxane coating was modified by incorporating different mono and di- carbinol functional siloxane. The contact angle and surface free energy tests suggested that the carbinol functional siloxane were distributed on both the coating-air interface and the coating-substrate interface. AFM phase images showed the self-segregating behavior of the PDMS chains from carbinol functional siloxane by forming distinct domain structures on the surface of the coating. XPS depth profiling of the coating on both the top and bottom sides suggested that all the components of the coating, including urea, siloxane, and carbinol functional siloxane were distributed throughout the coating. Carbinol functional siloxane incorporation on the base coating lowered the ice adhesion strength and interfacial toughness of the coating making it a promising candidate for ice-shedding and fouling release applications.

3.6. References

1. Segercrantz H (1989) Icebreakers Their Historical and Technical Development. Interdisciplinary Science Reviews 14:77–85. https://doi.org/10.1179/ISR.1989.14.1.77
2. Verma S, Mohanty S, Nayak SK (2019) A review on protective polymeric coatings for marine applications. J Coat Technol Res 16:307–338. https://doi.org/10.1007/S11998-018-00174-2
3. Shi K, Duan X (2021) A review of ice protection techniques for structures in the arctic and offshore harsh environments. Journal of Offshore Mechanics and Arctic Engineering 143:. https://doi.org/10.1115/1.4050893/1107900
4. Lejars M, Margaillan A, Bressy C (2012) Fouling release coatings: A nontoxic alternative to biocidal antifouling coatings. Chem Rev 112:4347–4390. https://doi.org/10.1021/CR200350V
5. Kreder MJ, Alvarenga J, Kim P, Aizenberg J (2016) Design of anti-icing surfaces: smooth, textured or slippery? Nature Reviews Materials 2016 1:1 1:1–15. https://doi.org/10.1038/natrevmats.2015.3
6. Qiu H, Feng K, Gapeeva A, et al (2022) Functional polymer materials for modern marine biofouling control. Prog Polym Sci 127:101516. https://doi.org/10.1016/J.PROGPOLYMSCI.2022.101516
7. Nistal A, Sierra-Martín B, Fernández-Barbero A (2023) On the Durability of Icephobic Coatings: A Review. Materials 2024, Vol 17, Page 235 17:235. https://doi.org/10.3390/MA17010235
8. Lagerström M, Wrange AL, Oliveira DR, et al (2022) Are silicone foul-release coatings a viable and environmentally sustainable alternative to biocidal antifouling coatings in the

Baltic Sea region? Mar Pollut Bull 184:114102. https://doi.org/10.1016/J.MARPOLBUL.2022.114102

9. Zhuo Y, Xiao S, Amirfazli A, et al (2021) Polysiloxane as icephobic materials – The past, present and the future. Chemical Engineering Journal 405:127088. https://doi.org/10.1016/J.CEJ.2020.127088

10. Irajizad P, Al-Bayati A, Eslami B, et al (2019) Stress-localized durable icephobic surfaces. Mater Horiz 6:758–766. https://doi.org/10.1039/C8MH01291A

11. Jung S, Dorrestijn M, Raps D, et al (2011) Are superhydrophobic surfaces best for icephobicity? Langmuir 27:3059–3066. https://doi.org/10.1021/LA104762G

12. Bharathidasan T, Kumar SV, Bobji MS, et al (2014) Effect of wettability and surface roughness on ice-adhesion strength of hydrophilic, hydrophobic and superhydrophobic surfaces. Appl Surf Sci 314:241–250. https://doi.org/10.1016/J.APSUSC.2014.06.101

13. Ozbay S, Yuceel C, Erbil HY (2015) Improved Icephobic Properties on Surfaces with a Hydrophilic Lubricating Liquid. ACS Appl Mater Interfaces 7:22067–22077. https://doi.org/10.1021/ACSAMI.5B07265

14. Dhyani A, Wang J, Halvey AK, et al (2021) Design and applications of surfaces that control the accretion of matter. Science (1979) 373:. https://doi.org/10.1126/SCIENCE.ABA5010

15. Benda J, Stafslien S, Vanderwal L, et al (2021) Surface modifying amphiphilic additives and their effect on the fouling-release performance of siloxane-polyurethane coatings. Biofouling 37:309–326. https://doi.org/10.1080/08927014.2021.1901891

16. Bodkhe RB, Stafslien SJ, Daniels J, et al (2015) Zwitterionic siloxane-polyurethane fouling-release coatings. Prog Org Coat 78:369–380. https://doi.org/10.1016/J.PORGCOAT.2014.07.011

17. Galhenage TP, Hoffman D, Silbert SD, et al (2016) Fouling-Release Performance of Silicone Oil-Modified Siloxane-Polyurethane Coatings. ACS Appl Mater Interfaces 8:29025–29036. https://doi.org/10.1021/ACSAMI.6B09484

18. Dai G, Xie Q, Ai X, et al (2019) Self-Generating and Self-Renewing Zwitterionic Polymer Surfaces for Marine Anti-Biofouling. ACS Appl Mater Interfaces 11:41750–41757. https://doi.org/10.1021/ACSAMI.9B16775

19. Tao C, Bai S, Li X, et al (2018) Formation of zwitterionic coatings with an aqueous lubricating layer for antifogging/anti-icing applications. Prog Org Coat 115:56–64. https://doi.org/10.1016/J.PORGCOAT.2017.11.002

20. Upadhyay V, Galhenage T, Battocchi D, Webster D (2017) Amphiphilic icephobic coatings. Prog Org Coat 112:191–199. https://doi.org/10.1016/J.PORGCOAT.2017.07.019

21. Rahimi AR, Murphy M, Upadhyay V, et al (2021) Amphiphilically modified self-stratified siloxane-glycidyl carbamate coatings for anti-icing applications. J Coat Technol Res 18:83–97. https://doi.org/10.1007/S11998-020-00402-8

22. Liang B, Zhang G, Zhong Z, et al (2019) Superhydrophilic Anti-Icing Coatings Based on Polyzwitterion Brushes. Langmuir 35:1294–1301. https://doi.org/10.1021/ACS.LANGMUIR.8B01009

23. Rao Q, Lu Y, Song L, et al (2021) Highly Efficient Self-Repairing Slippery Liquid-Infused Surface with Promising Anti-Icing and Anti-Fouling Performance. ACS Appl Mater Interfaces 13:40032–40041. https://doi.org/10.1021/ACSAMI.1C09491

24. Li S, Zhao F, Bai Y, et al (2022) Slippery liquid-infused microphase separation surface enables highly robust anti-fouling, anti-corrosion, anti-icing and anti-scaling coating on diverse substrates. Chemical Engineering Journal 431:133945. https://doi.org/10.1016/J.CEJ.2021.133945

25. Wang C, Guo Z (2020) A comparison between superhydrophobic surfaces (SHS) and slippery liquid-infused porous surfaces (SLIPS) in application. Nanoscale 12:22398–22424. https://doi.org/10.1039/D0NR06009G

26. Buddingh J V., Hozumi A, Liu G (2021) Liquid and liquid-like surfaces/coatings that readily slide fluids. Prog Polym Sci 123:101468. https://doi.org/10.1016/J.PROGPOLYMSCI.2021.101468

27. Benda J, Narikiyo H, Stafslien SJ, et al (2022) Studying the Effect of Pre-Polymer Composition and Incorporation of Surface-Modifying Amphiphilic Additives on the Fouling-Release Performance of Amphiphilic Siloxane-Polyurethane Coatings. ACS Appl Mater Interfaces 14:37229–37247. https://doi.org/10.1021/ACSAMI.2C10983

28. Stein J, Truby K, Wood CD, et al (2003) Silicone Foul Release Coatings: Effect of the Interaction of Oil and Coating Functionalities on the Magnitude of Macrofouling Attachment Strengths. Biofouling 19:71–82. https://doi.org/10.1080/0892701031000089525

29. Li J, Jiao W, Jin H, et al (2023) Robust polyurea icephobic coatings with static large-scale de-icing and dynamic anti-icing performance. Chemical Engineering Journal 478:147339. https://doi.org/10.1016/J.CEJ.2023.147339

30. Du Y, Tang J, Li R, et al (2024) A crosslinked silicone coating adjusted by an additive with promising antifouling and ice nucleation inhibition performance. New Journal of Chemistry 48:693–702. https://doi.org/10.1039/D3NJ03939K

31. Zhou Y, Liu C, Gao J, et al (2019) A novel hydrophobic coating film of water-borne fluoro-silicon polyacrylate polyurethane with properties governed by surface self-segregation. Prog Org Coat 134:134–144. https://doi.org/10.1016/J.PORGCOAT.2019.04.078

32. Majumdar P, Webster DC (2006) Influence of solvent composition and degree of reaction on the formation of surface microtopography in a thermoset siloxane–urethane system. Polymer (Guildf) 47:4172–4181. https://doi.org/10.1016/J.POLYMER.2006.02.085

33. Majumdar P, Webster DC (2007) Surface microtopography in siloxane–polyurethane thermosets: The influence of siloxane and extent of reaction. Polymer (Guildf) 48:7499–7509. https://doi.org/10.1016/J.POLYMER.2007.10.044

34. Pistone A, Scolaro C, Visco A (2021) Mechanical Properties of Protective Coatings against Marine Fouling: A Review. Polymers 2021, Vol 13, Page 173 13:173. https://doi.org/10.3390/POLYM13020173

35. Zheng Q, Lv J, Zhang J, Feng J (2021) Fabrication and application of icephobic silicone coatings on epoxy substrate. Prog Org Coat 161:106483. https://doi.org/10.1016/J.PORGCOAT.2021.106483

36. Zheng H, Liu G, Nienhaus BB, Buddingh J V. (2022) Ice-Shedding Polymer Coatings with High Hardness but Low Ice Adhesion. ACS Appl Mater Interfaces 14:6071–6082. https://doi.org/10.1021/ACSAMI.1C23483

37. Golovin K, Dhyani A, Thouless MD, Tuteja A (2019) Low-interfacial toughness materials for effective large-scale deicing. Science (1979) 364:371–375. https://doi.org/10.1126/SCIENCE.AAV1266

38. Mohseni M, Dijvejin ZA, Golovin K (2021) Designing scalable elastomeric anti-fouling coatings: Shear strain dissipation via interfacial cavitation. J Colloid Interface Sci 589:556–567. https://doi.org/10.1016/J.JCIS.2021.01.019

39. Azimi Dijvejin Z, Jain MC, Kozak R, et al (2022) Smart low interfacial toughness coatings for on-demand de-icing without melting. Nature Communications 2022 13:1 13:1–12. https://doi.org/10.1038/s41467-022-32852-6

40. Harper AN, Liu G (2020) Phase Equilibria of a Brush-Bearing Coating Swollen with a Lubricant and Regulation of Its Composition to Facilitate Ice Shedding. ACS Appl Polym Mater 2:4814–4824. https://doi.org/10.1021/ACSAPM.0C00785

41. Majumdar P, Stafslien S, Daniels J, Webster DC (2007) High throughput combinatorial characterization of thermosetting siloxane-urethane coatings having spontaneously formed microtopographical surfaces. J Coat Technol Res 4:131–138. https://doi.org/10.1007/S11998-007-9015-2

42. Nazifi S, Huang Z, Hakimian A, Ghasemi H (2022) Fracture-controlled surfaces as extremely durable ice-shedding materials. Mater Horiz 9:2524–2532. https://doi.org/10.1039/D2MH00619G

43. Wang P, Yang M, Zheng B, et al (2022) Soft and Rigid Integrated Durable Coating for Large-Scale Deicing. Langmuir 39:410. https://doi.org/10.1021/ACS.LANGMUIR.2C02612

44. Iezzi EB (2012) Single-component coating having alkoxysilane-terminated N-substituted urea resins. US Patent No 8,133,964

45. Moučka R, Sedlačík M, Osička J, Pata V (2021) Mechanical properties of bulk Sylgard 184 and its extension with silicone oil. Scientific Reports 2021 11:1 11:1–9. https://doi.org/10.1038/s41598-021-98694-2

46. Delplanque E, Aymard A, Dalmas D, et al (2014) Mechanical characterization of bulk Sylgard 184 for microfluidics and microengineering. Journal of Micromechanics and Microengineering 24:035017. https://doi.org/10.1088/0960-1317/24/3/035017

CHAPTER 4. SUSTAINABILITY ASSESSMENT OF LIGNIN-BASED FOAM

4.1. Abstract

Lignin is the second most abundant biopolymer on earth. The bulk of technical lignin produced is however burned as a low-value fuel. Valorizing lignin into higher-value chemicals can potentially create higher economic incentives for producers and lower their environmental footprint compared to conventional chemicals. Lignin valorization can be achieved through multiple possible pathways including depolymerization, chemical modification, and macromolecular application. However, before recommending any valorization pathway for scale-up and commercialization, economic and environmental assessments are needed. One promising application of lignin can be to produce rigid foams. The aromatic and aliphatic hydroxyl functional groups in lignin can be substituted with acetoacetate functionality to produce an acetoacetylated lignin resin. This resin can then be crosslinked with amines and a siloxane-blowing agent to obtain a rigid foam. In this study, we perform an economic and environmental assessment for lignin-based foam production. We used life-cycle environmental performance and cost as the two main indicators to evaluate the sustainability of the proposed product. Our results show that lignin-based foam has a minimum selling price of $6.5/kg compared to $9/kg for rigid polyurethane foam. Uncertainty analysis also shows that lignin-based foam has the potential to be economically competitive with polyurethane foam under a variety of possible circumstances. Similarly, life cycle assessment shows lignin-based foam performs better in all impact categories except ozone depletion and fossil fuel depletion. For both economic and environmental analysis, tert-butyl acetoacetate (a lignin functionalizing chemical) and amine crosslinker have the greatest contribution. Additionally, our analysis shows that due to

the higher density of lignin foam, selecting a mass-based functional unit favors lignin foam while a volume-based functional unit will support polyurethane foam's environmental performance.

4.2. Introduction

There is a growing interest in biobased products in both academia and industry. A primary reason for the interest in biobased products is due to the wide availability of biomass, potential environmental benefits from biobased products, improvement in rural economy, and environmental concerns around fossil-based products [1]. Biomass is composed of three fundamental building blocks: cellulose, hemicellulose, and lignin. Lignin is currently mainly produced as the by-product of paper and pulp industries and can potentially be produced from second-generation biorefineries. Conventional use of lignin is mostly limited to a low-value fuel for generating heat and electricity by industries [2]. Lignin valorization to higher value products can improve the economy of the biobased industries and potentially provide a more environmentally friendly substitute to fossil-based products.

Lignin is the second most abundant biopolymer found on earth. It is a polyphenolic, three-dimensional heteropolymer that has both aliphatic and aromatic hydroxyl functional groups that can be used for various applications [3]. One area of growing interest is the application of lignin in the production of polyurethane foams. The global market of polyurethane foam was more than $60 billion in 2017 and has an annual growth rate of more than 10% [4]. Commercial foams can be generally divided into rigid and flexible foams: the primary difference between them is the cell structure in the foam: flexible foam has an open cell structure and rigid foam has a closed cell structure. Polyurethane foams are prepared by reacting isocyanates with polyols to form carbamate ester linkages. The aliphatic and aromatic hydroxyl groups in lignin make it a good candidate for replacing polyol in polyurethane foam formulations [4]. Macromolecular

lignin can be either directly employed in the formulation or they can be modified [5]. Direct use of unmodified lignin is limited because the hydroxyl groups are less reactive due to steric hindrances. Direct use of lignin also limits the amount of lignin that can be incorporated into a formulation. A higher amount of lignin in the formulation may result in poor mechanical properties [6]. Lignin reactivity and lignin substitution ratio in the formulation can be improved by either depolymerizing lignin or functionalizing lignin with more reactive groups [7]. Lignin depolymerization into respective monolignols can increase its reactivity, but this is a more costly and energy-intensive process. Lignin can also be functionalized with other functional groups to increase its reactivity. Lignin has been used in foam formulation in a previous study where it showed comparable results to commercial foams [8]. In addition to having a higher renewable content, some of those studies also showed that lignin-based foams can have higher biodegradability [9, 10].

Apart from some of the above advantages, there are still challenges in the commercial supply of lignin with consistent properties, uncertainties in market prices of lignin, and collaborative works between concerned stakeholders for the adoption and commercialization of the lignin-based products technologies [11]. In addition to identifying the synthetic routes for new products, it is also essential to determine the economic viability and life cycle impact of the synthesis process to understand the sustainability stance of the product. Economic assessment helps to determine the cost of the product, identify the major cost contributors, and compare it to similar conventional products. This is a very important tool in the early stages of a product's design to assess the commercial viability of the product. Similarly, environmental parameters are also necessary while synthesizing new products. This helps to identify the environmental hotspots in the synthesis steps and shows further research direction on the areas that need to be

improved. Many biobased products are still in the early stages of development and may not necessarily be more environmentally friendly than their conventional counterparts. Biomass needs to be processed and processing can be energy and chemical-intensive intensive which can result in higher environmental impacts [12]. A recent study on lignin-based rigid polyurethane foam showed a potential reduction in environmental impacts compared to traditional polyurethane foam [13]. Lignin-based products have shown better environmental performance in many applications, however, many of the conclusions are based upon the choice of the functional unit and allocation methods [14].

In this work, we perform the sustainability assessment of a rigid foam which is made by functionalizing lignin with acetoacetate groups and reacting with amine crosslinker and a polysilane foaming agent [15]. The advantage of this process is that the functionalizing step of lignin uses a reactive diluent, 1,4-butanediol (BDO) which is also functionalized with acetoacetate groups and does not need to be removed from the final product. The process is also waste-free as no extra solvents are used in the process. The by-product tert-butanol, formed in the process is obtained in a relatively pure form and can be directly sold in the market.

The objective of this study is to assess the economic and environmental performance of lignin-based rigid foam and compare it with commercially available rigid polyurethane foam. Techno-economic assessment (TEA) and life cycle assessment (LCA) are conducted to determine economic and environmental performance.

4.3. Methods

We used techno-economic and life cycle assessment methods to assess the sustainability of the lignin-based foam. We used laboratory scale data from a previous experimental work [15] and developed a scaled-up process model that represented a commercial scale production. The

scaled-up mass and energy balance results from process simulation were used to build the TEA and LCA models. The deterministic TEA results were also tested for uncertainty for higher confidence in the results. In the following sections, we describe the foam synthesis process, process modeling and simulation, and assumptions for TEA, LCA, and uncertainty analyses.

4.3.1. Process description

The production of foam is achieved in two steps: first producing a resin and then crosslinking the resin with a crosslinker and a blowing agent [15]. The resin is produced by reacting lignin, 1,4-butanediol (BDO), and tert-butyl acetoacetate (tBAA) at 130℃ for 24 hours. The aromatic and aliphatic hydroxyl groups in lignin are thus functionalized with acetoacetate groups. Similarly, BDO acts as a reactive diluent in order to solubilize the lignin and is simultaneously functionalized with the acetoacetate group. Tert-butyl alcohol (TBA) leaves the reaction as a distillate which is a by-product of the process. The by-product is relatively pure and can be sold directly in the market. Resin, which is the acetoacetate functionalized lignin and BDO remains in the reactor. This resin is then reacted with tris(2-aminoethyl)amine (TAEA) crosslinker and polymethylhydrosiloxane (PMHS). TAEA reacts with resin to form a three-dimensional crosslinked structure and water comes out as a byproduct. The amine functional end in TAEA also reacts with PMHS and releases hydrogen gas (H2) resulting in a cellular foam structure [16]. For industrial production, a proper ventilation system is required to release hydrogen gas into the atmosphere as hydrogen is flammable at a concentration of 4-75% [17].

4.3.2. Process design and simulation

Aspen Plus V10 (AspenTech, Massachusetts, USA) was used for foam production process design and simulation. Process simulation provides mass and energy balances for the process. The POLYNRTL (Polymer Non-Random Two-liquid) physical property method was

used as an activity coefficient model to predict liquid-liquid and liquid-vapor equilibrium. POLYNRTL method has the advantage over other methods as it covers a wider range of compositions and temperatures and includes the functionalities of the NRTL method [18]. All the components except lignin, TAEA, and PMHS were present in Aspen databanks. Lignin is modeled based on the National Renewable Energy Laboratory (NREL) property database for biofuel components [19]. Similarly, TAEA is defined by its molecular structure while PMHS is modeled to be similar to PDMS. Resin synthesis is modeled in a stoichiometric reactor based on known stoichiometry from laboratory experiments. A separation unit is considered to separate resin and the by-product to simplify the process, even though in the actual process the by-product comes out as a distillate. Foam production is modeled in a yield reactor. Foam is defined based on the functional groups and the reaction steps between resin, crosslinker, and blowing agent. The process is designed for a 10 MT resin/day production capacity which results in $4400 MT foam/year.

The process flow diagram and system boundary for foam production are shown in Figure 4.1. The process is separated into two sections: resin production and foam production.

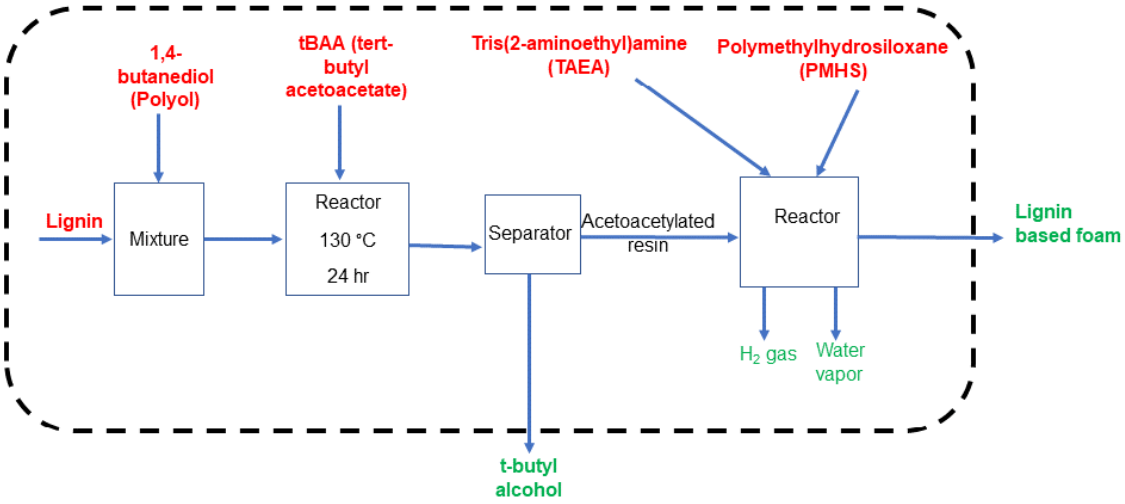

Figure 4.1. Process flow diagram of lignin foam production (dashed line represents system boundary)

4.3.3. Economic analysis

Based on the experimental and simulated results, the capital and operating costs of producing resin and foam were estimated. Aspen Plus Economic Analyzer estimates the capital costs, utilities costs, and labor and maintenance costs. Raw material costs are obtained from a variety of market reports, vendor quotes, and previous research articles. A discounted cash flow analysis was conducted to obtain the minimum selling price (MSP) of the product. All the costs are reported in 2019 dollars. The assumptions for economic analysis are presented in Table 4.1.

Table 4.1. Economic analysis assumptions

Items	Value
Plant life	20 years
Annual operating hours	8410 hours
Construction and start-up period	1 year
Working capital	5%
Tax rate	40%
Discount rate	20%
Products escalation	5%
Raw materials price escalation	3.5%
Labor and maintenance	5%
Depreciation method	MACRS
Salvage value	0%

The raw materials prices are presented in Table 4.2. The utility prices are estimated from Aspen Process Economic Analyzer.

Table 4.2. Prices of the inputs

Materials	Price
Lignin ($/MT)	250[20]
BDO ($/MT)	2250[a]
tBAA ($/MT)	4250[b]
TAEA ($/MT)	9000[b]
PMHS ($/MT)	3000[b]
Electricity (S/kWh)	0.08[c]
Steam ($/kg)	1.90E-06[c]
Cooling water ($/$m^3$)	0.03[c]
By-product credit (t-butanol) ($/MT)	2000[b]

[a] BASF quote, [b] alibaba.com, [c] AspenPlus

4.3.3.1. Uncertainty in Economic Analysis

Uncertainty analysis is a powerful method to determine the risks associated with deterministic results. Cost uncertainty analysis was performed using Monte Carlo simulation with 1000 iterations using Crystal Ball software (Oracle, California, USA). The analysis is done by first identifying the major uncertain input parameters that can impact the forecasting value (usually the selling price of the product). Once the uncertain parameters are identified, the probability distribution of their values is defined either by fitting a distribution to the price dataset or assigning a certain distribution when enough data points are not available. The input probability distribution of uncertain parameters is used to forecast the output. In this work, the uncertain input parameters included prices of raw materials, capital cost, tax rate, and discount rate while output included minimum selling price of the product. The historical prices of the raw materials were obtained using their chemical price index, capital cost was obtained based on plant cost index, discount rate, and tax rate were defined as triangular and uniform distribution respectively with ±20%. The assumptions for uncertainty analysis are presented in Table 4.3.

Table 4.3. Uncertainty inputs of economic analysis

Inputs	Probability distribution
Lignin ($/kg)	Min-extreme
BDO ($/kg)	Min-extreme
tBAA ($/kg)	Min-extreme
TAEA ($/kg)	Weibull
PMHS ($/kg)	Weibull
Capital cost (million $)	Triangular
Tax rate (%)	Uniform
Discount rate (%)	Triangular
t-butanol ($/kg)	Min-extreme

4.3.4. Life cycle assessment

To determine the life cycle environmental performance of foam and its comparison with commercial polyurethane foam, the LCA method was employed following ISO standards [21]. SimaPro V8.3 and Tool for Reduction and Assessment of Chemicals and Other Environmental Impacts (TRACI II) method were used for building the model and performing the analysis [22]. TRACI II method incorporates 10 different impact categories such as global warming, ozone depletion, and fossil fuel depletion.

4.3.4.1. Goal, scope, and functional unit

The goal of this study is to perform a life cycle assessment of producing lignin-based foam and compare its environmental performance with commercial rigid polyurethane foam. The functional unit for our cradle-to-gate LCA is mass-based and equal to 1 kg of foam.

4.3.4.2. Life cycle inventory data collection

The primary data for our analysis were based on mass and energy balance from process simulation. The lignin extraction process in our analysis was based on Bernier et al. [12]. We also compared the environmental performance of kraft lignin with biorefinery lignin. Biorefinery lignin was modeled based on NREL's dilute acid processing of corn stover [23]. The LCA of

kraft lignin production, biorefinery lignin production, and the comparison between kraft and biorefinery lignin are provided in the Appendix C (Figures C1, C2, and C3). Biorefinery lignin performed better than kraft lignin in almost all categories. For the chemicals that were not available in LCA databases, patents were used. All other chemicals were either obtained from Ecoinvent, the USLCI database, or other sources (Table C1 in Appendix C).

4.4. Results and discussion

4.4.1. Process modeling

The mass balance obtained from the Aspen Plus process model is presented in Figure 4.2. The electricity required for foam production is 111 kW, the steam required is 130,600 kJ/h, and the cooling water required is 11 m^3/h.

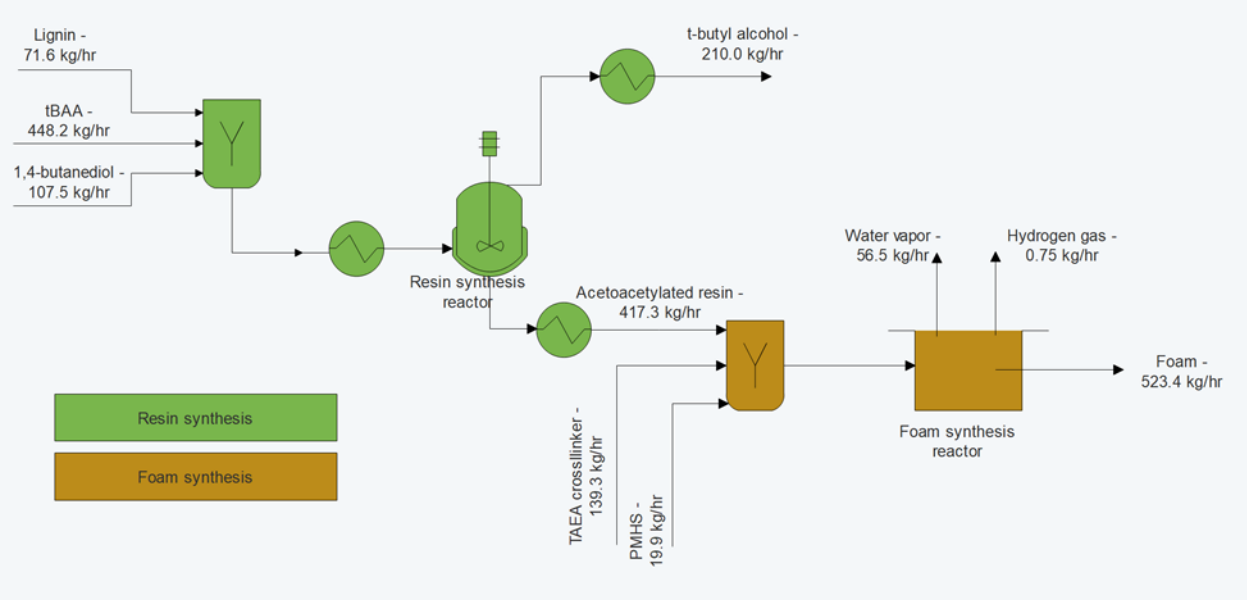

Figure 4.2. Mass balance for the production of lignin-based foam

4.4.2. Economics

The results of the economic analysis are presented in Table 4.4 with the breakdown of different costs. The minimum selling price (MSP) of the lignin-based foam was found to be $6.5/kg. For comparison, the price of commercial rigid polyurethane foam is in the range of $6-

9/kg [24]. This means that lignin-based foam has the potential to be competitive with commercially available foam. Annual revenues from foam account for ~90%, while the rest comes from by-product credit.

Table 4.4. Economic analysis results

Cost	Value
Capital cost ($)	4,363,626
Total operating cost ($)	33,218,700
Raw materials cost ($/year)	29,257,060
Utilities cost ($/year)	75,184
Product cost ($/kg)	6.5

Capital cost contributed less than 5% to the MSP. The only costlier equipment for this process was the reactor for resin synthesis (Table 4.5).

Table 4.5. Equipment costs

Equipment	Cost
Resin synthesis reactor ($)	239,209
Foam synthesis reactor ($)	32,186
Mixture 2 ($)	31,513
Heat exchanger 1 ($)	9,084
Heat exchanger 2 ($)	9,869
Heat exchanger 3 ($)	8,972

Within operating costs, raw material costs accounted for about 90%. The breakdown of raw material costs shows that tBAA has the highest contribution followed by TAEA crosslinker (Figure 4.3). The reason for the higher contribution of tBAA is due to its higher volume use and higher cost compared to others. For TAEA, the higher cost contribution is because of its relatively higher cost per unit mass. Lignin production cost contribution accounts for less than 1% because of its low price and low volume used.

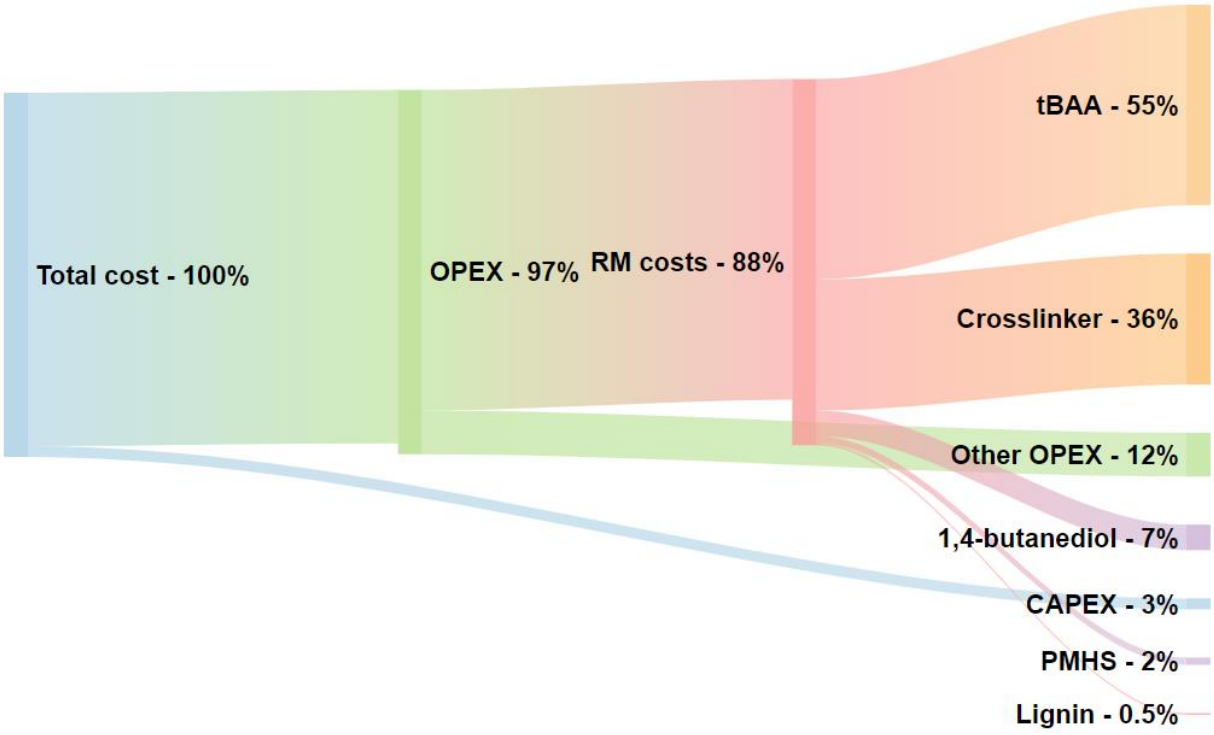

Figure 4.3. Cost breakdown of lignin foam production process (RM - raw material, OPEX - operating costs, CAPEX - capital costs)

4.4.3. Sensitivity and uncertainty analysis in economics

The forecasted value of MSP based on Monte Carlo analysis of the TEA model showed that the MSP varies between $4-$7/kg foam (Figure 4.4). The mean value is around $5.7/kg, and the median value is around $5.8/kg foam. This bigger range in MSP was mainly due to high uncertainty in fossil-based raw material prices. The lower mean value compared to the base case scenario tells us that there is a higher chance that the lignin foam MSP may be lower than the estimated MSP. There is a small overlap between the price range of lignin-based foam and commercial polyurethane foam ($6-$9/kg polyurethane foam) which means that lignin-based foam in the majority of scenarios can be economically competitive with commercially available rigid foams.

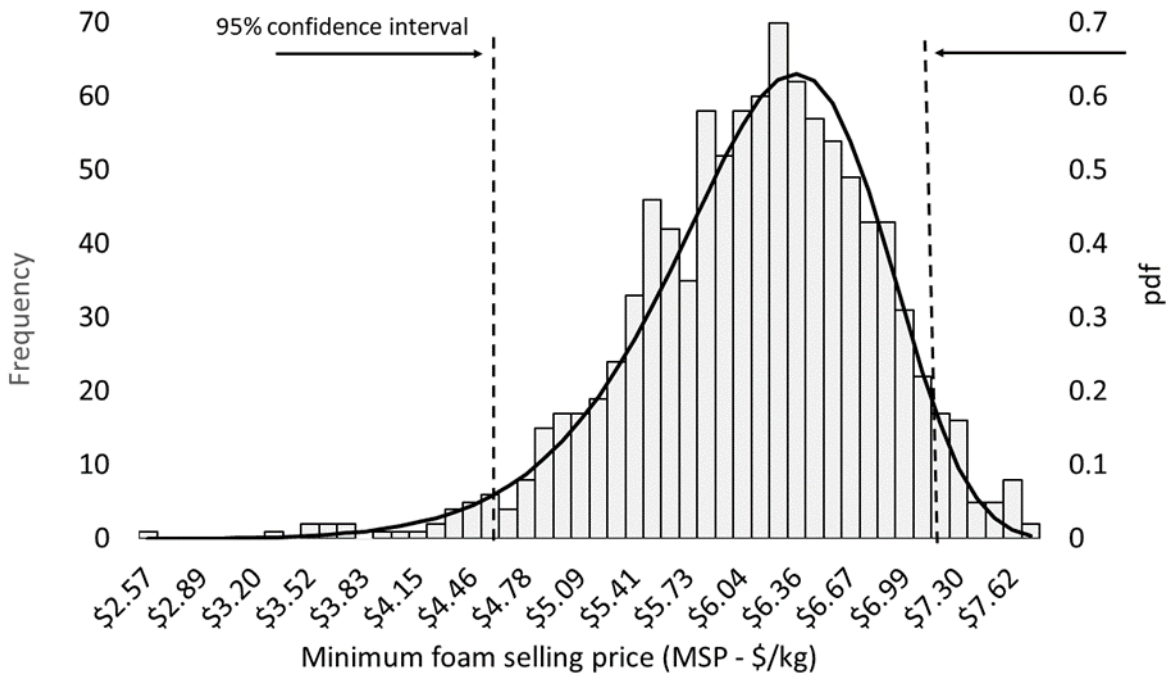

Figure 4.4. Uncertainty analysis of lignin foam production process

We also performed the sensitivity analysis to see MSP sensitivity to input parameters (Figure 4.5). The result shows that MSP is highly sensitive to tBAA and TAEA crosslinker prices. To further improve the economics of lignin foam production, further work should be carried out to find a less costly lignin functionalizing chemical and resin crosslinker. The prices of the chemicals are based on market reports and online marketplace. The true price of the chemicals may differ based on location and cost of shipment. However, the effect of this should not be significant for bulk chemicals.

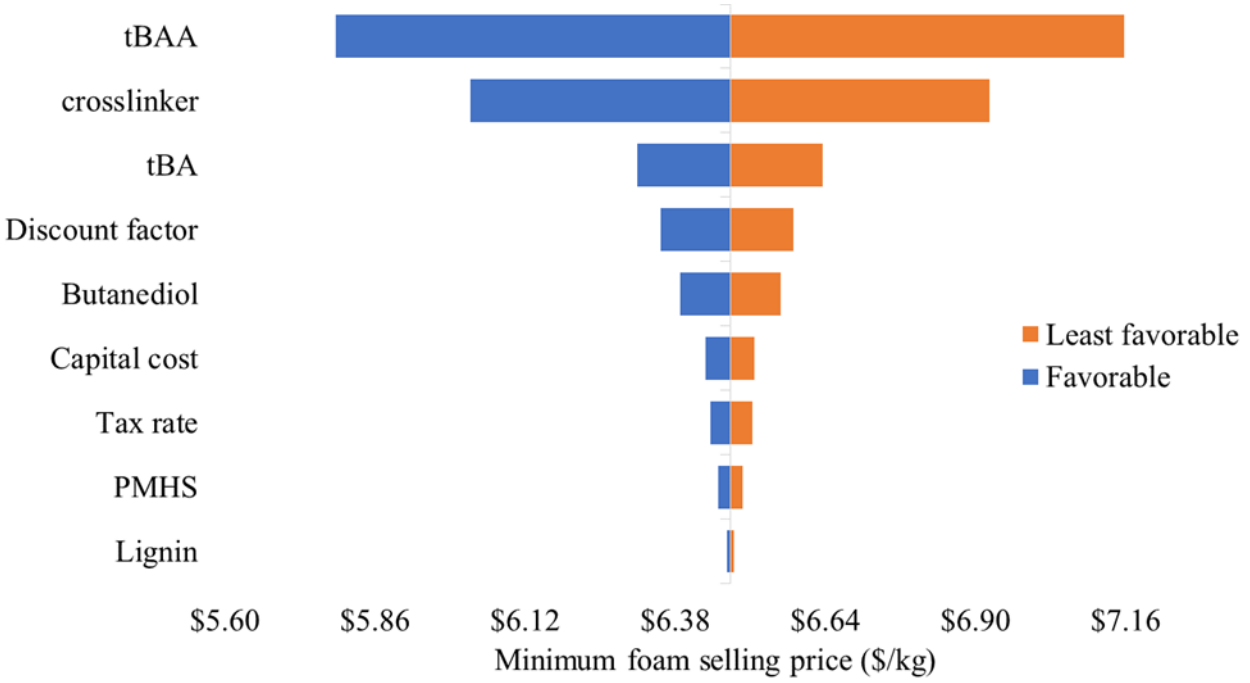

Figure 4.5. Sensitivity analysis of lignin foam production process (all parameters were varied ±20%)

4.4.4. Environmental performance of foam

The resin production process consists of two products: resin and t-butanol. The mass-based allocation LCA result shows that TBAA has the highest contribution in most of the tested environmental impact categories followed by 1,4-butanediol (Figure 4.6). Within tBAA, diketene production has the major contribution. The carbon credit from lignin is very small compared to carbon emission from other chemicals and processes, primarily due to the low volume of lignin used in the synthesis and the higher impact from other sources. The LCA result of resin production considering t-butanol as an avoided product (a system expansion approach) is shown in Appendix C (Figure C4).

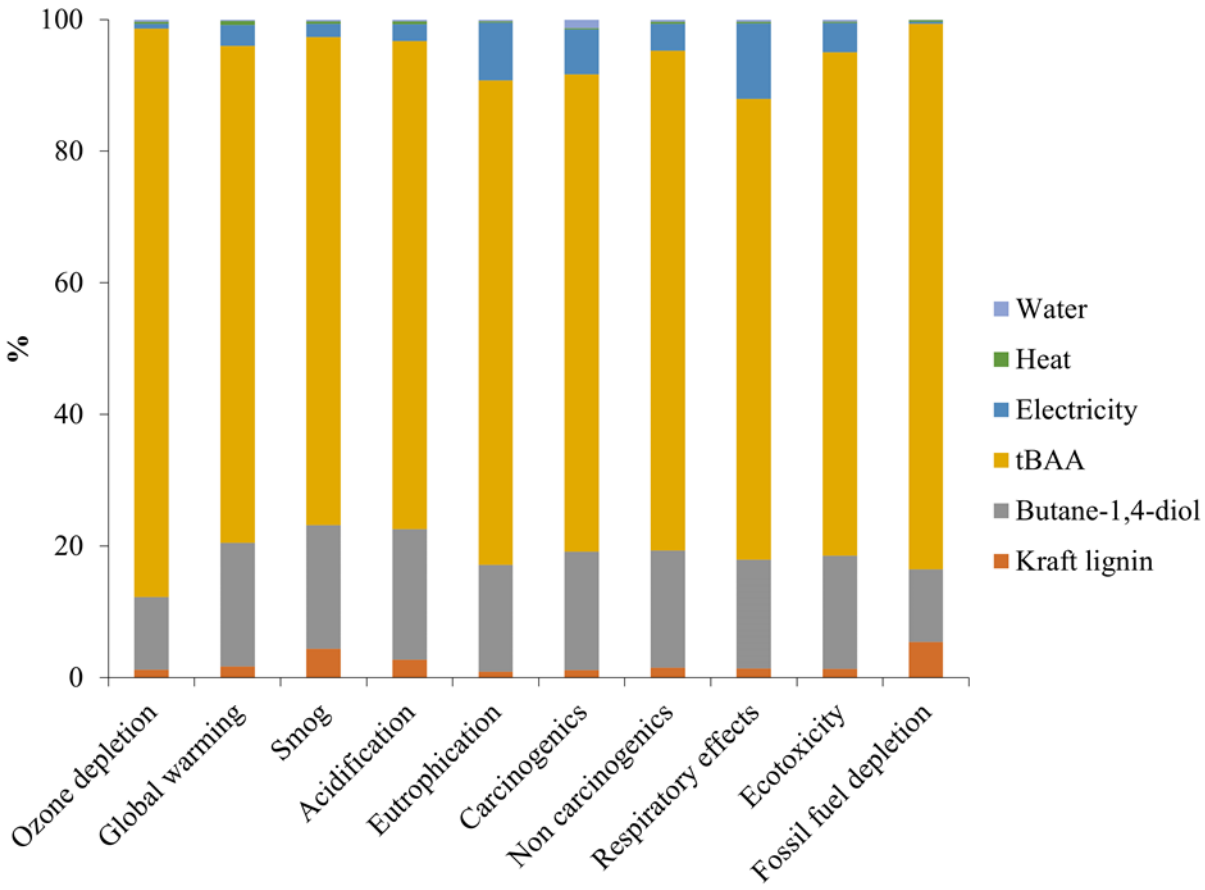

Figure 4.6. Life cycle analysis results of resin production

Similarly, the environmental impact of lignin foam (Figure 4.7) shows that resin production has the highest contribution followed by TAEA amine crosslinker. In the ozone depletion impact category, PMHS blowing agent has almost 100% contribution. The reason for that is due to the use of a chlorinated compound for the synthesis of PMHS.

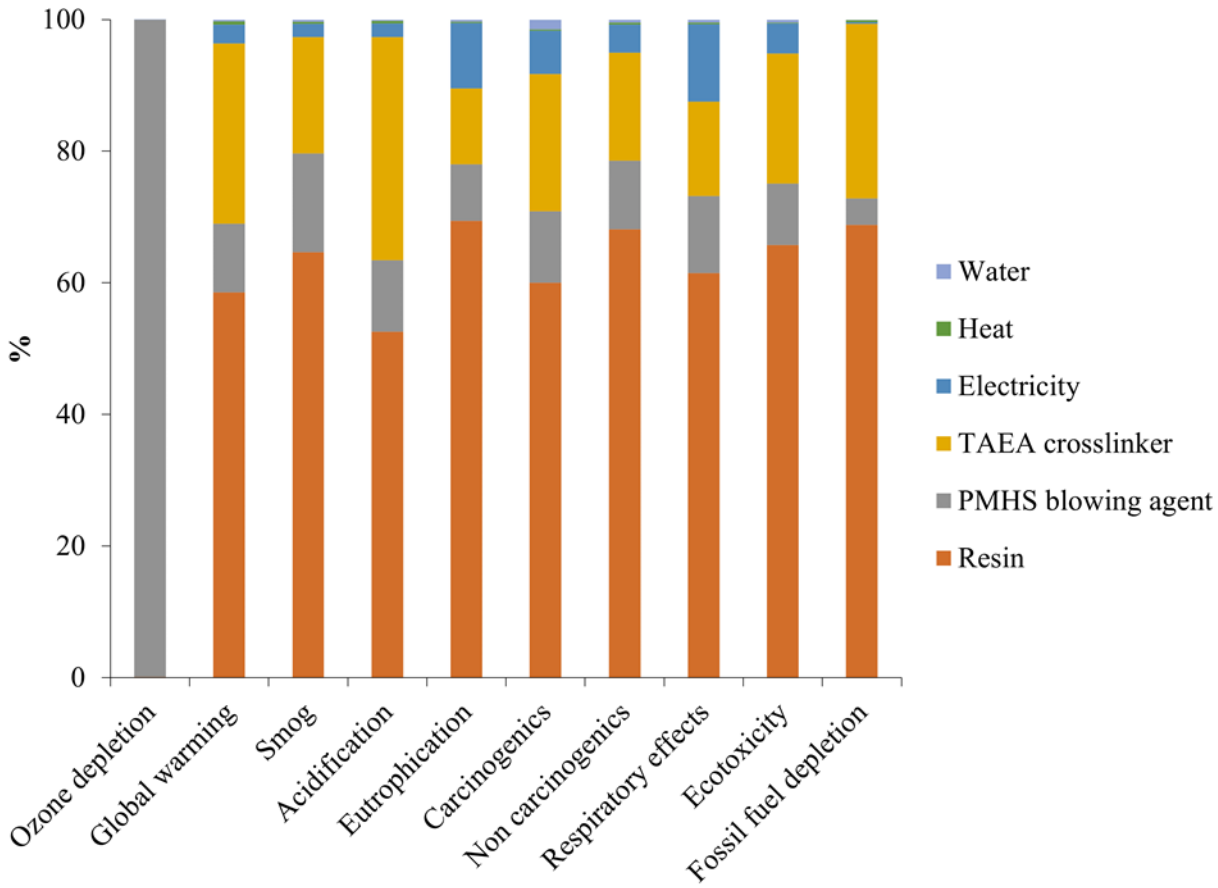

Figure 4.7. Life cycle analysis results of lignin-based foam production

Additionally, we compared the environmental impacts of lignin-based foam with commercial rigid polyurethane foam (Figure 4.8). The result shows that lignin-based foam performed better in all categories except ozone depletion and fossil fuel depletion. The greenhouse gas emissions of lignin-based foam and polyurethane foam are 5.67 kg CO2 eq. and 6.64 kg CO2 eq., respectively. The primary reason for the higher impact on ozone depletion was due to the use of PMHS while the higher impact on fossil fuel depletion was contributed mostly due to tBAA. This suggests that an environmentally better blowing agent and lignin functionalizing agent needs to be used. Diketene can be directly used in functionalizing lignin instead of tBAA, but diketene is toxic and difficult to handle. Another option for functionalizing lignin could be using an acetone adduct of diketene. In this case, acetone would be the by-

product instead of tBA. One advantage of using acetone adduct of diketene is a faster reaction rate which can reduce the overall reaction time for acetoacetylation. However, these new processes should further be analyzed to determine if they are economically and environmentally better alternatives. A previous study suggested LCA results are highly uncertain in ozone depletion and eutrophication categories [25]. We should also note that commercial production data were not used for all input chemicals as they were not available on the SimaPro database or in any other published reports. Life cycle inventory datasets for some chemicals in this study were created based on patents. This can generate some uncertainty as the processes on patents may not be fully optimized. However, the general trend from this study suggests the hotspots and areas of improvement for better environmental performance.

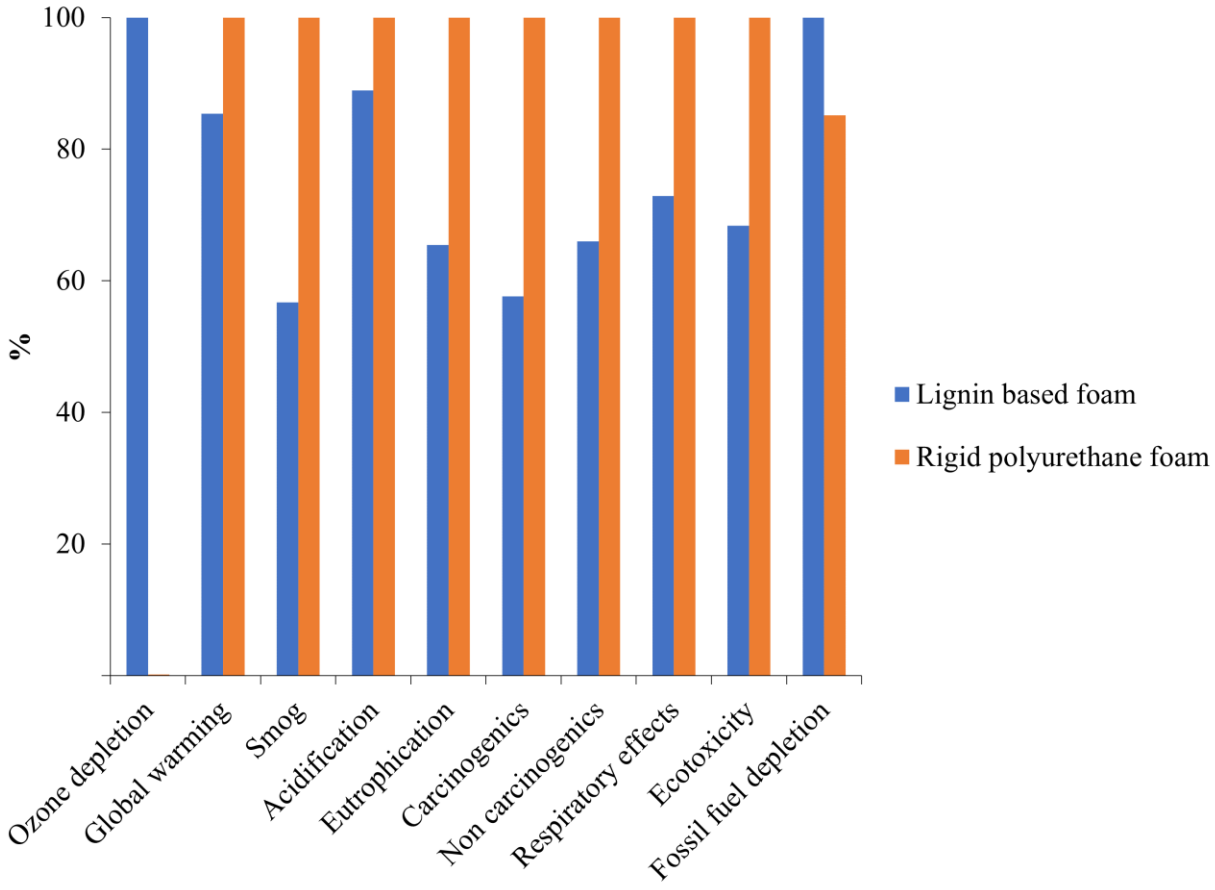

Figure 4.8. Life cycle analysis comparison of lignin-based foam and rigid polyurethane foam

4.4.5. Choice of functional unit

The TEA and LCA results can vary based on the functional unit we choose. For example, lignin-based foam has higher mass density compared to commercial foam. This means that for the same volume of foam, a higher mass of foam components is required for lignin-based foam. Density and thermal conductivity are important parameters of foam that dictate its commercial application and environmental performance during production [25]. Usually, in terms of application, foams are sold on a volume basis. The economic value and environmental performance will increase in the order of ratio between density of lignin-based foam and commercial foam in which case, both economic and environmental performance of lignin-based foam can be higher. Similarly, the result of life cycle analysis can vary based on the allocation method and criteria we use. In this study, we used mass allocation for all the calculations, but if we use economic allocation, the result can change. Given the higher economic value of foam compared to a by-product on a per unit mass basis, the environmental impact of lignin-based foam can be higher. Also, the analysis could vary if we considered a system expansion and assumed that the by-product produced can be used to replace the chemicals used in the synthesis of inputs.

4.4.6. Biobased content

The biobased content of this lignin-based foam is around 15% considering only lignin as biobased raw material input. This value increases to more than 30% when biobased 1,4-butanediol is used instead of fossil-based 1,4-butanediol. For reference, the USDA BioPreferred program requires the product to have at least 25% renewable biobased content to be certified as a biobased product. The use of biobased diol not only certifies it as a biobased product but can

improve its environmental performance. The life cycle environmental performance of biobased diol is better than fossil-based diol with a relative carbon footprint of <90% [26].

4.5. Conclusion

Economic and life cycle analyses of lignin-based foam were performed and compared with commercial rigid polyurethane foam. Lignin-based foam can be overall economically competitive and environmentally better than commercial foam in terms of mass basis. The economic analysis showed lower cost of production for lignin-based foam than commercial foam. Lignin functionalizing agent and crosslinker were the major contributors in both minimum selling price and environmental impacts. The price of lignin foam is highly sensitive to a functionalizing chemical and a crosslinker. However, the result is based on mass basis functional unit. If a different functional unit is chosen, the result may show a different pattern. For improving the process and product economic and environmental performance, a better lignin functionalizing chemical and crosslinker may be needed along with replacing the fossil-based diol with a biobased diol.

4.6. References

1. Dahiya S, Katakojwala R, Ramakrishna S, Mohan & SV (2020) Biobased Products and Life Cycle Assessment in the Context of Circular Economy and Sustainability. Materials Circular Economy 2020 2:1 2:1–28. https://doi.org/10.1007/S42824-020-00007-X
2. Mimini V, Kabrelian V, Fackler K, et al (2019) Lignin-based foams as insulation materials: A review. Holzforschung 73:117–130. https://doi.org/10.1515/HF-2018-0111
3. Bertella S, Luterbacher JS (2020) Lignin Functionalization for the Production of Novel Materials. Trends Chem 2:440–453

4. Alinejad M, Henry C, Nikafshar S, et al (2019) Lignin-Based Polyurethanes: Opportunities for Bio-Based Foams, Elastomers, Coatings and Adhesives. Polymers 2019, Vol 11, Page 1202 11:1202. https://doi.org/10.3390/POLYM11071202
5. Yang L, Wang X, Cui Y, et al (2014) Modification of renewable resources-lignin-by three chemical methods and its applications to polyurethane foams. Polym Adv Technol 25:1089–1098. https://doi.org/10.1002/pat.3356
6. Xue BL, Wen JL, Sun RC (2014) Lignin-based rigid polyurethane foam reinforced with pulp fiber: Synthesis and characterization. ACS Sustain Chem Eng 2:1474–1480. https://doi.org/10.1021/SC5001226
7. Li Y, Ragauskas AJ (2012) Kraft Lignin-Based Rigid Polyurethane Foam. Journal of Wood Chemistry and Technology 32:210–224. https://doi.org/10.1080/02773813.2011.652795
8. Merle J, Birot M, Deleuze H, et al (2016) New biobased foams from wood byproducts. Mater Des 91:186–192. https://doi.org/10.1016/J.MATDES.2015.11.076
9. Amaral JS, Sepúlveda M, Cateto CA, et al (2012) Fungal degradation of lignin-based rigid polyurethane foams. Polym Degrad Stab 97:2069–2076. https://doi.org/10.1016/J.POLYMDEGRADSTAB.2012.03.037
10. Luo X, Xiao Y, Wu Q, Zeng J (2018) Development of high-performance biodegradable rigid polyurethane foams using all bioresource-based polyols: Lignin and soy oil-derived polyols. Int J Biol Macromol 115:786–791. https://doi.org/10.1016/J.IJBIOMAC.2018.04.126

11. Lettner M, Hesser F, Hedeler B, et al (2020) Barriers and incentives for the use of lignin-based resins: Results of a comparative importance performance analysis. J Clean Prod 256:120520. https://doi.org/10.1016/j.jclepro.2020.120520

12. Bernier E, Lavigne C, Robidoux PY (2013) Life cycle assessment of kraft lignin for polymer applications. International Journal of Life Cycle Assessment 18:520–528. https://doi.org/10.1007/S11367-012-0503-Y

13. Zhang X, Jeremic D, Kim Y, et al (2018) Effects of Surface Functionalization of Lignin on Synthesis and Properties of Rigid Bio-Based Polyurethanes Foams. Polymers 2018, Vol 10, Page 706 10:706. https://doi.org/10.3390/POLYM10070706

14. Moretti C, Corona B, Hoefnagels R, et al (2021) Review of life cycle assessments of lignin and derived products: Lessons learned. Science of The Total Environment 770:144656. https://doi.org/10.1016/J.SCITOTENV.2020.144656

15. Webster D, Krall E, KM Sutko - US Patent 10 851,244, 2020 (2020) Acetoacetylated and (meth) acrylated lignin and thermosets therefrom

16. Cornille A, Dworakowska S, Bogdal D, et al (2015) A new way of creating cellular polyurethane materials: NIPU foams. Eur Polym J 66:129–138. https://doi.org/10.1016/J.EURPOLYMJ.2015.01.034

17. Cashdollar KL, Zlochower IA, Green GM, et al (2000) Flammability of methane, propane, and hydrogen gases. J Loss Prev Process Ind 13:327–340. https://doi.org/10.1016/S0950-4230(99)00037-6

18. Seavey KC, Khare NP, Liu YA, et al (2003) A New Phase-Equilibrium Model for Simulating Industrial Nylon-6 Production Trains. https://doi.org/10.1021/IE030112

19. Wooley RJ, Putsche V (1996) Development of an ASPEN PLUS physical property database for biofuels components. https://doi.org/10.2172/257362

20. Abbati De Assis C, Greca LG, Ago M, et al (2018) Techno-Economic Assessment, Scalability, and Applications of Aerosol Lignin Micro- and Nanoparticles. ACS Sustain Chem Eng 6:11853–11868. https://doi.org/10.1021/ACSSUSCHEMENG.8B02151

21. Finkbeiner M, Inaba A, Tan RBH, et al (2006) The new international standards for life cycle assessment: ISO 14040 and ISO 14044. International Journal of Life Cycle Assessment 11:80–85. https://doi.org/10.1065/LCA2006.02.002

22. SimaPro (2016) PRé Consultants. https://network simapro.com/esuservices

23. Humbird D, Davis R, Tao L, et al (2011) Process Design and Economics for Biochemical Conversion of Lignocellulosic Biomass to Ethanol: Dilute-Acid Pretreatment and Enzymatic Hydrolysis of Corn Stover. Golden, CO (United States)

24. Kulas DG, Thies MC, Shonnard DR (2021) Techno-Economic Analysis and Life Cycle Assessment of Waste Lignin Fractionation and Valorization Using the ALPHA Process. ACS Sustain Chem Eng 9:5388–5395. https://doi.org/10.1021/ACSSUSCHEMENG.1C00267

25. Manzardo A, Marson A, Roso M, et al (2019) Life Cycle Assessment Framework to Support the Design of Biobased Rigid Polyurethane Foams. ACS Omega 4:14114–14123. https://doi.org/10.1021/ACSOMEGA.9B02025

26. QIRA - Sustainability. https://www.myqira.com/qira-sustainability. Accessed 4 Feb 2022

CHAPTER 5. SCREENING OF SALT HYDRATES AND CELLULOSE NANOCRYSTAL COMPOSITES FOR THERMOCHEMICAL ENERGY STORAGE USING LIFE CYCLE ASSESSMENT[1]

5.1. Abstract

Salt hydrate systems via thermochemical reactions can provide thermal storage for renewable-sourced alternatives to traditional heating systems like natural gas. In this study, we use life cycle analysis (LCA) along with the material prices to screen salts based on environmental impact and cost. Additionally, we performed LCA of producing a composite material of salt and cellulose nanocrystals (CNC) at a weight ratio of four to one. CNC is a stabilizing agent for salt. We assessed the salt-CNC composites based on a laboratory scale and scaled-up processing to identify low environmental impact formulations and to identify high environmental impact processes in the composite production. In general, lanthanum chloride, lithium hydroxide, and lithium chloride should be avoided due to high environmental impact or cost. For pure salts, our results showed magnesium sulfate, zinc sulfate, and calcium chloride are typically preferred with a close second tier of magnesium and strontium chlorides and strontium bromide. For the composite material, magnesium sulfate was preferred followed by zinc sulfate, sodium sulfide, and strontium chloride. CNC has a significant environmental impact, contributing over 50% of the environmental impact for these composites. Therefore, CNC production with lower environmental impacts needs to be pursued. In composite production, the

[1] The material in this chapter was co-authored by Ramsharan Pandey, Ghasideh Pourhashem, and Adam C. Gladen. Ramsharan had primary responsibility for conceptualization, methodology, formal analysis, visualization, writing original draft, and review and editing. Ghasideh Pourhashem and Adam C. Gladen supervised and revised the work. This chapter is published in 'Sustainable Materials and Technologies' journal. To cite: Pandey, R., Pourhashem, G., & Gladen, A. C. (2024). Screening of salt hydrates and cellulose nanocrystal composites for thermochemical energy storage using life cycle assessment. Sustainable Materials and Technologies, 40, e00889. DOI: https://doi.org/10.1016/j.susmat.2024.e00889.

environmental impact of mixing and sonication can be reduced by scaling production. However, drying remains a high-impact process. These results can help guide salt selection for other salt-based thermochemical materials and further development of the salt-CNC composite.

5.2. Introduction

Residential heating is one of the major consumers of energy in the United States (US). In 2020, more than 95% of housing in the US used space heating equipment [1]. The major fuel sources for the residential areas included natural gas (48%) and electricity (42%). Water heating had a similar mix of fuel sources. Data on energy consumption in the year 2020 in the US showed that more than 42% of household energy consumption went to space heating while water heating consumed more than 18% [2]. Annual greenhouse gas emissions from household energy use in the US was 0.96 Gt CO2 eq/year in 2019 [3]. To reduce the environmental carbon footprint of burning fossil fuels for domestic heating, several alternatives have been explored. Among them, thermal energy storage (TES) systems to store energy from solar or other thermal systems, e.g. heat pumps, are one of the most promising ones.

TES includes sensible, latent, and thermochemical energy storage (TCES) systems [4]. Sensible heat storage utilizes the specific heat capacity of the storage material, i.e., energy is stored in the material through the absorption and release of thermal energy when its temperature increases or decreases. Latent heat storage utilizes the latent heat of fusion or vaporization, i.e., it primarily stores energy in changing the phase of the heat storage material. The main drawbacks of these two systems are that they require a large volume of space, have higher energy loss, and are not suitable for long-term heat storage. To overcome these challenges, TCES has been considered a viable option. Thermochemical heat storage stores energy in the enthalpy of a chemical reaction. One thermochemical reaction of interest for thermal loads in buildings is the

hydration and dehydration of salts. This system is based on the absorption and desorption of water molecules attached to hygroscopic compounds. Different hygroscopic salts have been tested for such thermochemical energy storage [5, 6]. The general working principle of energy storage by salts can be represented by equation 5.1.

$$Salt{\cdot}nH2O(s) + Heat \leftrightharpoons Salt(s) + nH2O(g) \quad (5.1)$$

Numerous salts, e.g., $MgSO_4$, $CaCl_2$, $SrCl_2$, LiOH, have been suggested for TCES applications and each of these salts has its advantages and disadvantages. Different factors such as energy density, reaction kinetics, thermal conductivity, cycle stability, and working temperatures have been studied previously [5]. One of the major concerns for the salt systems is their cycle instability. The salts tend to agglomerate, melt, or thermally degrade during cycling which reduces their functionality over time [7–9]. Different measures have been tested to improve salt stability including using blends of different salts, polymer membranes to immobilize salt particles, and using different porous host materials such as clay, expanded graphite, and carbon nanotubes [10–15]. Cellulose nanocrystals (CNC) have been used recently with salt particles to form a salt-CNC composite [16]. CNC is a rod-shaped nanomaterial with very high crystallinity and at least one dimension <100 nm [17]. These nanomaterials have been used in a wide array of applications including films, coatings, and sensors as precursor molecules, reinforcing agents, or rheology modifiers [18]. CNC can help to stabilize and enhance the energy storage ability of the salt-CNC composite over multiple cycles [16, 19]. CNC can stabilize salt particles by physical interlocking and interaction such that salt particles do not agglomerate, thus helping to provide more surface area for salt hydration.

To screen salts for energy storage applications, previous studies mostly considered the technical performance parameters such as energy density, stability, and reaction kinetics, e.g.,

[20]. However, the environmental impact of these materials is equally important from a sustainability standpoint and needs to be considered for the proper selection of materials. The production of salt composites can have significant environmental burdens that need to be considered. For example, CNC production is very energy-intensive [21]. Similarly, salts and other host materials or processes in the composite synthesis can also have high environmental burdens. To help ensure that early-stage technologies can promise a more sustainable alternative or to identify the product (or process) with the least environmental impact, performing a life cycle assessment (LCA) can be instrumental. To the best of our knowledge, there are no prior studies that compared different energy-storage salts based on environmental impacts. So, to overcome this research gap we focused on doing the LCA of different salt hydrates.

As to LCA for TES, there are only a few studies available. Most of those studies are focused on the system level for systems containing phase change materials [22–26] rather than on raw materials selection and development. In most cases, TES systems are used as auxiliary heating systems in conjunction with conventional systems such as natural gas heating [27]. TES systems with solar heating have been shown to lower environmental impacts compared to conventional heating systems [23, 24, 27]. One of the main reasons behind the lower environmental impact of TES systems is the use of renewable solar energy and minimal use of conventional energies during its operational phase. As such, it is during the manufacturing phase of the TES and the impact of the raw materials used in the fabrication of the system which are some of the major contributors to the system's environmental impact [24, 28, 29]. Thus, it is imperative to perform the LCA of different materials early in the product design stage to screen for the materials that have lower environmental impacts. With this in view, both prospective and anticipatory LCAs are important aspects to consider for emerging technologies to address data

uncertainty along with possible future trends given the market dynamics [30]. Therefore, the main objective of this study is to screen the salt-CNC composites for TCES applications by using LCA as a screening tool. This LCA screening analysis will help to identify process hotspots and composites with lower environmental impact and to guide future experimental work.

Ten different salts are considered in this analysis for the preparation of the composite. The salts identified for this study are $MgSO_4$, $CaCl_2$, $SrBr_2$, LiOH, Na_2S, $MgCl_2$, $SrCl_2$, $ZnSO_4$, $LiCl_2$, and $LaCl_3$ This selection is based on previous studies which have identified these salts as promising based on their technical performances such as energy density, stability, reaction kinetics, corrosiveness, and cost [20, 31, 32]. For example, N'Tsoukpoe et al. conducted a screening analysis of 125 different salts and identified $SrBr_2$, $LaCl_3$, and $MgSO_4$ based on their criteria (e.g. toxicity, theoretical energy density, max charge temperature of 105 °C) for heat storage for a micro combined heat and power system for households [20]. Ritcher et al. considered hundreds of theoretical anion-cation combinations for a thermochemical-based heat pump and suggested $SrBr_2$ based on their criteria such as reversibility, deliquesce point, and ability to discharge above 150 °C [32]. Clark et al. considered 41 salts and empirically tested 5 to identify $SrCl_2$ and Na_3PO_4 based on criteria such as energy density, cost, safety, and dehydration temperature below 100 °C [33]. Kubota et al. evaluated the theoretical performance of 30 salts and identified LiOH for low temperature (<100 °C) heat storage and utilization because of its high theoretical energy density while only needing one mole of water uptake per mole of salt [34]. Other salts identified as promising based on energy density were $ZnSO_4$, Na_3PO_4, and $Ba(OH)_2$. However, Na_3PO_4, and $Ba(OH)_2$ require high amounts of water uptake at 12 and 8 moles H_2O per mole of salt. van Essen et al. empirically investigated four different salts and identified $MgSO_4$ as promising due to its high energy density while the chlorides of $CaCl_2$ and

$MgCl_2$ had higher temperature lifts [9, 35]. Additionally, Rammelberg et al. recommended a blend of $CaCl_2$ and $MgCl_2$ based on improved stability compared to the individual salts [31]. Trausel et al. recommended $MgCl_2$, Na_2S, $CaCl_2$, and $MgSO_4$ based on the theoretical energy densities calculated from the enthalpies of formation and estimated the current material costs [36]. However, Na_2S has toxicity and corrosivity concerns [20]. LiCl has also been investigated because of its high energy density and relatively low recharge temperature [37, 38].

We will start our analysis with the LCA of CNC production followed by salt production. We will then examine the process of salt-CNC composite production. We will assess salts, CNC, and salt-CNC composites using different metrics including life cycle environmental impacts, cumulative energy demand, cost of materials, and weighted average of cost and life cycle environmental impacts. This study can provide a baseline for future studies that look at the sustainability aspect of different salt hydrates for thermochemical energy storage.

5.3. Methods

As shown by the overview diagram of Figure 5.1, the research methodology employed in this research includes an initial laboratory scale LCA process model followed by consideration of scale-up factors, and then a scaled-up LCA model. We considered process energy efficiency improvements (e.g. mixing, ultrasonication, and drying) as a scale-up factor along with the prices of the raw materials in our assessment. Based on these factors and our environmental life cycle model, we will suggest possible research directions for future work.

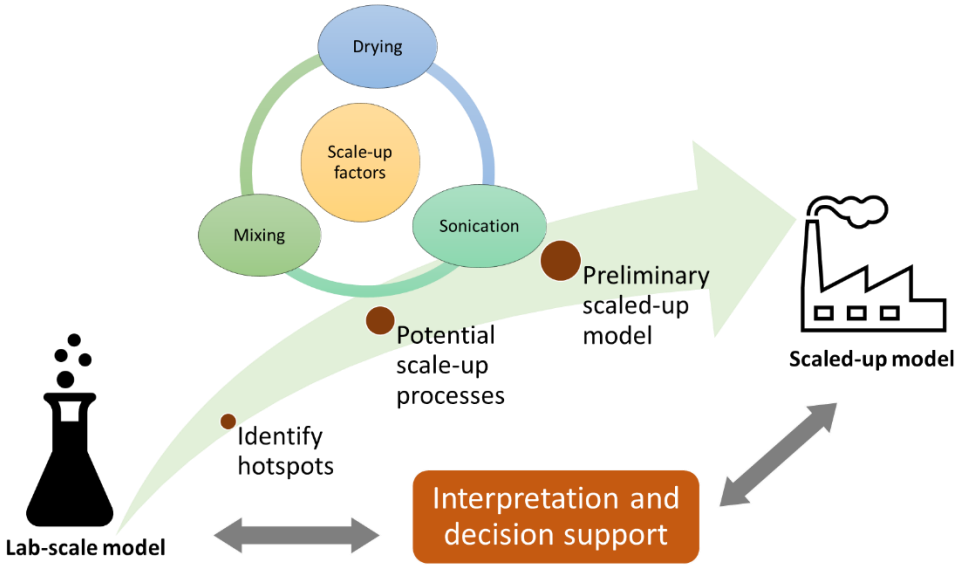

Figure 5.1. Framework in this research

5.3.1. Salt-CNC composite preparation

For the analysis, it is assumed that the CNC and salt were mixed at a weight ratio of 4:1 (salt-CNC). Other ratios, including 1:1, 2:1, and 10:1, were also tested in our previous study [16]. Our current experimental work indicated that 4:1 is a good salt-CNC ratio with consistent performance over multiple cycles, so we considered this ratio for the baseline model. However, the basic results presented here can be used as a roadmap for any composition variations. Additionally, the results for other ratios will scale between pure salt and CNC which are also presented. CNC is assumed to be produced in a standalone facility. The production model for CNC is based on Rajendran et. al. [39]. This study developed a scaled CNC production (100 tons per day) for wood pulp based on sulfuric acid hydrolysis. The authors considered both with and without acid recovery processes. In our study, we are using data from the acid recovery process. Sulfuric acid is recovered by separating the acid-water mixture from the hydrolyzed sugar mixture using a membrane filter and then using an evaporator. CNC is transported to a composite processing facility. The average transportation distance is assumed to be 1400 km similar to the

distance assumed for pulp transportation [21]. We did a quick analysis of the impact of transportation by varying the transportation distance by ±20%. We saw that it has minimal influence on the total environmental impact. The production model of salt-CNC composite is based on a laboratory study which is similar to a prior synthesis approach [19]. CNC is dispersed at 2.5% w/v in DI water and salt is dispersed at 10% w/v in DI water. A stirrer with a rated power consumption of 3.6 W is used to stir 10 g CNC in 400 ml water for 8 hours and the same stirrer is used for stirring 40 g of salt in 400 ml water. An ultrasonicator with a rated power of 1000 W is used to sonicate the same volume of each CNC and salt suspension for 5 minutes. For obtaining a mixture of salt-CNC, 5 g CNC dispersed in 200 ml water and 20 g salt dispersed in 200 ml water were mixed. The mixture of this salt and CNC is also stirred with the same power stirrer as previous processes. Drying of the salt-CNC composite is done using a dryer. The energy required for drying is calculated assuming 60% thermal efficiency [40, 41] of the dryer (e.g. convective air dryer) and based on the sensible energy required to heat water from 25 ℃ to 100 ℃ and then vaporize it as expressed by the enthalpy of vaporization. We considered 100 ℃ drying temperature because both biomass and salt hydrates are typically dried at temperatures near 100 ℃ [20, 33, 42]. The final salt-CNC composite is assumed to have 10% moisture. The laboratory scale mass and energy data, based on batches of 25g of CNC-salt material in 400 ml water, are linearly extrapolated to a per kg of salt or CNC basis. Therefore, for 1 kg of salt-CNC material, multiple smaller batches need to be processed due to the limitation of the lab equipment size. The scaled-up production analysis uses industrial-sized mixers and sonicators.

5.3.2. Life cycle analysis (LCA)

LCA of producing salt-CNC composite is performed following the ISO standard [43]. The mass and energy balances for CNC production are based on Rajendran et. al. [39]. LCA

modeling is used as a decision-making tool to guide the selection of salts and identify the environmental hotspots in the composite production process so that they can be minimized.

5.3.2.1. Goal, scope, and system boundary

The goal of this study is to explore the environmental impacts of the production of CNC, different hygroscopic salts, and salt-CNC composite. The process flow diagram of the salt-CNC production process (Figure 5.2) includes all the major steps in the production of CNC and salt-CNC composite. The system boundary for our analysis is cradle-to-gate which includes raw materials acquisition and all the processes up to the production of salt-CNC composite. Thus, the system boundary for our analysis ends at the composite production stage and the end use of the composite is not included in the analysis. Even though end-use and end-of-life are important considerations. An analysis that considers these aspects, i.e. cradle-to-grave, requires knowledge of aspects such as the long-term stability of the salt and salt-CNC composites, practical energy density, design of the overall system, achievable efficiency, etc. However, since these materials are still under development, these aspects are still under investigation. Therefore, we are focusing our analysis only up to the material production step. However, these results will still be valid and useful for future work when more data are available to evaluate thermochemical systems.

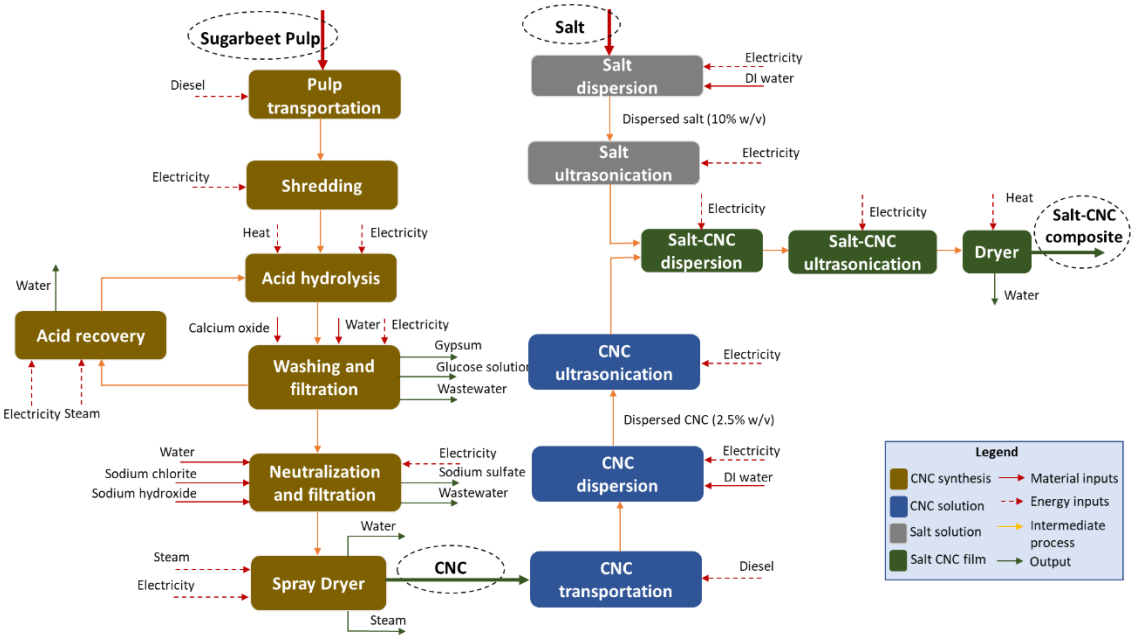

Figure 5.2. Process flow diagram of salt impregnation in cellulose nanocrystals (CNC production shown on the left is adapted from [39] while the composite production is based on our laboratory process)

5.3.2.2. Functional unit

Both mass and energy-based functional units are useful to the objectives of the study and are related (equation 2). We use the following convention for functional unit:

- CNC – mass-based functional unit
- Salt – primary functional unit is on an energy-stored basis
- Salt-CNC composite – primary functional unit is on an energy-stored basis

The salt and salt-CNC are considered primarily on an energy basis because the function of the salt-CNC composite is to store thermal energy. However, when discussing pure CNC, a mass-based functional unit must be used, because it is conservatively assumed to have an energy density of 0 kJ/kg (even though CNC is hydrophilic [44] and thus may participate in the reaction). The mass-based results for the salt and salt-CNC are provided in the supplemental material. These are provided because the produced salt or composites will potentially be sold in

terms of mass. Also, presenting the LCA results in terms of mass-based functional unit allows it to easily be converted to energy-based unit for different systems.

For a mass-based functional unit, 1 kg of product (salt, CNC, or salt-CNC) is used while for the energy-based functional unit, we use 1 MJ theoretical energy stored by the product. The conversion from mass-basis to energy-basis is based on dividing the mass-basis values by the theoretical gravimetric energy density of the material (gravimetric energy density for each salt hydrate reaction and composite is given in Table 5.2) as given by equation 2.

$$(Life\ cycle\ impact)_{energy-basis} = \frac{(Life\ cycle\ impact)_{mass-basis}}{Theoretcial\ Gravimetric\ Energy\ Density} \quad (2)$$

The theoretical energy density is used in equation 2 because it provides a consistent basis for comparison since the achieved energy storage capacity in a system depends on factors, e.g. system design and mode of operation, not considered in the current analysis due to the ending system boundary for the LCA being the composite production stage.

5.3.2.3. Inventory collection and impact assessment

The mass and energy data for producing CNC is based on Rajendran et. al. [39]. The energy and chemical inputs in the model are from different databases (Table 5.1).

Similarly, the data for salts are taken from databases and other published literature (Table 5.2). For lanthanum chloride, lanthanum oxide is considered a proxy because it is available in the database while lanthanum chloride is not. However, lanthanum chloride can be produced by reacting lanthanum oxide either with ammonium chloride or hydrochloric acid [45]. So, due to the extra step, the environmental impacts are likely underestimated for lanthanum chloride. The theoretical energy density of the salts is also included in Table 5.2. For salt-CNC composites, the energy density only accounts for the amount of salt present in the composite. Thus, the energy storage ability of the composite scales proportionately according to their ratio, i.e., as the ratio of

salt-to-CNC decreases or increases, the energy storage value approaches the value of pure CNC or pure salt, respectively.

Table 5.1. Inventory of salt-CNC composite production

#	Inputs	Unit	Value	Source
1 kg CNC production [39]				
1	Bleached kraft pulp	kg	1.98	USLCI - at mill
2	Pulp transportation	tkm	77.9	USLCI - combination truck, 100% diesel
3	Sulfuric acid	kg	1.73	USLCI - at plant
4	Water	kg	95.88	Ecoinvent 3 - RoW
5	Sodium hydroxide	kg	0.02	USLCI - at plant
6	Calcium oxide	kg	0.96	USLCI – at plant
7	Sodium chlorite (sodium chlorate used as a proxy)	kg	0.01	Ecoinvent 3 - RoW
8	Steam, in chemical industry	kg	29.49	Ecoinvent 3 - Global
9	Electricity, medium voltage, US average	kWh	3.47	Ecoinvent 3, US average
1 kg Salt-CNC composite production (lab scale process)				
10	CNC	kg	0.2	
11	Electricity, medium voltage, US average	kWh	8.972	Ecoinvent 3, US average
12	Heat, natural gas, US only	kWh	18.94	Ecoinvent 3, US average
13	Water	kg	16	Ecoinvent 3 - RoW
14	Salt	kg	0.8	

USLCI – United States Life Cycle Inventory; RoW – Rest of the World

The impact assessment of CNC, salt, and composite production is conducted in SimaPro v8.3 using the Tool for Reduction and Assessment of Chemicals and Other Environmental Impacts (TRACI II) method developed by the United States Environmental Protection Agency (US EPA). TRACI II method has 10 different impact categories:

- ozone depletion,
- global warming,
- smog,

- acidification,
- eutrophication,
- carcinogenics,
- non-carcinogenics,
- respiratory effects,
- ecotoxicity,
- fossil fuel depletion

Table 5.2. The data source for LCA and theoretical energy density of different salts

#	Salt	Inventory source	Theoretical energy density (kJ/kg)	Energy density source	Salt-CNC (4:1) energy density (kJ/kg)*
1	Magnesium sulfate ($MgSO_4$)	Ecoinvent 3 - RoW	1667 ($MgSO_4 \cdot 7H_2O \rightarrow MgSO_4$)	[46]	1334
2	Calcium chloride ($CaCl_2$)	Ecoinvent 3 - RoW	842 ($CaCl_2 \cdot 2H_2O \rightarrow CaCl_2$)	[46]	674
3	Strontium bromide ($SrBr_2$)	[47]	947 ($SrBr_2 \cdot 6H_2O \rightarrow SrBr_2$)	[20]	758
4	Lithium hydroxide (LiOH)	Ecoinvent 3 - Global	1440 ($LiOH \cdot H_2O \rightarrow LiOH$)	[34]	1152
5	Sodium sulfide (Na_2S)	Ecoinvent 3 - Global	1786 ($Na_2S \cdot 5H_2O \rightarrow Na_2S$)	[20]	1429
6	Magnesium chloride ($MgCl_2$)	[48]	1253 ($MgCl_2 \cdot 6H_2O \rightarrow MgCl_2$)	[20]	1002
7	Strontium chloride ($SrCl_2$)	[49]	1282 ($SrCl_2 \cdot 7H_2O \rightarrow SrCl_2$)	[20]	1026
8	Zinc sulfate ($ZnSO_4$)	Ecoinvent 3 - RoW	1747 ($ZnSO_4 \cdot 7H_2O \rightarrow ZnSO_4$)	[50]	1398
9	Lanthanum chloride ($LaCl_3$) (La_2O_3 used as a proxy)	Ecoinvent 3 - RoW	958 ($LaCl_3 \cdot 7H_2O \rightarrow LaCl_3$)	[20]	766
10	Lithium chloride (LiCl)	Ecoinvent 3 - Global	1030 ($LiCl \cdot H_2O \rightarrow LiCl$)	[20]	824

RoW – Rest of the World; *conservatively assumes gravimetric energy density of CNC is zero

We also performed cumulative energy demand (CED) analysis of the salts and composites following the method by Ecoinvent version 2 which is available in SimaPro as well. This method uses the higher heating values (HHV) of the inputs.

To help screen the salts and salt-CNC pairs at the scaled-up production level, we also compared salt-CNC pairs using different metrics. The metrics included i) the cost and global warming potential (GWP) per MJ, ii) the weighted average of cost and GWP, and iii) the weighted average of cost and all the environmental impacts. The cost of each salt is given in Table S1 in Supporting Information. The cost of each composite is calculated by considering just the cost of salt and CNC. The choice of salt-CNC pairs was ranked using a single metric based on the weighted average of cost and GWP of each salt-CNC composite. We chose GWP as the main environmental metric because it is the most widely used metric for environmental assessment and is easy to relate with most other systems. We first calculated the normalized value of the costs of each composite (based on the cost of salt and CNC) on a scale of 0 to 100 wherein the material with the highest cost is set to 100. We also normalized the value of global warming potential for each composite pair on a scale of 0 to 100. We considered a series of different weighting factors between cost and GWP at 25% increments, e.g. 100% cost-0% GWP, 75% cost-25%GWP. The weighted average is then calculated using Equation 3.

$$Weighted\ avearge = \frac{Weighing\ factor \times normalized\ cost + Weighing\ factor \times normalized\ GWP}{100} \quad (3)$$

Once we calculated the weighted average values for all the salt-CNC pairs, we created a point plot with each point representing a different weighting factor distribution. Ideally, the composite will have a low value for the points and a small spread between points. The plot can also be used for a single set of weighting factors, e.g. only comparing the 50% cost-50% GWP points if both are considered equally important. We also considered all the life cycle

environmental impacts for salt-CNC, instead of just global warming potential, in the calculation of weight average values. The normalized value for LCA impacts was calculated considering all the impact categories with equal weights. Thus, if the overall environmental impact is weighted at 50%, each of the ten categories has a weighting of 5%. The weighted average is then calculated as described for the weighted average of cost and GWP.

5.4. Results and discussion

5.4.1. CNC production

Based on the mass and energy balance of CNC production from Rajendran et. al. [39], we performed the LCA of CNC production. Our LCA results varied from [39] results (LCA results in SI Figure S1). The reason for the slight variation in our results is due to possible updates in the newer versions of the database and the geographical differences in the inputs. The LCA result showed a high global warming impact (16.04 kg CO_2 eq/kg CNC) for producing CNC compared to producing the salts which is in the range of 0.5 – 15 kg CO_2 eq/kg salts. The major contributor in each impact category as shown in Figure S1 included steam and electricity. A large amount of electricity is consumed in the membrane filtration process while a large amount of steam is consumed in sulfuric acid recovery. Kraft pulp is also one of the major hotspots in the CNC production process. Other studies have also conducted the life cycle assessment of nanocellulose production, though most of them are for lab-scale processes (Table 5.3). The global warming potential (GWP) of nanocellulose production reported in those studies varied between 11 to 1100 kgCO_2 eq/kg of nanocellulose. This large range in the results is due to the differences in the system boundary considered in different studies as well as process differences. However, CNC production is energy and chemical-intensive.

Table 5.3. Different LCA studies on nanocellulose

#	Cellulose source	Method	Global warming potential ($kgCO_2$ eq/kg)	Scale	Reference
1	Carrot waste	Enzymatic depolymerization and homogenization	96	Lab	[51]
2	Wood pulp	*TOHO	190	Lab	[52]
		*CESO	1160	Lab	
		*CEHO	360	Lab	
		*TOSO	980	Lab	
3	Coconut and cotton fibers	Sulfuric acid hydrolysis	Coconut fibers – 1086 Cotton fibers – 122	Lab	[53]
4	Wood pulp	-Enzymatic production -Carboxymethylation -No pretreatment		Lab	[54]
5	Wood pulp (USDA FPL)	Sulfuric acid hydrolysis	29.64 (CED – 992.7 MJ/kg)	Pilot	[21]
6	Sugarcane bagasse	Sulfuric acid hydrolysis	13.7 -16.7	Lab	[55]
7	Wood pulp	Sulfuric acid hydrolysis	11.39 – with acid recovery 11.18 – without acid recovery	100 MT/day	[39]

*TOHO: TEMPO oxidation with homogenization; *CESO: Chloroacetic acid etherification with sonication; *CEHO: Chloroacetic acid etherification with homogenization; *TOSO: TEMPO oxidation with sonication

5.4.2. Salt production

Lanthanum chloride has the highest contribution in all the impact categories (Appendix D Figure D3). This high impact is because lanthanum chloride is produced from a rare earth metal lanthanum. Due to the high environmental impact of lanthanum chloride, Figure 5.3 presents the environmental impact of the other salts while excluding lanthanum chloride. Lithium hydroxide and lithium chloride have a higher impact in most of the impact categories compared to the rest of the salts. One reason lithium-containing salts have a higher environmental impact is due to the

higher energy required for the extraction of lithium. Lithium is extracted from many rare minerals [56]. Based on the result, magnesium sulfate, calcium chloride, strontium bromide, and zinc sulfate have the lowest impacts compared to other salts in most of the categories. Magnesium sulfate performs the best in all impact categories. It has the best performance because, on a mass basis, magnesium sulfate has a fairly low impact, and it has a high energy density. Higher energy-density salts require less material to achieve the same storage capacity, i.e., 1 MJ of storage. Thus, if the material has a low environmental impact to produce a unit mass of it and then small amounts of material are needed to store 1 MJ due to high energy density, the overall environmental impact on an energy basis will be low. As such, a typical feature of low environmental impact salts is the environmental abundance of the anions and cations (e.g. magnesium, calcium, sulfur) and high energy density. Note: LCA results of salts on a mass basis are given in Supporting info.

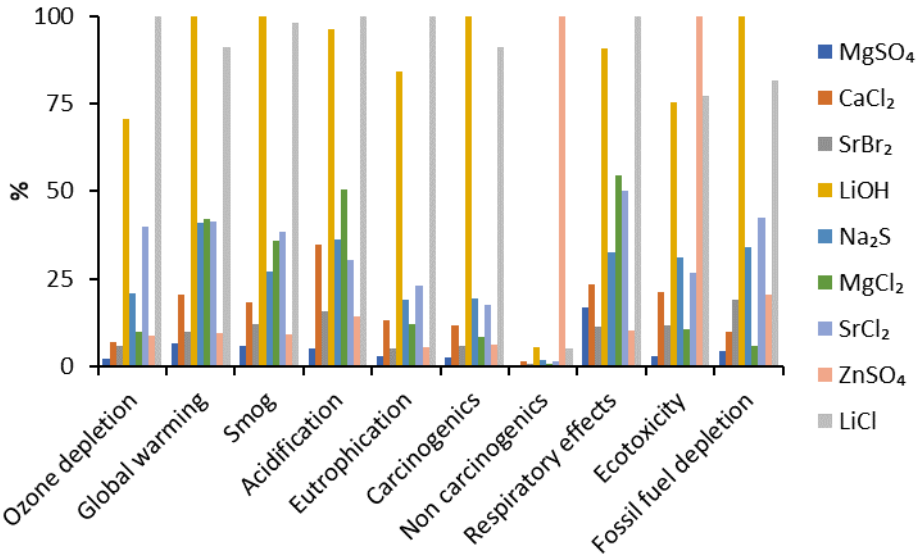

Figure 5.3. Comparison of LCA results of different salts based on theoretical salt energy density

5.4.3. Salt-CNC composite – Lab Scale

Based on the laboratory scale data, we performed LCA of salt-CNC production. Similar to the results for pure salts, composites containing magnesium sulfate, zinc sulfate, and sodium sulfide show the least global warming potential impact. The second tier includes strontium chloride, magnesium chloride, and lithium hydroxide. One major observation from the result is that, since the environmental impact of CNC production is higher than the salts (Appendix D Figure D4), the impact is also higher for the composite per MJ when the composite contains salt with lower energy density. As discussed with pure salts, lower energy density for the salt means that to achieve the same energy capacity (i.e. 1 MJ), more composite material is needed, and thus more CNC material is used. Thus, salts with lower theoretical energy density such as calcium chloride have a relatively high environmental impact when combined with CNC. Lanthanum chloride has the double drawback of low energy density and the salt itself having a high environmental impact. Therefore, it is important to reduce the use of CNC in the composite (in terms of percent weight) while maintaining high energy density. However, the effect that reducing the CNC has on other parameters such as cycle stability of the composites should also be considered while continuing to develop the material. Having a higher percent weight of CNC in the composite may increase the lifetime of the composite which may counteract some of the impact of initial production.

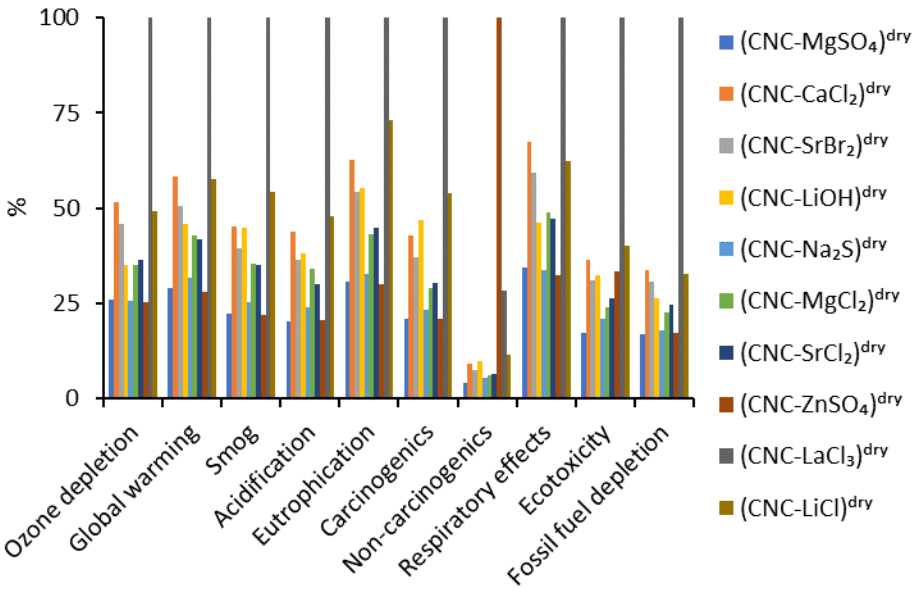

Figure 5.4. LCA result of salt-CNC composite on energy-basis

The global warming potential of different salt-CNC composites based on per MJ energy stored shows that magnesium sulfate has the least impact and lanthanum chloride has the highest impact (Figure 5.5). The major hotspots in the lab scale production of the salt-CNC composite are energy used in dispersion and CNC use. Lab scale processes for mixing and ultrasonication of salt, CNC, and salt-CNC mixtures in DI water are not optimized and thus use high amounts of energy. Drying is also a significant hot spot because water has a high enthalpy of vaporization and a significant amount of water must be removed to take the material from suspension to ten percent moisture content.

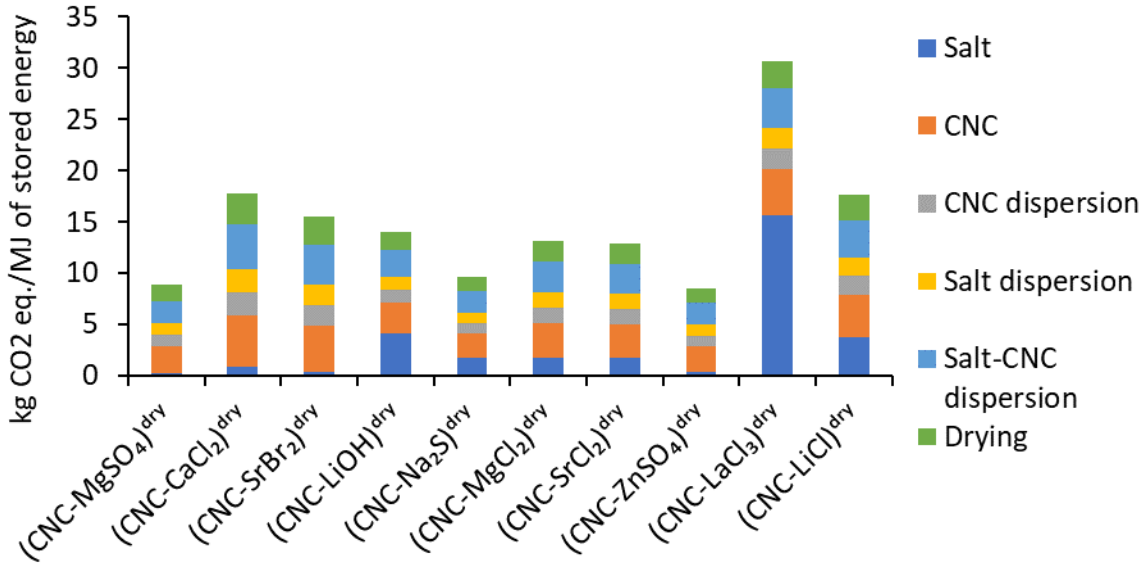

Figure 5.5. Global warming potential comparison of different salt-CNC composites on energy-basis

5.4.4. Scale-up and industrial processing

The data for CNC processing used here is based on a process model from Rajendran et. al. [21] which was modeled for a 100 ton/day processing capacity. We used an acid recovery case. Acid recycling can be beneficial, but it also requires additional energy and capital costs [21]. CelluForce Inc. (Canada) and Melodea Ltd. (Israel) commercially produce CNC while using acid recovery systems, however, they have not disclosed the details of their technology publicly [57, 58]. Since the technology for the production of CNC is still in the early stage, there is still room for improvement in terms of reducing the cost and environmental impacts of CNC production. These improvements should be actively pursued.

Our results from the lab scale process to fabricate the salt-CNC composite (Figure 5.5) showed that energy for mixing, ultrasonication, and drying are the major hotspots in composite production. We considered the energy requirement for mixing and sonication based on laboratory data. The process is not optimized, and the energy requirement can be significantly higher compared to a commercial-scale facility. Since mixing and sonicating are hot spots based

on the lab-scale data, we looked at industrial-scale mixers and sonicators to understand their energy consumption in large-scale processes. Based on the data (Figure 5.6), we found that the energy for mixing, and sonication can be reduced by more than an order of magnitude.

Drying is another energy-intensive process that needs to be considered for scaled-up analysis. For our lab scale process analysis, we modeled convective air drying with 60% efficiency [41]. For scaled-up production, we also considered different potential drying technologies that can be used for drying the salt-CNC composite. The candidates for drying can be conventional convective force drying, spray drying, and freeze drying [59].

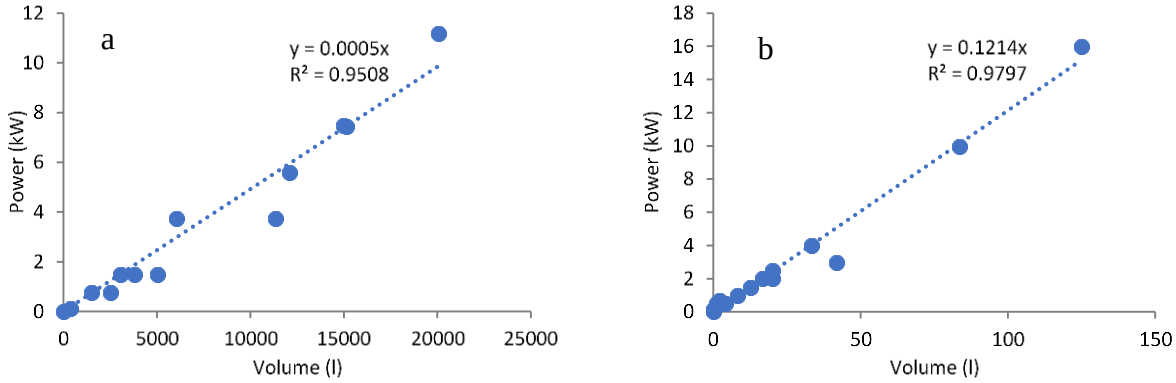

Figure 5.6. Relationship between volume processing and power requirements for (a) mixers (Data from IKA[60] and Reciprotor[61]), (b) sonicators (Data from: Hielscher[62] and Qsonica[63])

Using convective forced-air drying may not be practical for large scale due to its slower operation. While less efficient, spray drying can be a potential solution due to its higher throughput. Spray drying has been used for drying CNC [64]. However, the stability of salt-CNC after drying and its impact on the morphology due to higher temperature operation would need to be assessed [59]. Freeze drying is another option, however, the process is slower, energy-intensive, and expensive [59]. Thus, for our scaled-up process, we used a spray dryer due to its higher throughput capability and ability to handle higher moisture content compared to a convective dryer. The energy required for operating a spray dryer is based on the model from a

previous study [65]. The energy required is calculated based on the capacity of dryers. Based on Baker et. al., the fuel energy consumption on average for industrial-scale dryers comes to around 4.87 GJ/ton of water evaporated. The electrical energy required to operate the dryers is calculated based on the fuel energy consumption of the dryer. Fuel energy consumption on average is 27 times higher than electricity consumption.

5.4.5. Salt-CNC – Scaled-up

We scaled up our lab scale model to a larger scale capacity with 10-ton-per-day composite production. For a scaled-up model (using a scaled-up mixer, sonicator, and spray dryer), we see a significant reduction in global warming impact (Figure 5.7) (similar reductions were obtained in the other impact categories as well, but not shown here). The reduction is primarily driven by significant reductions in energy required for the mixing and dispersion process. With this new result, the hotspots are the CNC, the drying process, and the salts. Reduced use of CNC or improvements in CNC production can significantly reduce the overall environmental impact. As a new material, the production of CNC likely is not as efficient as the salts which are more mature and produced at greater scale. The drying process is one of the major hotspots. Even when convection drying is used instead of spray drying for scaled-up production, drying is still a major hotspot. Therefore, drying significantly influences the magnitude of environmental impacts. For our analysis, we used natural gas as a heat source and grid electricity as an electrical energy source. However, alternatives with lower environmental impact are possible. For example, co-locating the composite production facility with another industrial facility with sufficient waste heat and using the exhaust heat from that facility to dry the material would greatly reduce the environmental impact.

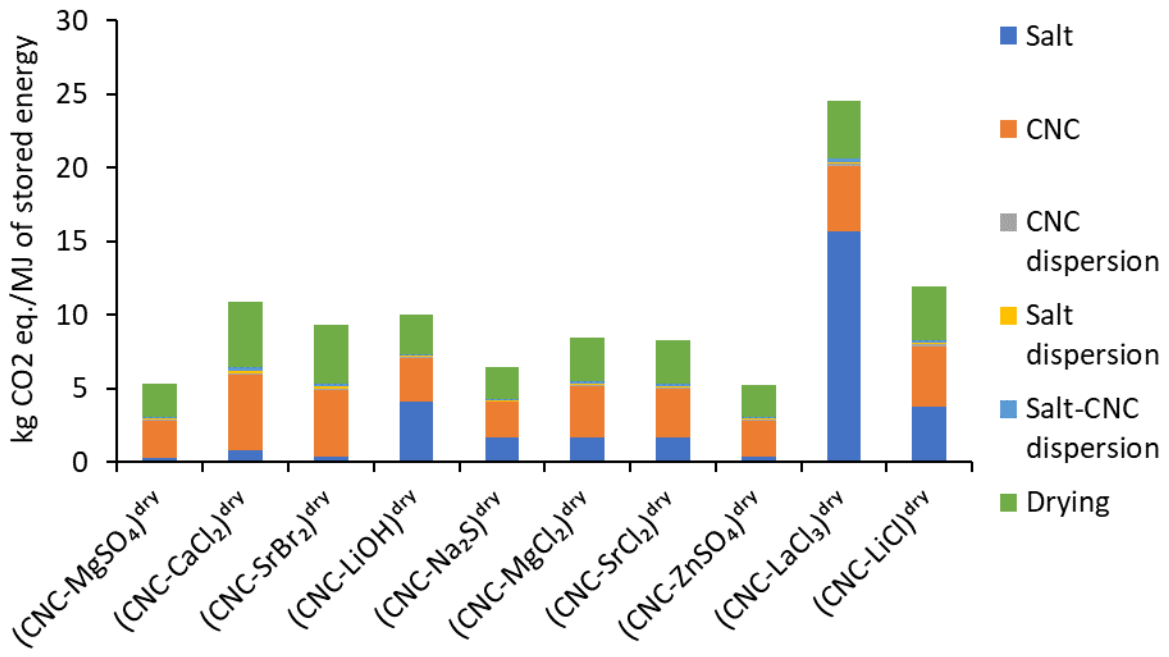

Figure 5.7. Global warming potential comparison of different salt-CNC composites

The comparison of global warming potential between the lab-scale model and industrial-scale model is shown in Table 5.4. It demonstrates the significant benefits obtained at larger-scale production.

Table 5.4. Comparison of global warming potential of salt-CNC composites based on per MJ of composite material for lab and industrial scale

S. No.	Salt-CNC composite (4:1 %w/w ratio)	GWP of salt-CNC composite (kg CO2 eq./MJ energy of composite)	
		Laboratory scale	Industrial scale
1	Magnesium sulfate ($MgSO_4$)	8.83	5.35
2	Calcium chloride ($CaCl_2$)	17.81	10.92
3	Strontium bromide ($SrBr_2$)	15.49	9.36
4	Lithium hydroxide (LiOH)	14.03	10.00
5	Sodium sulfide (Na_2S)	9.69	6.44
6	Magnesium chloride ($MgCl_2$)	13.13	8.50
7	Strontium chloride ($SrCl_2$)	12.84	8.31
8	Zinc sulfate ($ZnSO_4$)	8.57	5.25
9	Lanthanum chloride ($LaCl_3$)	30.61	24.56
10	Lithium chloride (LiCl)	17.61	11.98

5.4.6. Cumulative energy demand (CED) analysis of salt-CNC composites

CED or embodied energy represents the amount of energy that is required throughout the life cycle of the product manufacturing. Figure 5.8 provides the mass-based CED of CNC and compares it to different salts. CNC and lanthanum chloride have very high energy requirements for their production. For CNC production, significant energy is consumed in the production of steam and electricity, followed by pulp production and transportation. For lanthanum chloride, the major energy consumption comes from the chemicals used during their production. We also see that lithium-containing salts and sodium sulfide also have higher energy requirements compared to other salts. For lithium-containing salts, the major contribution comes from lithium carbonate production while for sodium sulfide, the production of sodium sulfate has the highest energy demand. Magnesium sulfate, strontium bromide, and calcium chloride have the least energy demand for their production because of simpler production processes, and less use of energy and harsh chemicals.

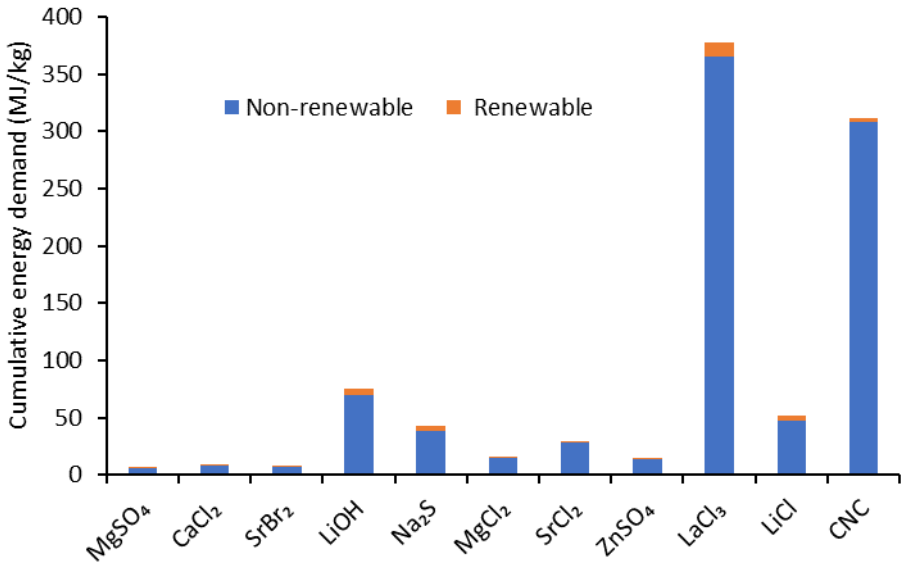

Figure 5.8. CED of different salts and CNC on a mass basis

The energy-based CED result of different salts (Figure 5.9a) shows that magnesium sulfate is the best-choice salt followed by zinc sulfate and strontium bromide. Conversely, lanthanum chloride, lithium hydroxide, and lithium chloride have the highest CED per MJ of stored energy of the salt. These three have significantly higher CED than the other salts. Lithium hydroxide and lithium chloride have double the CED of the next highest salt while lanthanum chloride is a different order of magnitude. Based on these we can rank the choice of salts into three different tiers: magnesium sulfate, zinc sulfate, strontium bromide, calcium chloride, and magnesium chloride as the first tier; sodium sulfide and strontium chloride as the second tier; and the rest of the salts as the third-tier choices. The energy-based CED of different salt-CNC composites for the scaled-up production process (Figure 5.9b) shows that magnesium sulfate and zinc sulfate are the best-choice salts followed by sodium sulfide. Second-tier composites are magnesium chloride, strontium chloride, and lithium hydroxide. The main reason for the better performance of these salt composites is their higher energy density. For the same unit of theoretical energy storage capacity (1 MJ), the total required amount of composite material depends on the energy density of the composite. While the mass ratio of salt-to-CNC is the same in all the formulations, composites containing higher energy density salts require less total composite material to achieve 1 MJ of storage capacity and thus less total amounts of CNC. Since CNC has such a high CED relative to most salts, differences in the energy densities of the composites can make significant changes in the composite CED. For example, sodium sulfide ranks as the seventh-choice salt, but due to its high energy density, the sodium sulfide-CNC composite is ranked as third based on CED.

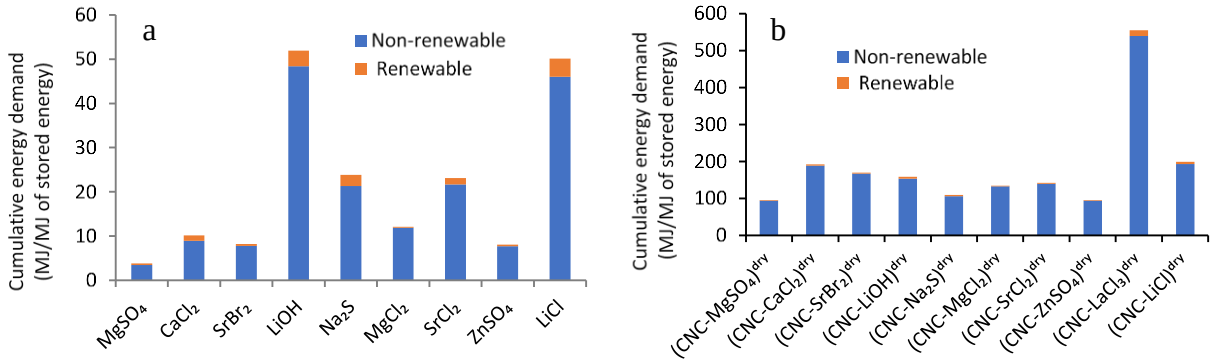

Figure 5.9. Ratio of CED and energy density of different (a) salts (lanthanum chloride not shown because of very high ratio – 395), (b) salt-CNC composites

5.4.7. Screening of salt-CNC pairs

The comparison of global warming potential and the cost of different salts (Figure 5.10) shows that lanthanum chloride, lithium hydroxide, and lithium chloride can be ruled out for future studies based on the cost and global warming potential. Lanthanum chloride has a very high global warming potential while lithium hydroxide is very costly. Lithium chloride has the second-highest global warming potential. Calcium chloride has a very low cost, but its energy density is lower than most of the other salts. Lithium hydroxide and strontium bromide are the most expensive salts while calcium chloride is the least expensive.

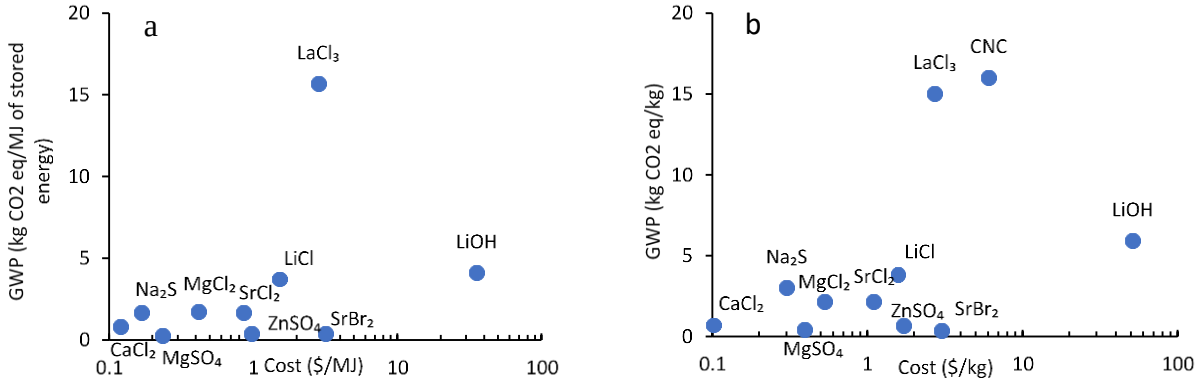

Figure 5.10. Cost and global warming potential comparison of different salts on, (a) energy basis, (b) mass basis (to compare to CNC)

As we see in Figure 10b, CNC has a high global warming potential compared to all other salts. It is important to reduce the use of CNC in the formulation to improve its environmental

performance. Additionally, cost-effective and lower environmental impact processes for CNC production should be actively pursued. Although CNC has a higher environmental impact, it has the important functionality of improving the stability of salt-CNC composites over multiple hydration-dehydration cycles. The impact of using CNC on the long-term stability and practical storage efficiencies of salt-CNC composites is currently under investigation. If the CNC significantly extends the lifetime of storage material, the added advantage of the extended lifetime may offset the one-time production impacts. Therefore, future studies can consider extending the system boundary of the LCA analysis to include the operational phase performance of the composite materials once more data are available. This analysis will help to determine the tradeoffs between CNC composition and the lifetime impact of the composite.

Magnesium sulfate and sodium sulfide are the best-performing salt-CNC composites based on the comparison between the GWP and the cost of the salt-CNC composite (Figure 5.11). In general, the major impact on the performance is influenced by the total amount of CNC needed. However, salts such as lithium hydroxide and lanthanum chloride which have cost or global warming potential of similar or greater magnitude also significantly contribute to the results for the composites. The salts with higher energy density have better performance due to a lower total amount of CNC.

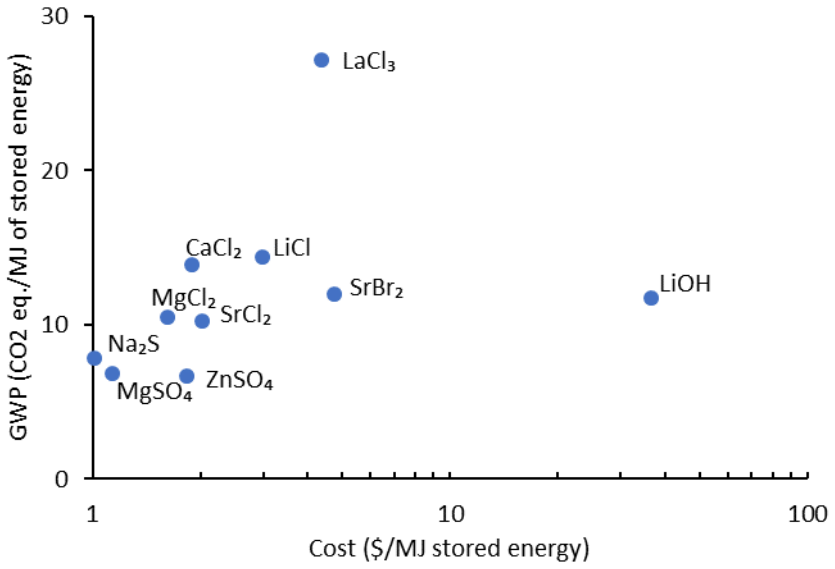

Figure 5.11. Global warming potential cost (per MJ of salt) comparison of different salt-CNC composites

The results of ranking based on weighted average cost and GWP (Figure 5.12a) show that CNC-$MgSO_4$, CNC-$ZnSO_4$, and CNC-Na_2S are the first-choice salts. However, Na_2S is corrosive [20] and ZnSO4 can contaminate soil and water [66], thus they must be used with care and are likely not recommended to use for these applications. So, among these salts, MgSO4 would present a better choice. Second choice salts are CNC-$CaCl_2$, CNC-$MgCl_2$, CNC-$SrCl_2$, CNC-$SrBr_2$, and CNC-LiCl. CNC-$LaCl_3$ and CNC-LiOH are the worst-choice salts, so they can be ruled out for future consideration.

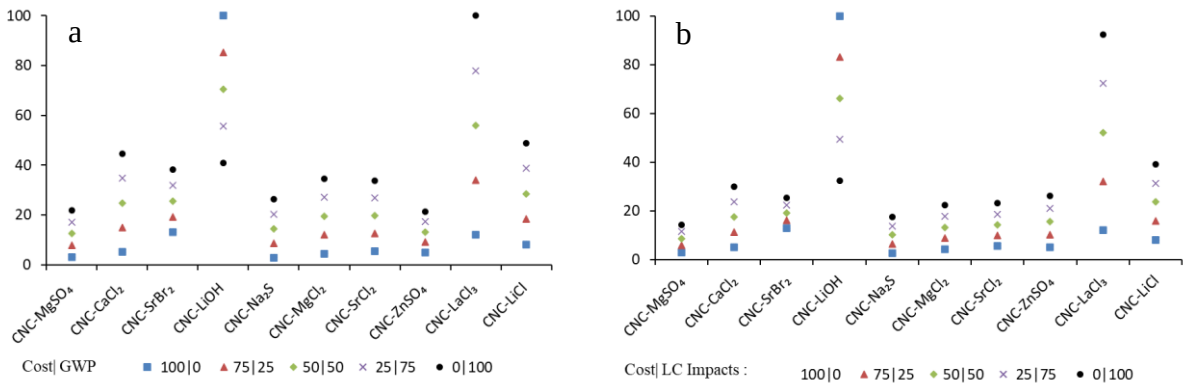

Figure 5.12. Ranking of salt-CNC pairs based on (a) weighted average cost and global warming potential, (b) weighted average cost and 10 different life cycle impact indicators

A similar trend was observed when ranking the salts-CNC pairs considering cost and all the 10 impact categories of LCA (Figure 5.12b). We noticed a similar trend in our results as we saw in Figure 5.12a with the same salts in the respective tiers except with ZnSO4 placed into the second tier due to having high contributions from the non-carcinogenics and ecotoxicity categories.

Similar point plots for just salts are given in Supporting Information (Appendix Figure D11 and D12). In Figure D11, when considering cost and GWP, magnesium sulfate, zinc sulfate, and calcium chloride have a narrower spread. These three salts have low environmental impacts and relatively lower costs than other salts, and thus represent the top tier. Excluding LiCl, LiOH, and LaCl3, the other salts can be grouped in a second tier. Lithium hydroxide and lanthanum chloride have a wider spread and are the least recommended salts. Considering all the impact factors (Figure D12), magnesium sulfate is the first choice. The second tier consists of calcium chloride, zinc sulfate, strontium bromide, sodium sulfide, magnesium chloride, and strontium chloride. At a 50-50 weighting factor these salts are similar, however some salts, e.g. SrBr2 and ZnSO4, have more of a spread as the weighting factors are changed. Lithium chloride is close to this second tier of salts. The least favorite or third-choice salts are lithium hydroxide and lanthanum chloride.

Summarizing, magnesium sulfate salt is the top choice or in the top grouping of salts/composites, regardless of the methods used to rank the different salts or composites. Zinc sulfate and sodium sulfide are often ranked near the top as well. However, sodium sulfide has corrosion concerns. The evaluation identified second-tier salts (strontium chloride, calcium chloride, magnesium chloride, and strontium bromide) with slight differences in ranking depending on the evaluation method used. For example, strontium bromide slips down from this

group when evaluated on a CED-to-energy density ratio or purely on cost, while strontium chloride is nearly always in the second tier. However, lithium hydroxide and lanthanum chloride always resulted in poor performance. The results and methods used here are useful in future studies focusing on similar salts or salt hybrid applications. Our findings demonstrated how cost and environmental impact information can be integrated into the decision-making for better selection of the materials early in the process design leading to a more sustainable final product.

5.5. Conclusions

We performed a prospective LCA of pure salts and salt-CNC composites and compared the laboratory scale and scaled-up model. We considered various evaluation metrics such as the ratio of CED-to-energy density and the weighted average of environmental impact and cost. The result shows that, in general, sulfur-containing salts perform better environmentally than other salts. Lanthanum chloride and lithium-containing salts (lithium hydroxide and lithium chloride) can be ruled out for future studies due to either high environmental impacts or high costs. For pure salts, the best-performing salts were magnesium sulfate, zinc sulfate, and calcium chloride with a close second tier of sodium sulfide, strontium chloride, strontium bromide, and magnesium chloride. For the composite, CNC and salt energy density are significant. Higher energy density salts like magnesium sulfate, zinc sulfate, sodium sulfide, and strontium chloride performed better on an energy basis due to requiring less total amounts of CNC to store the same amount of energy. Composites with magnesium sulfate consistently scored good marks regardless of the metric used. After these salts, the next tier consists of magnesium and calcium chloride, and strontium bromide. Cumulative energy demand also showed similar trends in the impact of salts and composites compared to LCA impact categories. Hotspots in the composite formulation were identified, and we found that scaled-up performance resulted in a significant

reduction in environmental impact (around 40% reduction for most of the salts), due to better mixing and ultrasonicating capability for industrial scale processes. Overall, this study has provided a framework for assessing and identifying salt hydrates and salt hydrate composites for thermochemical energy storage based on environmental impacts. It has identified preferred salts and ways to improve the processing of salt-CNC composites.

5.6. References

1. EIA (2022) U.S. Energy Information Administration - EIA - Independent Statistics and Analysis. https://www.eia.gov/consumption/residential/data/2020/#fueluses. Accessed 1 Jan 2023
2. EIA (2023) U.S. Energy Information Administration - EIA - Independent Statistics and Analysis. https://www.eia.gov/consumption/residential/data/2020/c&e/pdf/ce3.1.pdf. Accessed 10 Jul 2023
3. Berrill P, Gillingham KT, Hertwich EG (2021) Drivers of change in US residential energy consumption and greenhouse gas emissions, 1990–2015. Environmental Research Letters 16:034045. https://doi.org/10.1088/1748-9326/ABE325
4. Alva G, Liu L, Huang X, Fang G (2017) Thermal energy storage materials and systems for solar energy applications. Renewable and Sustainable Energy Reviews 68:693–706. https://doi.org/10.1016/J.RSER.2016.10.021
5. Clark RJ, Mehrabadi A, Farid M (2020) State of the art on salt hydrate thermochemical energy storage systems for use in building applications. J Energy Storage 27:101145. https://doi.org/10.1016/J.EST.2019.101145

6. Zbair M, Bennici S (2021) Survey Summary on Salts Hydrates and Composites Used in Thermochemical Sorption Heat Storage: A Review. Energies 2021, Vol 14, Page 3105 14:3105. https://doi.org/10.3390/EN14113105

7. Donkers PAJ, Pel L, Adan OCG (2016) Experimental studies for the cyclability of salt hydrates for thermochemical heat storage. J Energy Storage 5:25–32. https://doi.org/10.1016/J.EST.2015.11.005

8. Li W, Zeng M, Wang Q (2020) Development and performance investigation of MgSO4/SrCl2 composite salt hydrate for mid-low temperature thermochemical heat storage. Solar Energy Materials and Solar Cells 210:110509. https://doi.org/10.1016/J.SOLMAT.2020.110509

9. Van Essen VM, Cot Gores J, Bleijendaal LPJ, et al (2009) Characterization of salt hydrates for compact seasonal thermochemical storage

10. Zhao Q, Lin J, Huang H, et al (2021) Optimization of thermochemical energy storage systems based on hydrated salts: A review. Energy Build 244:111035. https://doi.org/10.1016/J.ENBUILD.2021.111035

11. Li W, Klemeš JJ, Wang Q, Zeng M (2022) Salt hydrate–based gas-solid thermochemical energy storage: Current progress, challenges, and perspectives. Renewable and Sustainable Energy Reviews 154:111846. https://doi.org/10.1016/J.RSER.2021.111846

12. Shen Z, Oh K, Kwon S, et al (2021) Use of cellulose nanofibril (CNF)/silver nanoparticles (AgNPs) composite in salt hydrate phase change material for efficient thermal energy storage. Int J Biol Macromol 174:402–412. https://doi.org/10.1016/J.IJBIOMAC.2021.01.183

13. Mauran S, Lahmidi H, Goetz V (2008) Solar heating and cooling by a thermochemical process. First experiments of a prototype storing 60 kW h by a solid/gas reaction. Solar Energy 82:623–636. https://doi.org/10.1016/J.SOLENER.2008.01.002

14. Jo B, Banerjee D (2015) Enhanced specific heat capacity of molten salt-based carbon nanotubes nanomaterials. J Heat Transfer 137:. https://doi.org/10.1115/1.4030226/375304

15. Liu H, Nagano K, Sugiyama D, et al (2013) Honeycomb filters made from mesoporous composite material for an open sorption thermal energy storage system to store low-temperature industrial waste heat. Int J Heat Mass Transf 65:471–480. https://doi.org/10.1016/J.IJHEATMASSTRANSFER.2013.06.021

16. Gladen AC, Bajwa D (2022) An Improved Thermochemical Energy Storage Material Using Nanocellulose to Stabilize Calcium Chloride Salt. J Sol Energy Eng 144:. https://doi.org/10.1115/1.4053904/1136904

17. Trache D, Hussin MH, Haafiz MKM, Thakur VK (2017) Recent progress in cellulose nanocrystals: sources and production. Nanoscale 9:1763–1786. https://doi.org/10.1039/C6NR09494E

18. George J, Sabapathi SN (2015) Cellulose nanocrystals: Synthesis, functional properties, and applications. Nanotechnol Sci Appl 8:45–54. https://doi.org/10.2147/NSA.S64386

19. Gladen A, Bajwa D (2021) A Novel Composite Material of Hygroscopic Salt Stabilized by Nanocellulose for Thermochemical Energy Storage. Proceedings of the ASME 2021 15th International Conference on Energy Sustainability, ES 2021. https://doi.org/10.1115/ES2021-63814

20. N'Tsoukpoe KE, Schmidt T, Rammelberg HU, et al (2014) A systematic multi-step screening of numerous salt hydrates for low temperature thermochemical energy storage. Appl Energy 124:1–16. https://doi.org/10.1016/J.APENERGY.2014.02.053

21. Gu H, Reiner R, Bergman R, Rudie A (2015) LCA study for pilot scale production of Cellulose Nano Crystals (CNC) from wood pulp

22. Pelay U, Azzaro-Pantel C, Fan Y, Luo L (2020) Life cycle assessment of thermochemical energy storage integration concepts for a concentrating solar power plant. Environ Prog Sustain Energy 39:e13388. https://doi.org/10.1002/EP.13388

23. Masruroh NA, Li B, Klemeš J (2006) Life cycle analysis of a solar thermal system with thermochemical storage process. Renew Energy 31:537–548. https://doi.org/10.1016/J.RENENE.2005.03.008

24. Bernal DC, Muñoz E, Manente G, et al (2021) Environmental assessment of latent heat thermal energy storage technology system with phase change material for domestic heating applications. Sustainability (Switzerland) 13:11265. https://doi.org/10.3390/SU132011265/S1

25. Horn R, Burr M, Fröhlich D, et al (2018) Life Cycle Assessment of Innovative Materials for Thermal Energy Storage in Buildings. Procedia CIRP 69:206–211. https://doi.org/10.1016/J.PROCIR.2017.11.095

26. Nienborg B, Gschwander S, Munz G, et al (2018) Life Cycle Assessment of thermal energy storage materials and components. Energy Procedia 155:111–120. https://doi.org/10.1016/J.EGYPRO.2018.11.063

27. De Laborderie A, Puech C, Adra N, et al (2011) Environmental Impacts of Solar Thermal Systems with Life Cycle Assessment. Renewable Energy Congress 2011-Sweden Climate Change Issues (CC). https://doi.org/10.3384/ecp110573678ï

28. Lamnatou C, Motte F, Notton G, et al (2018) Building-integrated solar thermal system with/without phase change material: Life cycle assessment based on ReCiPe, USEtox and Ecological footprint. J Clean Prod 193:672–683. https://doi.org/10.1016/J.JCLEPRO.2018.05.032

29. Kylili A, Fokaides PA, Ioannides A, Kalogirou S (2018) Environmental assessment of solar thermal systems for the industrial sector. J Clean Prod 176:99–109. https://doi.org/10.1016/J.JCLEPRO.2017.12.150

30. Wender BA, Foley RW, Prado-Lopez V, et al (2014) Illustrating anticipatory life cycle assessment for emerging photovoltaic technologies. Environ Sci Technol 48:10531–10538. https://doi.org/10.1021/ES5016923

31. Rammelberg HU, Osterland T, Priehs B, et al (2016) Thermochemical heat storage materials – Performance of mixed salt hydrates. Solar Energy 136:571–589. https://doi.org/10.1016/J.SOLENER.2016.07.016

32. Richter M, Habermann EM, Siebecke E, Linder M (2018) A systematic screening of salt hydrates as materials for a thermochemical heat transformer. Thermochim Acta 659:136–150. https://doi.org/10.1016/J.TCA.2017.06.011

33. Clark R-J, Gholamibozanjani G, Woods J, et al (2022) Experimental screening of salt hydrates for thermochemical energy storage for building heating application. J Energy Storage 51:104415

34. Kubota M, Matsumoto S, Matsuda H, et al (2014) Chemical Heat Storage with LiOH/LiOH·H2O Reaction for Low-Temperature Heat below 373 K. Adv Mat Res 953–954:757–760. https://doi.org/10.4028/WWW.SCIENTIFIC.NET/AMR.953-954.757

35. Van Essen VM, Zondag HA, Gores JC, et al (2009) Characterization of MgSO 4 hydrate for thermochemical seasonal heat storage. J Sol Energy Eng 131(4): 041014. https://doi.org/10.1115/1.4000275

36. Trausel F, De Jong AJ, Cuypers R (2014) A Review on the Properties of Salt Hydrates for Thermochemical Storage. Energy Procedia 48:447–452. https://doi.org/10.1016/J.EGYPRO.2014.02.053

37. Frazzica A, Brancato V, Caprì A, et al (2020) Development of "salt in porous matrix" composites based on LiCl for sorption thermal energy storage. Energy 208:118338. https://doi.org/10.1016/J.ENERGY.2020.118338

38. Yu N, Wang RZ, Lu ZS, Wang LW (2014) Development and characterization of silica gel–LiCl composite sorbents for thermal energy storage. Chem Eng Sci 111:73–84. https://doi.org/10.1016/J.CES.2014.02.012

39. Rajendran N, Runge T, Bergman RD, et al (2023) Techno-economic analysis and life cycle assessment of cellulose nanocrystals production from wood pulp. Bioresour Technol 377:128955. https://doi.org/10.1016/J.BIORTECH.2023.128955

40. Cheng F, Zhou X, Liu Y (2018) Methods for Improvement of the Thermal Efficiency during Spray Drying. 53:1031. https://doi.org/10.1051/e3sconf/20185301031

41. Kudra T (2012) Energy Performance of Convective Dryers. Drying Technology 30:1190–1198. https://doi.org/10.1080/07373937.2012.690803

42. Chakraverty A, Singh RP (2014) Theory of Grain Drying. Postharvest Technology and Food Process Engineering 62–105. https://doi.org/10.1201/B15587-7

43. Finkbeiner M, Inaba A, Tan RBH, et al (2006) The new international standards for life cycle assessment: ISO 14040 and ISO 14044. International Journal of Life Cycle Assessment 11:80–85

44. Habibi Y, Lucia LA, Rojas OJ (2010) Cellulose nanocrystals: Chemistry, self-assembly, and applications. Chem Rev 110:3479–3500. https://doi.org/10.1021/CR900339W

45. Meyer G, Garcia E, Corbett JD (1989) The Ammonium Chloride Route to Anhydrous Rare Earth Chlorides—The Example of Ycl3. Inorganic Syntheses 25:146–150. https://doi.org/10.1002/9780470132562.CH35

46. Yan T, Wang RZ, Li TX, et al (2015) A review of promising candidate reactions for chemical heat storage. Renewable and Sustainable Energy Reviews 43:13–31. https://doi.org/10.1016/J.RSER.2014.11.015

47. Gilles D, Segato T, Courbon E, Degrez M (2018) Affordable process for the production of strontium bromide used in low grade heat recovery applications. Procedia CIRP 69:383–388

48. Carre A, Crossin E (2015) A comparative life cycle assessment of two multi storey residential apartment buildings. Forest and wood products Australia Limited, Melbourne

49. Tsang M, Philippot G, Aymonier C, et al Anticipatory life-cycle assessment of supercritical fluid synthesis of barium strontium titanate nanoparticles. pubs.rsc.org

50. Rehman AU, Shah MZ, Ali A, et al (2021) Thermochemical heat storage ability of ZnSO4·7H2O as potential long-term heat storage material. Int J Energy Res 45:4746–4754. https://doi.org/10.1002/ER.6077

51. Piccinno F, Hischier R, Seeger S, Som C (2015) Life cycle assessment of a new technology to extract, functionalize and orient cellulose nanofibers from food waste. ACS Sustain Chem Eng 3:1047–1055. https://doi.org/10.1021/ACSSUSCHEMENG.5B00209

52. Li Q, McGinnis S, Sydnor C, et al (2013) Nanocellulose life cycle assessment. ACS Sustain Chem Eng 1:919–928. https://doi.org/10.1021/SC4000225

53. De Figueirêdo MCB, De Freitas Rosa M, Lie Ugaya CM, et al (2012) Life cycle assessment of cellulose nanowhiskers. J Clean Prod 35:130–139. https://doi.org/10.1016/J.JCLEPRO.2012.05.033

54. Arvidsson R, Nguyen D, Svanström M (2015) Life cycle assessment of cellulose nanofibrils production by mechanical treatment and two different pretreatment processes. Environ Sci Technol 49:6881–6890. https://doi.org/10.1021/ACS.EST.5B00888

55. Leão RM, Miléo PC, Maia JMLL, Luz SM (2017) Environmental and technical feasibility of cellulose nanocrystal manufacturing from sugarcane bagasse. Carbohydr Polym 175:518–529. https://doi.org/10.1016/J.CARBPOL.2017.07.087

56. Kudryavtsev P (2016) Lithium in nature, application, methods of extraction (review). Scientific Israel: Technological Advantages 18.3.

57. Rudie A (2017) Commercialization of cellulose nanofibril (CNF) and cellulose nanocrystal (CNC): pathway and challenges. In: Kargarzadeh, Hanieh; Ahmad, Ishak; Thomas, Sabu; Duiresne, Alain, eds Handbook of nanocellulose and cellulose nanocomposites, first edition 761-797 Chapter 23 761–797

58. Delepierre G, Vanderfleet OM, Niinivaara E, et al (2021) Benchmarking Cellulose Nanocrystals Part II: New Industrially Produced Materials. Langmuir 37:8393–8409. https://doi.org/10.1021/ACS.LANGMUIR.1C00550

59. Barbosa J, Borges S, Amorim M, et al (2015) Comparison of spray drying, freeze drying and convective hot air drying for the production of a probiotic orange powder. J Funct Foods 17:340–351. https://doi.org/10.1016/J.JFF.2015.06.001

60. IKA (2023) Mixers. https://www.ikaprocess.com/en/Products/Agitators-jet-stream-mixer-cph-1/TURBOTRON-csb-TURBO/Technical-Data-cspt.html. Accessed 22 Jan 2023

61. Reciprotor (2023) Industrial Mixers. http://www.reciprotor.com/Files/Varer/SEKO/Industrial-Mixer.pdf. Accessed 22 Jan 2023

62. Hielscher (2023) Ultrasonic Homogenizers for Liquid Processing. https://www.hielscher.com/ultrasonic-homogenizers-for-liquid-processing-3.htm. Accessed 22 Jan 2023

63. Qsonica (2023) Sonicators | Qsonica. https://www.sonicator.com/collections/sonicators. Accessed 22 Jan 2023

64. Peng Y, Han Y, Gardner DJ (2012) Spray-Drying Cellulose Nanofibrils: Effect of Drying Process Parameters on Particle Morphology and Size Distribution. Wood and Fiber Science 448–461

65. Baker CGJ, McKenzie KA (2007) Energy Consumption of Industrial Spray Dryers. 23:365–386. http://dx.doi.org/101081/DRT-200047665

66. Kabata-Pendias A, Mukherjee AB (2007) Trace elements from soil to human. Trace Elements from Soil to Human 1–550. https://doi.org/10.1007/978-3-540-32714-1

CHAPTER 6. A PRELIMINARY LIFE CYCLE ASSESSMENT OF MOLTEN-SALT BIOMASS TORREFACTION SYSTEM

6.1. Abstract

Biomass torrefaction is an effective way to improve biomass thermophysical properties for downstream applications such as combustion, pyrolysis, gasification, storage, transportation, and soil amendment. In this study, we use life cycle assessment (LCA) to assess the environmental impact of producing torrefied biomass using a molten salt torrefaction system and identify key areas for improvement. We consider several different salt blends and two biomass feedstocks: pine and switchgrass in our analysis. LCA was conducted considering a constant mass yield for all the analyzed salt blend conditions. All the analyzed processes resulted in auto-thermal conditions when the torrgas produced were assumed to be combustible. The LCA results show that salts have the highest environmental impact followed by biomass preprocessing such as size reduction and drying. Choice of salt is very important to reduce environmental impact. Lithium nitrate has the highest environmental impact among all the salts. Future studies should focus on reducing the use of lithium nitrate salt and finding alternative salts with lower environmental impact, but better catalyzing effects. The choice of salts also determines the scope of application of the torrefied biomass such as pyrolysis, gasification, co-firing, or soil amendment.

6.2. Introduction

Biomass is one of the major energy sources used widely throughout the world. However, biomass is inherently bulky and hygroscopic in nature. Thus, it has very low volumetric energy density, susceptible to microbial degradation, and has poor combustion properties [1]. To improve the energy density of biomass, storage life, and improve combustion properties, several

methods have been explored and used including biomass briquetting, pelleting, and torrefaction [1]. Torrefaction is a thermochemical process carried out to increase the carbon content of biomass, remove volatiles, and lower moisture content, thus, increase the biomass energy density, improve uniformity in composition, grindability, and fuel properties [2]. Torrefied biomass can be used in a wide array of downstream applications including co-firing with coal in a power plant due to improved combustion properties, feedstock for gasification and pyrolysis process, and for soil amendment [3–7]. Biochar helps to improve soil quality by increasing the soil's water-holding capacity and reducing the loss of nitrogen and dissolved organic carbon [8].

Recently, thermal processing of biomass in a molten salt has been suggested. Thermal processing includes gasification, pyrolysis, and torrefaction. Gasification occurs at high temperatures in the range of 800-1200 ℃ with controlled oxygen while pyrolysis occurs at temperatures around 300-800 ℃, mostly in the absence of oxygen [9]. Torrefaction is a mild form of thermal processing occurring at temperatures below 300 ℃ [9]. Gasification yields a gaseous fuel, mostly syngas while pyrolysis yields a mixture of fuels in the form of bio-oil, syngas, and biochar. Torrefaction yields a solid biochar along with volatile organic compounds. The use of different molten salts has been studied for pyrolysis and gasification of biomass. Alkali metal, alkaline earth metal, as well as transition metal salts have been studied in the molten salt pyrolysis process [10–13]. The anions included carbonates, acetates, nitrates, nitrites, and chlorides [14–17]. The molten salt pyrolysis process has shown higher quality pyrolysis products (biochar, bio-oil, and synthetic gas) due to the catalytic effect of salts on biomass [18]. Similarly, molten salt torrefaction, done at a lower temperature than traditional torrefaction, improved the syngas yields by catalyzing the breakage of aromatic rings and propyl chains in lignin, breakdown of hemicellulose, and efficient deoxygenation [19].

Traditional torrefaction is a mild form of pyrolysis where biomass is heated at temperatures between 200-300℃ at low oxygen, gaseous environment to yield solid biochar and volatiles called torrgas. Recently, molten salt-biomass torrefaction has been proposed as an alternative to the traditional method of torrefaction [14,20,21] to reduce the torrefaction temperature. Molten-salt torrefaction has also shown improved torrefied products at lower temperatures compared to traditional torrefaction processes done at similar or higher temperatures [20]. In the molten salt-biomass torrefaction process, biomass is surrounded by liquefied salt which is composed of a blend of various individual salts to achieve a low melting temperature. These salts melt below torrefaction temperature and help to catalyze the biomass torrefaction process. The catalyzing effect of these salts reduces the overall temperature required for the torrefaction process. These salts can improve torrefaction efficiency with better heat transfer to the biomass. Several salts and their mixtures have been explored for the torrefaction process including sodium acetate, potassium acetate, lithium nitrate, sodium nitrate, potassium nitrate, and zinc chloride [14,17,20,21]. The cation in these salts helps to catalyze the process. Among these salts, lithium nitrate is the most catalyzing salt [20]. An advantage of molten-salt biomass torrefaction can be the use of renewable solar energy for torrefaction systems. Traditional torrefaction is carried out at around 200-300℃. However, this high temperature is very hard to achieve through solar thermal collectors with low levels of concentration and in areas with low fractions of direct solar irradiation. Temperatures in the range of 150-250℃ are viable to achieve through solar thermal collectors with low levels of radiation concentration, for example through an evacuated tube or compound parabolic collector [22]. Molten-salt biomass torrefaction can be done are temperatures below 250℃ and still obtain good torrefied products compared to traditional systems done at higher temperatures than this. The higher processing

temperature for torrefaction also demands higher energy input and thus higher economic and environmental costs.

Molten-salt biomass torrefaction system is a fairly new technology. To determine the environmental impact of the molten salt torrefaction process and identify processes with high environmental, a life cycle assessment (LCA) of this new system needs to be conducted. LCA is a powerful tool to assess the environmental impact of any new processes or products. It not only determines the overall environmental impact of the process/product but also identifies the hotspots or higher environmental impact contributing sources in the manufacturing steps such that those hotspots can be minimized or replaced with more sustainable methods or materials. There are few studies available in the literature on the LCA of biomass torrefaction as given in Table 6.1.

Table 6.1. Summary of previous LCA studies on biomass torrefaction

Biomass source	Method of processing	System boundary	Functional unit	Application	Working temperature and time	Biochar yield (mass), %	Global warming potential	Ref
Wheat straw, pine, woodchips, grape pomace, manure, algae	Wet and dry torrefaction	Cradle to grave	1 kWh energy of torrefied biomass	Power plant	190-297°C; 30 min		200-1400 g CO2 eq/kWh	[20]
Rice straw	Torrefaction	Cradle to gate	10 g rice straw (initial feedstock)	Not specified	200-300°C; 15-60 min	52-97	0.15-0.27 kg CO2 eq/10 g	[21]
Pine	Wood pellet production with and without torrefaction	Cradle to gate	1 MJ of wood pellet or torrefied pellet	Power plant	250°C for 30 min	70	17.5 g CO2 eq/MJ - torrefied pellet 27.6 g CO2 eq/MJ – wood pellet	[22]
Olive husk	Torrefaction	Gate to gate	1 ton of torrefied biomass	Not specified	Not specified	42-50	35-120 kg CO2 eq/ton	[23]
Rice husk	Torrefaction	Cradle to gate	1 MJ of torrefied biomass		240-300°C; 30 min	47-90	12.5-36.9 g CO2 eq/MJ	[24]
Corn stover	Torrefaction	Cradle to gate	1 MJ of the torrefied biomass	Power plant	250-300°C; 1-5 min		11.35 g CO2 eq/MJ	[25]
Algae	Torrefaction	Cradle to gate	1 kg of torrefied biomass		300°C; 60 min		6.86 kg CO2 eq/kg	[26]

To the best of our knowledge, there are no prior LCA studies on the molten-salt biomass torrefaction system. Therefore, the primary objective of this study is to do the life cycle assessment of producing torrefied biomass following the molten salt-biomass torrefaction process and determine the major factors contributing to environmental impact. Through LCA we want to identify areas that can be improved to reduce the environmental impact of molten salt-biomass torrefaction system. We will also compare the traditional torrefaction with the molten salt torrefaction of pine and switchgrass that uses a blend of different salts. To make the comparison simple, the torrefaction biomass yield is fixed at 70% for pine and 60% for switchgrass. This study can also provide a baseline environmental impact comparison for future studies using molten salts for biomass thermochemical processing.

6.3. Methods

6.3.1. Torrefaction system

We conducted both traditional and molten salt-biomass torrefaction to compare their environmental performance. The process flow diagram for the traditional torrefaction system is shown in Figure 6.1. The process starts with the biomass obtained from the field which is dried to remove excess moisture. The dried biomass is then sent to a torrefaction reactor. The reactor is maintained at a predefined torrefaction temperature. After the desired torrefaction residence time, biomass is taken out from the reactor. The torrefaction system has another output in the form of torrgas in which much of the composition is carbon dioxide and carbon monoxide. There are available heats from different unit processes which can be used to dry the initial biomass feedstock. The heat can be recovered from the steam generated after drying biomass which is usually done at around 120℃. Another source of heat that can be used is from torrgas and hot torrefied biomass.

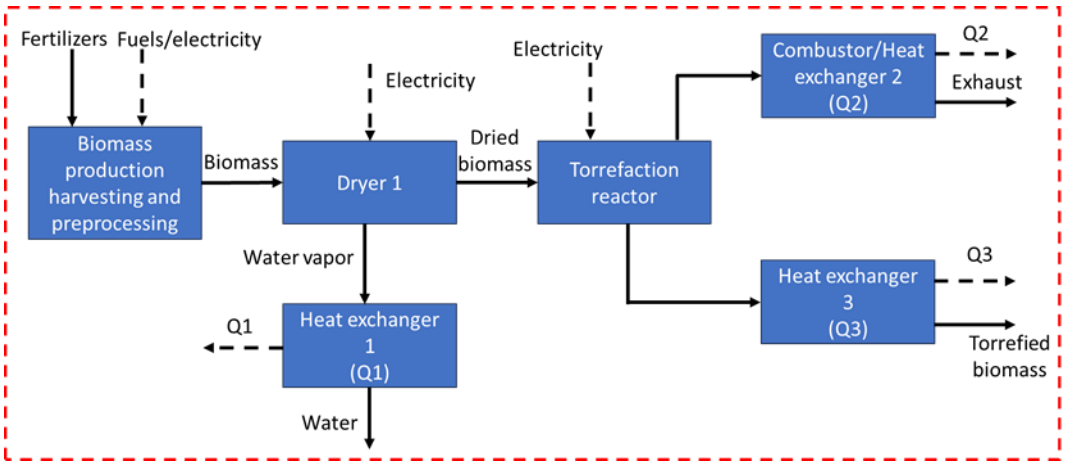

Figure 6.1. Process flow diagram of traditional torrefaction system (dotted red line represents our system boundary for analysis)

The process flow diagram for the molten-salt torrefaction used in our analysis is shown in Figure 6.2. The process starts with the biomass obtained from the field which is dried to remove excess moisture. The dried biomass is then sent to a torrefaction reactor consisting of a molten salt bath. The molten salt bath is maintained at the desired torrefaction temperature. After the desired torrefaction residence time, biomass is taken out from the molten salt bath. A portion of salt (around 10%) comes out with biomass. The torrefied biomass is then washed and dried. The torrefaction system has another output in the form of torrgas in which much of the composition is carbon dioxide and carbon monoxide. There are available heats from different unit processes which can be used to dry the initial biomass feedstock or the washed torrefied biomass. The heat can be recovered from the steam generated after drying biomass which is usually done at around 120℃. Similarly, another source of heat that can be used is from torrgas and hot torrefied biomass.

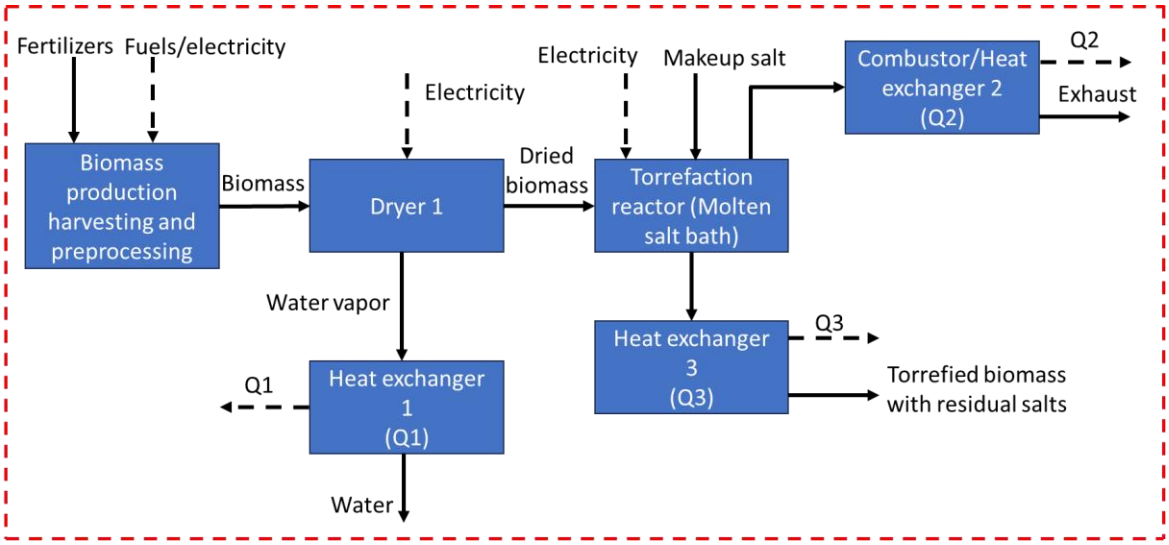

Figure 6.2. Process flow diagram of molten salt-biomass torrefaction system (dotted red line represents our system boundary for analysis)

6.3.2. Mass and energy balance of the torrefaction system

We performed traditional torrefaction for pine and molten-salt biomass torrefaction for two feedstocks: pine and switchgrass. Biomass from the field is harvested and transported to a torrefaction plant where drying and grinding of the biomass occurs. We do not consider the loss factor for biomass in any of these processes. The dried biomass goes through the torrefaction reactor for the torrefaction process. After the torrefaction process, the mass of solid torrefied biomass is measured and mass yield is determined. Using the conservation of mass principle, the mass of torrgas is calculated by subtracting the mass of torrefied biomass from the initial mass of dried biomass. The initial higher heating value (HHV) of raw biomass and torrefied biomass is measured using a bomb calorimeter. The combustion energy of torrgas is then calculated by subtracting the energy of torrefied biomass from the raw biomass. We also considered a scenario when energy cannot be extracted from torrgas through combustion. For both traditional and molten-salt biomass torrefaction, we determine the condition to achieve a 60% mass yield of torrefied biomass compared to the dry biomass feed. We are not considering the energy used in

the washing/filtration step of torrefied biomass for the molten salt biomass torrefaction system. The torrefaction energy calculation is done similar to the previous study [30] and using a process model developed in our group for the torrefaction system. The energy required to dry the biomass is calculated based on sensible energy to heat the biomass and moisture in biomass to 120℃ and the enthalpy of vaporization of water at 100℃. We consider a loss factor of 10% during drying. Similarly, the energy required for torrefaction is calculated by considering the energy required to heat the dried biomass and the makeup salt to the torrefaction temperature. The enthalpy of fusion of the salt blends is accounted for in the calculation for the molten salt biomass torrefaction system since the salt blend melts below the torrefaction temperature. The loss factor for heat energy during torrefaction is considered to be 40%. We also account for the energy that can be extracted from the steam from the dryer, hot torrefied biomass, hot torrgas, and HHV of the torrgas that can be obtained through its combustion. The loss factor for steam, torrgas, and torrefied biomass solid heat exchangers is considered to be 20%, 20%, and 40%, respectively. We assume 10% of salts come with biomass after the torrefaction step for the molten salt system. This number is based on our experience from experimental works. The amount of water required to wash the torrefied biomass in the molten salt system is considered to be 40 times the amount of salt in biomass. This is the amount of water we use for our lab-scale process. However, the washing step is not considered in the LCA analysis. Table 6.2 lists salt blends used in this study for LCA. The melting temperature of the salt blends is calculated based on a previous study [31].

Table 6.2. Salt blends considered for molten salt biomass torrefaction system

	Composition				
Salt blend	Potassium nitrate (KNO_3)	Lithium nitrate ($LiNO_3$)	Sodium nitrate ($NaNO_3$)	Sodium nitrite ($NaNO_2$)	Melting temperature (°C)
Pine					
Salt A	54.07	25.92	20.01	0	118
Salt B	60	20	20	0	158
Salt C	50	30	20	0	127
Salt D	70	30	0	0	139
Salt E	60	40	0	0	143
Salt F	45	0	20	35	140
Switchgrass					
Salt G	55	45	0	0	161
Salt H	65	35	0	0	132

Table 6.3 lists the value of each parameter considered in the calculation of mass and energy for the torrefaction system. The specific heat capacity of biomass is calculated using the Siebel equation [32]. The specific heat capacity of salt blends is taken from a previous study [33]. We used the same value of specific heat capacity for all the salt blends because there is not a big difference in specific heat capacity between different salt blends. The enthalpy of fusion is also taken from the same study [33]. We used the same enthalpy of fusion for all salt blends as well due to a lack of data availability. For salt blend F, the specific heat capacity and enthalpy of fusion are taken from another study [34]. There is not a huge difference in the composition of lithium nitrate for most of the salt blends we considered, so it would be safe to assume a similar enthalpy of fusion for all salt blends for the comparison purpose of this study. However, once more data are available, the model can be updated to get more accurate results. The loss factors are taken from a previous study [30]. Steam heat exchanger loss factor based on another study assuming similar efficiency as air-to-air heat exchangers [35]. Electricity generation efficiency was taken to be 35% combining both combustion and generator efficiencies [36].

Table 6.3. Parameters used in the mass and energy calculation

Parameters	Value	Unit
Specific heat capacity of wet biomass	2.000	kJ/kg.K
Specific heat capacity of dry biomass	1.598	kJ/kg.K
Specific heat capacity of torrefied biomass	1.472	kJ/kg.K
Specific heat capacity of solid salt blend F	1.28	kJ/kg.K
Specific heat capacity of liquid salt blend F	1.50	kJ/kg.K
Specific heat capacity of other solid salt blends	1.12	kJ/kg.K
Specific heat capacity of other liquid salt blends	1.46	kJ/kg.K
Specific heat capacity of liquid water	4.180	kJ/kg.K
Enthalpy of vaporization for water	2.257	MJ/kg
Enthalpy of fusion for salt blend F	0.121	MJ/kg
Enthalpy of fusion for other salt blends	0.0582	MJ/kg
Water vaporization temperature	100	℃
Biomass drying temperature	120	℃
Ambient temperature	25	℃
Effective temperature for heat extraction	50	℃
Moisture content of biomass from the field	30	%
Moisture content of torrefaction feed biomass	0	%
Percentage of salt that comes out with torrefied biomass	10	%
Steam heat exchanger loss factor	20	%
Torgas combustion and heat exchanger loss factor	35	%
Torrefied biomass solid heat exchanger loss factor	40	%
Loss factor for drying	35	%
Loss factor for torrefaction	40	%
Combustion to turbine generator efficiency	35	%

We use the conditions to achieve a 70% torrefied mass yield as a baseline for the LCA comparison between traditional and molten salt biomass torrefaction for pine and 60% for switchgrass. The choice of these cut-off points is arbitrary and based on our data availability. Correlations were developed from the mass yield-temperature and HHV-temperature datapoints from previous studies. This relationship is used to determine the condition to achieve a 70% or 60% mass yield of torrefied biomass for pine and switchgrass, respectively. The torrefaction conditions and HHV values used in this study are given in Table 6.4. The data for pine is based

on the Backer et al. study [20] and the data for switchgrass is based on the Kohlin et al. study [37]. The data for salt blend F, without any lithium content, for pine is based on Kohlin et al. [38].

Table 6.4. Torrefaction conditions used in this study

S.No.	Torrefaction	Feedstock	Temperature (°C)	Raw biomass HHV (MJ/kg)	Torrefied biomass HHV (MJ/kg)	Yield (%)
Pine						
1	Traditional	Pine	272	20.2303	22.5822	70
2	Salt A	Pine	229	20.2303	23.237	70
3	Salt B	Pine	244	20.2303	23.0742	70
4	Salt C	Pine	218	20.2303	22.2761	70
5	Salt D	Pine	230	20.2303	22.8867	70
6	Salt E	Pine	207	20.2303	22.2724	70
7	Salt F	Pine	186	20.2303	20.9536	70
Switchgrass						
1	Traditional	Switchgrass	283	17.623	22.4562	60
2	Salt G	Switchgrass	200	17.623	19.8137	60
3	Salt H	Switchgrass	217	17.623	20.4941	60

The mass and energy balance data for each of the torrefaction conditions used in this study is given in Table 6.5. We did not consider the sensible energy that could be extracted from torrgas as it was very low compared to other streams and there is high uncertainty in determining the composition.

Table 6.5. Mass and energy balance data

Torrefaction	Traditional torrefaction	Salt blend A	Salt blend B	Salt blend C	Salt blend D	Salt blend E	Salt blend F
Feedstock	Pine						
Biomass in (kg)	2.2	2.2	2.2	2.2	2.2	2.2	2.2
Dry biomass in (kg)	1.43	1.43	1.43	1.43	1.43	1.43	1.43
Torrefied biomass (kg)	1	1	1	1	1	1	1
Makeup salt (kg)	0	0.1	0.1	0.1	0.1	0.1	0.1
Torgas (kg)	0.43	0.43	0.43	0.43	0.43	0.43	0.43
$Q_{dryer\ 1}$ (MJ)	2.91	2.91	2.91	2.91	2.91	2.91	2.91
$Q_{hx\ 1}$ (MJ)	1.57	1.57	1.57	1.57	1.57	1.57	1.57
$Q_{hx\ 2}$ (MJ)	0.33	0.28	0.3	0.26	0.28	0.25	0.22
$Q_{hx\ 3}$ (MJ)	3.79	3.4	3.5	3.97	3.61	3.98	4.77
$Q_{torrefaction}$ (MJ)	0.58	0.47	0.53	0.42	0.47	0.38	0.31

Feedstock	Switchgrass		
	Traditional torrefaction	Salt blend G	Salt blend H
Biomass in (kg)	2.56	2.56	2.56
Dry biomass in (kg)	1.67	1.67	1.67
Torrefied biomass (kg)	1	1	1
Makeup salt (kg)	0	0.1	0.1
Torgas (kg)	0.67	0.67	0.67
$Q_{dryer\ 1}$ (MJ)	3.39	3.39	3.39
$Q_{hx\ 1}$ (MJ)	1.83	1.83	1.83
$Q_{hx\ 2}$ (MJ)	0.34	0.24	0.26
$Q_{hx\ 3}$ (MJ)	4.15	5.73	5.33
$Q_{torrefaction}$ (MJ)	0.72	0.72	0.72

6.3.3. Life cycle assessment (LCA)

6.3.3.1. Goal and system boundary

The goal of this study is to conduct the life cycle assessment of producing torrefied biomass following both traditional and molten salt-biomass torrefaction systems and identify process hotspots for each of these systems. The results of LCA between these two systems are then compared to determine if the molten salt-biomass torrefaction system is environmentally favorable. The system boundary for our study includes biomass production, logistics, drying, and torrefaction process. Therefore, it is a cradle-to-gate system assessment. The end-use of torrefied biomass is not included in our analysis. Biomass production includes all the inputs such as fertilizers and harvesting required for production. Logistics include biomass transportation via road using a truck. Biomass is bone-dried at the torrefaction. Torrefaction is done as a semi-batch system where the biomass is immersed into a molten salt bath already maintained at the desired torrefaction temperature for a certain duration of time. The heat required for the molten salt bath is provided by a natural gas furnace. For the traditional system, biomass is heated inside a pressure chamber through hot air obtained from a natural gas furnace.

6.3.3.2. Functional unit

The functional unit for our study is 1 kg of the torrefied biomass. This unit was used to compare the traditional torrefaction system and the molten-salt biomass torrefaction system. The 1 kg of the torrefied biomass is based on a 70% mass yield for pine and a 60% mass yield for switchgrass. However, the same mass yield does not necessarily result in a similar product, most often they have different characteristics such as different carbon content, nitrogen content, higher heating value, and such.

6.3.3.3. Inventory collection

The materials and energy input for traditional and molten-salt biomass torrefaction systems are given in Table 2. The production of switchgrass is based on a previous study [39] which is available in the GREET database developed by Argonne National Laboratory. The energy for chopping and grinding switchgrass is taken from a previous study as well [40]. The production of pine is also based on a previous study [41] which is also available in the GREET database. Pine is harvested and chopped into smaller pieces on site then transported to torrefaction plant. The moisture content at this stage is 30%. It is then bone-dried before conducting fine grinding. The energy to dry is calculated similar to switchgrass. The energy for chopping and grinding is taken from previous studies [42,43]. The energy to dry both switchgrass and pine is calculated considering the sensible heat of biomass and water and enthalpy of vaporization of water, and considering the drying temperature to be 120℃. The inventory for lithium nitrate salt is obtained from a previous study [44]. The inventory for the remaining salts was obtained from the Ecoinvent database within SimaPro. The details of the inventory and their source are provided in Table 6.6.

Table 6.6. Data source for life cycle inventory analysis

S.No.	Item	Source
1	KNO_3	Ecoinvent: Potassium nitrate production (RNA)
2	$LiNO_3$	[40]
3	$NaNO_2$	Ecoinvent: Sodium nitrite production (RoW)
4	$NaNO_3$	Ecoinvent: Sodium nitrate production (RoW)
5	Switchgrass	GREET: [35,36]
6	Pine	GREET: [37–39]
7	Heat	Ecoinvent: Heat, district or industrial, natural gas (MRO, US only)
8	Electricity	Ecoinvent: Electricity, medium voltage, at grid, 2019/US US-EI U

We did not account for the biogenic carbon in our calculation. The carbon in the biomass is renewable and all the carbon dioxide emitted from the biogenic carbon will get absorbed by

the growing plants. This assumption is valid as long as the rate of biomass consumption is equal to the rate of biomass growth, thereby creating a closed carbon loop. In contrast to this, the fossil which has been sequestered for millions of years when released into the atmosphere results in a net increase in atmospheric carbon dioxide.

6.3.3.4. Impact assessment

We used SimaPro V9.1 to build our LCA model. The life cycle impacts are then calculated using the tool for reduction and assessment of chemicals and other environmental impacts II (TRACI II) method. TRACI II is a method developed by the US EPA. It consists of 10 different life cycle impact categories including global warming, ozone depletion, and fossil fuel depletion.

6.4. Results and discussion

6.4.1. Pine vs Switchgrass production

The LCA result of pine and switchgrass production is shown in Figure 6.3. The result is for the feedstock used directly for torrefaction, therefore all the preprocessing conditions are included. Preprocessing has the highest environmental impact for both biomasses. Preprocessing includes chopping, drying, and fine grinding of biomass. Fine grinding is the major hotspot. Pine required higher energy for size reduction compared to switchgrass.

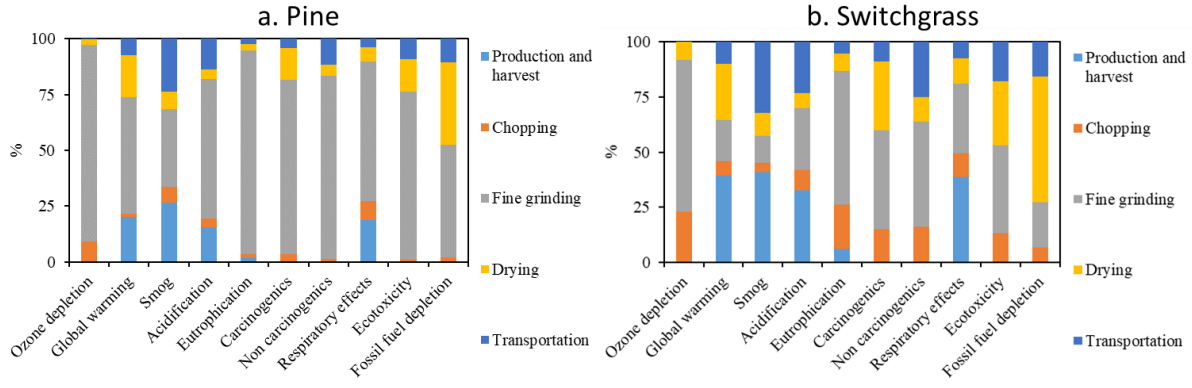

Figure 6.3. LCA result of pine and switchgrass production

LCA comparison between pine and switchgrass production (Figure 6.4) shows that pine production has higher environmental impacts. Preprocessing, specifically, size reduction for pine has higher impacts than switchgrass which contributes to the higher environmental impact of pine.

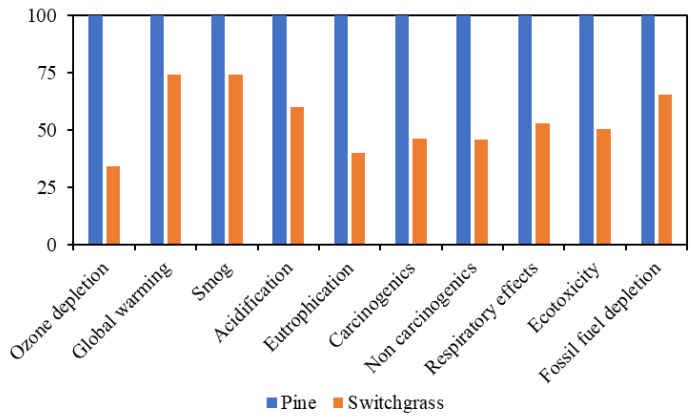

Figure 6.4. Comparison of LCA of pine and switchgrass production

6.4.2. Torrefaction

LCA results of traditional and molten-salt torrefaction using 6 different salt blends (Table 6.2) when torgas combustion is considered for pine are shown in Figure 6.5. The result shows that biomass has the highest contribution compared to other input materials for all the conditions. For traditional torrefaction, the by-product credit from heat and electricity generation by combusting torrgas provides higher environmental impact mitigation in most of the impact categories compared to the environmental impact of input materials and the torrefaction process. For molten-salt torrefaction, lithium nitrate is the second major hotspot. Lithium nitrate production has a higher environmental impact compared to other salts followed by sodium nitrate, sodium nitrite, and potassium nitrate. The torrefaction process in itself has a very low environmental impact compared to the material inputs. The environmental impact of the input materials and torrefaction process outweighs the benefits obtained from by-product credit.

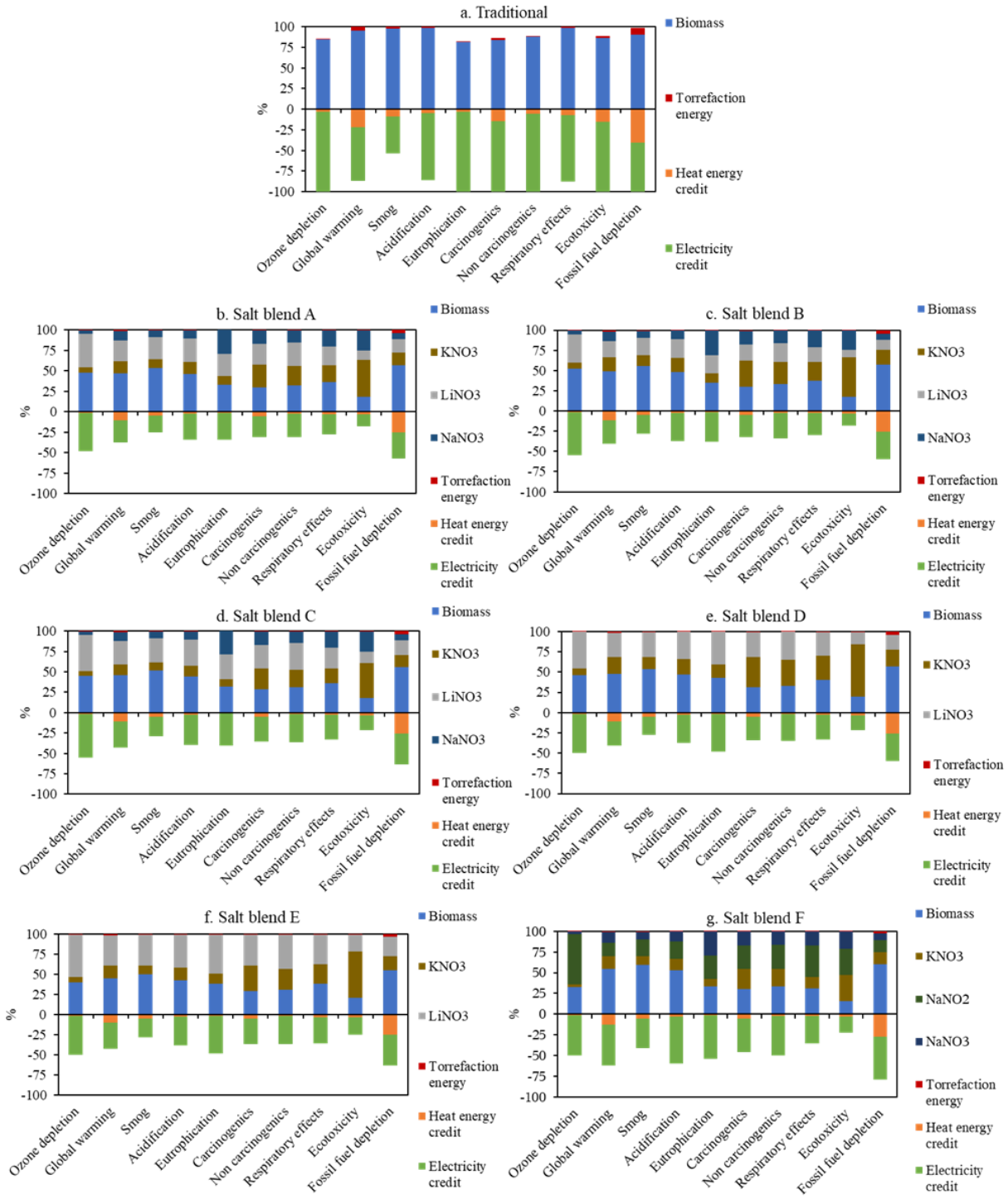

Figure 6.5. LCA results of traditional and molten-salt torrefaction of pine when torrgas combustion is considered

LCA results of traditional and molten-salt torrefaction for pine, when torrgas combustion is not considered, are shown in Figure 6.6. The difference in results between Figures 6.5 and 6.6

is the heat energy and electricity credit. For the condition when torrgas cannot be combusted, there is no electricity credit and the heat energy credit is lower because the only extracted heat available is through heat exchangers for steam and hot torrefied biomass. However, for the condition with the combustion of torrgas, the heat generated is enough to dry and torrefy the biomass along with extra heat to generate electricity. Sensible energy from torrgas is not included as it is small compared to others and it is complex to determine the accurate composition of torrgas to get the exact amount of extractable energy.

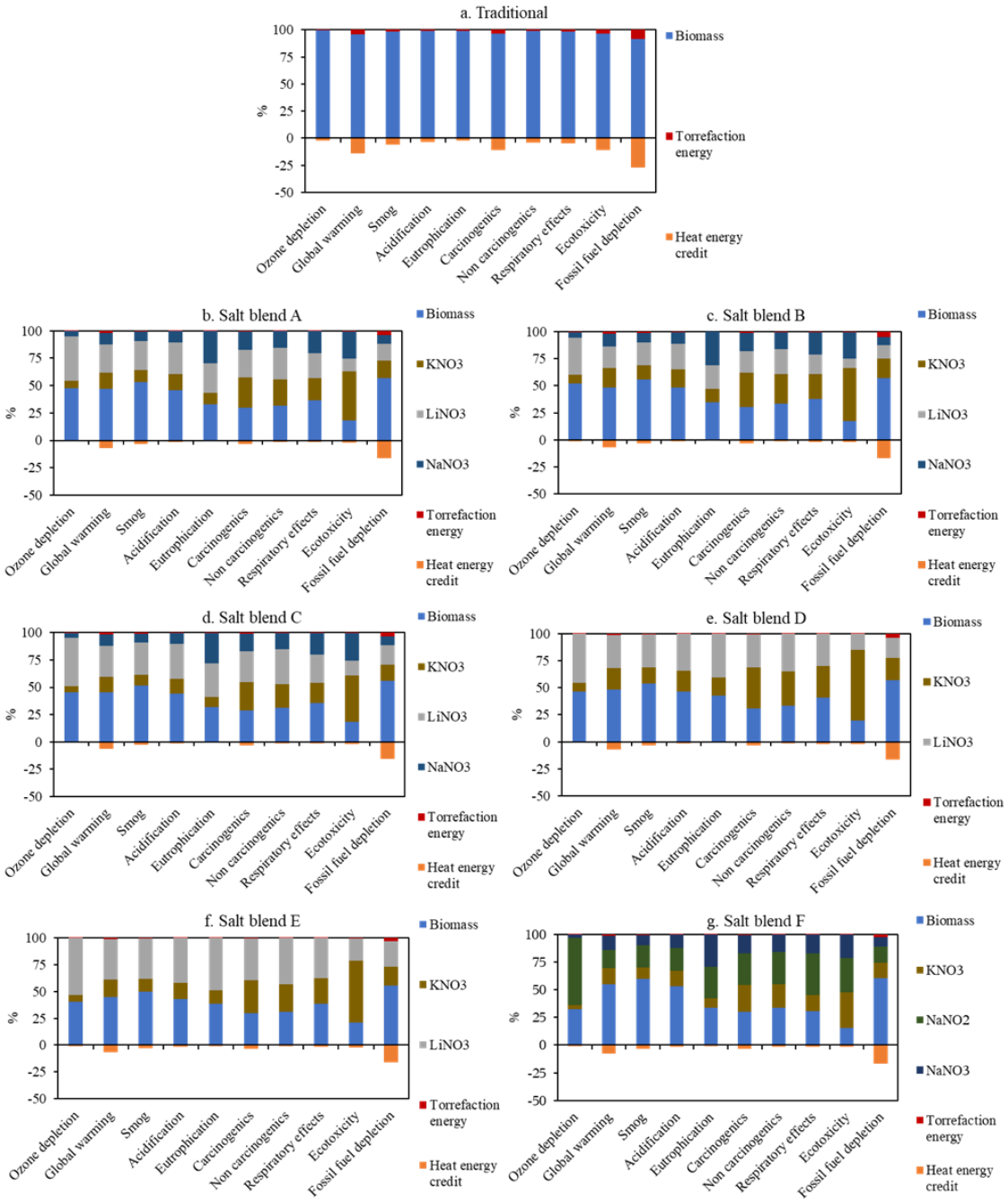

Figure 6.6. LCA results of traditional and molten-salt torrefaction of pine when torrgas combustion is not considered

Similar to pine torrefaction, switchgrass also shows a similar trend for the condition when torgas is combustion (Figure 6.7). There are higher by-product benefits in traditional torrefaction

of switchgrass. Lithium nitrate is the major hotspot for molten-salt torrefaction. This is because of the use of higher amounts of lithium nitrate in the salt blends.

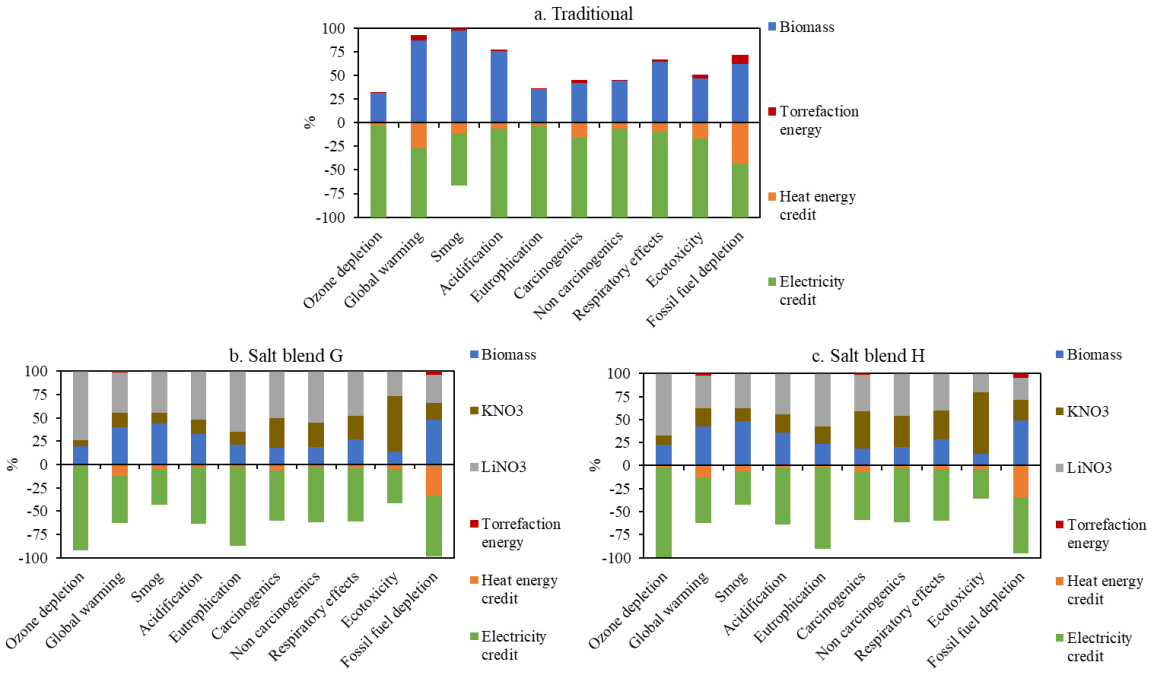

Figure 6.7. LCA results of traditional and molten-salt torrefaction of switchgrass when torrgas combustion is considered

For the case when torrgas is not combustible for switchgrass (Figure 6.8), the trend is similar to pine. There is a lower heat energy credit and not electricity credit.

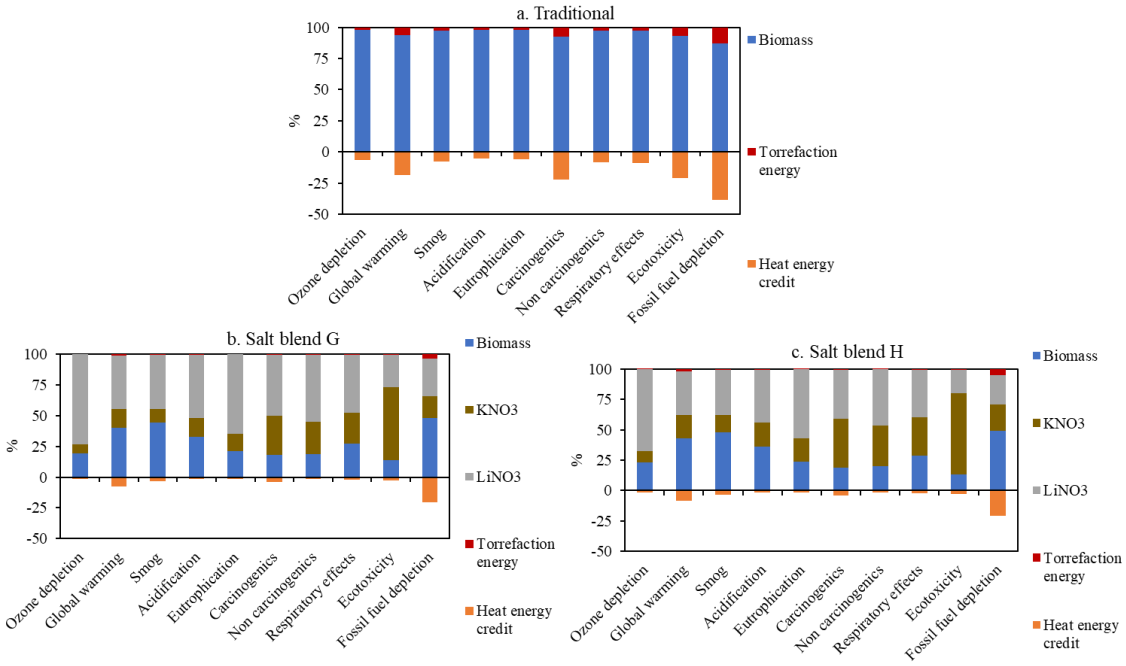

Figure 6.8. LCA results of traditional and molten-salt torrefaction of switchgrass when torrgas combustion is not considered

The summary of LCA results of both pine and switchgrass torrefaction is given in Table 7 for the case with torgas combustion and in Table 8 for the case without torgas combustion. For the case with torrgas combustion, since all the analyzed processes resulted in auto thermal conditions and extra electricity was generated, the net environmental impact is lower compared to when torrgas combustion was not considered when external heat is required. The global warming potential for molten-salt torrefaction is a magnitude higher than the traditional torrefaction when torgas combustion is considered and around 100% increase when torgas combustion is not considered. This trend is similar in other impact categories. Therefore, the major hotspot for molten-salt torrefaction is in the use of salts. Salt blend F has the lowest impact among all the salts. This is because this blend does not contain lithium nitrate. To reduce the environmental impacts of molten salt torrefaction, the use of lithium nitrate should be reduced. Since, salts have higher impacts, using salts with less environmental impact at higher torrefaction

temperatures can be one option to improve the process. However, the increase in environmental impacts for conditions without torrgas combustion is higher. This is due to the high impact of energy required for drying, and no electricity credit.

6.4.3. Discussion

Molten salt torrefaction can reduce the torrefaction temperature significantly. This opens up an opportunity to perform torrefaction powered solely by a solar thermal reactor, which is a renewable form of energy and has less environmental impact. The higher temperature required to achieve desired torrefied products, may not be attainable through the solar thermal reactor for the traditional torrefaction process. Traditional torrefaction is usually done at higher temperatures usually above 250℃. Molten-salt torrefaction can significantly reduce the temperature of torrefaction and an equivalent degree of traditional torrefaction can be achieved way below 250℃ using molten-salt torrefaction such that solar thermal reactors can be employed effectively in such cases. This increases the options on the geographical location where the torrefaction process can be conducted. Even in a place with lower solar irradiance, the torrefaction temperature can be achievable through the solar thermal reactor. Therefore, using a solar thermal reactor to dry biomass as well as run a torrefaction process can significantly reduce the environmental impact. Among the salts, lithium nitrate has the highest environmental impact, but it also has a higher catalytic effect in the severity of torrefaction. Future experimental studies need to focus on reducing its use and finding alternative salts. Nitrite salts have shown higher catalytic effects than nitrates in some of our experimental tests, however further tests need to be conducted to confirm their applicability and effectiveness.

One of the other hypotheses for using molten-salt torrefaction was the usefulness of salts in downstream application areas. For example, salts such as potassium and sodium nitrate are

used as fertilizers, therefore, torrefied biomass that has residual salts in it can be used for soil amendment purposes without further treatment [45–48]. This can be done either by using the torrefied product as is with the salts in it or by washing the torrefied product to recover salt. The wash water can be used to spray the soil as a fertilizer if the salts are beneficial [49]. However, only a few salts qualify for this application. Salts such as lithium nitrate and other heavy metal salts may not be good for soil health. So, they need to be avoided. Washing also has another drawback, the need for extra energy to dry torrefied products.

Even though the mass yield was fixed for all the conditions, the product properties and quality of torrefied biomass are different for each condition. Molten salt-biomass torrefaction has shown better quality products compared to traditional torrefaction [20,37]. Molten salt torrefied products have pH levels close to neutral or slightly alkaline while the traditional torrefied product is more acidic. Molten salt-torrefied biomass can be beneficial for acidic soils to improve their properties [50]. The nitrogen content of molten salt torrefied pine and switchgrass is higher compared to traditional torrefied pine and switchgrass [37]. Therefore, molten salt-torrefied biomass can be beneficial for soil that requires higher nitrogen levels.

Another application of the molten-salt torrefied products is pyrolysis. The residual cations in torrefied biomass can be beneficial in further catalyzing the pyrolysis process yielding a better product as suggested by previous studies [17,21,51]. But, further analysis needs to be conducted to see if there are any environmental benefits. The third application of torrefied biomass is for power generation purposes, used as a fuel, by co-firing along with coal in power plants. However, in such applications, salts may need to be removed through washing before use.

Table 6.7. Summary of LCA results of traditional and molten-salt torrefaction of Pine and Switchgrass when torrgas combustion is considered (Functional unit: 1 kg torrefied biomass)

S. No.	Torrefaction	Feed-stock	Impact categories									
			Ozone depletion	Global warming	Smog	Acidifi-cation	Eutro-phication	Carcino-genics	Non carcino-genics	Respiratory effects	Eco-toxicity	Fossil fuel depletion
			kg CFC-11 eq	kg CO2 eq	kg O3 eq	kg SO2 eq	kg N eq	CTUh	CTUh	kg PM2.5 eq	CTUe	MJ surplus
Pine												
1	Traditional torrefaction	Pine	-1.67E-09	0.05	0.0097	0.0002	-9.90E-05	-1.52E-09	-4.00E-09	9.86E-06	-0.10	-0.01
2	Salt A	Pine	1.03E-08	0.52	0.0289	0.0018	8.91E-04	2.23E-08	7.06E-08	1.59E-04	3.65	0.40
3	Salt B	Pine	8.14E-09	0.48	0.0267	0.0017	7.98E-04	2.11E-08	6.51E-08	1.50E-04	3.72	0.37
4	Salt C	Pine	9.32E-09	0.49	0.0283	0.0017	8.32E-04	2.09E-08	6.64E-08	1.51E-04	3.42	0.34
5	Salt D	Pine	1.02E-08	0.48	0.0278	0.0017	5.53E-04	2.02E-08	6.44E-08	1.31E-04	3.16	0.37
6	Salt E	Pine	1.18E-08	0.50	0.0298	0.0018	6.04E-04	2.04E-08	6.69E-08	1.34E-04	2.89	0.35
7	Salt F	Pine	1.47E-08	0.27	0.0204	0.0010	6.23E-04	1.70E-08	4.85E-08	1.70E-04	4.04	0.18
Switchgrass												
1	Traditional torrefaction	Switch grass	-8.01E-09	-0.03	0.0062	-0.0003	-0.00037	-6.61E-09	-2.14E-08	-2.55E-05	-0.49	-0.18
2	Salt A	Switch grass	1.49E-09	0.32	0.0230	0.0010	0.00013	1.12E-08	3.56E-08	7.16E-05	2.02	0.01
3	Salt B	Switch grass	1.04E-10	0.30	0.0212	0.0009	0.00008	1.11E-08	3.36E-08	6.98E-05	2.30	0.04

Table 6.8. Summary of LCA results of traditional and molten-salt torrefaction of Pine and Switchgrass when torrgas combustion is not considered (Functional unit: 1 kg torrefied biomass)

S. No.	Torrefaction	Feed-stock	Impact categories									
			Ozone depletion	Global warming	Smog	Acidifi-cation	Eutro-phication	Carcino-genics	Non carcino-genics	Respiratory effects	Eco-toxicity	Fossil fuel depletion
			kg CFC-11 eq	kg CO2 eq	kg O3 eq	kg SO2 eq	kg N eq	CTUh	CTUh	kg PM2.5 eq	CTUe	MJ surplus
Pine												
1	Traditional torrefaction	Pine	9.32E-09	0.35	0.0199	0.0013	4.43E-04	8.72E-09	3.17E-08	7.79E-05	0.74	0.42
2	Salt A	Pine	1.96E-08	0.78	0.0376	0.0028	1.35E-03	3.10E-08	1.01E-07	2.17E-04	4.37	0.78
3	Salt B	Pine	1.79E-08	0.74	0.0358	0.0026	1.28E-03	3.02E-08	9.67E-08	2.11E-04	4.47	0.76
4	Salt C	Pine	2.08E-08	0.80	0.0389	0.0029	1.40E-03	3.16E-08	1.04E-07	2.22E-04	4.29	0.79
5	Salt D	Pine	2.03E-08	0.76	0.0372	0.0027	1.05E-03	2.97E-08	9.72E-08	1.94E-04	3.94	0.77
6	Salt E	Pine	2.32E-08	0.81	0.0403	0.0030	1.17E-03	3.11E-08	1.04E-07	2.05E-04	3.76	0.80
7	Salt F	Pine	2.91E-08	0.66	0.0336	0.0024	1.33E-03	3.03E-08	9.52E-08	2.59E-04	5.13	0.73
Switchgrass												
1	Traditional torrefaction	Switch grass	3.59E-09	0.29	0.0169	0.0009	2.02E-04	4.27E-09	1.64E-08	4.65E-05	0.40	0.28
2	Salt A	Switch grass	1.89E-08	0.78	0.0389	0.0027	9.85E-04	2.73E-08	9.21E-08	1.79E-04	3.33	0.67
3	Salt B	Switch grass	1.60E-08	0.72	0.0358	0.0024	8.68E-04	2.59E-08	8.52E-08	1.68E-04	3.51	0.64

6.5. Conclusion

LCA of traditional and molten-salt biomass torrefaction for pine and switchgrass was conducted. Different salts were considered in molten-salt torrefaction consisting of binary and ternary salt blends. The salts under consideration were lithium nitrate, sodium nitrate, sodium nitrite, and potassium nitrate. The result shows that traditional torrefaction has a lower environmental impact compared to molten-salt torrefaction. The higher environmental impact of molten-salt torrefaction is primarily contributed by salts. Salt production has higher environmental impacts compared to other inputs. Among salts, lithium nitrate has the highest environmental impact followed by sodium nitrate, sodium nitrite, and then potassium nitrate. The use of lithium in the salt blends can limit the use of torrefied biomass in soil amendment applications since lithium is not good for soil health. Therefore, future studies should look into alternatives and those that have potential in wide application areas such as soil amendment, pyrolysis, and co-firing. Among the biomass, switchgrass has a lower environmental impact compared to pine. The higher impact for pine comes with higher energy required in preprocessing such as size reduction compared to switchgrass. However, molten salt torrefaction can offer several options to reduce its environmental impact such as using a solar thermal reactor, and several salt blend options. It also results in higher quality products with wider scope in downstream application areas.

6.6. References

1. Tumuluru JS, Wright CT. A review on biomass densification technologies for energy application 2010. https://doi.org/10.2172/1016196.
2. Cahyanti MN, Doddapaneni TRKC, Kikas T. Biomass torrefaction: An overview on process parameters, economic and environmental aspects and recent advancements. Bioresour Technol 2020;301:122737. https://doi.org/10.1016/J.BIORTECH.2020.122737.
3. Sher F, Yaqoob A, Saeed F, Zhang S, Jahan Z, Klemeš JJ. Torrefied biomass fuels as a renewable alternative to coal in co-firing for power generation. Energy 2020;209:118444. https://doi.org/10.1016/J.ENERGY.2020.118444.
4. Dudyński M, Van Dyk JC, Kwiatkowski K, Sosnowska M. Biomass gasification: Influence of torrefaction on syngas production and tar formation. Fuel Processing Technology 2015;131:203–12. https://doi.org/10.1016/J.FUPROC.2014.11.018.
5. Prins MJ, Ptasinski KJ, Janssen FJJG. More efficient biomass gasification via torrefaction. Energy 2006;31:3458–70. https://doi.org/10.1016/J.ENERGY.2006.03.008.
6. Boateng AA, Mullen CA. Fast pyrolysis of biomass thermally pretreated by torrefaction. J Anal Appl Pyrolysis 2013;100:95–102. https://doi.org/10.1016/J.JAAP.2012.12.002.
7. Singh H, Northup BK, Rice CW, Prasad PVV. Biochar applications influence soil physical and chemical properties, microbial diversity, and crop productivity: a meta-analysis. Biochar 2022;4:1–17. https://doi.org/10.1007/S42773-022-00138-1/FIGURES/7.
8. Brassard P, Godbout S, Lévesque V, Palacios JH, Raghavan V, Ahmed A, et al. Biochar for soil amendment. Char and Carbon Materials Derived from Biomass: Production,

Characterization and Applications 2019:109–46. https://doi.org/10.1016/B978-0-12-814893-8.00004-3.

9. Chen WH, Lin BJ, Lin YY, Chu YS, Ubando AT, Show PL, et al. Progress in biomass torrefaction: Principles, applications and challenges. Prog Energy Combust Sci 2021;82:100887. https://doi.org/10.1016/J.PECS.2020.100887.

10. Jalalabadi T, Moghtaderi B, Allen J. The interplay between ternary molten carbonate and biomaterials during pressurized slow pyrolysis. React Chem Eng 2022;7:674–90. https://doi.org/10.1039/D1RE00544H.

11. Nygård HS, Olsen E, Nygård HS, Olsen E. Molten salt pyrolysis of milled beech wood using an electrostatic precipitator for oil collection. AIMS Energy 2015 3:284 2015;3:284–96. https://doi.org/10.3934/ENERGY.2015.3.284.

12. Sun M, Zhu X, Wu C, Masek O, Wang CH, Shang J, et al. Customizing high-performance molten salt biochar from wood waste for CO2/N2 separation. Fuel Processing Technology 2022;234:107319. https://doi.org/10.1016/J.FUPROC.2022.107319.

13. Zhu X, Sun M, Zhu X, Guo W, Luo Z, Cai W, et al. Molten salt shielded pyrolysis of biomass waste: Development of hierarchical biochar, salt recovery, CO2 adsorption. Fuel 2023;334:126565. https://doi.org/10.1016/J.FUEL.2022.126565.

14. Purnomo V, F Luo. Torrefaction of biomass in molten salts to obtain useful bioproducts as renewable chemical resources. The 10th joint conference on chemistry, 2015.

15. Yang Y, Hu H, Yang F, Tang H, Liu H, Yi B, et al. Thermochemical conversion of lignocellulosic bio-waste via fast pyrolysis in molten salts. Fuel 2020;278:118228. https://doi.org/10.1016/J.FUEL.2020.118228.

16. Zeng K, Yang X, Xie Y, Yang H, Li J, Zhong D, et al. Molten salt pyrolysis of biomass: The evaluation of molten salt. Fuel 2021;302:121103. https://doi.org/10.1016/J.FUEL.2021.121103.

17. Su Y, Liu L, Dong Q, Xie Y, Wang P, Zhang S, et al. Investigation of molten salt in wet torrefaction and its effects on fast pyrolysis behaviors. Energy Sources, Part A: Recovery, Utilization, and Environmental Effects 2020;42:577–85. https://doi.org/10.1080/15567036.2019.1587104.

18. Xie Y, Zeng K, Flamant G, Yang H, Liu N, He X, et al. Solar pyrolysis of cotton stalk in molten salt for bio-fuel production. Energy 2019;179:1124–32. https://doi.org/10.1016/J.ENERGY.2019.05.055.

19. Liu Y, Zhang J, Hu H, Dai Q, Zou C, Cao C, et al. Influence mechanisms of torrefaction on syngas production from bio-waste molten salt thermal treatment. Fuel 2024;363:130965. https://doi.org/10.1016/J.FUEL.2024.130965.

20. Backer M, Gladen A. Impact of salt composition and temperature on low-temperature torrefaction of pine in molten nitrate salts. Energy 2023;263:126044. https://doi.org/10.1016/J.ENERGY.2022.126044.

21. Wang H, Zhang F, Li L, Yu H, Tu R, Jia Z, et al. Influence of Molten Salt Torrefaction Pretreatment on Upgrading of Bio-Oil from Camellia Oleifera Shell. SSRN Electronic Journal 2021. https://doi.org/10.2139/SSRN.3899840.

22. Kalogirou S. The potential of solar industrial process heat applications. Appl Energy 2003;76:337–61. https://doi.org/10.1016/S0306-2619(02)00176-9.

23. Akbari M, Oyedun AO, Gemechu E, Kumar A. Comparative life cycle energy and greenhouse gas footprints of dry and wet torrefaction processes of various biomass

feedstocks. J Environ Chem Eng 2021;9:105415. https://doi.org/10.1016/J.JECE.2021.105415.

24. Zhang C, Yang W, Chen WH, Ho SH, Pétrissans A, Pétrissans M. Effect of torrefaction on the structure and reactivity of rice straw as well as life cycle assessment of torrefaction process. Energy 2022;240:122470. https://doi.org/10.1016/J.ENERGY.2021.122470.

25. Adams PWR, Shirley JEJ, McManus MC. Comparative cradle-to-gate life cycle assessment of wood pellet production with torrefaction. Appl Energy 2015;138:367–80. https://doi.org/10.1016/J.APENERGY.2014.11.002.

26. Christoforou EA, Fokaides PA. Life cycle assessment (LCA) of olive husk torrefaction. Renew Energy 2016;90:257–66. https://doi.org/10.1016/J.RENENE.2016.01.022.

27. Thengane SK, Burek J, Kung KS, Ghoniem AF, Sanchez DL. Life cycle assessment of rice husk torrefaction and prospects for decentralized facilities at rice mills. J Clean Prod 2020;275:123177. https://doi.org/10.1016/J.JCLEPRO.2020.123177.

28. Kaliyan N, Morey RV, Tiffany DG, Lee WF. Life Cycle Assessment of Corn Stover Torrefaction Plant Integrated with a Corn Ethanol Plant and a Coal Fired Power Plant. American Society of Agricultural and Biological Engineers Annual International Meeting 2013, ASABE 2013 2013;1:1-. https://doi.org/10.13031/AIM.20131580611.

29. Ubando AT, Rivera DRT, Chen WH, Culaba AB. Life cycle assessment of torrefied microalgal biomass using torrefaction severity index with the consideration of up-scaling production. Renew Energy 2020;162:1113–24. https://doi.org/10.1016/J.RENENE.2020.08.068.

30. Shah A, Darr MJ, Medic D, Anex RP, Khanal S, Maski D. Techno-economic analysis of a production-scale torrefaction system for cellulosic biomass upgrading. Biofuels, Bioproducts and Biorefining 2012;6:45–57. https://doi.org/10.1002/BBB.336.

31. Carveth HR. Study of a three-component system. Journal of Physical Chemistry 1898;2:209–28. https://doi.org/10.1021/J150004A001.

32. Uknowledge U, Schiavone DF. Heat and Mass Transfer in Baled Switchgrass for Storage and Bioconversion Applications. Theses and Dissertations--Biosystems and Agricultural Engineering 2016. https://doi.org/http://dx.doi.org/10.13023/ETD.2016.136.

33. Wang T. Theoretical and experimental determination of chemical and physical properties of novel high thermal energy density molten salt systems for concentrating solar 2014.

34. Janz GJ, Truong GN. Melting and Premelting Properties of the KN03-NaN02-NaN03 Eutectic System. J Chem Eng Data 1983;28:201–2. https://doi.org/10.1021/JE00032A022/ASSET/JE00032A022.FP.PNG_V03.

35. Dakota N, Hellevang K. Air-to-air heat exchangers for healthier energy-efficient homes 2009.

36. Manouchehrinejad M, Bilek EMT, Mani S. Techno-economic analysis of integrated torrefaction and pelletization systems to produce torrefied wood pellets. Renew Energy 2021;178:483–93. https://doi.org/10.1016/J.RENENE.2021.06.064.

37. Kohlin L, Pritchard H, Gladen AC, Bajwa D. Molten Salt Biomass Torrefaction – A Sensitivity Analysis of Process Conditions. Ind Crops Prod 2024;UNDER REVIEW:1–39.

38. Kohlin L, Pritchard H, Heidari DehKordi B, Gladen AC, Bajwa D. Investigation on the catalytic ability of alkaline earth metal cations and nitrite anions on low temperature

molten salt torrefaction. ASME 18th International Conference on Energy Sustainability, Anaheim, CA 2024;Under Review.

39. Wang Z, Dunn J, Han J, Wang M. Material and energy flows in the production of cellulosic feedstocks for biofuels for the GREET model 2013.

40. Jannasch R, Quan Y, R Samson. A process and energy analysis of pelletizing switchgrass. Prepared by REAP-Canada (Www Reap-Canada Com) for Natural Resources 2001.

41. Cai H, Dunn J, Pegallapati A, Li Q, Canter C, Tan EC, et al. Supply Chain Sustainability Analysis of Renewable Hydrocarbon Fuels via Indirect Liquefaction, Fast Pyrolysis, and Hydrothermal Liquefaction: Update of the 2016 State-of-Technology Cases and Design Cases 2017. https://doi.org/10.2172/1569969.

42. Mcnamee P, Adams PWR, McManus MC, Dooley B, Darvell LI, Williams A, et al. An assessment of the torrefaction of North American pine and life cycle greenhouse gas emissions. Energy Convers Manag 2016;113:177–88. https://doi.org/10.1016/J.ENCONMAN.2016.01.006.

43. Winjobi O, Shonnard DR, Bar-Ziv E, Zhou W. Life cycle greenhouse gas emissions of bio-oil from two-step torrefaction and fast pyrolysis of pine. Biofuels, Bioproducts and Biorefining 2016;10:576–88. https://doi.org/10.1002/BBB.1660.

44. Deng Y, Li J, Li T, Gao X, Yuan C. Life cycle assessment of lithium sulfur battery for electric vehicles. J Power Sources 2017;343:284–95. https://doi.org/10.1016/J.JPOWSOUR.2017.01.036.

45. Kaya C, Ak BE, Higgs D. Response of Salt-Stressed Strawberry Plants to Supplementary Calcium Nitrate and/or Potassium Nitrate. J Plant Nutr 2003;26:543–60. https://doi.org/10.1081/PLN-120017664.

46. Zheng Y, Jia A, Ning T, Xu J, Li Z, Jiang G. Potassium nitrate application alleviates sodium chloride stress in winter wheat cultivars differing in salt tolerance. J Plant Physiol 2008;165:1455–65. https://doi.org/10.1016/J.JPLPH.2008.01.001.

47. Subbarao G V., Ito O, Berry WL, Wheeler RM. Sodium—A Functional Plant Nutrient. CRC Crit Rev Plant Sci 2003;22:391–416. https://doi.org/10.1080/07352680390243495.

48. Kaya C, Higgs D. Supplementary Potassium Nitrate Improves Salt Tolerance in Bell Pepper Plants. J Plant Nutr 2003;26:1367–82. https://doi.org/10.1081/PLN-120021048.

49. Silber A, Xu G, Wallach R. High irrigation frequency: The effect on plant growth and on uptake of water and nutrients. Acta Hortic 2003;627:89–96. https://doi.org/10.17660/ACTAHORTIC.2003.627.10.

50. Dai Z, Zhang X, Tang C, Muhammad N, Wu J, Brookes PC, et al. Potential role of biochars in decreasing soil acidification - A critical review. Science of The Total Environment 2017;581–582:601–11. https://doi.org/10.1016/J.SCITOTENV.2016.12.169.

51. Gao M, Ji D, Yu F, Ai N, Jiang H, Ji J. Influence of molten salts on pyrolysis characteristics of rice straw. Proceedings of 2012 International Conference on Biobase Material Science and Engineering, BMSE 2012 2012:151–5. https://doi.org/10.1109/BMSE.2012.6466201.

CHAPTER 7. OVERALL CONCLUSION AND FUTURE WORK

This dissertation was divided into two sections: one investigating the use of urea-siloxane coating for ice and fouling release applications and the other one using the economic and life cycle analysis tools for sustainability assessment of early-stage technologies including biobased chemical production, thermochemical energy storage materials, and molten salt biomass torrefaction system.

In Chapter 2, the polyurea-siloxane coating was prepared and modified with non-reactive silicone oils. The silicone oils included dimethyl-siloxane, phenylmethyl-dimethyl-siloxane, phenylmethyl-siloxane, and phenylmethyl-diphenyl-siloxane. These oils were tested at different percentages with polyurea-siloxane base coating for ice and fouling release applications. Different surface characterization techniques such as atomic force microscopy (AFM), contact angle, surface free energies, and XPS depth profiling were also performed. The base coating showed good mechanical properties. The addition of dimethyl and phenylmethyl dimethyl silicone oils lowered ice adhesion strength without any negative impact on the mechanical properties of the coating. AFM images showed the presence of silicone oils on the coating surface. Contact angle characterization showed a high-water contact angle, above 105°. Similarly, surface free energy was also low in the range of 20-30 mN/m. Higher molecular weight dimethyl and phenylmethyl dimethyl silicone oils showed low ice adhesion strength. These same formulations also showed low interfacial toughness less than 0.2 J/m2. The results of biofouling assays did not show any specific trend. Some formulations were better with one organism compared to the other. However, there was a positive correlation between ice adhesion strength and barnacle adhesion strength.

A possible future work for this study could be performing the durability tests of these coatings and determining how they perform over a long duration of icing deicing cycles. These sets of coatings could also be field tested to determine their actual performance on the field. In terms of the base matrix, there could be a lot of different modifications that could be tried. For example, the HDI trimer could be replaced with other isocyanates like IPDI. Similarly, the amino-functional silane could be different. There are a range of different alkoxy-functional amino-silane options that could be tested along with other di-substituted amines. Hydroxyl-terminated and methoxy-terminated PDMS oils could also be incorporated into the base matrix to improve the durability of the coating.

To improve the durability issue of using non-reactive silicone oils in the urea-siloxane matrix, chapter 3 investigates the use of reactive carbinol functional siloxanes. Carbinol functional poly(dimethylsiloxane) (PDMS) oils with different molecular weights were investigated. Both mono and di-functional siloxanes were used in the formulation. A total of 6 different formulations varying the siloxane type and quantity of siloxane were tested. The experiment was successful in grafting PDMS chains from the silicone oil into the matrix through the reaction between the hydroxyl group of the silicone oil and isocyanate. The remaining isocyanate reacted with amino-silane. NMR spectra were able to confirm the completion of the reactions. The surface characterization of the coatings through contact angles and surface-free energies showed that the grafted PDMS might be on both the top and bottom sides of the coating. This was confirmed through XPS depth profiling results. The results showed a similar amount of silicone presence on both the top and bottom sides. This might suggest that the PDMS domains are spread throughout the coating uniformly. AFM images confirmed the self-segregating property of PDMS chains through the formation of distinct domains on the coating surface.

Modulus measurements of the coatings showed that the modulus decreases with a higher amount of PDMS grafted to the matrix. Ice adhesion and interfacial toughness measurements showed that all the coatings showed improved performance compared to base coating. Interfacial toughness was lower than 1 J/m2 for all the formulations with PDMS grafted on it. Formulations with mono-functional PDMS oils showed the lowest interfacial toughness value. Similarly, ice adhesion was also lower for these formulations with less than 100 kPa. Overall, all the formulations showed promising performance for ice-shedding applications.

Previous studies in the Webster research group have shown promising performances of self-segregating coating in biofouling assays. The formulations developed in this study could be tested in a range of biofouling assays to determine their effectiveness. A possible future work for this study could be exploring the use of amine-terminated PDMSs. Amine-terminated PDMSs can react with isocyanate and form urea linkage. This would be more compatible with the base matrix which also has a urea backbone. Several di-block and triblock hydrophobic and amphiphilic copolymers developed in the Webster research group that have been studied with siloxane-polyurethane coatings could also be studied with this coating matrix. There are not many studies that performed ice adhesion and interfacial toughness tests with these coating chemistries.

In Chapter 4, techno-economic analysis (TEA) and life cycle assessment (LCA) tools were employed to assess the sustainability of producing lignin-based foam. Laboratory scale data were used to scale up the process and conduct process simulation in the Aspen Plus chemical process simulator. The mass and energy balance obtained from the process simulation were used to perform TEA and LCA. The economic analysis results determined the minimum selling price of the lignin-based foam to be $6.5/kg which is lower than the price of commercial rigid

polyurethane foam. The uncertainty analysis in economic analysis results shows that the price of lignin-based foam has the potential to lower the selling price further. LCA results also showed the environmental impact of producing lignin-based foam is lower in most impact categories compared to rigid polyurethane foam in terms of mass basis. The global warming potential of producing 1 kg of lignin-based foam was found to be 5.67 kg CO2 eq. However, the conclusion might be different if a volume-based functional unit was used. This is because lignin-based foam has a higher mass density than commercial rigid polyurethane foam. If a volume-based functional unit is chosen, lignin-based foam would cost more and would have a higher environmental impact compared to rigid polyurethane foam. Both economic and LCA results showed tert-butyl acetoacetate (tBAA) to have the highest impact followed by amine crosslinker. Lignin-based foam can qualify for the USDA BioPreferred program because it can contain more than 30% of biobased carbon.

Future work for this study can consider using an alternative functionalizing chemical. tBAA had the highest contribution in most of the environmental impact categories. One option could be using diketene directly instead of tBAA. However, diketene is very reactive and toxic, so it requires proper handling. Another option could be using an acetone adduct of diketene instead of tBAAA. However, further analysis is needed if they are better alternatives than tBAA. Future work can also explore the use of biorefinery lignin. Compared to kraft lignin, biorefinery lignin is more reactive, pure, and has a low molecular weight. Due to the superior quality of biorefinery lignin, a higher amount of lignin could also be incorporated into the formulation. It would be good to compare the properties of foam produced by using these two different lignin sources.

Chapter 5 used the LCA tool to screen materials for thermochemical energy storage applications. A cradle-to-gate LCA was conducted along with cumulative energy demand and cost analyses. Ten different salt hydrates cellulose nanocrystal (CNC) composites were analyzed for their environmental performance. Both laboratory scale models and scaled-up models were considered for the synthesis of salt-CNC composites. The result showed that sulfur-containing salts performed environmentally better than other salts. Salts such as lanthanum chloride, lithium chloride, and lithium hydroxide have either higher environmental impacts or costs, so they can be ruled out as a choice. The best-performing salt was magnesium sulfate. CNC, which was used in the formulation to improve the salt cycle stability was the major hotspot in environmental impacts. However, CNC has the advantage of prolonging the life of the composite. An expanded LCA up to the product application stage can provide more insights into this and whether using more CNC is environmentally not favorable. The lab scale process showed higher environmental impact from mixing and sonication processes. A scaled-up process showed almost 40% reduction in energy usage and thus less environmental impact. The ranking of salts and salt-CNC composites based on the weighted average of costs of materials and their environmental impact again showed magnesium sulfate to be the first-choice salts with a close tier of other salts such as zinc sulfate, sodium sulfide, strontium chloride, strontium bromide, and magnesium chloride.

A possible future work for this project would be to consider doing the techno-economic analysis and determining the cost of producing salt-CNC composites. A detailed economic analysis can help identify areas that need to be improved to make the product economically competitive. In our current analysis, CNC was shown to be one of the major hotspots. Therefore, future studies can look into cost-effective and low-environmental impact methods of producing CNC. One pathway can potentially be looking at alternative feedstock for CNC production, for

example, sugar beet pulp which is cheaper than Kraft pulp. Future experimental work can also consider directly using a cellulose nanofiber (CNF) instead of CNC. CNF is easier to produce and less energy-chemical intensive than CNC, thus can be produced at a lower cost and with less environmental impact. The analysis considered here was cradle-to-gate analysis. However, including the end-of-life part of the salt-CNC composite in the analysis can provide a better estimate. Since, CNC is used as a stabilizing agent, considering the whole life of the product might reduce its overall impact. However, there is some challenge in performing this analysis because salt-CNC is a new kind of material and there are no data on long-term usage of these materials.

In Chapter 6, the LCA tool was again used to identify the major process hotspots in the molten salt-biomass torrefaction system. The molten salt-biomass torrefaction system is a fairly new technology and the LCA tool can help to identify areas for improvement to reduce its environmental impacts. A total of 6 different salt blends were considered for pine torrefaction and 2 salt blends for switchgrass torrefaction. Traditional torrefaction was also considered for both feedstocks. The LCA results showed that salts were the major hotspots in the torrefaction process. Among the salt constituents, lithium nitrate had the highest environmental impact. Feedstock was the second major hotspot. The primary reason for this was due to the energy consumed in preprocessing of the feedstock which included processes like drying and size reduction. When torgas combustion was considered, assuming the total energy of biomass is conserved, the torrefaction plant runs in auto thermal condition and there can be surplus energy that could be used to generate electricity. However, it is still doubtful if the torrgas could be combustible or not. So, the LCA analysis without torrgas combustion was also performed. The heat required to dry and torrefy biomass could be replaced by some renewable source. One

example would be solar thermal reactors. Salt torrefaction broadens the scope of using solar thermal reactors because salt torrefaction reduces torrefaction processing temperature which could be achievable in wider geographical location. This might make salt torrefaction viable even on smaller scales, without it needing to be processed in a large central biorefinery, which again complicates biomass logistics.

This study mostly considered using lithium nitrate as one of the constituents of salt blends. Since lithium nitrate has a very high environmental impact compared to other salts, future work can consider using salt blends that do not use lithium nitrate. This can also expand the scope of the application of torrefied biomass. For example, if the torrefied biomass does not use lithium nitrate, it can be used for soil amendment purposes since lithium nitrate is not beneficial for soil and other salts like potassium and sodium nitrate are. The benefit of salt-torrefied biomass in downstream applications such as pyrolysis and gasification can also be quantified in future work. This will further highlight the benefits of using molten salt-biomass torrefaction through the reduction in the processing temperatures of pyrolysis and gasification process, and the production of better-quality products. Another future work to consider could be using a mild form of torrefaction as a pretreatment process for biomass deconstruction, without losing many saccharides, and then using that torrefied biomass in enzymatic hydrolysis and fermentation process. Few studies suggested that torrefied biomass does not inhibit hydrolysis and fermentation, however further tests must be conducted to confirm.

Overall, both experimental and computational techniques were employed in this dissertation to develop novel, environment-friendly, and sustainable materials.

APPENDIX A. CHAPTER 2 SUPPLEMENTAL INFORMATION

A.1. Biological assays – water aging

Coatings used for biological assays were pre-leached for 28 days in running tap water. After the completion of water immersion preconditioning regimen, 1.0 mL of artificial sea water (ASW)-based growth medium was added to the preconditioned coatings prepared in 24-well plates, placed on an orbital shaker (150 rpm) for 24hr at ambient laboratory conditions, and the resulting coating leachates/extracts were collected. The collected leachates were inoculated with a 0.05 ml suspension of 107 cells of bacteria in biofilm growth medium (BGM; 0.5 g of peptone and 0.1 g of yeast extract per liter ASW) or 0.05 ml of a 0.03 OD600 microalgae suspension in Guillard's F/2 medium and 0.2 ml aliquots of the inoculated coating leachates were transferred in triplicate to a 96-well plate. Bacteria leachate plates were incubated for 24 hours at 28°C and for 48 h at 18°C in an illuminated growth cabinet with a 16:8 light:dark cycle (photon flux density 33 mmol m-2 s-1) for microalgae. The bacteria plates were rinsed 3x with deionized water and the retained biofilms stained with 0.5 ml of crystal violet dye solution in deionized water for 15 minutes. Then, 0.5 ml of 33% glacial acetic acid was added to each coating well to extract the crystal violet dye and absorbance measurements was made at 600 nm with a multi-well plate spectrophotometer. Microalgae leachate plates were quantified for growth by measuring chlorophyll fluorescence (excitation: 360 nm; emission: 670 nm). Coating leachates that exhibit a >25% reduction in the amount of bacteria solution/biofilm growth or microalgae biofilm growth compared with a positive growth control were considered as a consequence of toxic components released from the coating into the overlying medium.

A.2. Bacterial (*Cellulophaga lytica*) biofilm growth and adhesion

Overnight cultures of the marine bacterium, *Cellulophaga lytica*, in marine broth was harvested by centrifugation (10,000×g for 10 min) and rinsed three times with sterile ASW. The resulting *C. lytica* pellet was then re-suspended in ASW and used to inoculate BGM to achieve a final cell density of 107 to 108 cells/mL. Subsequently, 1.0 ml of the *C. lytica* resuspension in BGM was added to each well of the coating plates and incubated at 28°C for 24 hours, rinsed 3x with deionized (DI) water, and stained with crystal violet dye for 15 min, followed by an additional 3x rinse with DI water, and dried for 1 hour at ambient laboratory conditions. The biofilm-bound crystal violet was extracted from the biofilms on the coating surfaces by adding 0.5 ml of 33% acetic acid for 15 min and the resulting eluates transferred to a 96-well plate and measured for absorbance at 600 nm using a multi-well plate spectrophotometer to quantify biofilm growth.

Subsequent to crystal violet staining of 24-hour biofilm surface growth, the coating plates were imaged with a digital camera to enable percentage surface coverage measurements for biofilm retraction calculations that provide an indicator of FR performance.

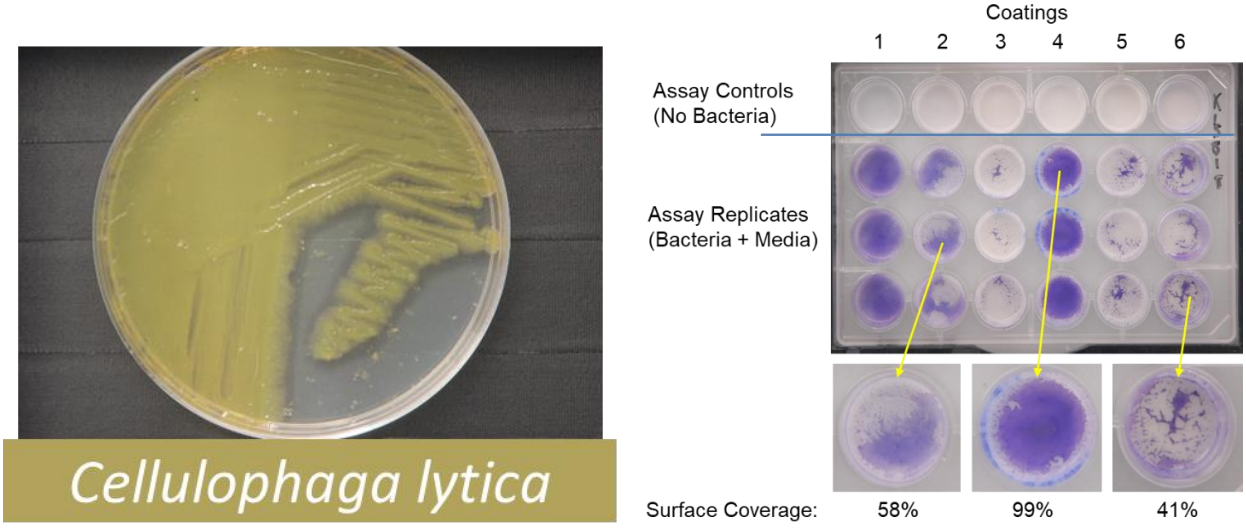

Figure A1. Samples used in *C. lytica* bioassay

A.3. Diatom (*Navicula incerta*) growth and release, and Green microalgae (*Chlorella vulgaris*) cell attachement and biofilm growth

Five-day old cultures of the marine brown microalgae diatom *Navicula incerta* or the green microalgae *Chlorella vulgaris* was re-suspended in fresh Guillard's F/2 medium prepared in ASW to achieve a final cell density of 105 cell/mL. Subsequently, 1.0 ml of the resulting microalgae suspension was added to each well of the coating plates and incubated at 18°C for 2 hours or 48 hours in an illuminated growth cabinet with a 16:8 light:dark cycle (photon flux density 33 mmol m-2 s-1) to facilitate cell attachment and biofilm growth, respectively. The coatings were then extracted with 0.6 mL (cell attachment) or 1.0 mL (biofilm growth) of DMSO for 20 minutes and 0.15 mL of the resulting eluates was transferred to a 96-well plate and measured for fluorescence of chlorophyll (Ex: 360 nm; Em: 670 nm) using a multi-well plate spectrophotometer to quantify cell attachment and/or biofilm growth.

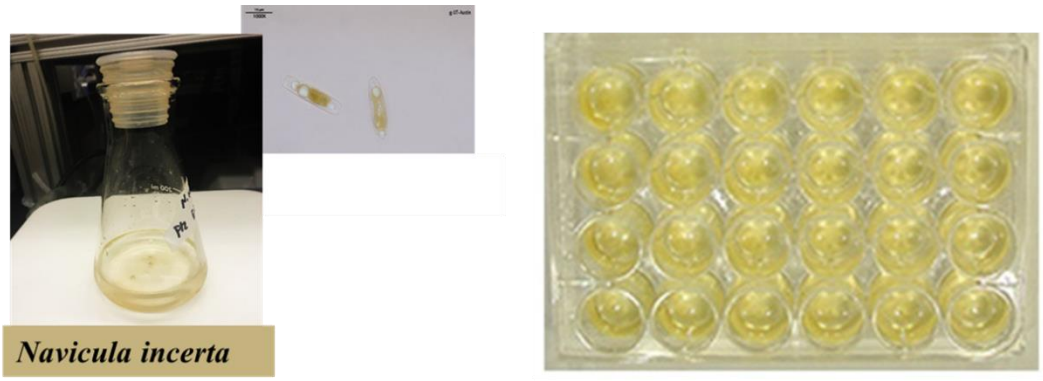

Figure A2. Samples used in *N. incerta* bioassay

After microalgae 2-hour cell attachment and 24-hour bacteria biofilm growth, the coating plates were transferred to the deck of an automated water-jet apparatus and the coatings were subjected to water-jet treatments at two different nozzle pressures of 10 and 20 psi for 5-10 seconds. Percent bacteria biofilm and microalgae cell removal calculations were determined by

comparing the total biomass on the coating surfaces before and after the water-jet treatments as follows:

$$\%\ Biofilm\ Removal = \left(1 - \frac{TBMJ}{TBMNJ}\right) \times 100$$

where *TBMJ* is the mean crystal violet absorbance/chlorophyll fluorescence value of three replicate jetted samples and *TBMNJ* is the mean crystal violet absorbance/chlorophyll fluorescence value of three replicate non-jetted samples.

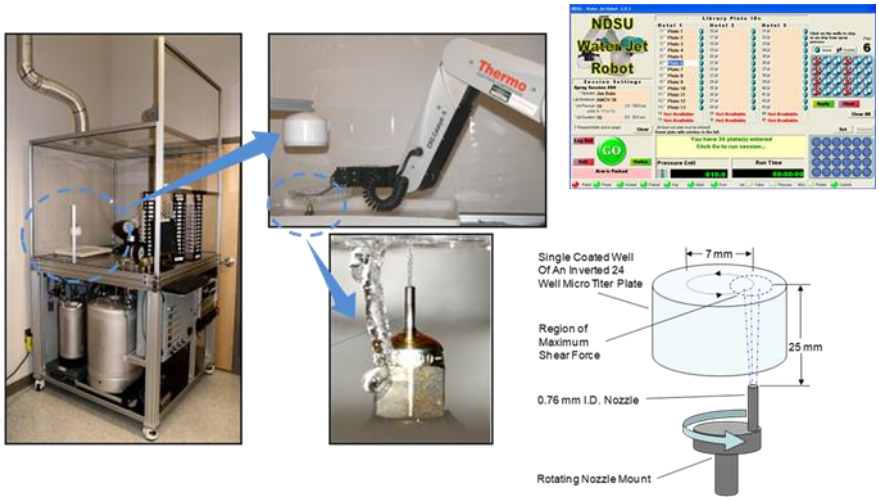

Figure A3. Test setup for *C. vulgaris* bioassay

A.4. Adult barnacle (*Amphibalanus amphitrite*) 2-week attachment and adhesion

Six adult barnacles (Amphibalanus amphitrite) of a testable size (>5 mm basal diameter) were placed on the surface of the experimental coatings, immobilized with a custom template and immersed in an ASW tank system. The reattached barnacles were fed daily with freshly hatched brine shrimp nauplii (Artemia sp.). After 14 days of immersion, the immobilization templates were removed, and the adhered barnacles were dislodged from the coating surfaces using a semi-automated force gage in shear to measure the peak force at release. The area of the barnacle base plates was measured, and the adhesion strengths (MPa) calculated by dividing the force required to remove the barnacles by the basal area. Barnacle adhesion was reported as the

mean value of the total number of barnacles that had a measurable detachment force. Barnacles that had no measurable force for detachment were counted as "not attached" and were omitted in the adhesion calculations.

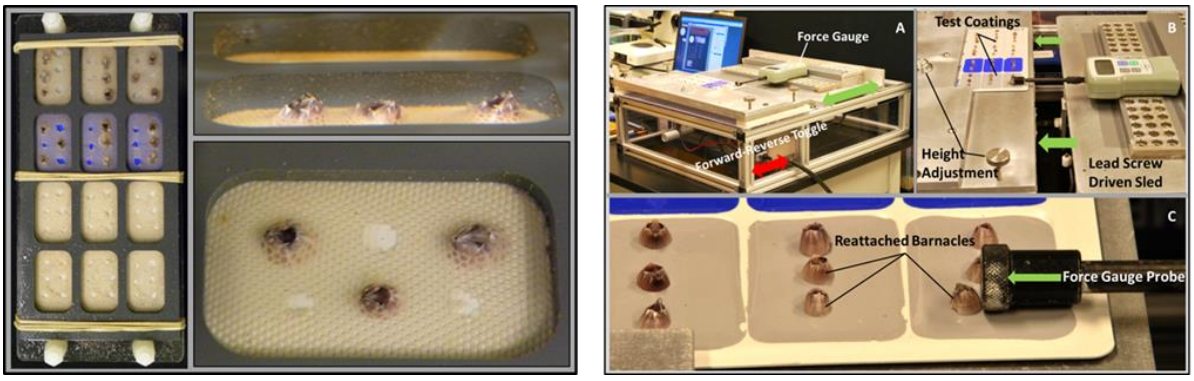

Figure A4. Test setup for *A. amphitrite* bioassay

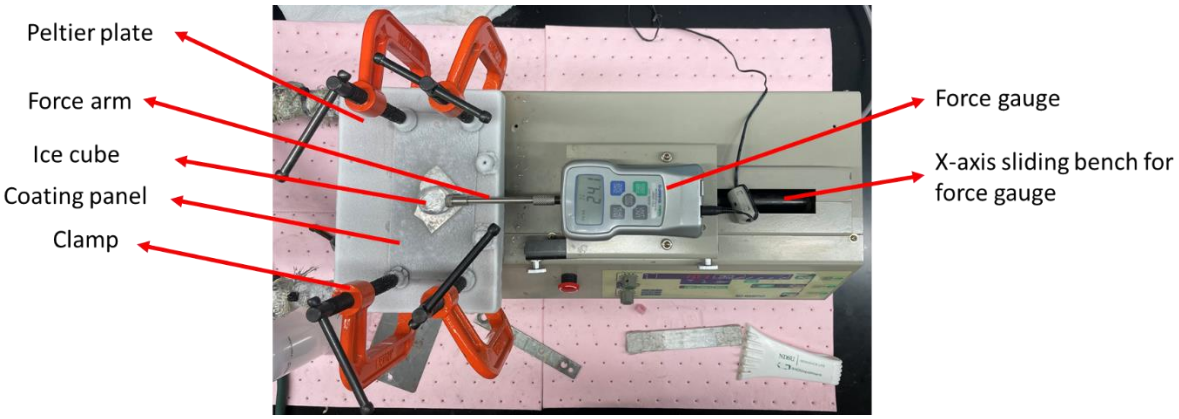

Figure A5. Ice adhesion test setup (at North Dakota State University)

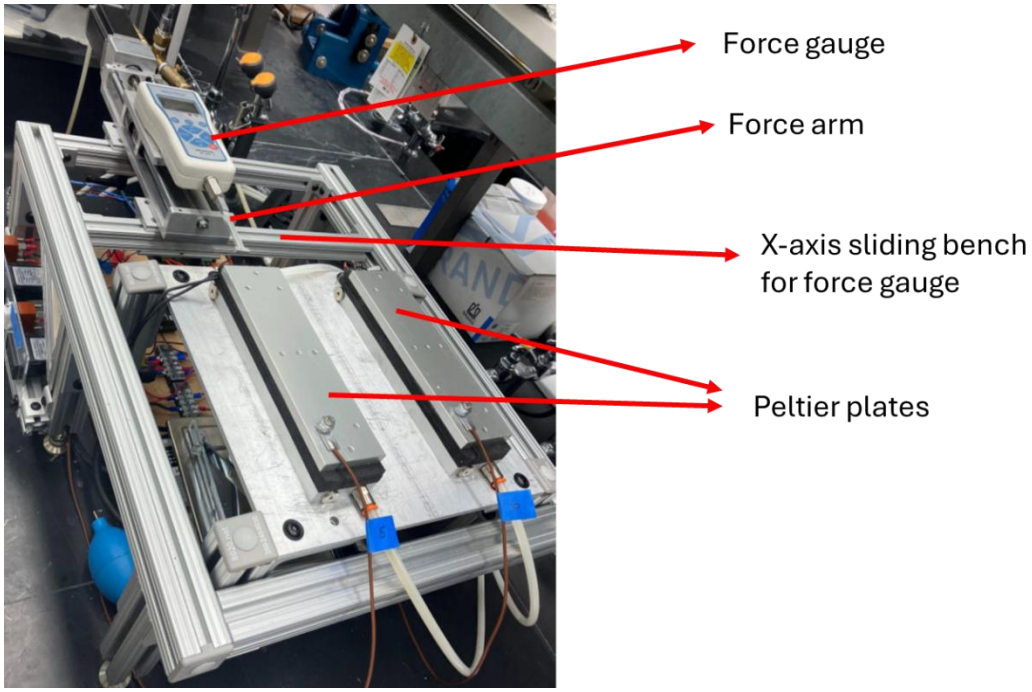

Figure A6. Interfacial toughness measurement setup (at University of Michigan)

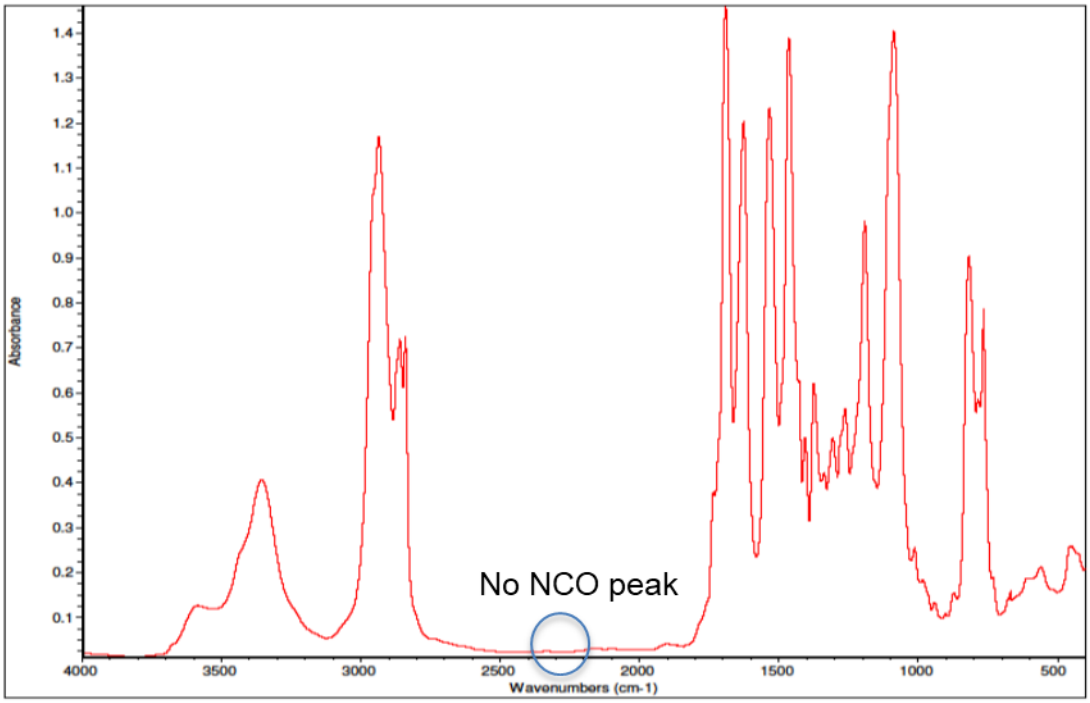

Figure A7. FTIR spectra of synthesized urea-siloxane resin

Table A1. The results of mechanical tests for coatings with different silicone oils at different percentages

Formula-tions	Film thickness (μm)	Pendulum hardness (s)	Pencil hard-ness	MEK double rubs	Conical mandrel	Cross-hatch adhesion	Impact resistance (lbs.in)	
							Front	Back
F-0	57.95±7.83	85.33±2.52	1H	200+	Pass	5B	164+	164+
F-1	48.63±3.69	107.25±2.06	HB	200+	Pass	5B	164+	164+
F-2	48.78±3.07	40±14.11	1B	200+	Pass	5B	164+	164+
F-3	51.0±4.82	74.67±1.15	1B	200+	Pass	5B	164+	164+
F-4	48.8±8.54	44.2±9.98	1B	200+	Pass	5B	164+	164+
F-5	49.55±3.82	25.33±6.03	1B	200+	Pass	5B	164+	164+
F-6	46.13±3.89	26±10.15	HB	200+	Pass	5B	164+	164+
F-7	48.98±10.31	57.33±2.31	2B	200+	Pass	5B	164+	164+
F-8	61.86±7.37	39.67±13.05	2H	200+	Pass	5B	164+	164+
F-9	48.23±5.16	65.33±7.77	HB	200+	Pass	5B	164+	164+
F-10	55.47±7.48	34.33±5.69	HB	200+	Pass	5B	164+	114
F-11	61.4±13.04	124.67±32.01	1H	200+	Pass	5B	122	67
F-12	51.27±4.63	94.67±4.04	1B	200+	Pass	5B	164+	110
F-13	83.53±7.75	103.33±2.08	2H	200+	Pass	5B	90	43
F-14	60.46±6.96	45.0±6.08	1H	95	Pass	5B	164+	164+
F-15	50.25±4.59	84.67±4.04	1B	190	Pass	5B	164+	164+
F-16	50.23±4.16	82.0±5.29	1B	200+	Pass	5B	164+	164+

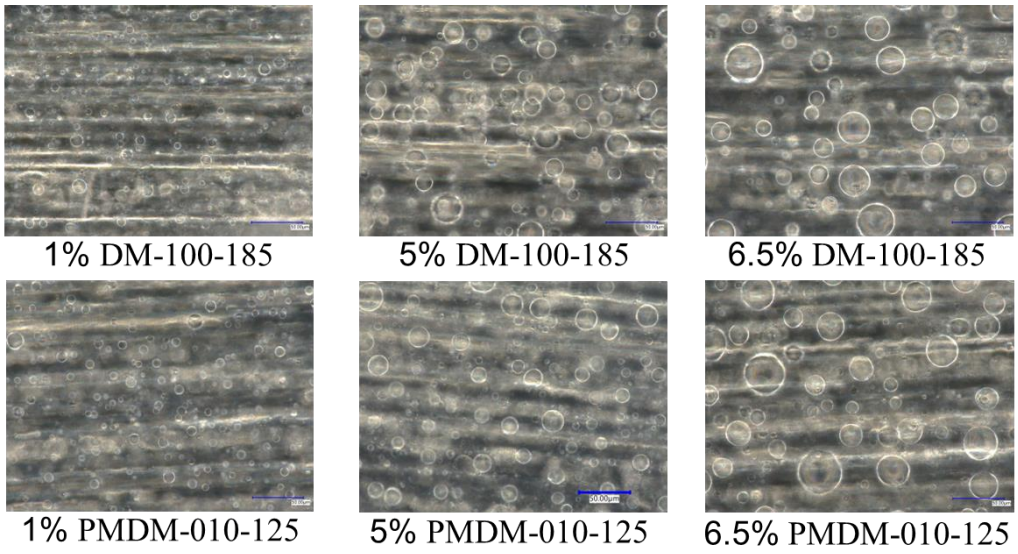

Figure A8. Digital microscope images of different formulations

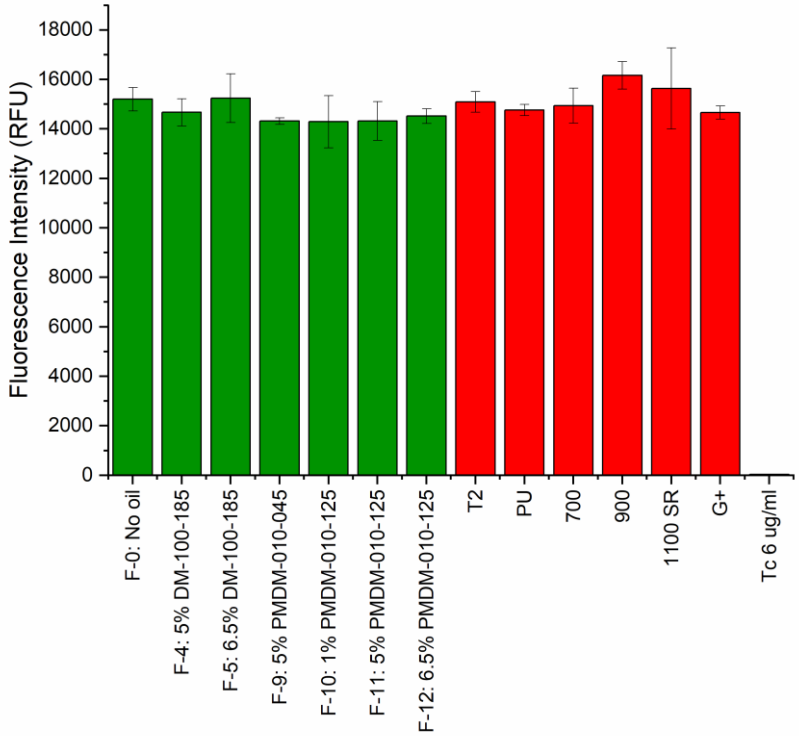

Figure A9. *N. incerta* leachate toxicity

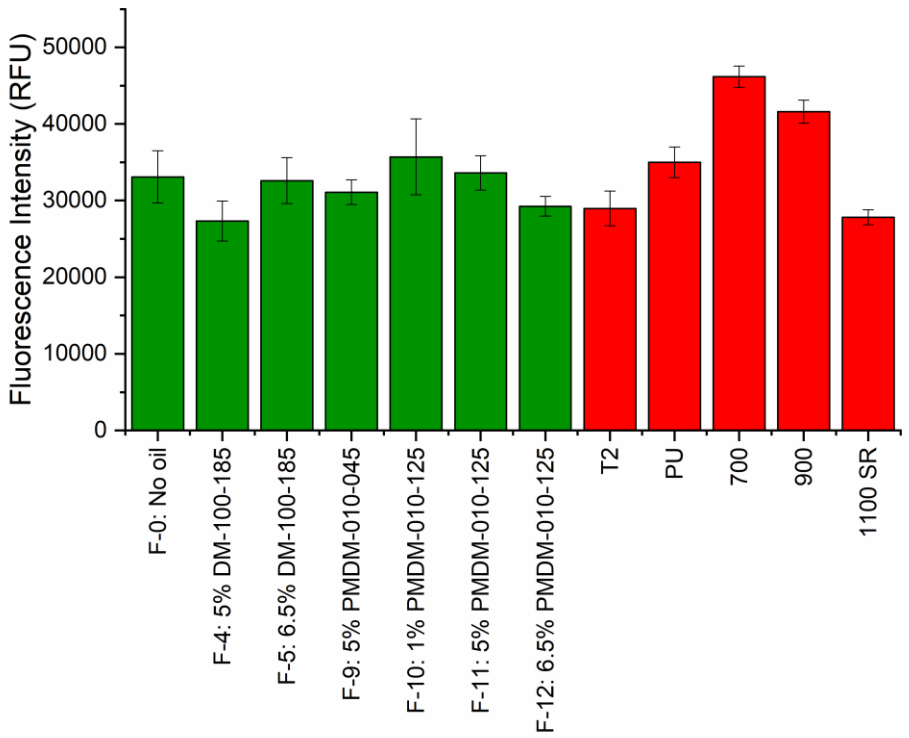

Figure A10. Biofilm growth of *N. incerta*

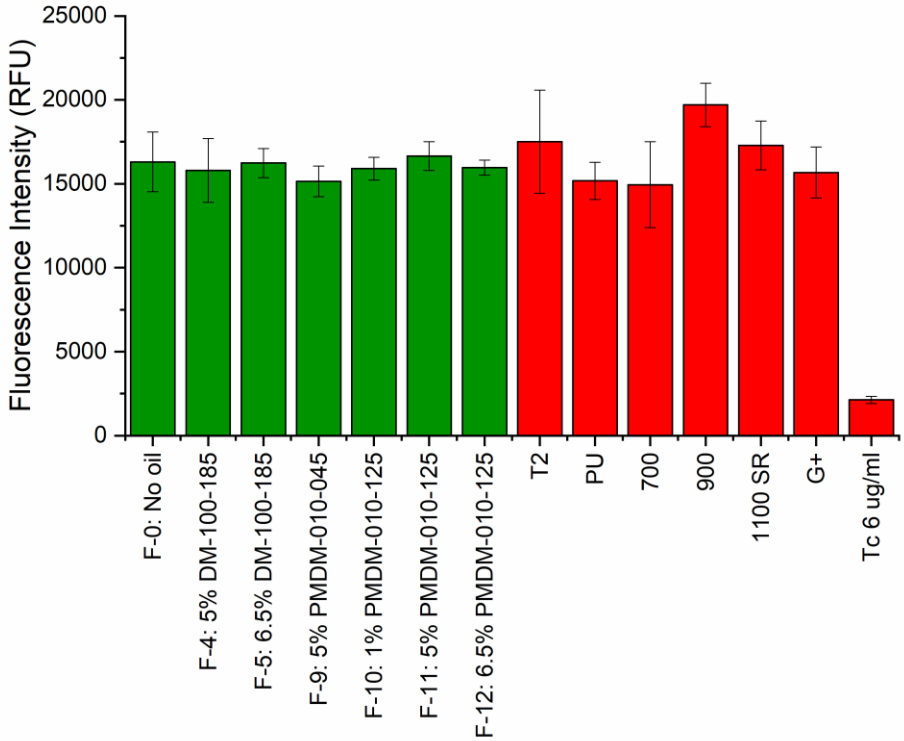

Figure A11. Leachate toxicity of *C. vulgaris*

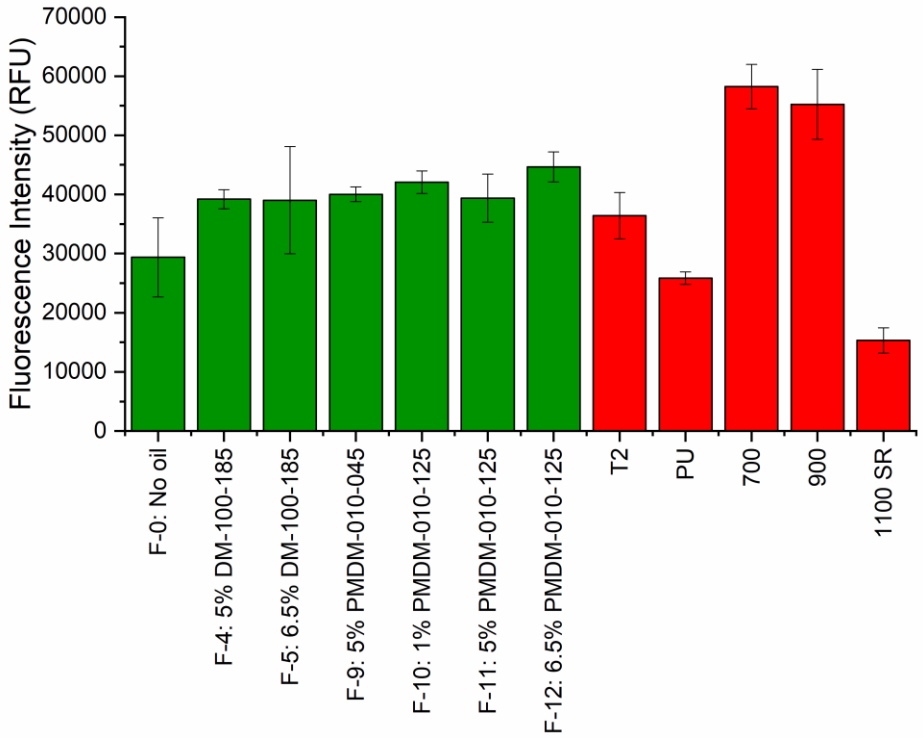

Figure A12. *C. vulgaris* biofilm growth after 48 hours

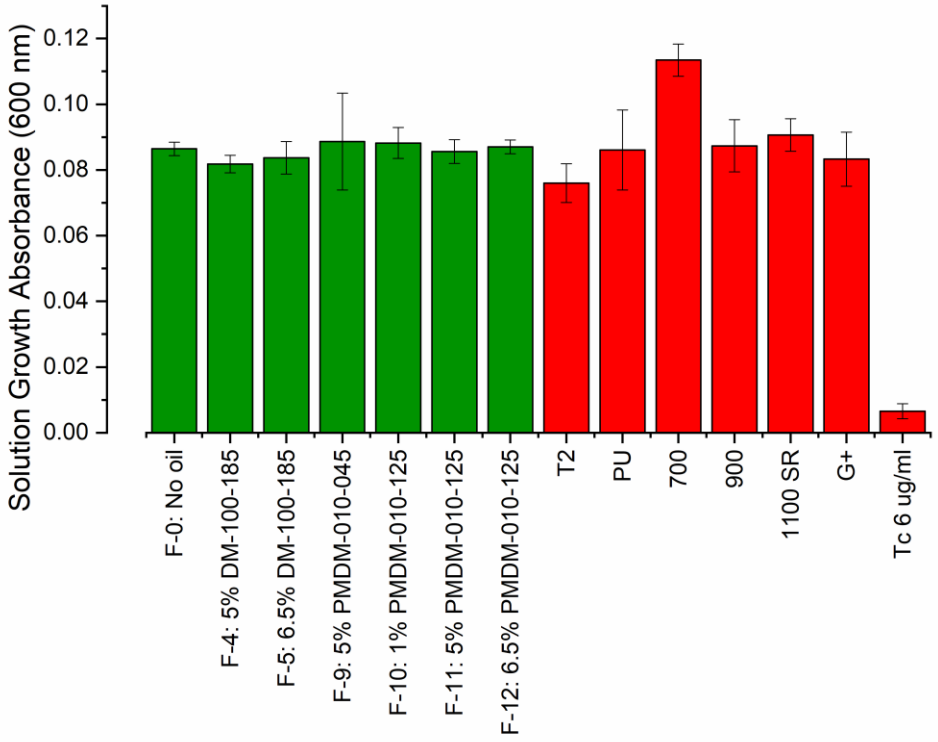

Figure A13. *C. lytica* leachate toxicity – solution growth

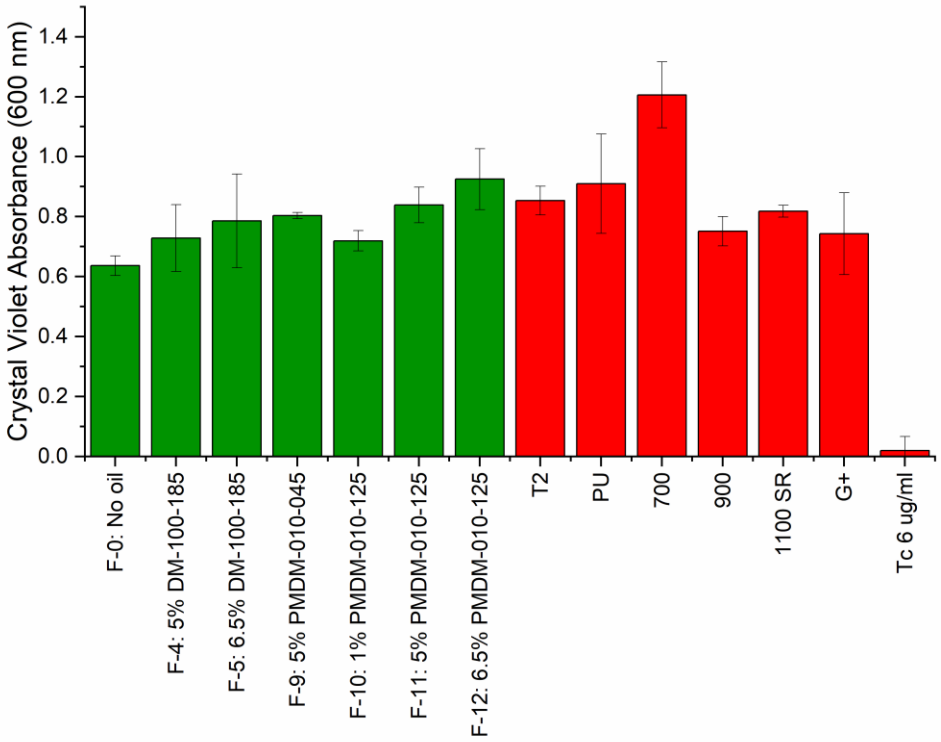

Figure A14. *C. lytica* leachate toxicity – biofilm growth

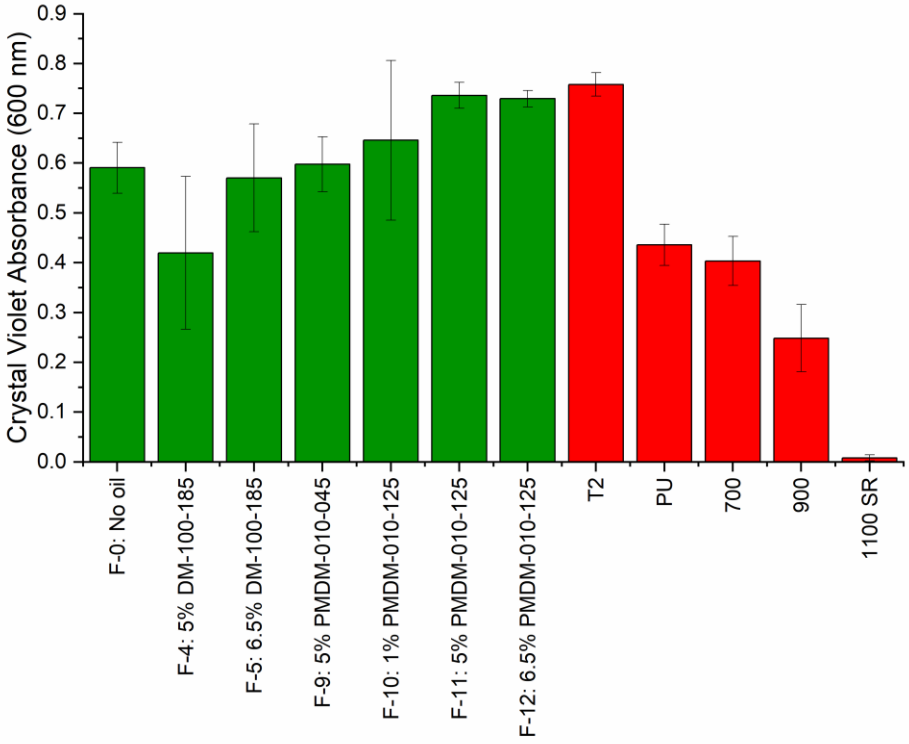

Figure A15. Bacterial biofilm growth of *C. lytica* after 24 hours

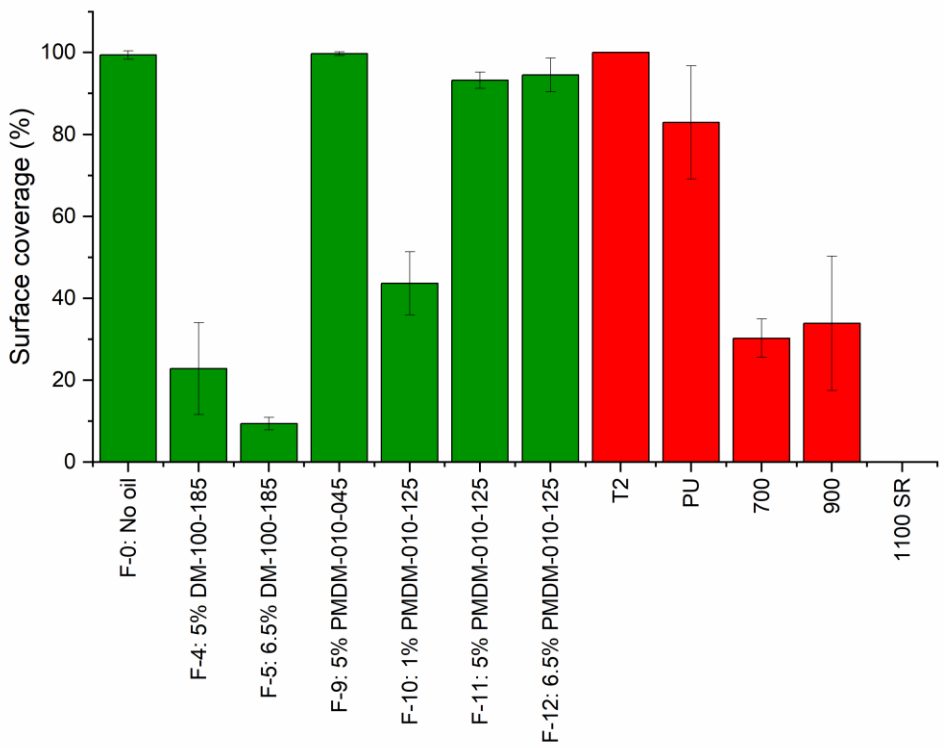

Figure A16. Bacterial biofilm retraction of *C. lytica* after 24 hours

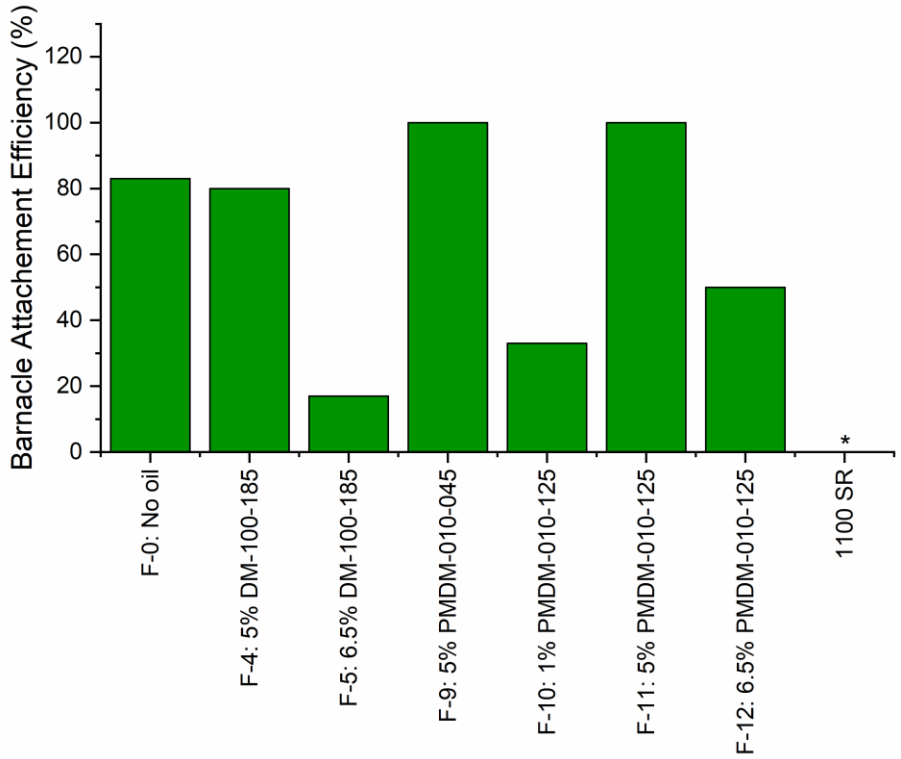

Figure A17. *A.* amphitrite barnacle attachment efficiency. * represents no barnacle attachment

APPENDIX B. CHAPTER 3 SUPPLEMENTAL INFORMATION

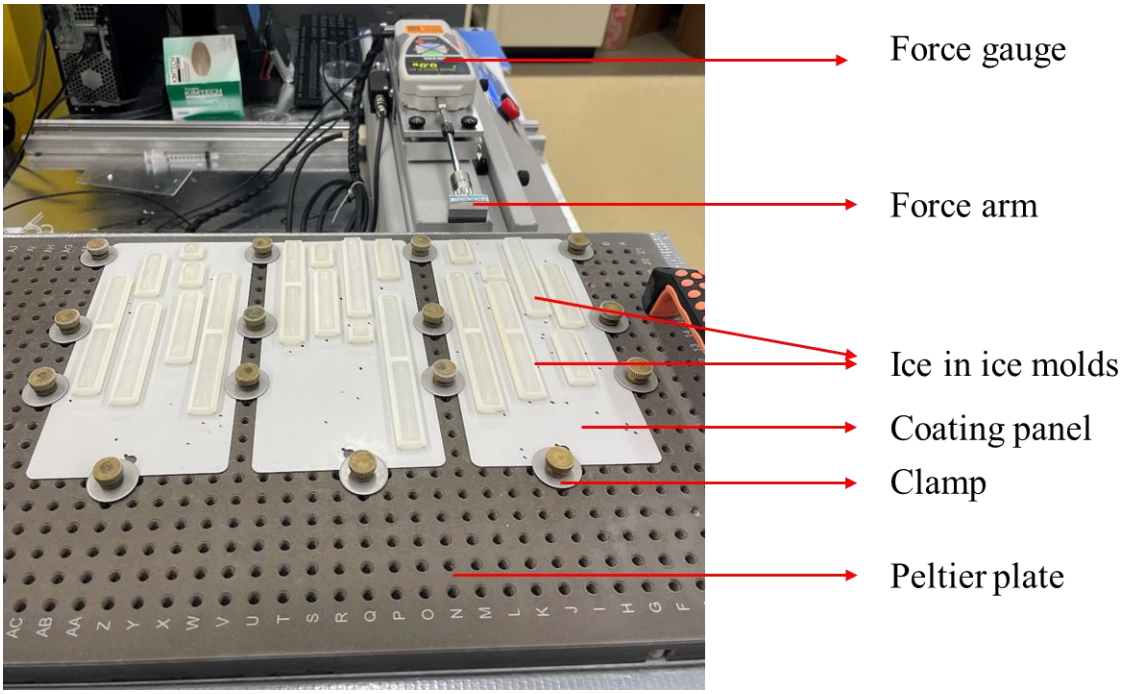

Figure B1. Ice adhesion test setup

B.1. NMR of MCR-C12 (representative of mono-functional carbinols)

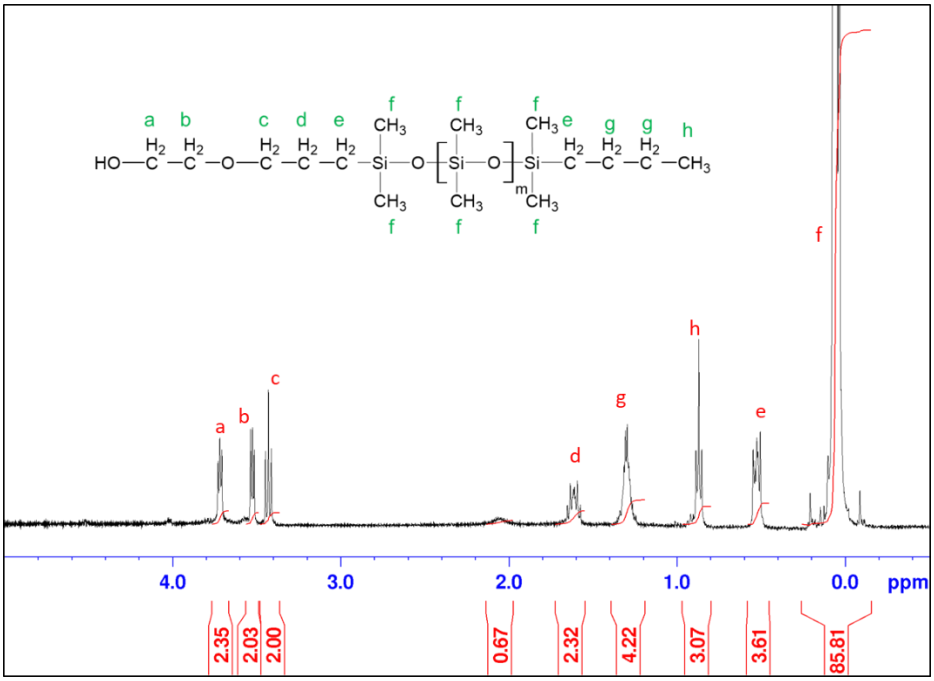

Figure B2. NMR spectra of MCR-C12 (representative of mono-functional carbinol terminated siloxane)

δ = 0.02-0.10 (m, [6 × m + 12]H, C$\underline{H}_3$-Si), δ = 0.49-0.56 (m, 4H, Si-C$\underline{H}_2$-CH_2), δ = 0.88 (t, 3H, CH_2-C$\underline{H}_3$, $^3J_{HH}$ = 6.9 Hz), δ = 1.24-1.36 (m, 2H, Si-CH_2-C$\underline{H}_2$-CH_2; 2H, CH_2-C$\underline{H}_2$-CH_3), δ = 1.57–1.66 (m, 2H, CH_2-C$\underline{H}_2$-CH_2-O), δ = 3.44 (t, 2H, CH_2-C$\underline{H}_2$-O-CH_2, $^3J_{HH}$ = 7.0), δ = 3.53 (t, 2H, HO-CH_2-C$\underline{H}_2$-O-CH_2, $^3J_{HH}$ = 4.6 Hz), δ = 3.73 (t, 2H, HO-C$\underline{H}_2$-CH_2-O-CH_2, $^3J_{HH}$ = 4.6 Hz).

t = triplet, m = multiplet.

Peak a was attributed based on Sonderbaek et al. [1].

Peaks b and c were attributed based on Pasek-Allen et al. [2].

Peak d was attributed based on Boucher et al. [3].

B.2. NMR of DMS-C15 (representative of di-functional carbinols)

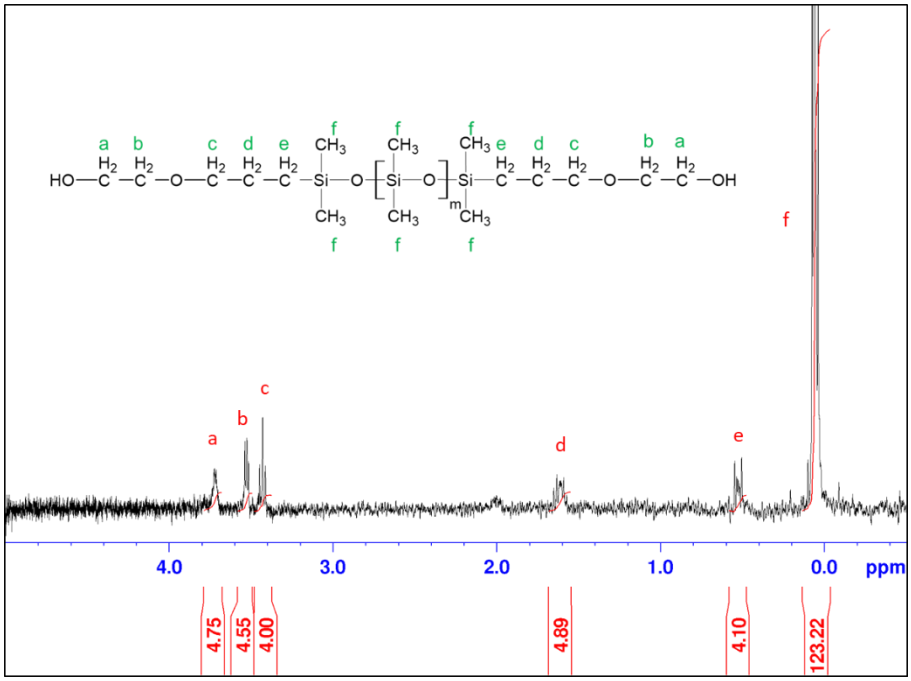

Figure B3. NMR spectra of DMS-C15 (representative of di-functional carbinol terminated siloxane)

δ = 0.02-0.10 (m, [6 × m + 12]H, C$\underline{H}_3$-Si), δ = 0.49-0.56 (m, 4H, Si-C$\underline{H}_2$-CH_2), δ = 1.57–1.66 (m, 4H, CH_2-C$\underline{H}_2$-CH_2-O), δ = 3.44 (t, 4H, CH_2-C$\underline{H}_2$-O-CH_2, $^3J_{HH}$ = 7.0), δ = 3.53 (t, 4H, HO-CH_2-C$\underline{H}_2$-O-CH_2, $^3J_{HH}$ = 4.6 Hz), δ = 3.73 (t, 4H, HO-C$\underline{H}_2$-CH_2-O-CH_2, $^3J_{HH}$ = 4.6 Hz).

t = triplet, m = multiplet.

Peak a was attributed based on Sonderbaek et al. [1].

Peaks b and c were attributed based on Pasek-Allen et al. [2].

Peak d was attributed based on Boucher et al. [3].

B.3. NMR of SIB1932.2 (n-BUTYLAMINOPROPYLTRIMETHOXYSILANE referred as Aminosilane)

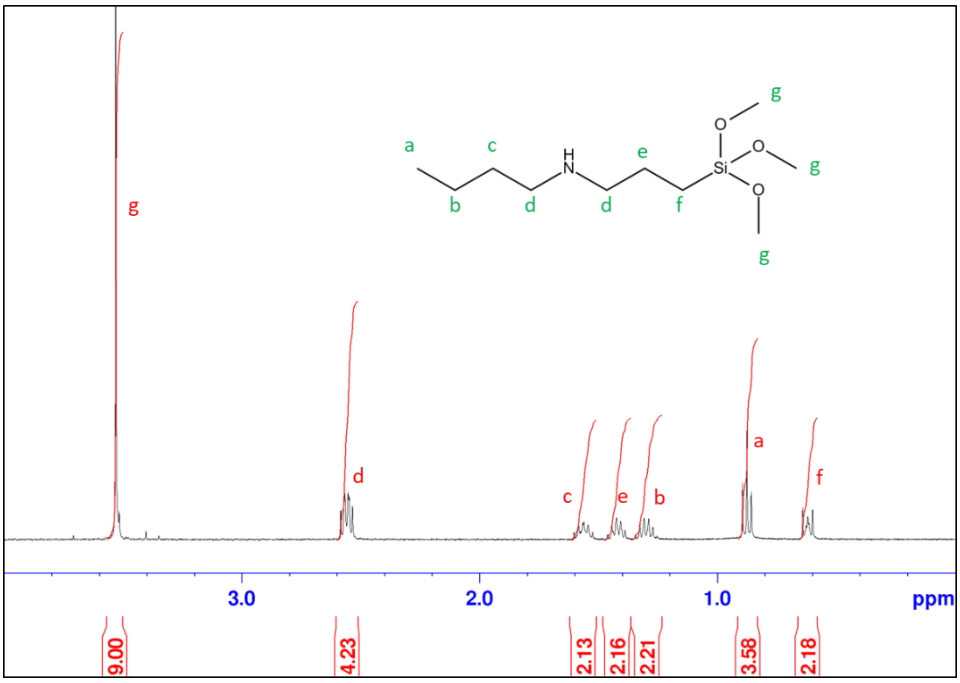

Figure B4. NMR spectra of SIB1932.2 (n-BUTYLAMINOPROPYLTRIMETHOXYSILANE referred as Amino-silane)

δ = 0.58-0.65 (m, 2H, Si-C<u>H</u>$_2$-CH$_2$), δ = 0.88 (t, 3H, CH$_2$-C<u>H</u>$_3$, $^3J_{HH}$ = 7.2 Hz), δ = 1.25-1.35 (s_x, 2H, CH$_3$-C<u>H</u>$_2$-CH$_2$-CH$_2$, $^3J_{HH}$ = 7.6 Hz), δ = 1.38-1.47 (m, 2H, HN-CH$_2$-C<u>H</u>$_2$-CH$_2$-Si), δ = 1.52-1.61 (m, 2H, HN-CH$_2$-C<u>H</u>$_2$-CH$_2$-CH$_3$), δ = 2.56 (dt, 4H, HN-C<u>H</u>$_2$-CH$_2$, $^2J_{HH}$ = 5.3 Hz, $^3J_{HH}$ = 7.2 Hz), δ = 3.53 (s, 9H, Si-O-C<u>H</u>$_3$).

s = singlet, t = triplet, m = multiplet, s_x = sextet, dt = doublet of triplet

B.4. NMR of Desmodur N3600 (referred as Isocyanate)

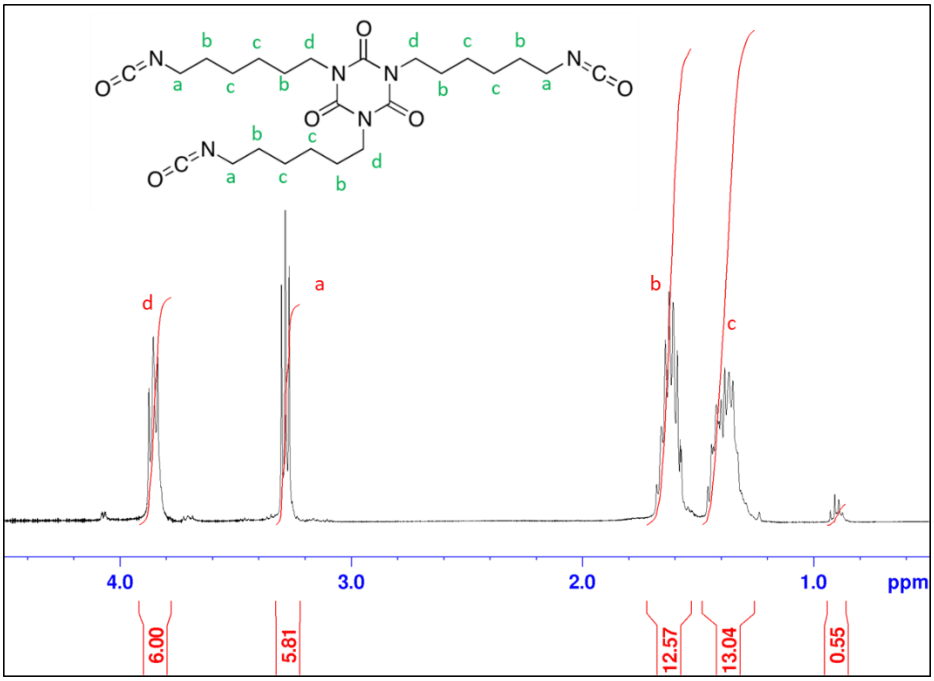

Figure B5. NMR spectra of Desmodur N3600 (referred as Isocyanate)

δ = 1.27-1.47 (m, 12H, CH_2-C<u>H</u>$_2$-CH_2), δ = 1.55-1.70 (m, 12H, CH_2-C<u>H</u>$_2$-CH_2-N), δ = 3.29 (t, 6H, CH_2-C<u>H</u>$_2$-NCO, $^3J_{HH}$ = 6.7 Hz), δ = 3.86 (t, 6H, CH_2-C<u>H</u>$_2$-N, $^3J_{HH}$ = 7.5 Hz).

t = triplet, m = multiplet

Peaks a and d were attributed based on Decostanzi et al. [4] and Nguyen et al. [5].

B.5. NMR of carbinol reaction

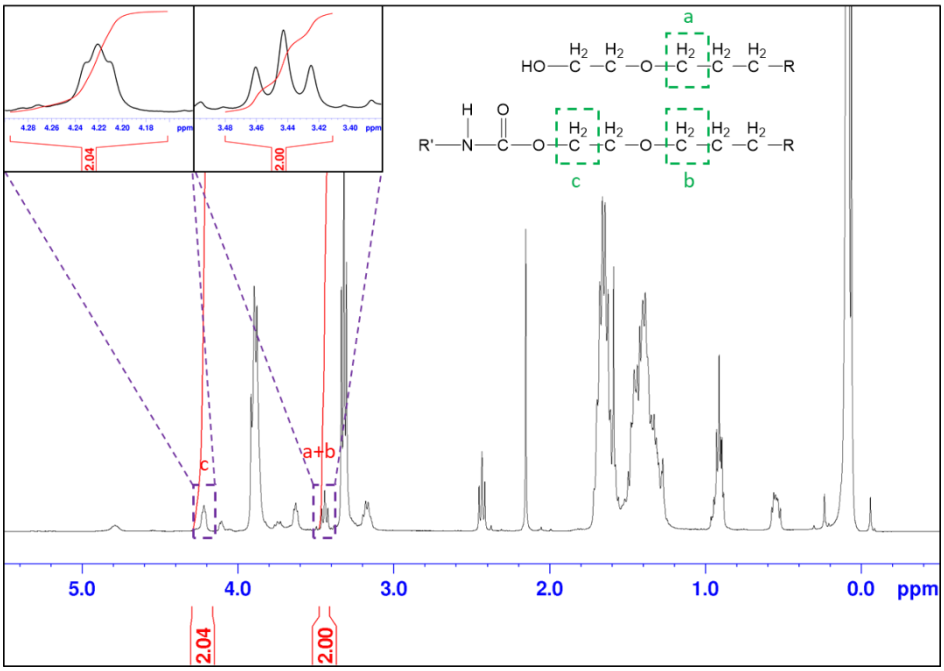

Figure B6. NMR spectra confirmation for Carbinol Reaction

Peaks a, b, and c were attributed based on Pasek-Allen et al. [2].

B.6. NMR of Aminosilane reaction

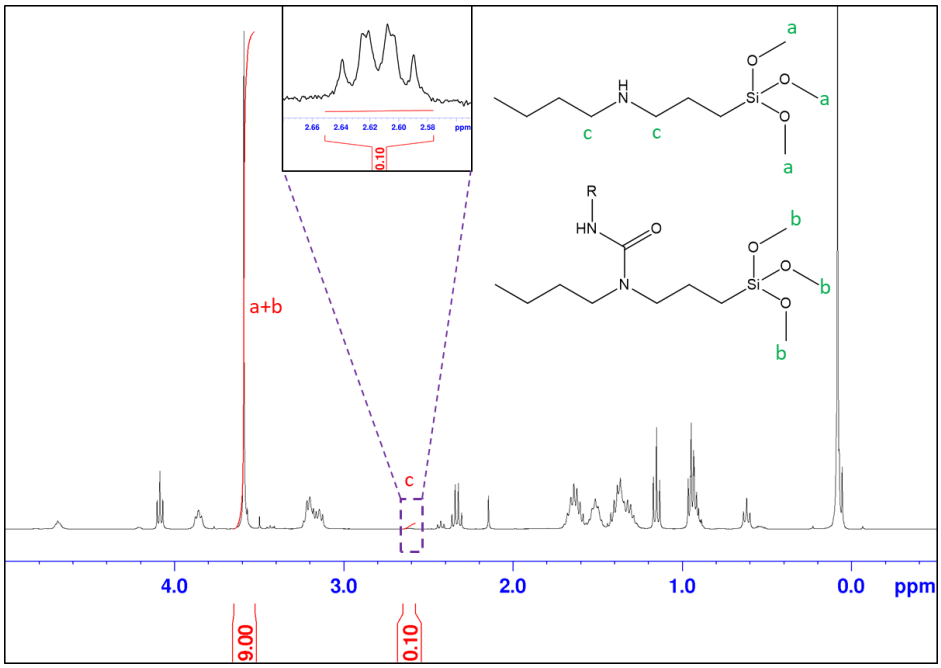

Figure B7. NMR spectra confirmation for Amino-silane reaction

B.7. Results for formulations with partially reacted carbinol functional silicone oils

All results from this point forward are for the formulations with partially reacted carbinol functional siloxane. When the carbinol functional siloxane was mixed with isocyanate at room temperature for 24 hours, around 30% of the hydroxyl groups from the carbinol functional siloxane reacted and the rest of the siloxane act as free/unreacted oils. Because of the partial reaction, there are also some unreacted isocyanate in the prepolymer.

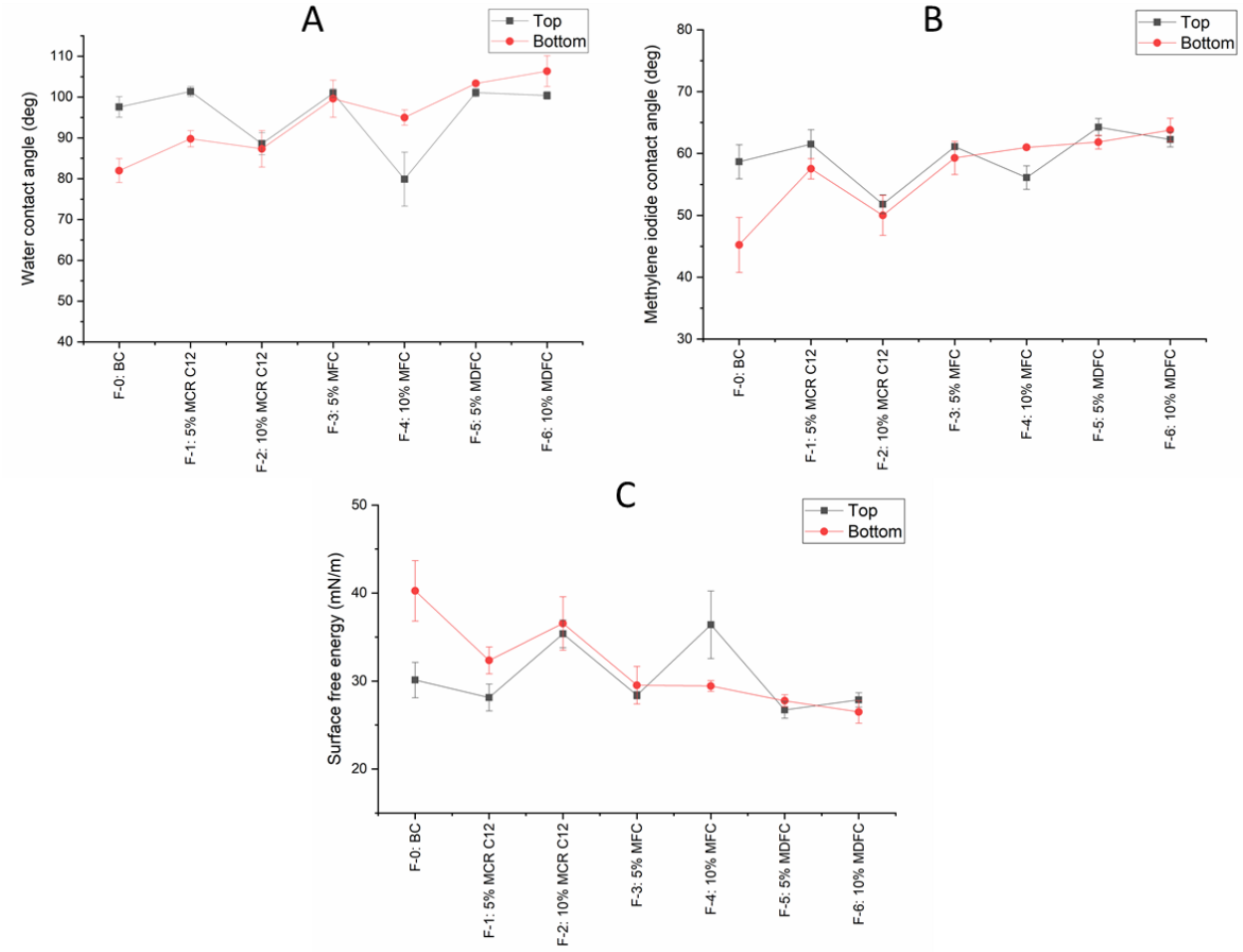

Figure B8. A. Water contact angle; B. Methylene iodide contact angle; and C. Surface free energy: E. Top side, F: Bottom side

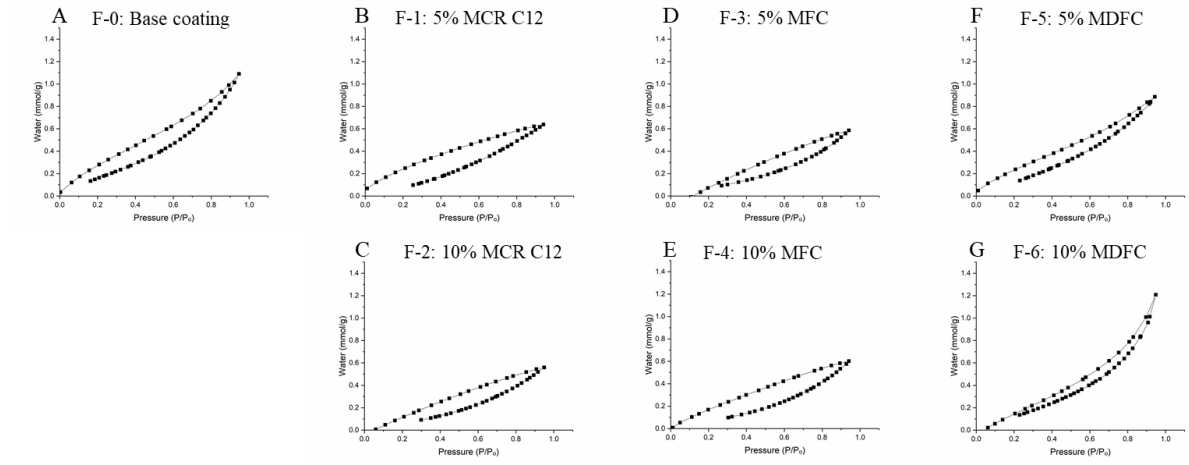

Figure B9. Water vapor absorption and desorption profile for base coating and other formulations

Initially, for the formulations with partially reacted carbinols we looked at the effect of time of mixing of the siloxane (Silres SY 231 resin) with the urea-urethane prepolymer. The AFM phase images of partially reacted MFC and MDFC coatings showed that there is no effect of time of mixing on the presence, size, and distribution of domains (Figure S10). However, we see that MFC coatings have a more uniform and smaller domain size compared with the MDFC coatings. Since there was no effect of mixing time, all the coatings were prepared with a 1 hour mixing time of siloxane with the prepolymer.

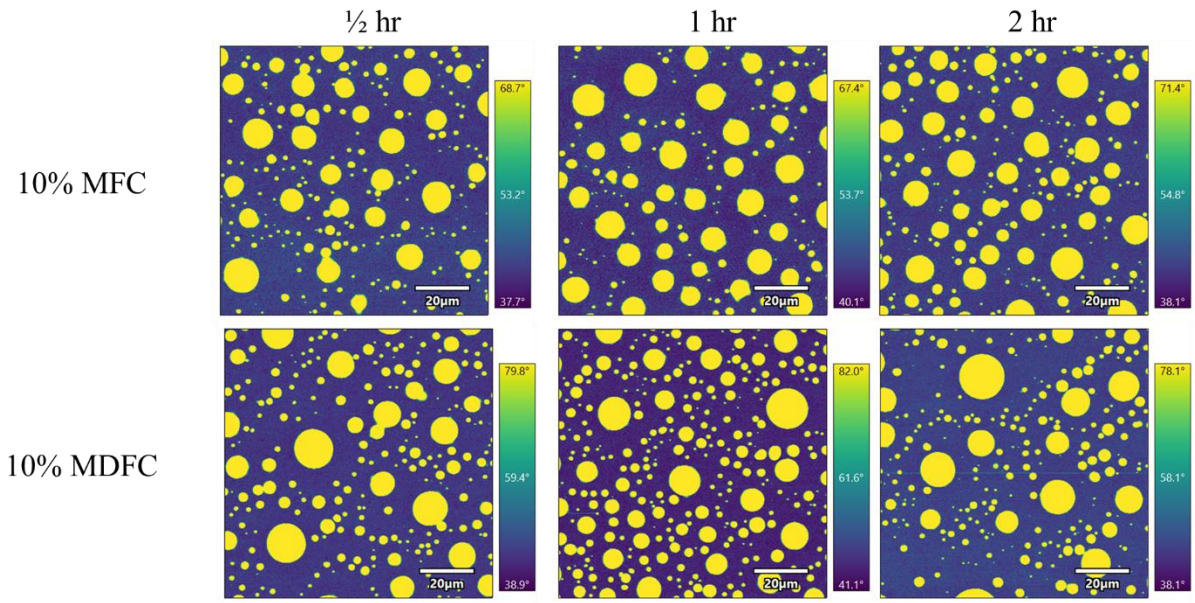

Figure B10. AFM phase images of the coatings to see the effect of mixing

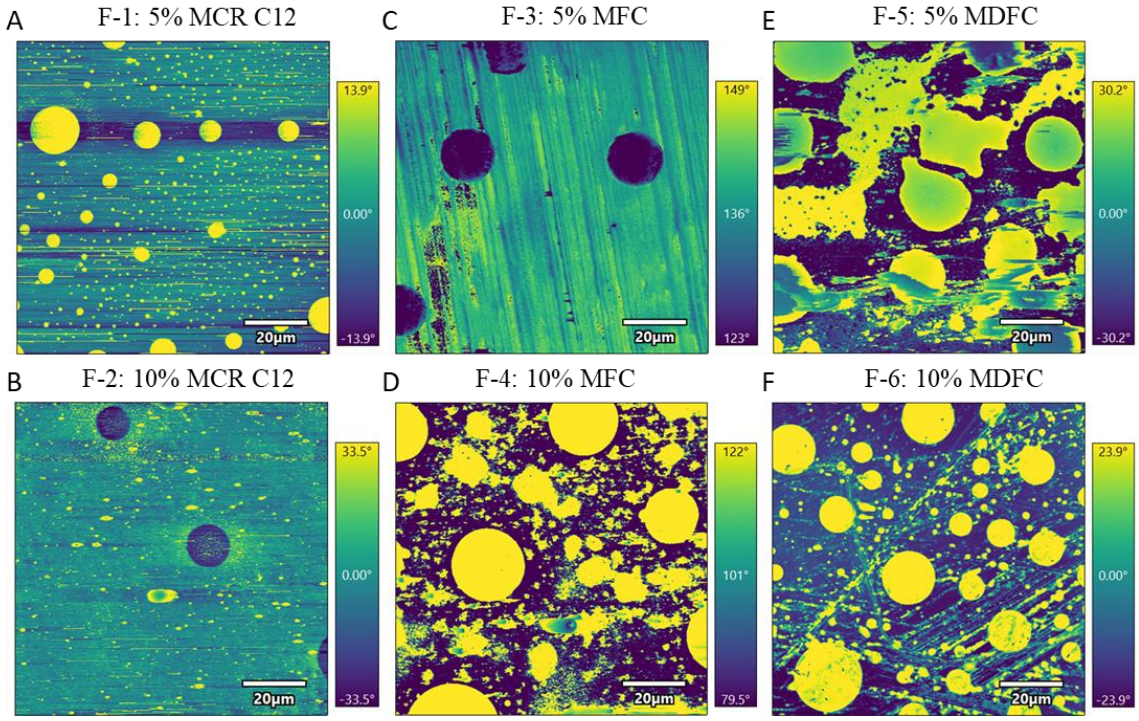

Figure B11. AFM phase images of the coatings

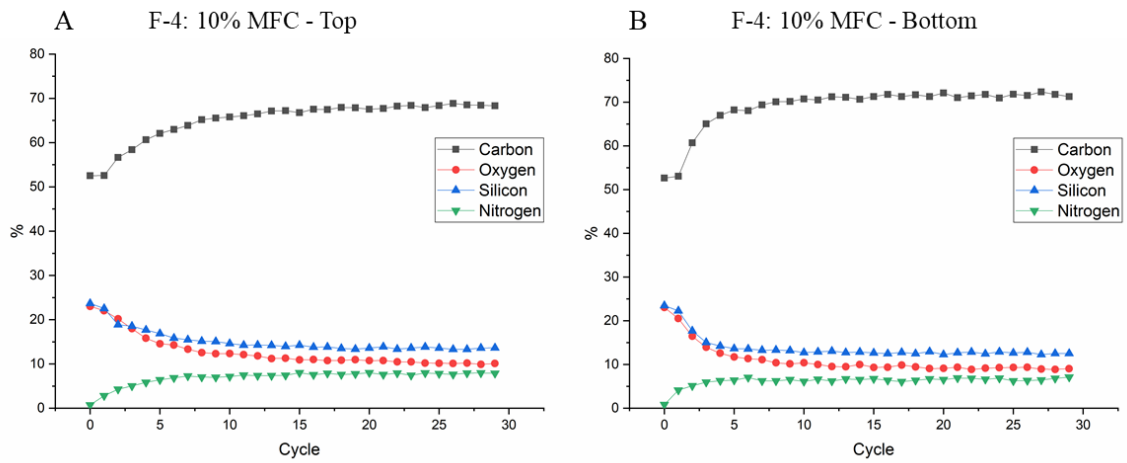

Figure B12. XPS depth profiling on the top and bottom side of the coating film

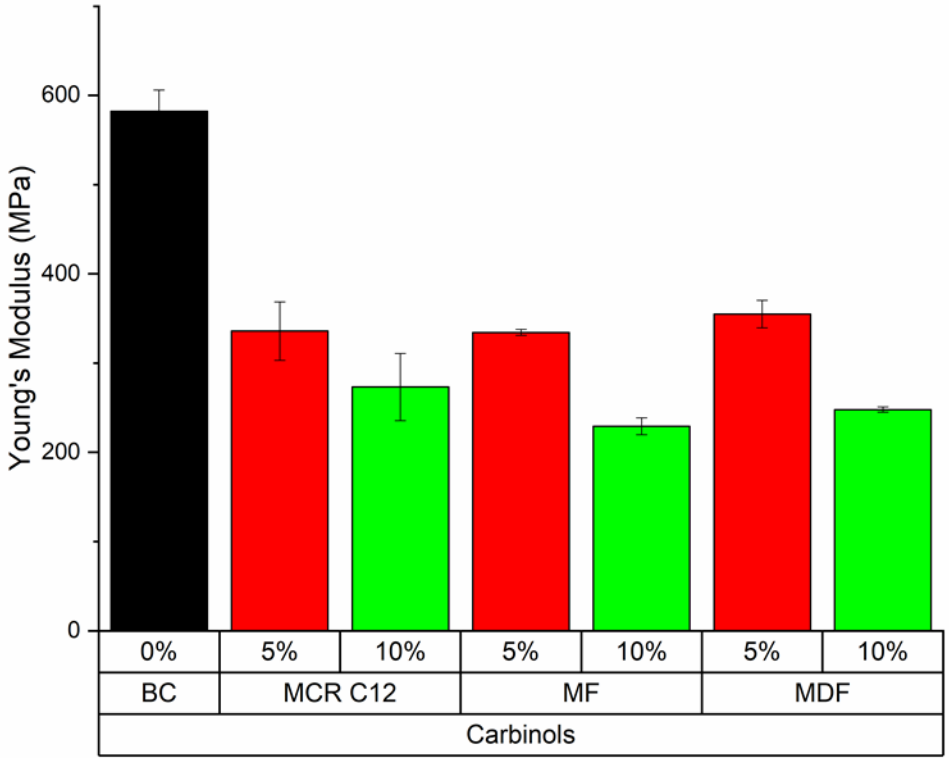

Figure B13. Young's modulus of base coatings and different formulations

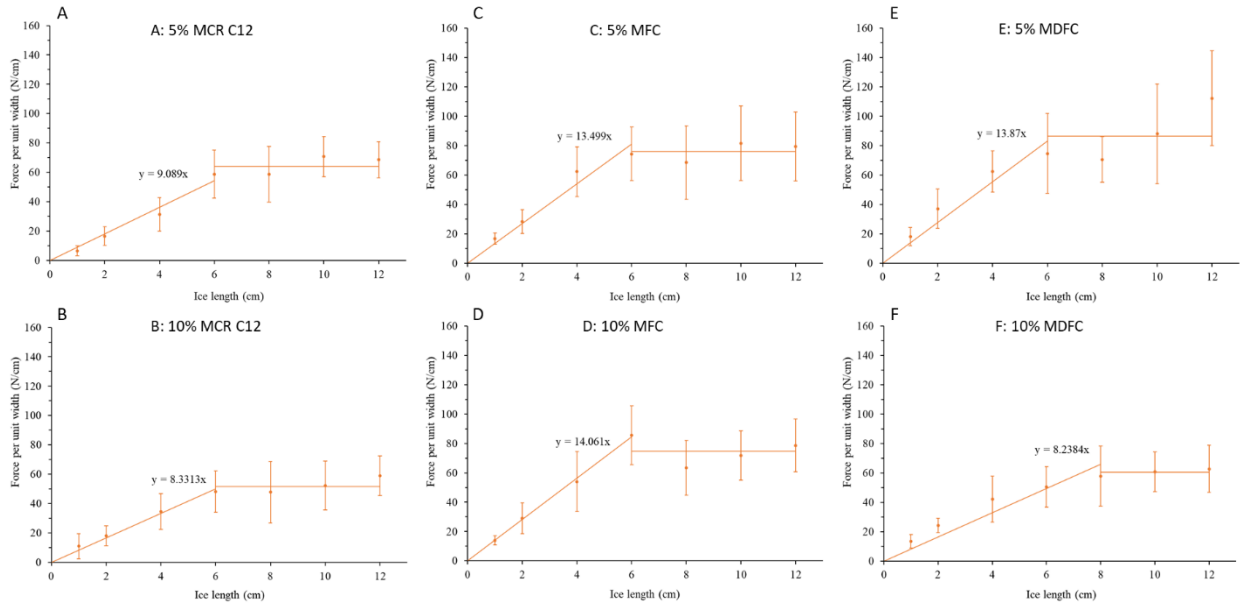

Figure B14. Force per unit width for different ice lengths for different formulations

Table B1. Summary of results of interfacial toughness measurement

Formulation	Film thickness (μm)	τ_{ice} (kPa)	Γ (J/m^2)	L_{cr} (cm)	F_{cr} (N/cm)
F-1: 5% MCR C12	66.2±17.6	90.89±26.50	0.40±0.081	6.0±3.02	64.25±6.41
F-2: 10% MCR C12	92.0±15.3	83.31±39.14	0.26±0.053	6.0±4.55	51.83±5.21
F-3: 5% MFC	76.6±17.5	134.99±24.65	0.57±0.087	6.0±1.51	76.02±5.83
F-4: 10% MFC	71.9±11.3	140.61±24.10	0.55±0.139	6.0±1.63	74.84±9.46
F-5: 5% MDFC	133.7±22.2	138.70±28.79	0.73±0.318	6.0±2.77	86.45±18.79
F-6: 10% MDFC	74.2±9.7	82.38±28.04	0.36±0.030	8.0±3.17	60.49±2.50

τ_{ice}: Ice adhesion strength, Γ: Interfacial toughness, L_{cr}: Critical length, F_{cr}: Critical force

References

1. R. Sønderbæk-Jørgensen, S. Meier, K. Dam-Johansen, A.L. Skov, A.E. Daugaard, Reactivity of Polysilazanes Allows Catalyst-Free Curing of Silicones, Macromol Mater Eng (2022). https://doi.org/10.1002/MAME.202200157.

2. J.L. Pasek-Allen, R.K. Wilharm, J.C. Bischof, V.C. Pierre, NMR Characterization of Polyethylene Glycol Conjugates for Nanoparticle Functionalization, ACS Omega 18 (2022) 6. https://doi.org/10.1021/ACSOMEGA.2C07669.
3. D. Boucher, J. Madsen, N. Caussé, N. Pébère, V. Ladmiral, C. Negrell, Hemiacetal Ester Exchanges, Study of Reaction Conditions and Mechanistic Pathway, Reactions 2020, Vol. 1, Pages 89-101 1 (2020) 89–101. https://doi.org/10.3390/REACTIONS1020008.
4. M. Decostanzi, R. Auvergne, E. Darroman, B. Boutevin, S. Caillol, Reactivity and kinetics of HDI-iminooxadiazinedione: Application to polyurethane synthesis, Eur Polym J 96 (2017) 443–451. https://doi.org/10.1016/J.EURPOLYMJ.2017.09.032.
5. L.T.T. Nguyen, X.K.D. Hillewaere, R.F.A. Teixeira, O. Van Den Berg, F.E. Du Prez, Efficient microencapsulation of a liquid isocyanate with in situ shell functionalization, Polym Chem 6 (2015) 1159–1170. https://doi.org/10.1039/C4PY01448K.

APPENDIX C. CHAPTER 4 SUPPLEMENTAL INFORMATION

Table C1. Inventory for LCA

Name of the component	Database	Year	Location	Comment
Electricity	Ecoinvent 3	2018	US midwest	
Heat	Ecoinvent 3	2018	RoW*	
Cooling water	Ecoinvent 3	2018	RoW*	
PMHS blowing agent	Ecoinvent 3	2020	Global	Modeled similar to PDMS
TAEA crosslinker				Based on US patent CA2009364C
NTAN				Based on US patent 4731465
Formaldehyde	Ecoinvent 3	2017	Global	
Sulfuric acid	Ecoinvent 3	2017	Global	
Hydrogen cyanide	Ecoinvent 3	2018	RoW*	
Hydrogen	Plastics europe	2005		
Ammonia	Plastics europe	2005		
Nickel catalyst	Ecoinvent 3	2018	Global	
1,4-butanediol	Ecoinvent 3	2018	Global	
tBAA				Based on US patent 5109131
Diketene	Ecoinvent 3	2018	RoW*	Modeled similar to acetic anhydride
Pyridine	Ecoinvent 3	2018	RoW*	
t-butanol				Based on US patent 4011272
Deionized water	Ecoinvent 3	2018	RoW*	
Acetic acid	Ecoinvent 3	2020	RoW*	
Isobutylene	GREET	2019		
Lignin byproduct from biorefinery				Modeled based on NREL dilute acid model, economic allocation
Urea	Ecoinvent 3	2018	RoW*	
Nitrogen fertilizer	Ecoinvent 3	2018	RoW*	
Potassium sulfate	Ecoinvent 3	2018	RoW*	
Diesel	Ecoinvent 3	2018	Global	
Truck transport	USLCI	2018	US	

*RoW - Rest of the world

The data for Kraft lignin is based on Bernier et al. [1] and biorefinery lignin is based on Humbird et al. [2]. The biogenic carbon content in Kraft lignin is calculated assuming 30% lignin composition in hardwood, 60% carbon content in lignin, and 90% lignin in black liquor.

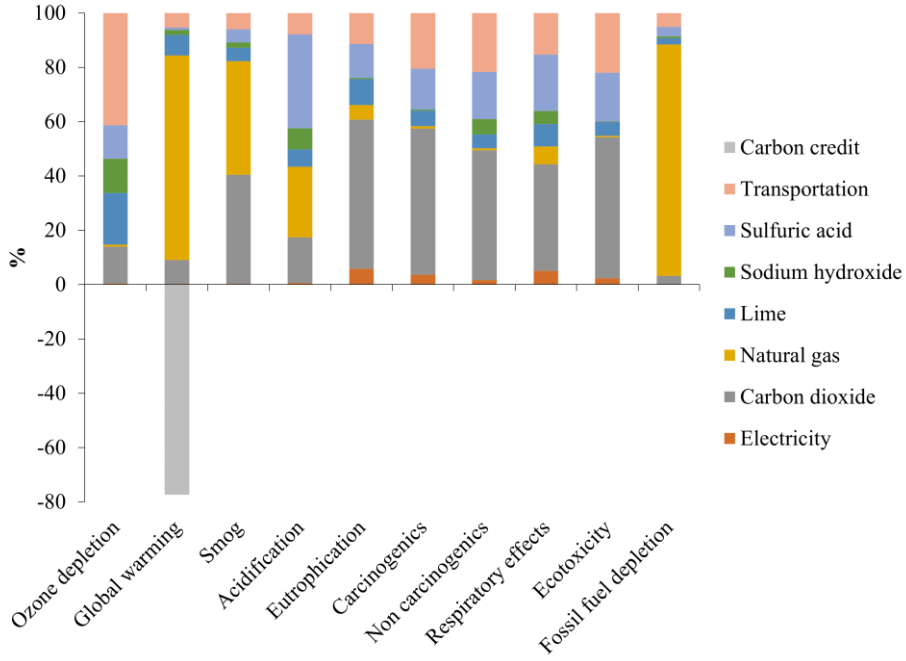

Figure C1. Life cycle analysis of kraft lignin [1]

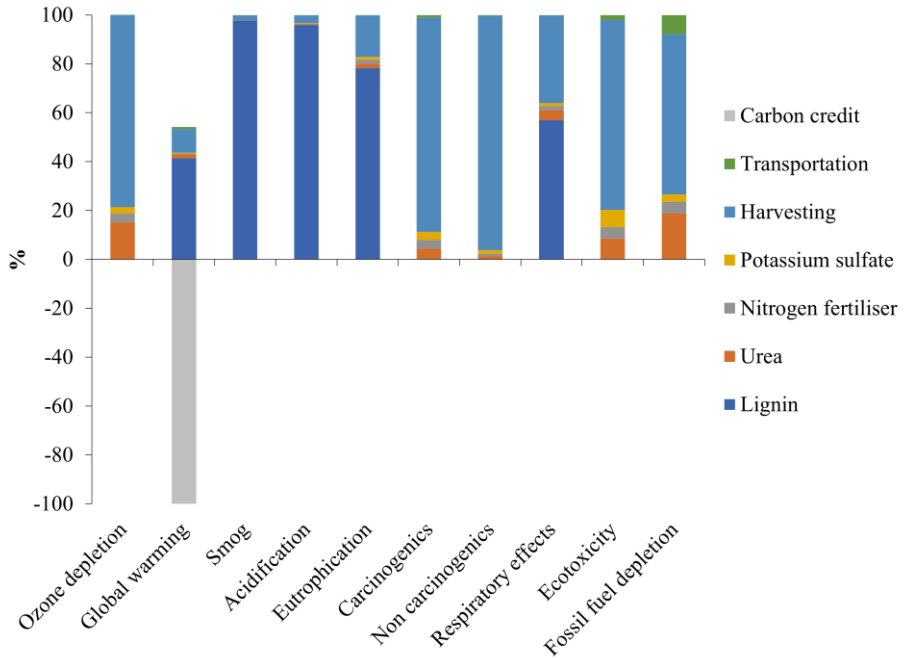

Figure C2. Life cycle analysis of biorefinery lignin [2]

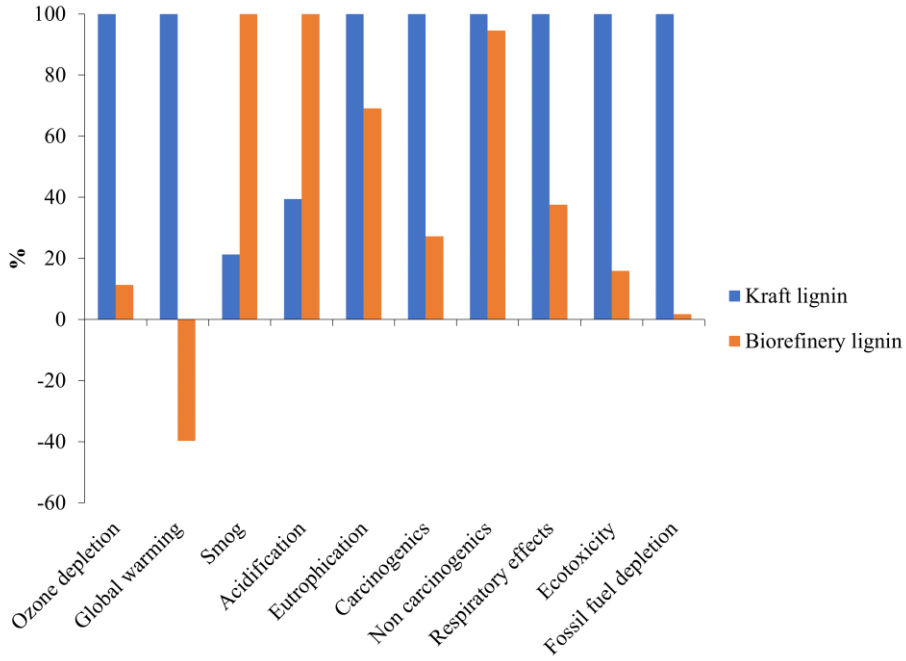

Figure C3. Life cycle analysis comparison of biorefinery lignin and Kraft lignin

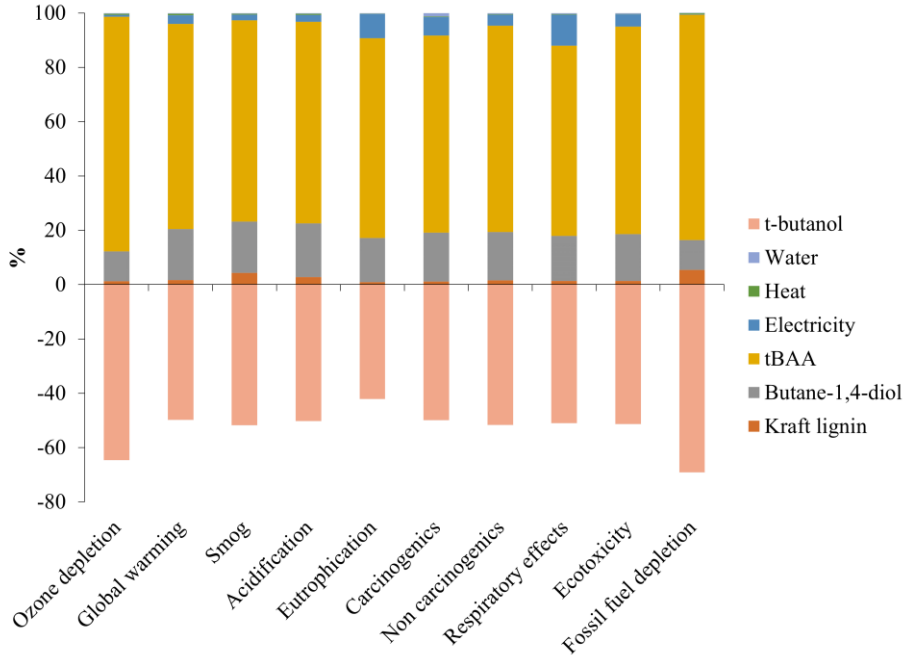

Figure C4. Life cycle analysis of resin production considering t-butanol as avoided product (system expansion)

References

1. Bernier E, Lavigne C, Robidoux PY (2013) Life cycle assessment of kraft lignin for polymer applications. International Journal of Life Cycle Assessment 18:520–528. https://doi.org/10.1007/S11367-012-0503-Y/FIGURES/3
2. Humbird D, Davis R, Tao L, et al (2011) Process Design and Economics for Biochemical Conversion of Lignocellulosic Biomass to Ethanol: Dilute-Acid Pretreatment and Enzymatic Hydrolysis of Corn Stover. Golden, CO (United States)

APPENDIX D. CHAPTER 5 SUPPLEMENTAL INFORMATION[1]

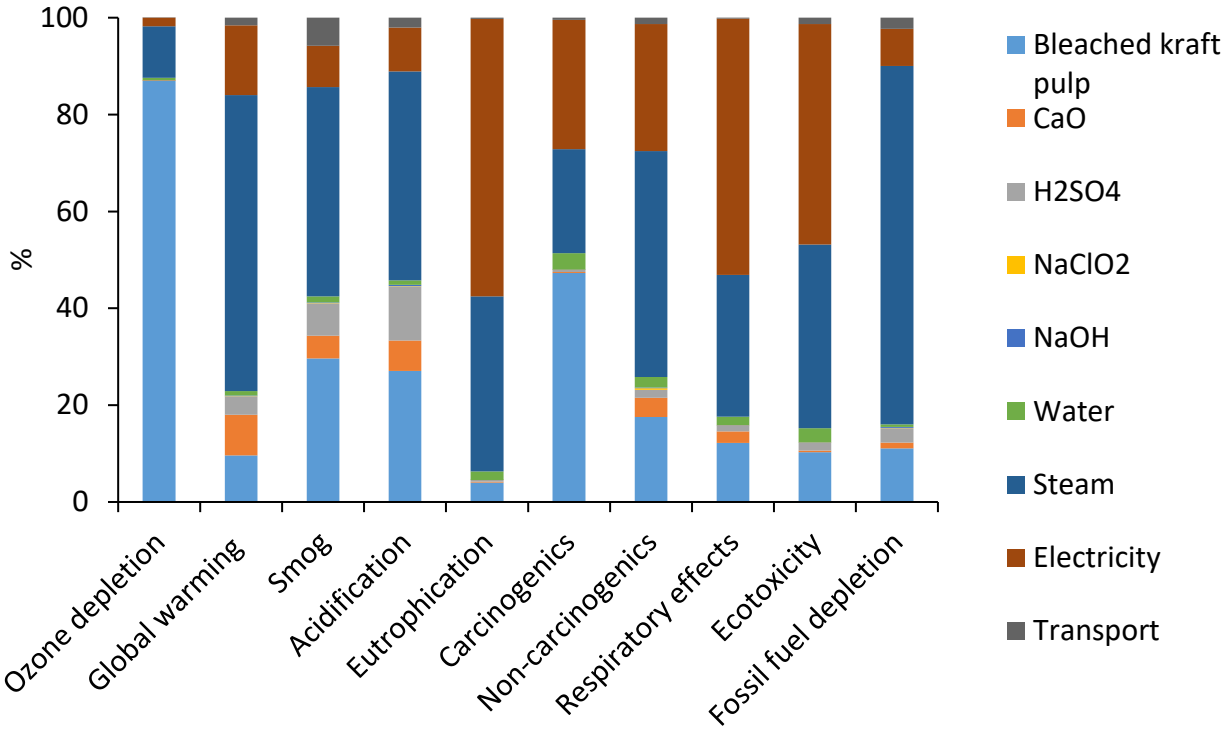

Figure D1. LCA result of CNC production with acid recovery based on Rajendran et. al. [1]

Based on Figure D2, magnesium sulfate, calcium chloride, strontium bromide, and zinc sulfate have the lowest impacts compared to other salts in most of the categories. The global warming potential of these salts is 0.44, 0.71, 0.38, and 0.69 kg CO2 eq. per kg of salt, respectively.

[1] The material in this chapter was co-authored by Ramsharan Pandey, Ghasideh Pourhashem, and Adam C. Gladen. Ramsharan had primary responsibility for conceptualization, methodology, formal analysis, visualization, writing original draft, and review and editing. Ghasideh Pourhashem and Adam C. Gladen supervised and revised the work. This chapter is published in 'Sustainable Materials and Technologies' journal. To cite: Pandey, R., Pourhashem, G., & Gladen, A. C. (2024). Screening of salt hydrates and cellulose nanocrystal composites for thermochemical energy storage using life cycle assessment. Sustainable Materials and Technologies, 40, e00889. DOI: https://doi.org/10.1016/j.susmat.2024.e00889.

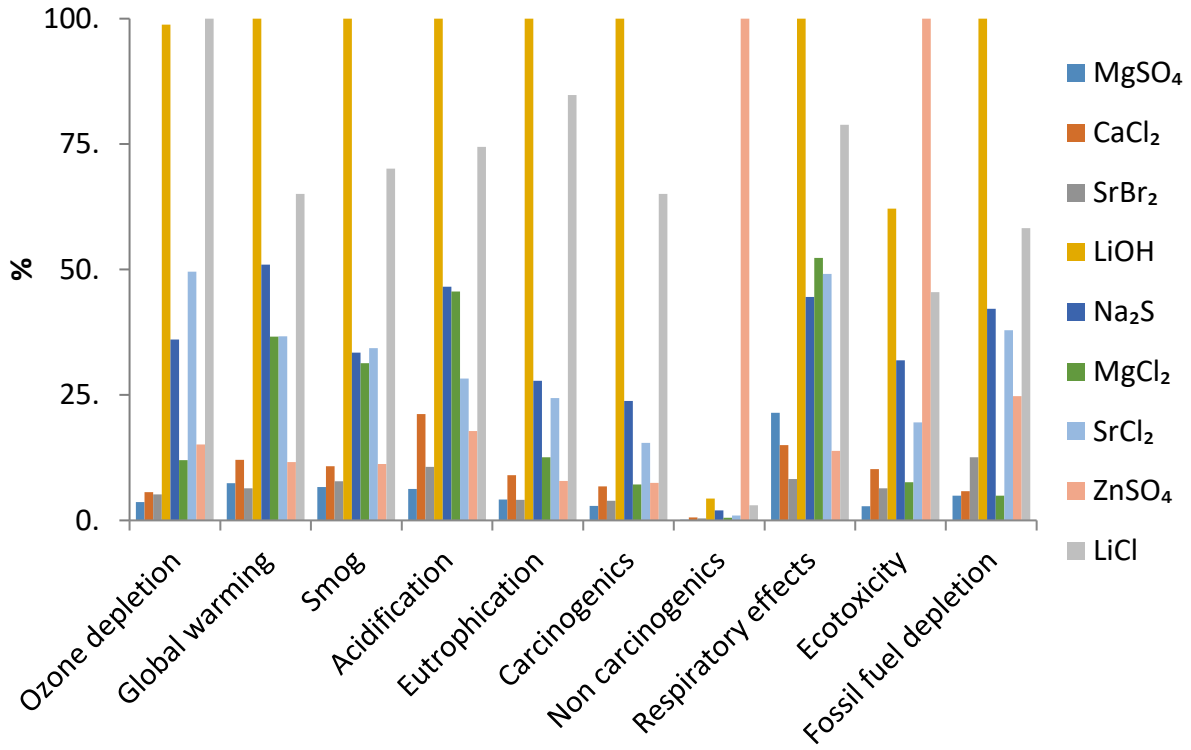

Figure D2. LCA result comparison of salts on mass basis

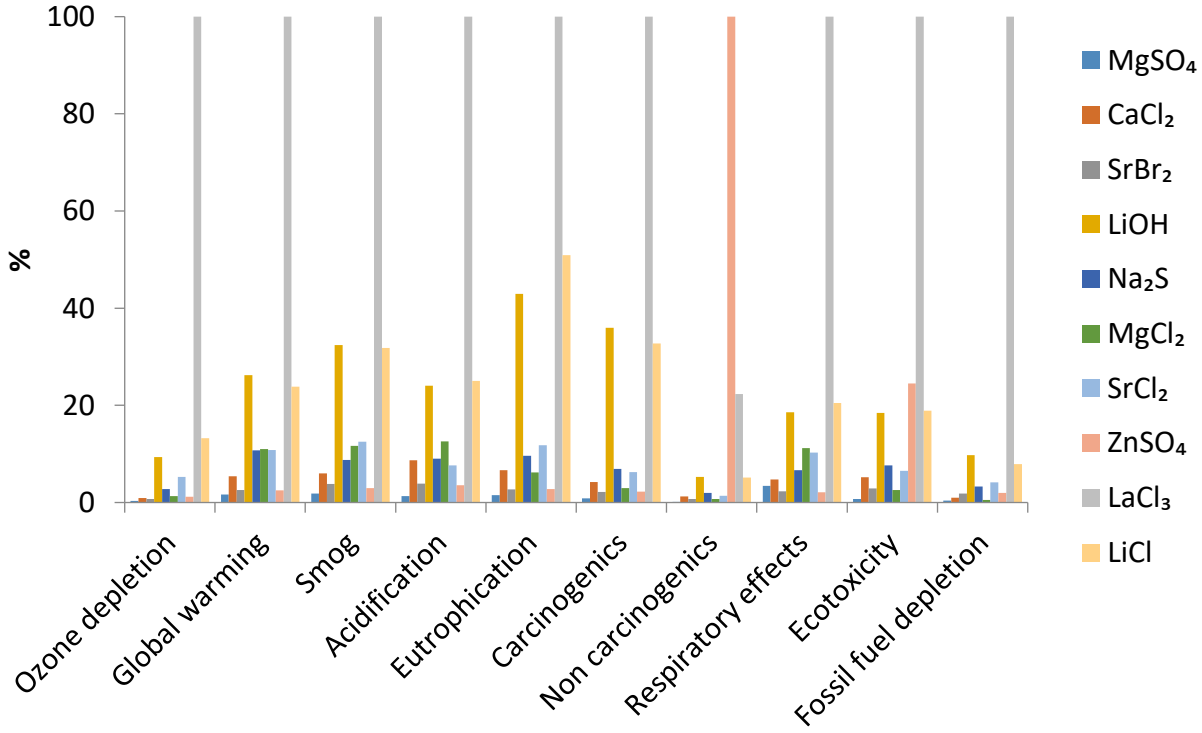

Figure D3. LCA result comparison of salts on energy basis

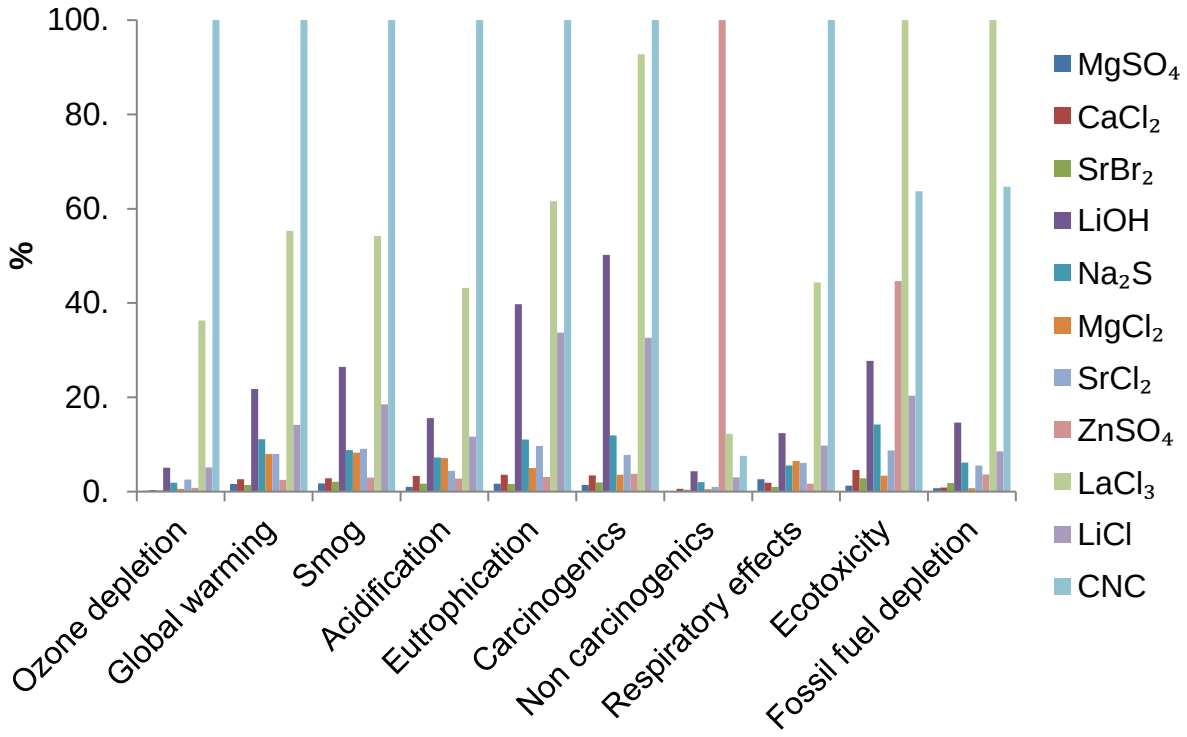

Figure D4. LCA result comparison of salts and CNC on mass basis (per kg)

Due to the relatively high impact of CNC, it amplifies the difference between salts when converted from mass basis to energy basis. We can see this effect in Figure D5 and Figure 4. For example, in Figure D5, the composite with strontium bromide has a lower or similar impact in all categories compared to strontium chloride on a mass basis, but in Figure 5.4, we can see that strontium chloride composite performs better than strontium bromide composite in all categories because strontium chloride has higher energy density.

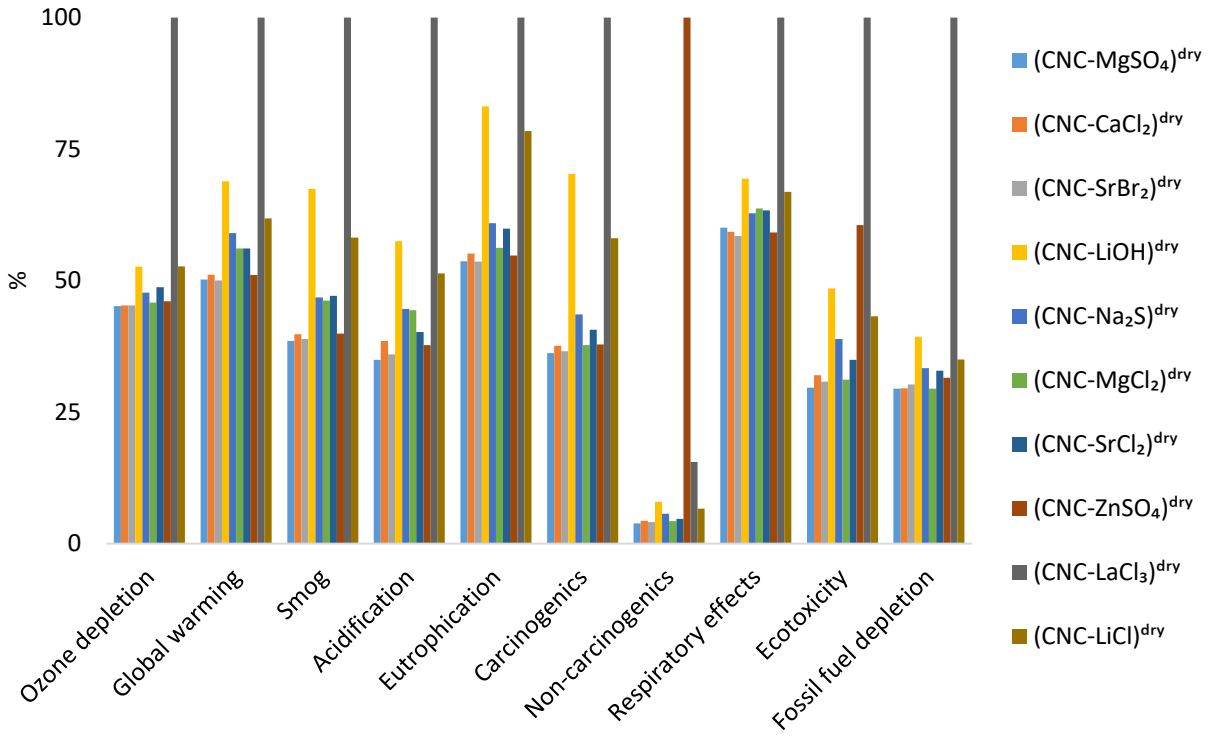

Figure D5. LCA result of salt-CNC composite on mass-basis (lab scale)

For mass basis, even though there is a less of a distinction between choice of the salt in the composite (Figure D6) due to higher impacts from other processes, strontium bromide, magnesium sulfate, zinc sulfate, and calcium chloride result in a composite that has fairly low global warming potentials compared to other salts. CNC is still a major impact contributor in all these composites.

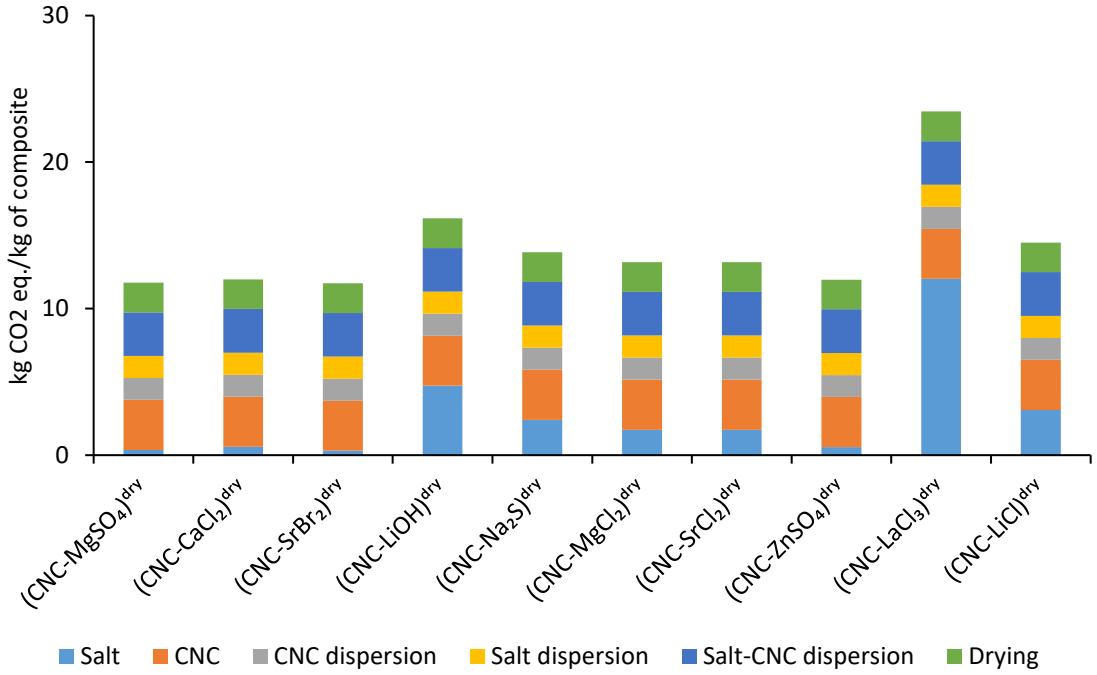

Figure D6. Global warming potential comparison of different salt-CNC composites on mass basis (lab scale)

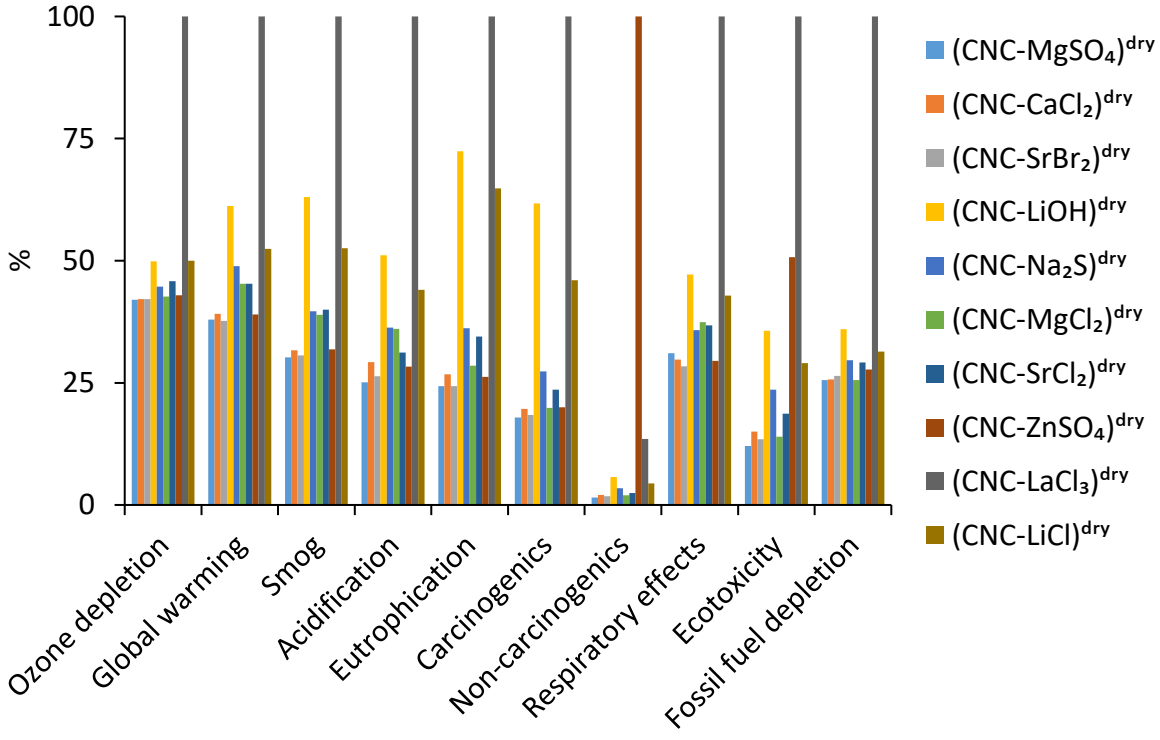

Figure D7. LCA result of salt-CNC composite on a mass-basis for a 10 ton per day composite production capacity

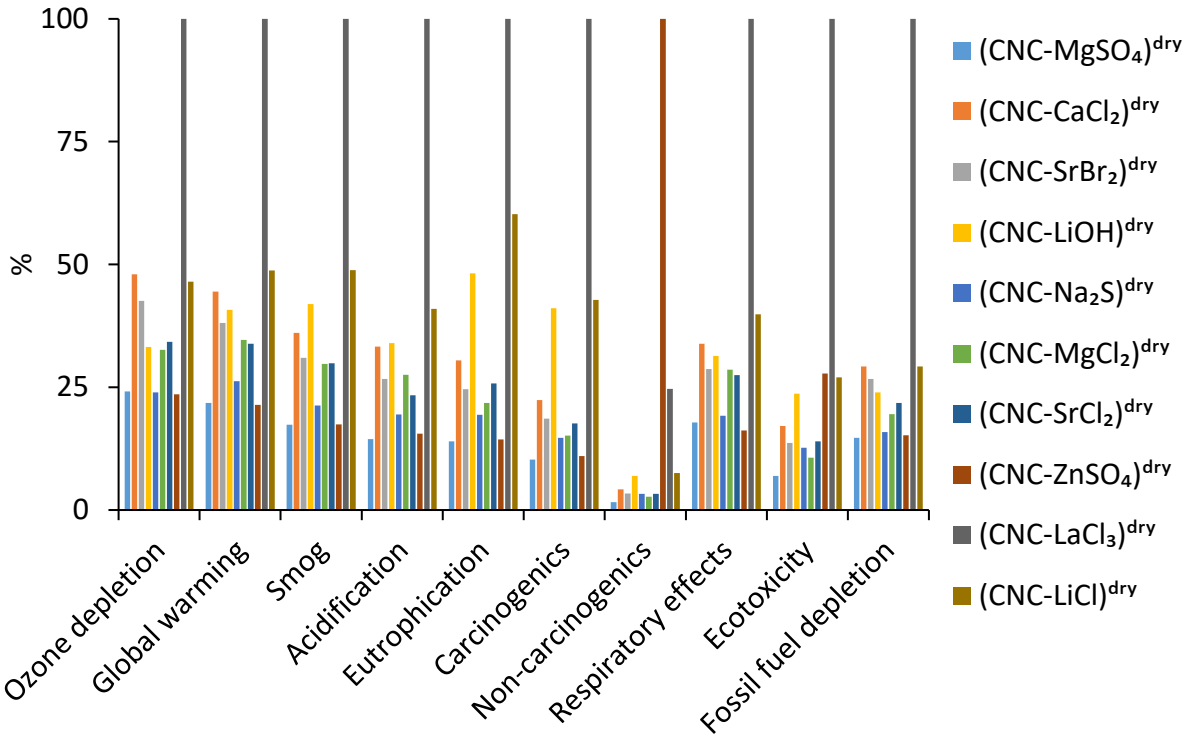

Figure D8. LCA result of salt-CNC composite on an energy-basis for a 10 ton per day composite production capacity

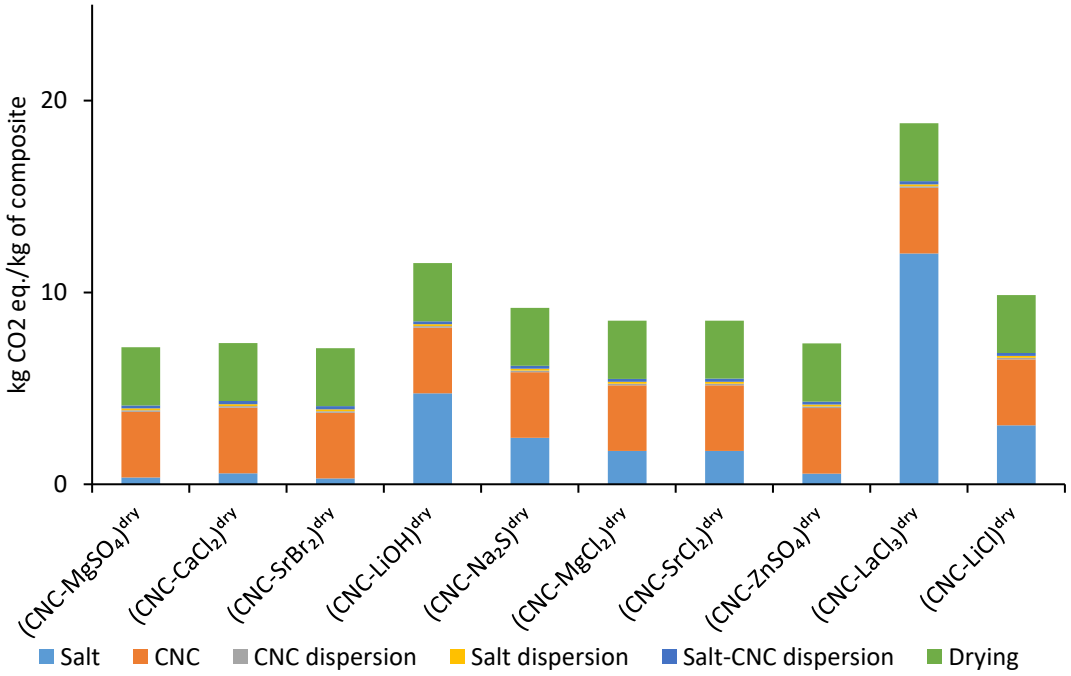

Figure D9. Global warming potential comparison of different salt-CNC composites for a 10 ton per day composite production capacity (mass basis)

For a lab-scale salt-CNC composite production, the mass based CED for different salt-CNC composites ranged between 200 to 500 MJ/kg composite (Figure D10a). Magnesium sulfate had the least embodied energy while lanthanum chloride had the highest. The scaled-up salt-CNC composite production showed a significant reduction in CED, which is due to the reduction in process energy. The scaled-up CED ranged between 140 to 440 MJ/kg composite (Figure D10b).

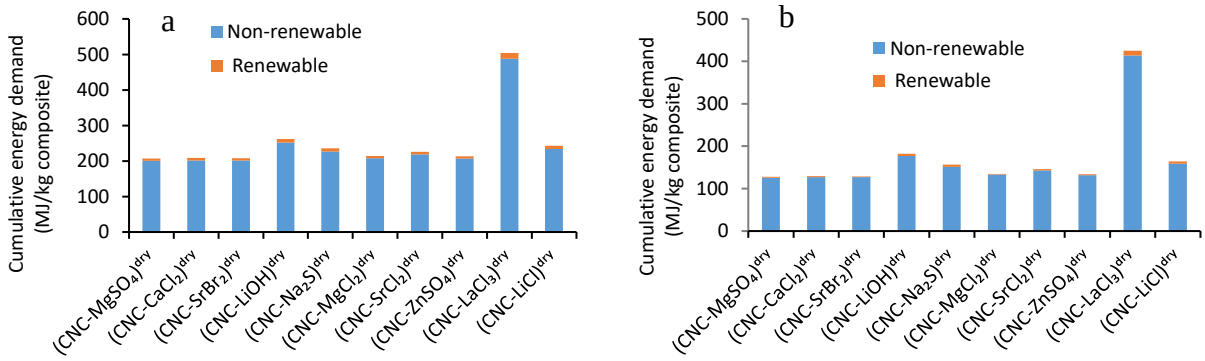

Figure D10. CED of different salt-CNC composites for (a) lab-scale model, and (b) scaled-up process (10 ton per day capacity)

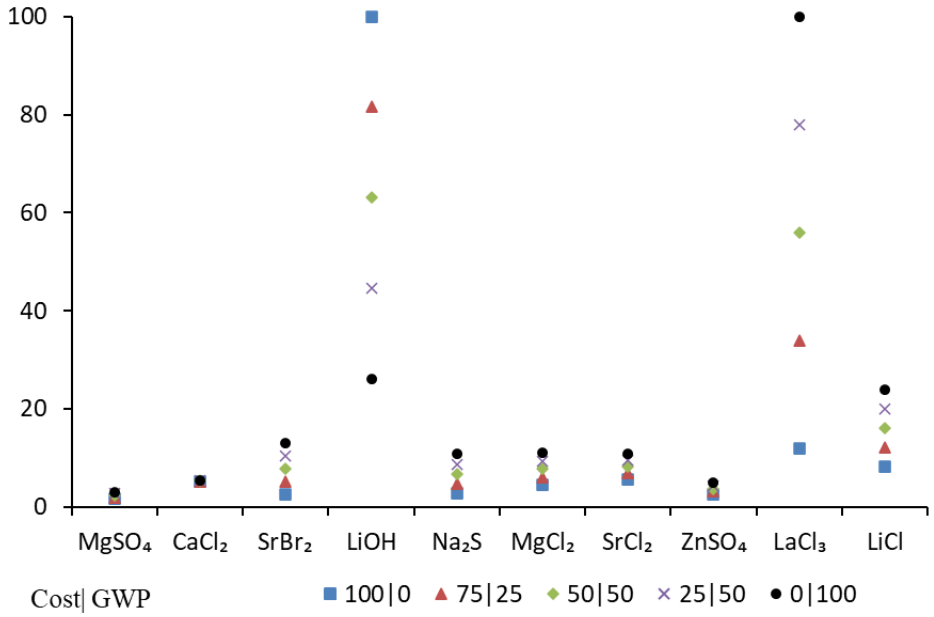

Figure D11. Ranking of salts based on a. weighted average cost and global warming potential, b. weighted average cost and global warming potential without lithium hydroxide and lanthanum chloride

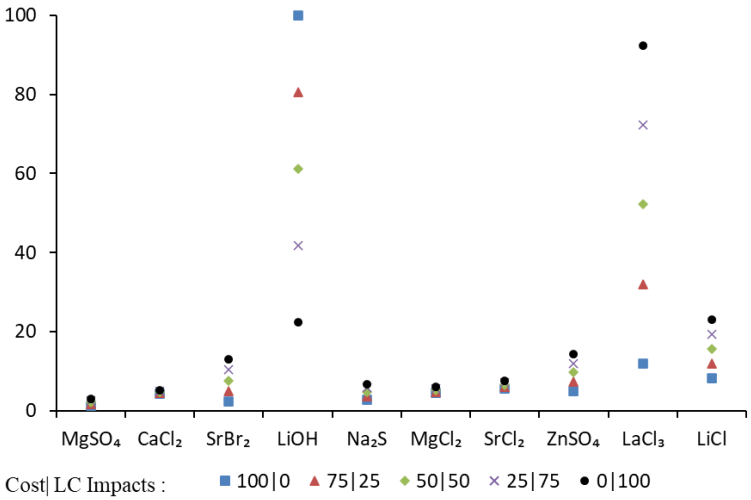

Figure D12. Ranking of salts based on a. weighted average cost and 10 different life cycle impact indicators, b. weighted average cost and 10 different life cycle impact indicators without lithium hydroxide and lanthanum chloride

Table D1. Price of different salts (All prices in 2022 US$ and converted to anhydrous salts)

S.No.	Salts	Unit	Price ($/unit)	Source	Comment
1	Magnesium sulfate ($MgSO_4$)	ton	$390	[3]	2022 (North America)
2	Calcium chloride ($CaCl_2$)	ton	$102	[4]	2018 (China)
3	Strontium bromide ($SrBr_2$)	ton	$3000 - 22000	[5]	2017 (€ 2,400 – 17,600) 1 € = 0.98 $
4	Lithium hydroxide (LiOH)	ton	$51,000	[6]	2022 (North America)
5	Sodium sulfide (Na_2S)	ton	$300-500	[7]	2022 (China)
6	Magnesium chloride ($MgCl_2$)	ton	$525	[8]	2022 (North America)
7	Strontium chloride ($SrCl_2$)	ton	$650	[9]	2022 (China)
8	Zinc sulfate ($ZnSO_4$)	ton	$1,700	[10]	2017 (China) - $1,340
9	Lanthanum chloride ($LaCl_3$)	ton	$1,800-2,000	[11]	2022 (China)
10	Lithium chloride (LiCl)	ton	$1,574-1,874	[12]	2022 (China)

The price of CNC is taken as $6/kg (2022), the average price from the two studies [1,2].

Calculation of Energy consumption in salt-CNC production for lab scale process

For CNC:

Stirrer for mixing: 3.6 W for 8 h

Ultrasonicator: 1000 W for 5 min

10 g CNC mixed in 400 ml DI water

- Energy for stirring 10 g CNC: $3.6\ W \cdot 8\ h\ \cdot \frac{3600\ s}{h} = 103.68\ kJ$ (per 10 g CNC)
- Energy for ultrasonication of 10 g CNC: $1000\ W \cdot 5\ min\ \cdot \frac{60\ s}{min} = 300\ kJ$ (per 10 g CNC)

Normalized value:

- Energy for stirring 1 kg CNC = $103.68\ kJ \cdot \frac{1000\ g}{10\ g} = 10368\ kJ = 10368\ kJ \cdot \frac{1\ h}{3600\ s} = 2.88\ kWh$
- Energy for ultrasonicating 1 kg CNC = $300\ kJ \cdot \frac{1000\ g}{10\ g} = 30000\ kJ = 30000\ kJ \cdot \frac{1\ h}{3600\ s} = 8.33\ kWh$

For salt:

Stirrer for mixing: 3.6 W for 8 h

Ultrasonicator: 1000 W for 5 min

40 g salt mixed in 100 ml DI water

- Energy for stirring 40 g salt: $3.6\ W \cdot 8\ h\ \cdot \frac{3600\ s}{h} = 103.68\ kJ$ (per 40 g salt)
- Energy for ultrasonication of 40 g salt: $1000\ W \cdot 5\ min\ \cdot \frac{60\ s}{min} = 300\ kJ$ (per 40 g salt)

Normalized value:

- Energy for stirring 1 kg salt = $103.68\ kJ \cdot \frac{1000\ g}{40\ g} = 2592\ kJ = 2592\ kJ \cdot \frac{1\ h}{3600\ s} = 0.72\ kWh$
- Energy for ultrasonicating 1 kg salt = $300\ kJ \cdot \frac{1000\ g}{40\ g} = 7500\ kJ = 7500\ kJ \cdot \frac{1\ h}{3600\ s} = 2.083\ kWh$

For composite:

Stirrer for mixing: 3.6 W for 8 h

Ultrasonicator: 1000 W for 5 min

5 g CNC in 200 ml DI water mixed with 20 g salt in 200 ml DI water

- Energy for stirring 25 g salt-CNC: $3.6\ W \cdot 8\ h\ \cdot \frac{3600\ s}{h} = 103.68\ kJ$ (per 25 g salt-CNC)
- Energy for ultrasonication of 25 g salt-CNC: $1000\ W \cdot 5\ min\ \cdot \frac{60\ s}{min} = 300\ kJ$ (per 25 g salt-CNC)

Normalized value:

- Energy for stirring 1 kg salt-CNC = $103.68\ kJ \cdot \frac{1000\ g}{25\ g} = 4147.2\ kJ = 4147.2\ kJ \cdot \frac{1\ h}{3600\ s} = 1.15\ kWh$
- Energy for ultrasonicating 1 kg salt-CNC = $300\ kJ \cdot \frac{1000\ g}{25\ g} = 12000\ kJ = 12000\ kJ \cdot \frac{1\ h}{3600\ s} = 3.33\ kWh$

1 kg composite = 200 g CNC + 800 g salt

Total energy for dispersion of 1 kg composite $= Energy\ for\ dispersing\ 200\ g\ CNC + Energy\ for\ dispersing\ 800\ g\ salt + Energy\ for\ dispersing\ 1\ kg\ salt - CNC\ compsoite$

$= \frac{200\ g}{1000\ g} \cdot (2.88\ kWh + 8.33\ kWh) + \frac{800\ g}{1000\ g} \cdot (0.72\ kWh + 2.083\ kWh) + (1.15\ kWh + 3.33\ kWh) = 2.242\ kWh + 2.242\ kWh + 4.48\ kWh = 8.97 kWh$

References

1. N. Rajendran, T. Runge, R.D. Bergman, P. Nepal, C. Houtman, Techno-economic analysis and life cycle assessment of cellulose nanocrystals production from wood pulp, Bioresour. Technol. 377 (2023) 128955. https://doi.org/10.1016/J.BIORTECH.2023.128955.
2. de Assis, C. A., Houtman, C., Phillips, R., Bilek, E. M. T., Rojas, O. J., Pal, L., Peresin, M. S., Jameel, H., & Gonzalez, R. (2017). Conversion Economics of Forest Biomaterials:

Risk and Financial Analysis of CNC Manufacturing. Biofuels, Bioproducts and Biorefining, 11(4), 682–700. https://doi.org/10.1002/BBB.1782

3. ChemAnalyst (2022) Magnesium Sulphate Prices. https://www.chemanalyst.com/Pricing-data/magnesium-sulphate-1249. Accessed on 14 Nov 2022
4. ECHEMI (2022) Calcium Chloride Price. https://www.echemi.com/productsInformation/temppid160705011137-calcium-chloride.html. Accessed on 14 Nov 2022
5. Gilles, D., Segato, T., Courbon, E., Degrez, M., & D'Ans, P. (2018). Affordable process for the production of strontium bromide used in low grade heat recovery applications. Procedia Cirp, 69, 383-388.
6. ChemAnalyst (2022) Lithium Hydroxide Prices. https://www.chemanalyst.com/Pricing-data/lithium-hydroxide-1267. Accessed on 14 Nov 2022
7. Made in China (2022) Sodium Sulfide Price. https://www.made-in-china.com/price/sodium-sulfide-price.html. Accessed on 14 Nov 2022
8. ChemAnalyst (2022) Magnesium Chloride Prices. https://www.chemanalyst.com/Pricing-data/magnesium-chloride-1403. Accessed on 14 Nov 2022
9. Made in China (2022) Strontium Chloride Price. https://ditaichem.en.made-in-china.com/product/xvaEbBijZwkU/China-High-Purity-Strontium-Chloride-Hexahydrate-Powder.html. Accessed on 14 Nov 2022
10. ECHEMI (2022) Zinc Sulphate Price. https://www.echemi.com/productsInformation/pid_Rock20790-zincsulphate.html. Accessed on 14 Nov 2022

11. Made in China (2022) Lanthanum Chloride Price. https://fitech.en.made-in-china.com/product/YXBQjmAyHdUx/China-White-Crystalline-Lacl3-7H2O-99-95-Lanthanum-Chloride.html. Accessed on 14 Nov 2022

12. Made in China (2022) Lithium Chloride Price. https://hebeiaifosen.en.made-in-china.com/product/uFwTSzqYbAUP/China-99-99-Anhydrous-Lithium-Chloride-CAS-7447-41-8.html. Accessed on 14 Nov 2022